Investigation of a semi-closed cycle small gas turbine for high altitude UAV propulsion

by

Jacopo Tacconi

As partial fulfillment of the requirements
for my degree in

Aerospace engineering
Master of Science

at Delft University of Technology

04 September 2018

Department of Propulsion and Power
Flight Performance and Propulsion

Delft University of Technology
Department of
Flight Performance and Propulsion

The hereby presented certifies that this thesis work, entitled "Investigation of a semi-closed cycle small gas turbine for high altitude UAV propulsion" and performed by Jacopo Tacconi in cooperation with the University of Sydney, Australia, under the supervision of professor Wilfried Visser and professor Dries Verstraete, has been accepted by the School of Aerospace Engineering of Delft University of Technology as partial fulfillment of the requirements for the degree of Master of Science in Aerospace Engineering.

Date: 04 September 2018

Department Chairholder:	.....
Delft University of Technology	Prof. Dr. Ir. P. Colonna
Supervisor:	.....
Delft University of Technology	Dr. Ir. W. P. J. Visser
Supervisor:	.....
The University of Sydney	Dr. Ir. D. Verstraete
Reader:	.....
Delft University of Technology	Prof. Dr. Ir. S. Klein

Page intentionally left blank

Summary

Semi-closed cycles have been successfully employed in different engineering areas, such as in marine and power generation. The primary characteristic of a semi-closed cycle arrangement is that a considerable portion of the total mass flow required for a certain power output is recirculated within the engine itself. As a consequence, the amount of inlet fresh air supplied has only to be sufficient to sustain the combustion process. The resultant gas turbines have shown competitive performance with a higher level of compactness with respect to conventional aero-derived open cycle solutions.

In the aerospace world, many authors have discussed the advantages of using heat exchangers to considerably improve the thermal efficiency of turboshaft and turboprop engines. In particular, for applications where the turbomachinery efficiency is dramatically limited by size and Reynolds effects. A considerable limitation of this approach is related to the increased engine weight due to the addition of intercoolers and/or recuperators. Therefore, resultant engines are always product of compromising solutions between size/weight and thermodynamic performance, leveling-off the heat exchangers introduction advantages.

Few publications have pointed out that the employment of semi-closed cycle architectures could be beneficial for aerospace applications that necessitate their usage for reaching good performance and contained weights, such as for the unmanned aerial vehicle (UAV) case. However, the only detailed semi-closed cycle assessment available in literature goes back to the 1995 under the NASA ERAST (Environmental Research Aircraft and Sensor Technology) program. The NASA study, focused on the technological development of high altitude long endurance UAVs for scientific purposes, showed the advantages introduced by a particular intercooled-recuperated semi-closed cycle arrangement, named Coleman engine, with respect to other conventional solutions, such as: spark ignition, diesel, rotary, fuel cells and shaft engines.

This Master thesis revisits the design case and some of the observations introduced within the ERAST program and presents a detailed performance comparison focused on gas turbine engines for high altitude UAV applications. In particular, the performance of two different semi-closed cycle configurations have been compared with the state-of-the-art open cycle equivalent, represented by the simple recuperated and the intercooled-recuperated engines, for different technological levels. The first semi-closed cycle arrangement has been taken from the NASA ERAST program, while, the second has been derived from further research studies conducted by the University of Florida for marine applications, which have also brought to the realization of a preliminary engine prototype in the early 2000s, under the so called HPRTE (High Pressure Regenerative Turbine Engine) program.

The thermodynamic cycle model of the four engines considered has been created with the support of the program NPSS (Numerical Propulsion System Simulation), an object oriented environment built in C++language, suitable for the cycle design and off-design steady state analysis of conventional and unconventional gas turbine configurations. This program has been coupled

with a detailed component performance and weight model, with the objective of assessing feasibility, design/off-design performance behavior and size/weight characteristics of primary engine components (compressors, turbines, combustor, heat exchangers, etc.) as function of given thermodynamic cycle parameters. Moreover, the developed tool has been coupled with an optimizer, which has direct control of the engine thermodynamics.

For each engine model, a multi-objective optimization has been carried out with minimum specific fuel consumption (SFC) and weight as target. The first objective has been defined from the evaluation of the engine design and part-power performance, while the second, as the sum of the individual component weights, estimated by means of the developed weight model. The Matlab evolutionary algorithm, called *gamultiobj*, has been employed for the optimization. Furthermore, the ERAST case study has been taken as reference to define the flight conditions and to set the engine design and off-design power output requirements for the analysis. In addition, the optimization has been performed assuming a single shaft architecture and equivalent turbomachinery features for all the engine models.

The final optimized Pareto solutions have been used to compare attainable performance and weights of the semi-closed cycle and the open cycle arrangements. Results have proven that a significant degree of compactness can be achieved by means of the semi-closed cycle configurations, leading to an overall engine weight more than two times lower than for a conventional intercooled-recuperated gas turbine. Further benefits have been observed in terms of design and part-power performance, where, for the same engine power output demand, semi-closed cycles have shown a slight reduction in SFC with respect to the equivalent open cycles analyzed.

Page intentionally left blank

Acknowledgment

Above all, I would like to express my gratitude to my supervisors, professor Dries Verstraete, for the precious guidance and great support throughout the entire project, and professor Wilfried Visser, for sharing his great experience on gas turbines and providing important suggestions, even from periodic and early Skype meetings. A special appreciation goes also to Adam J. Head, PhD candidate at Delft University of Technology, for the useful tips received during the initial phases of my project. Furthermore, I would like to thank professor Colonna and professor Sikke for reading and assessing my thesis work.

I also want to acknowledge the staff of the School of Aerospace, Mechanical and Mechatronic Engineering of the University of Sydney for their kindness and help in arranging and accommodating my stay in Sydney. In particular, I have to mention the head of the school, professor Stefan Williams, for putting me in contact with professor Dries and accepting me as a visitor student at the faculty of Aerospace, and the school administrative officer, Bronwyn Sexton, for supporting me with the visa application and sponsorship. A special appreciation goes to the PhD group of professor Dries, in particular, to Amrit and Durlabh, for making my stay at the University of Sydney particularly enjoyable.

Furthermore, I wish to extend my gratitude to professor William E. Lear from the University of Florida, for the inspiring conversation that we had regarding the potentiality of semi-closed cycles for aerospace applications. Professor Lear did a considerable amount of work with semi-closed cycles in the past, and, since I had the opportunity of getting in touch with him as a consequence of my work, I find important to acknowledge him here.

In addition, I would like to express my sincere thanks to the whole group of the NOMAD bouldering gym, for the always new and challenging climbs that kept most of my evenings busy in trying to solve them. A special appreciation goes to my dear friends Arnould and Jimmi, for having initiated me to the beauty of the outdoor rock climbing, and for the great time spent together. To my friend Luuk, for the unfortunately too short, but really intense, holidays around Queensland, to my roommates Camilo and Diegoo, and to all my friends, for making my stay in Australia unforgettable. Finally, my gratitude goes to my friends, Francesco and Giorgio, from Polytechnic of Milan, for having shared with me a big part of this MSc journey as well.

At last, a special thought goes to my parents, Paolo and Franca, whose constant support and sacrifice have made this entire adventure possible. I would never have achieved what I had without them and their unconditional trust and help. I will always treasure their lessons, knowing that if will ever become half of what they are, I shall be really proud. Finally, to the rest of my family, for their support during my entire career.

Delft, The Netherlands
04 September 2018

Jacopo Tacconi

Page intentionally left blank

Contents

Summary **VII**

Acknowledgment **IX**

List of Figures **XIV**

List of Tables **XVI**

Nomenclature **XXI**

1 Introduction **1**
1.1 Project Overview . . . 1
1.1.1 ERAST program . . . 2
1.1.2 The Coleman engine . . . 4
1.1.3 ERAST final considerations . . . 6
1.2 Objectives and Goals . . . 7
1.2.1 Model objectives . . . 8
1.2.2 Cycle analysis objectives . . . 9
1.2.3 Research questions . . . 9
1.3 Thesis Outline . . . 10

2 Literature Review **12**
2.1 Introduction . . . 12
2.2 Semi-Closed Cycles . . . 12
2.2.1 Cycle Thermodynamics . . . 13
2.2.2 Details on Advantages . . . 13
2.2.3 Cycle Arrangements . . . 15
2.3 Component Modeling . . . 16
2.3.1 Turbomachinery Modeling . . . 16
2.3.2 Heat Exchanger Modeling . . . 26
2.3.3 Combustor Modeling . . . 30
2.4 Weight Modeling . . . 34
2.4.1 Component Based Model . . . 35
2.4.2 Compressor and Turbine . . . 36
2.4.3 Heat Exchangers . . . 37
2.4.4 Combustor . . . 38
2.4.5 Shafts . . . 39
2.4.6 Gearbox and Accessories . . . 40

3 Thermodynamic Cycle **43**
3.1 Introduction . . . 43
3.2 NPSS Program Overview . . . 43
3.2.1 Elements in NPSS . . . 44
3.2.2 Ports & Links . . . 49
3.2.3 NPSS Numerical Solver . . . 50
3.3 Cycle Modeling . . . 51
3.3.1 Open Cycle Models . . . 51
3.3.2 Semi-Closed Cycles . . . 56
3.4 Bleed/Cooling Modeling . . . 61
3.4.1 Model Description . . . 62
3.4.2 Model Implementation . . . 62

4 Component Modelling **64**
4.1 Introduction . . . 64
4.2 Compressor Performance Modeling . . . 64
4.2.1 Detailed Design Performance Model . . . 64
4.2.2 Model Comparison . . . 67
4.2.3 Off-Design Performance . . . 68
4.3 Turbine Performance Modeling . . . 69
4.3.1 Detailed Design Performance Model . . . 69
4.3.2 Model Comparison . . . 72
4.3.3 Off-Design Performance . . . 72
4.4 Combustor Performance Modeling . . . 73
4.4.1 Model Description . . . 73
4.5 Weight Modeling . . . 75
4.5.1 Weight Modeling Details . . . 76
4.5.2 Final Considerations . . . 78

5 Optimization **80**
5.1 Introduction . . . 80
5.2 Optimization Theory . . . 80
5.2.1 Optimization Algorithms . . . 81
5.2.2 The Matlab Algorithm . . . 81
5.3 Problem Formulation . . . 82
5.3.1 Thermodynamic Design Variables . . . 83
5.3.2 Turbomachinery Design Variables . . . 85
5.3.3 Optimization Settings . . . 86
5.4 Objective Function Setup . . . 87
5.4.1 Recuperated Cycle . . . 87
5.4.2 Intercooled-Recuperated Cycle . . . 89
5.4.3 Semi-Closed Cycles . . . 89
5.4.4 NPSS Repairing Algorithm . . . 90

6 Results and Conclusions **92**
6.1 Introduction . . . 92
6.2 General Considerations . . . 92
6.3 Open Cycle Results . . . 95
6.3.1 Recuperated Engine . . . 96
6.3.2 Intercooled-Recuperated Engine . . . 100
6.4 Semi-Closed Cycle Results . . . 104
6.4.1 ERAST Coleman Engine . . . 104

6.4.2 HPRTE Engine . . . 109
6.5 Conclusions . . . 112
6.5.1 Results Summary . . . 113
6.5.2 Future Work . . . 113
6.5.3 Recommendations . . . 114

Bibliography **127**

Appendix A Centrifugal Compressor **A2**
A.1 Simple Models . . . A2
A.1.1 Compressor Scaling Technique . . . A2
A.1.2 Empirical Relations . . . A5
A.2 Advanced Models . . . A5
A.2.1 Compressor Meanline Method . . . A6
A.2.2 Galvas Loss Model . . . A18
A.3 Model Implementation . . . A24
A.3.1 Impeller Design . . . A25
A.3.2 Diffuser Design . . . A28
A.3.3 Performance Evaluation . . . A29

Appendix B Radial Turbine **A31**
B.1 Simple Models . . . A31
B.1.1 Turbine Scaling Technique . . . A31
B.1.2 Empirical Relations . . . A32
B.2 Advanced Models . . . A32
B.2.1 Turbine Meanline Method . . . A33
B.2.2 Turbine Loss Models . . . A40
B.3 Model Implementation . . . A43
B.3.1 Rotor Design . . . A43
B.3.2 Stator Design . . . A46
B.3.3 Performance Evaluation . . . A46

Appendix C Combustor **A48**
C.1 Design Methodology . . . A48
C.1.1 Case and Liner Characterization . . . A49
C.1.2 Combustor Zone Characterization . . . A52
C.2 Flame Temperature . . . A56
C.3 Wall Temperature . . . A58
C.3.1 Uncooled Wall Temperature . . . A59
C.3.2 Cooled Wall Temperature . . . A61

Appendix D Weight **A63**
D.1 Compressor Weight Model . . . A63
D.1.1 Material Considerations . . . A63
D.1.2 Disk and Blades . . . A64
D.2 Turbine Weight Model . . . A66
D.2.1 Material Considerations . . . A67
D.2.2 Disk and Blades . . . A67
D.3 Shaft Weight Model . . . A67

List of Figures

1.1 ERAST baseline aircraft [14]; all dimensions are expressed in feet 3
1.2 ERAST mission profile outline [14] 3
1.3 ERAST Coleman engine schematic: 90000 ft, 0.4 flight Mach number and 300 hp design point [14] 4
1.4 ERAST recuperated turboprop engine schematic: 90000 ft, 0.4 flight Mach number and 300 hp design point [14] 5
1.5 ERAST Coleman engine general arrangement [14] 6

2.1 Typical T-s diagrams of intercooled-recuperated open and semi-closed cycle architectures 13
2.2 Part power SFC curves comparison for open recuperated (AGT1500), intercooler-recuperated (WR21) and semi-closed cycle (HPRTE) turboshaft engines [10]. . . 14
2.3 HPRTE engine arrangement [10]. 15
2.4 ERAST engine arrangement [14]. 15
2.5 N_sD_s diagram for single disk pumps and low pressure ratio compressors [24] . . . 17
2.6 N_sD_s diagram for single disk turbines [24] 18
2.7 Recuperator design point performance as function of mass flow per unit of volume [67] 28
2.8 Typical recuperator performance map [7] 29
2.9 θ-parameter correlation for conventional combustor designs [70, 74] 32
2.10 Main combustor geometrical parameters, adapted from [70] 33
2.11 Combustor efficiency variation as function of burner loading [56] 34
2.12 Centrifugal compressor - radial turbine impeller schematic [84] 36
2.13 Burner duct model schematic [83, 84] 38
2.14 Burner wight model parameters schematic [83, 84] 39
2.15 Shaft schematic [83, 84] 39
2.16 Typical aviation gearbox arrangements [91] 41

3.1 Typical NPSS modeling logic of conventional gas turbines [92] 44
3.2 Typical subsonic inlet pressure recovery map as function of flight Mach number [96, 97] 46
3.3 RC/ICR engine schematic as realized in NPSS (.mdl file) 51
3.4 ERAST engine schematic as realized in NPSS (.mdl file) 56
3.5 HPRTE engine schematic as realized in NPSS (.mdl file) 57

4.1 Compressor performance whole diagram 65
4.2 ASME-89-GT-112 centrifugal compressor map [123] 69
4.3 Turbine performance whole diagram 70
4.4 Radial turbine n_sd_s diagram [41] 71
4.5 ASME-92-GT-93 radial turbine map [128] 73
4.6 Combustor performance model diagram 74

4.7 Compressor weight model diagram 77
4.8 Industrial impeller weight with diameter correlation [133] 77

5.1 Children generation schematic in the *gamultiobj* algorithm, adapted from [136] . 82
5.2 RC objective function schematic 88
5.3 ICR objective function schematic 89
5.4 ERAST/HPRTE objective function schematic 90

6.1 Open cycles Pareto optimality solutions 92
6.2 Semi-closed cycles Pareto optimality solutions 93
6.3 Part-power specific fuel consumption comparison 95
6.4 Effects of pressure ratio and rotational speed on the RC Pareto frontier 96
6.5 Effects of turbine inlet temperature on the RC Pareto frontier 97
6.6 Effect of recuperator performance parameters on the RC Pareto frontier 98
6.7 Effects of turbine and nozzle parameters on the RC Pareto frontier 98
6.8 Effects of turbomachinery variables on the ICR Pareto optimality 101
6.9 Effects of turbine inlet temperature on the ICR Pareto frontier 101
6.10 Effects of the intercooler parameters on the ICR Pareto frontier 102
6.11 Effects of the recuperator effectiveness and total pressure on the ICR Pareto frontier 102
6.12 Effects of turbine and nozzle parameters on the ICR Pareto frontier 103
6.13 Effects of pressure ratio and rotational speed on the ERAST Pareto frontier . . . 105
6.14 Effects of turbine inlet temperature and equivalence ratio on the ERAST Pareto frontier 106
6.15 Effect of recuperator performance parameters on the ERAST Pareto frontier . . 107
6.16 Effects of nozzle pressure ratio on the ERAST Pareto frontier 108
6.17 Effect of turbomachinery variables on the HPRTE Pareto frontier 109
6.18 Effect of combustor variables on the HPRTE Pareto frontier 110
6.19 Effects of the intercooler parameters on the HPRTE Pareto frontier 111
6.20 Effect of recuperator performance parameters on the HPRTE Pareto frontier . . 111

A.1 Relative Mach number as a function of inducer absolute Mach number and $\theta M_{u2}^2/(1-\nu^2)$ [26] A8
A.2 Slip effect on impeller exit velocity triangle ($\sigma = 1 - C_{slip}/U_2$) [26] A9
A.3 Blade angle and pressure ratio influence on inlet relative Mach number, for a given inlet blade angle, exit flow angle, compressor total-to-total efficiency, slip factor and inlet tip/shroud to exit radius ratio [26, 41] A11
A.4 Discharge blade height variation as function of r_{1s}/r_2 [26, 41] A11
A.5 Typical solely vaneless diffuser channel configurations [162] A14
A.6 Typical vaneless/vaned diffuser channel configurations [162] A14
A.7 Throat blockage and aspect ratio effects on pressure recovery coefficient [41] . . . A17
A.8 Vaned diffuser channel [41] A17
A.9 Typical channel diffuser map [162] A18
A.10 Ideal or optimal blade loading model [39] A21
A.11 Skin friction coefficient correlations plot [39] A24
A.12 Impeller design code schematic A26
A.13 Diffusion ratio as function of α_2 and β_2, assuming $\sigma = 0.85$, $r_{1s}/r_2 = 0.70$ and $\beta_{1s} = -60°$; adapted from [41] A27
A.14 Centrifugal compressor design code schematic A30

B.1 Typical flow streaklines disposition as function of turbine relative inlet flow angle [45] A34
B.2 Rotor inlet velocity triangles [41] A35

B.3 Optimal relative inlet flow angle as function of blade numbers, adapted from [41] A36
B.4 Absolute inlet flow angle as function of blade numbers, adapted from [41] A36
B.5 Absolute and relative exit Mach number as function of relative flow angle [41, 46] A37
B.6 Attainable radial turbine efficiency as function of velocity ratio, taken from [41] . A38
B.7 Predicted individual efficiency loss contribution as function of specific speed [41] A43
B.8 Rotor design code schematic A44
B.9 Radial turbine design code schematic A47

C.1 Reference area definition for different combustor types, adapted from [71] A49
C.2 Typical adiabatic temperature rise [70] A51
C.3 Liner pressure loss influence on optimum liner to case area ratio, adapted from [73]A53
C.4 Combustor front end geometrical diagram, adapted from [70] A55
C.5 Liner heat transfer process [74] A59
C.6 Cooling slots main geometrical parameters [71] A61

D.1 Temperature effects on UTS and UYS for typical compressor materials [132] . . . A64

List of Tables

1.1 ERAST Coleman engine main design features summary 5

2.1 Impeller loss model comparison, adapted from [42] 21
2.2 Dilution zone length estimation table 33
2.3 Intercooler and recuperator reference data from [17] 38

3.1 Engine design ambient flight condition 45
3.2 Combustor standard input data provided 46
3.3 List of NPSS input propeller data used in this project [14] 48
3.4 RC/ICR solver dependent variables list in design mode 53
3.5 RC/ICR solver independent variables list in design mode 53
3.6 RC/ICR solver dependent variables list in off-design mode 54
3.7 RC/ICR solver independent variables list in off-design mode 54
3.8 RC/ICR solver constraints variables list applied in off-design calculations 55
3.9 RC/ICR complete input variables list used in NPSS (.inp file) 55
3.10 ERAST/HPRTE design solver dependent/independent variables list 58
3.11 ERAST design recuperator dependent/independent variables list 58
3.12 HPRTE design recuperator dependent/independent variables list 58
3.13 ERAST mixer dependent/independent variables list 59
3.14 HPRTE mixer dependent/independent variables list 59
3.15 ERAST/HPRTE off-design solver dependent/independent variables list 59
3.16 ERAST/HPRTE complete input variables list used in NPSS (.inp file) 60

4.1 Validation main outcome with detailed reference data (compressor) 67
4.2 Different models output efficiency comparison (compressor) 67
4.3 Validation main outcome with detailed reference data (turbine) 72
4.4 Different models output efficiency comparison (turbine) 72

5.1 RC optimization design variables and relative bounds 83
5.2 ICR optimization design variables and relative bounds 84
5.3 ERAST/HPRTE optimization design variables and relative bounds 85
5.4 Compressor optimization design variables and relative bounds 85
5.5 Turbine optimization design variables and relative bounds 86
5.6 LPC exit Mach number design variable and relative bounds 86
5.7 Summary of the optimization initial settings per engine arrangement 86

6.1 Compressors design vector for minimum average SFC (RC engine) 99
6.2 Compressors design vector for minimum weight (RC engine) 99
6.3 Turbines design vector for minimum average SFC (RC engine) 100
6.4 Turbines design vector for minimum weight (RC engine) 100
6.5 Compressors design vector for minimum average SFC (ICR engine) 103
6.6 Compressors design vector for minimum weight (ICR engine) 104

6.7 Turbines design vector for minimum average SFC (ICR engine) 104
6.8 Turbines design vector for minimum weight (ICR engine) 104
6.9 Compressors design vector for minimum average SFC (ERAST engine) 108
6.10 Compressors design vector for minimum weight (ERAST engine) 108
6.11 Turbines design vector for minimum average SFC (ERAST engine) 108
6.12 Turbines design vector for minimum weight (ERAST engine) 109
6.13 Compressors design vector for minimum average SFC (HPRTE engine) 112
6.14 Compressors design vector for minimum weight (HPRTE engine) 112
6.15 Turbines design vector for minimum average SFC (HPRTE engine) 112
6.16 Turbines design vector for minimum weight (HPRTE engine) 112

C.1 Typical combustor pressure losses, adapted from [74] A50
C.2 Dilution zone length estimation [71] A53

D.1 Compressor materials main parameters A64

Nomenclature

Symbols

a	Reynolds independent loss fraction
A	Area
A_c	Heat exchanger minimum free flow area
Alt	Flight altitude
b	Flow passage width
	Gearbox number of planets
	Burner constant
B	Flow passage blockage factor
c_p	Pressure coefficient
C_p	Pressure recovery factor
C	Absolute velocity
	Flow capacity rate
	Gearbox volume factor
C_f	Skin friction coefficient
D	Diameter
D_f	Diffusion factor
D_{hyd}	Hydraulic diameter
D_s	Specific diameter
DR	Compressor diffusion ratio
e	Loss coefficient
f	Fanning friction factor
G	Heat exchanger flow stream mass velocity
h	Enthalpy
H_{ad}	Adiabatic head
i	Incidence angle
j	Colburn heat transfer
J	Objective function

K	General constant
L	Length
L_v	Compressor diffuser vane length
m_s	Gearbox planet gear to sun pinion ratio
$\dot{m}$	Mass flow rate
$\dot{m}_c$	Corrected mass flow rate
M	Mach number
	Gearbox weight factor
M_0	Overall gearbox ratio
n	Reynolds ratio exponent
N	Rotational speed, RPM
N_p	Optimization initial population size
N_s	Specific speed
P	Pressure
q	Dynamic pressure
$\dot{q}$	Heat flow rate
r	Radius
R	Gas constant
Re	Reynolds number
t	Wall thickness
T	Temperature
	Torque
U	Rotational speed, m/s
	Overall heat transfer coefficient
V	Volume
V_L	Compressor vane loading
$\dot{V}$	Volumetric flow rate
W	Relative velocity
	Component weight
$\dot{W}$	Power
x	Design vector
Z_B	Equivalent blade number
Z_{VD}	Diffuser vane number

Greek Symbols

α	Absolute flow angle, degree from meridional plane
β	Relative flow angle, degree from meridional plane

	Heat exchanger surface compactness
γ	Gas constant
Δ	Difference
ε	Cooling effectiveness
	Heat exchanger effectiveness
η	Efficiency
θ	Burner efficiency parameter
θ_c	Vaned diffuser angle
λ	Compressor/turbine working factor
μ	Dynamic viscosity
	Impeller/Rotor hub to tip radius ratio
ξ	Coolant fraction
	Combustion reaction time
ρ	Density
σ	Heat exchanger free flow area to frontal area ratio
	Normal stress
	Slip factor
τ	Shear stress
ϕ	Combustor equivalence ratio
ω	Impeller/rotor angular velocity
Ω	Burner loading parameter

Subscripts

a	Air
acc	Engine accessories
ad	Adiabatic
av	Average
ax	Axial direction
B	Burner
	Blades
c	Heat exchanger cold side
	Cooling flow
cr	Critical
C	Compressor
des	Design
$diff$	Diffuser
eng	Engine

g	Gas
$gear$	Engine gearbox
h	Heat exchanger hot side
	Impeller/rotor hub
i	Inner
id	Ideal
I	Impeller
m	Flow meridional component
	Root mean square location
map	Component performance map
max	Maximum
min	Minimum
mix	Mixer
N	Turbine nozzle/stator
Noz	Nozzle
o	Outer
opt	Optimal
$poly$	Polytropic
ref	Reference
s	Impeller/rotor shroud or tip
sh	Shaft
S	Stage
ts	Total to static
T	Turbine
w	Wall
θ	Tangential velocity component
0	Total quantities
	Turbine nozzle inlet
1	Compressor impeller inlet
	Turbine nozzle exit
	Heat exchanger inlet
2	Compressor impeller exit
	Turbine rotor inlet
	Heat exchanger outlet
3	Compressor vaneless diffuser exit
	Turbine rotor exit

	Combustor inlet
4	Compressor vaned diffuser exit
	Combustor outlet

Abbreviations

BL	Blade loading
BPR	Bypass ratio
CL	Clearance
DF	Disk friction
DZ	Combustor dilution zone
EX	Exit
FAR	Fuel to air ratio
FB	Full blade
FFR	Feedback flow ratio
HEX	Heat exchanger
HPC	High pressure compressor
IC	Intercooler
INC	Incidence
KE	Kinetic energy
LHV	Fuel low heat value
LPC	Low pressure compressor
$NPSS$	Numerical propulsion system simulation
OPR	Overall pressure ratio
P	Passage
PF	Pattern factor
PZ	Combustor primary zone
RC	Recuperator
RIT	Recuperator hot side inlet temperature
S	Stator
SB	Splitter blade
SF	Skin friction
	Scaling factor
SH	Shock
SHP	Shaft Power
SZ	Combustor secondary zone
VD	Vaned diffuser
VLD	Vaneless diffuser
TIT	Turbine inlet temperature

CHAPTER 1

Introduction

1.1 Project Overview

Recent years have seen a considerable development of unmanned aerial vehicles (UAVs) for multiple civilian and military applications. Current UAVs are limited in altitude and endurance by their propulsion systems. Small and micro gas turbines represent an interesting solution capable of expanding the operational range of these aircraft. Consequently, a lot of research has been focused on the development of more efficient gas turbines to better respond to different mission requirements.

Considerable improvements have been achieved so far through the detailed aerodynamic design and optimization of the turbomachinery engine section. As discussed by McDonald [1, 2], a further thermal efficiency increase cannot be expected from the refinement of compressors and turbines, whose efficiency rise has started to plateau. The introduction of heat exchangers into the engine architecture represents an applicable solution to considerably improve the overall engine thermal efficiency [3]. In addition, McDonald underlines how the employment of high-cost ceramic materials for all the engine hot components would produce a more significant amelioration [1]. However, the adoption of heat exchangers dramatically affects the overall engine weight and costs; in particular for highly efficient solutions where an advanced technological level is necessary. To overcome these disadvantages, a lot of research has been conducted on heat exchangers arrangements, shapes and materials that allow to build more compact and cheaper solutions [4–7]. Another aspect to be considered is the augmented engine surface area due to the presence of intercoolers and/or recuperators, which causes an increase of surface drag produced by the engine. It is therefore of interest to minimize not only the weight but also the surface area of the heat exchanger without too many losses in performance. Nonetheless, open cycle architectures with intercooler and/or recuperator represent the current state-of-the-art for micro and small gas turbines even if a lot of research is still ongoing [3].

Semi-closed cycles represent a relatively old concept that has been initially investigated for marine applications as an interesting alternative to conventional aero-derived intercooled-recuperated open cycle gas turbines [8, 9]. The main characteristic of these cycles is that part of the inlet mass flow is recirculated within the engine and only a portion of the whole mass flow is actually ejected. A typical semi-closed cycle features both intercooler and recuperator but, because of the recirculation nature, a higher degree of compactness has been observed for the same output power with respect to an equivalent open cycle [8]. More recent research has been done on semi-closed cycles with the attempt of establishing advantages and feasibility limits of the concept. Main advantages of semi-closed cycles with respect to intercooled-recuperated open cycles gas turbines (ICR) have been efficiently presented in [10] and can be summarized as follows:

(a) Lower inlet mass flow required for the same power output which leads to a specific power

(SP) output far grater than a conventional ICR gas turbine.

(b) Significantly improved overall engine compactness. As a result, it has been predicted that the engine size and weight would be reduced to almost half of the ICR equivalent.

(c) Almost flat part power specific fuel consumption (SFC) characteristic, extended to power level far below common operational limits.

(d) Considerable reduction of NO_x and CO_2 emissions.

(e) Reduction of inlet and exhaust ducting system weight due to lower inlet and exhaust mass flow requirements with respect to the equivalent open cycle.

Although these points will be treated extensively in section 2.2.2, it is important to mention them here and keep them in mind from this point of the discussion onwards. These advantages have been supported by noticeable research work performed by the University of Florida that led to the construction of a small semi-closed cycle prototype named HPRTE (High Pressure Regenerative Turbine Engine) to demonstrate the feasibility of the concept [11]. Although development difficulties have been encountered, some of the discussed advantages have been experimentally proven, in particular items (a) and (b) of the previous list. Item (c) has been partially proven due to a non-optimal engine control system. Most of the current work on semi-closed cycles available in open literature has been focused on marine and power generation applications, where semi-closed cycles have shown to be of a significant advantage [12, 13].

Considering the semi-closed cycle main characteristics presented so far, it becomes natural to ask whether this solution could be applicable to small UAVs gas turbines. A partial attempt to answer this question goes back to 1995, during the NASA ERAST (Environmental Research Aircraft and Sensor Technology) program. Here, a particular semi-closed cycle concept has been investigated for high altitude UAV propulsion. This program is extremely relevant to this Master thesis work, as it will become clearer later on. For this reason, the following section has been dedicated to a quick but comprehensive summary of the ERAST work and main findings. A complete documentation is available in reference [14].

1.1.1 ERAST program

The ERAST program was focused on the development of technology necessary to advanced unmanned aerial vehicles to meet the altitude and endurance required by the scientific community. The scientific mission of those UAVs was to analyze the presence of pollutants and atmospheric concentration of chemical species such as O_3, NO_x, CFCs, etc., in the stratosphere. During the program, an investigation involving different propulsion systems and technology levels has been carried out for a design altitude of 90000 ft (27432 m), a flight Mach number of 0.4 and a power output of 300 hp ($\sim$223.71 kW). Using these requirements, several engine types have been compared, including: diesel and spark ignition turbo-compounded and non-turbo-compounded, rotary, fuel cells, recuperated and non-recuperated turboshaft engines.

For each engine concept, individual component performance and weights have been assessed through scaling techniques or from previous studies, with the exception of the heat exchangers that have been preliminary designed with specific computer programs. The behavior of the baseline engines has been assessed in off-design, modeling part power, take-off and engine climb to cruise design altitude.

The obtained designs have been integrated with a baseline aircraft generated on external contract and reported in Figure 1.1. Engines and aircraft have been scaled to meet the mission requirements underlined in Figure 1.2.

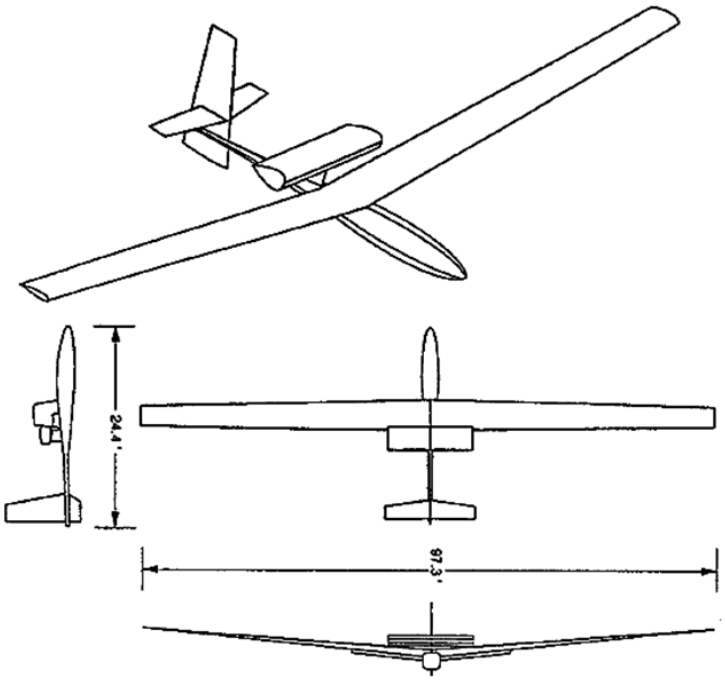

Figure 1.1: ERAST baseline aircraft [14]; all dimensions are expressed in feet

The aircraft mission has been identified by the following phases: engine start and warm up, take-off and climb at maximum rate of climb until design cruise has been reached, four hour cruise conducted at design flight speed and descent. The different mission phases have been identified by means of specific power requirements. The engine and aircraft size is changed iteratively to match the available fuel with the engine consumption throughout all the mission phases. No power requirement has been set for the descending phase, where the aircraft is assumed to glide back to the base.

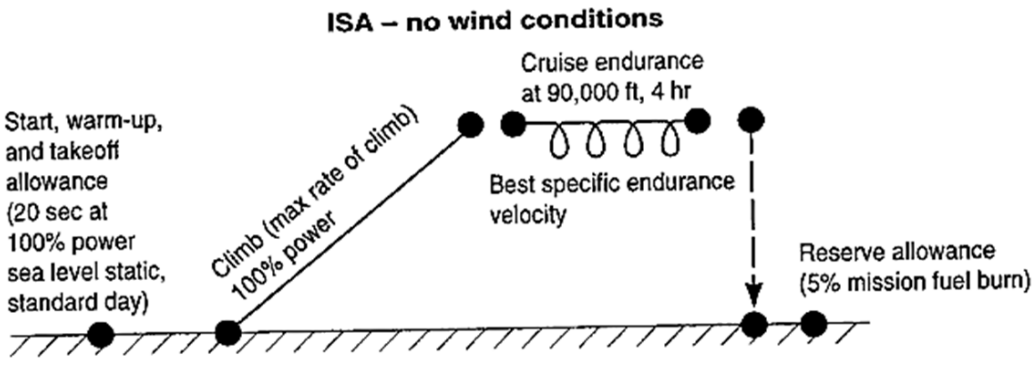

Figure 1.2: ERAST mission profile outline [14]

During the ERAST program, it has been identified that an intercooled-recuperated semi-closed cycle architecture, named the Coleman engine, represents the most promising near term solution for the high altitude long endurance UAV object of this study. The near term solution has been indicated as the one that requires little development before demonstration [14]. The following paragraph gives more technical details about the engine itself. The data below presented have been extracted from reference [14] and summarized to provide a general overview of the Coleman engine. Some of the presented arguments will become relevant in later parts of this work.

1.1.2 The Coleman engine

A schematic of the Coleman engine is reported in Figure 1.3. The image also provides numerical values of component design specifications and flow proprieties for each engine station at design point. In particular, total pressure, total temperature and corrected mass flow data are available. Note that the numerical value has been expressed in imperial units as reported in the reference. A comprehensive summary of the principal engine design features is reported in Table 1.1. The ERAST design featured two centrifugal compressors (LP comp and HP comp in the figure) connected by means of a single shaft to two axial turbines stages (HP turb and HP turb in the figure). Due to the recirculation, a much smaller inlet mass flow is required for a given power output. However, the high pressure compressor (HPC) and high pressure turbine (HPT) must be sized to handle the total mass flow within the engine. An intercooler and recuperator have been added to increase the thermal efficiency of the resultant cycle [14].

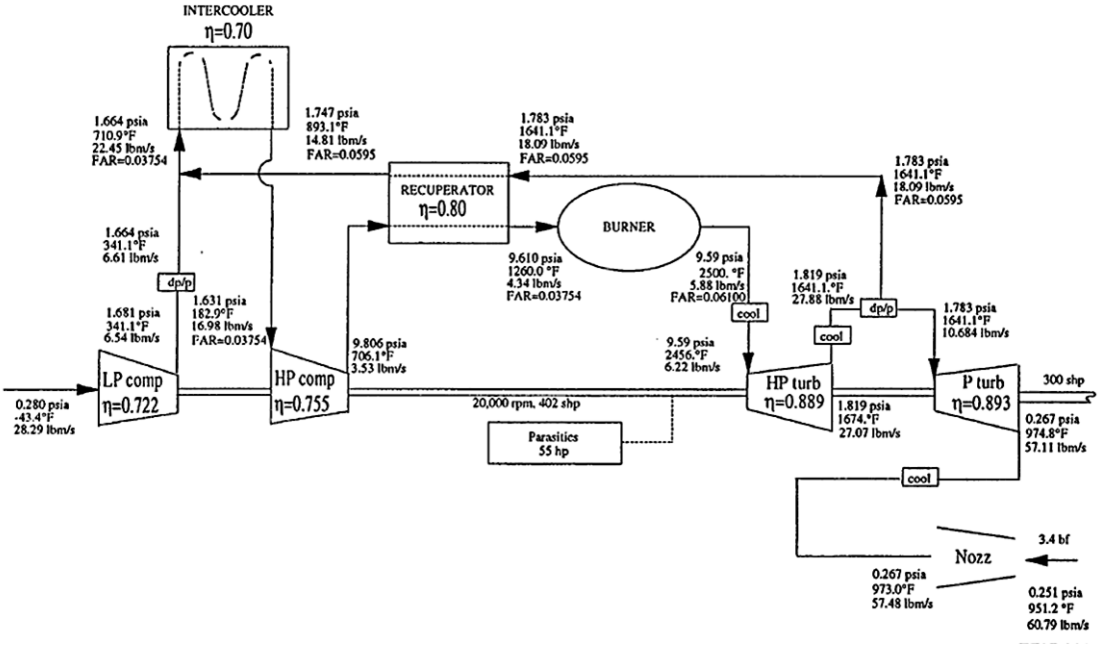

Figure 1.3: ERAST Coleman engine schematic: 90000 ft, 0.4 flight Mach number and 300 hp design point [14]

Component design characteristics have been chosen after a parametric study. In particular, the effect of changing the HPC and LPC pressure ratios have been addressed. Centrifugal compressors have been chosen due to the high design pressure ratios and for engine compactness [14]. The efficiency of the turbomachineries has been obtained by scaling from reference data corrected for Reynolds number effects. Effectiveness of intercooler and recuperator has been selected as 0.70 and 0.80 respectively, after performance and weight studies. The burner outlet temperature has been set to 2500°F (∼1644.3K) and the feedback flow ratio (FFR), defined as the ratio of the feedback flow to the engine inlet flow, has been set to keep the combustion at 90% stoichiometric value. The rotational speed has been assumed as 20000 RPM and a parasitic shaft power loss of 55 hp (∼41 kW) has been assumed to account for mechanical and heat losses. At design the work split between the turbines has been defined in order to allow a 5% pressure loss in the recirculation tubes. While more details are available in reference [14], the reasoning behind some of the design choices is not fully documented. Table 1.1 summarizes the ERAST Coleman engine design considerations in a more visual manner. Key thermodynamic parameters of the cycle are provided as explicitly mentioned in [14] or as extracted from the information provided.

Table 1.1: ERAST Coleman engine main design features summary

Π_{LPC}	6.0000
Π_{HPC}	6.0125
FFR	1.81
TIT	1644.3K
ε_{IC}	0.70
$\Delta P_{IC,h}$	0.02
η_B	-*
ΔP_B	0.002
ε_{RC}	0.80
$\Delta P_{RC,h}$	0.02
$\Delta P_{RC,c}$	0.02
Π_{Noz}	1.0638

As mentioned, among the engine solutions assessed during the ERAST program, non-recuperated and recuperated turboshaft architectures have also been investigated and designed for the same mission. The baseline engine size has been obtained though linear scaling of an existing reference and features multiple-stages axial compressor and turbine. A power turbine is used as mechanical link with the propeller. A schematic of the recuperated engine is reported below for reference, similarly to what done for the Coleman engine. For more details on the ERAST turboprop models, the reader is referenced to [14].

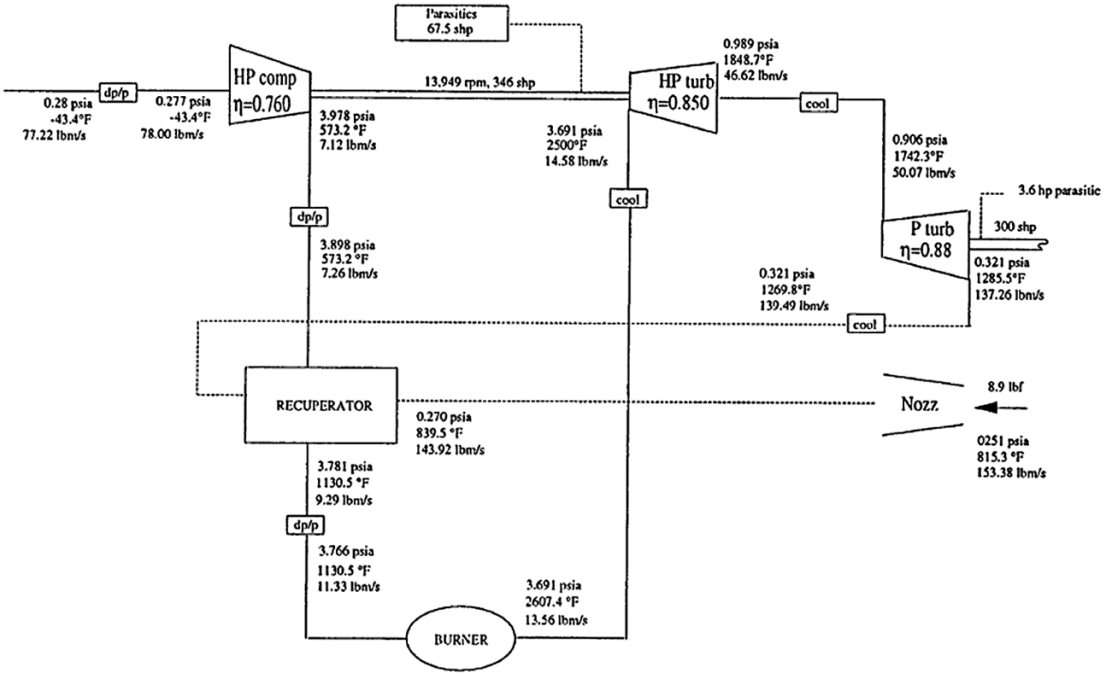

Figure 1.4: ERAST recuperated turboprop engine schematic: 90000 ft, 0.4 flight Mach number and 300 hp design point [14]

Although the engine-component philosophy is considerably different between the Coleman engine and the open cycles, some of the advantages of the semi-closed cycle discussed in the

*The burner efficiency has not been explicitly mentioned in the report for the Coleman engine. A value of 0.983 has been explicitly provided for the ERAST turboprop model, which could be reasonably assumed for this case as well.

previous list can be detected in the ERAST work. For the same flight and power output conditions, a significant difference in terms of overall engine weight and size is noticeable. In fact, the overall semi-closed cycle engine weight is more than half of the lightest non-recuperated turboshaft. No appreciable conclusions can be derived from the paper regarding SFC.

Most of the weight difference between open and semi-closed cycle is attributable to the reduced amount of mass flow elaborated by the engine. From a quick comparison between Figure 1.3 and 1.4, it can be noted that the engine inlet corrected mass flow of the recuperated turboshaft is more than two times of what needed by the Coleman engine. This leads to a considerable reduction of turbomachinery and combustor weights, considering that the materials employed in the different engine sections are the same.

To conclude this section, the general arrangement of the ERAST semi-closed cycle is reported in Figure 1.5, showing the baseline engine overall dimensions and component installation.

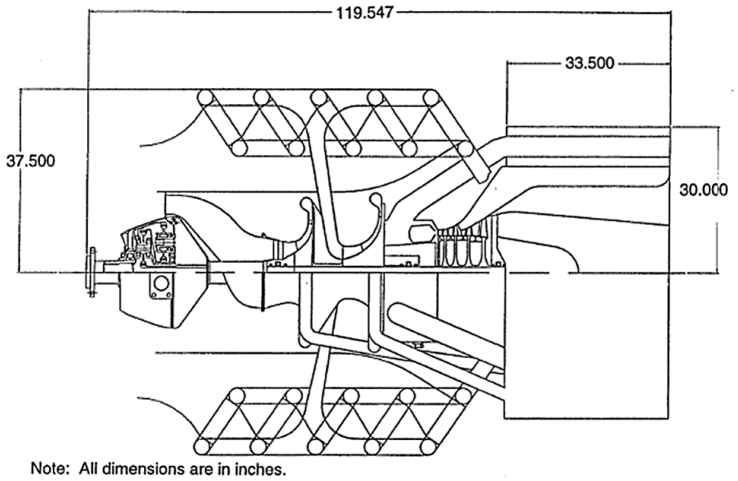

Figure 1.5: ERAST Coleman engine general arrangement [14]

A significantly large intercooler has been used to improve the heat transfer capacity at such high altitude. Parasitic engine drag has not been considered in [14], however, it is noted that this aspect might constitute a serious limitation of the Coleman engine and further study will have to be performed.

1.1.3 ERAST final considerations

As discussed, the ERAST program report represents the only detailed study available in the open literature on semi-closed cycles applied to UAVs. The ERAST program concluded that the Coleman engine represents a promising solution that can be developed in a relatively short time. There are, however, several aspects of this study that need to be deeper understood and analyzed. Those considerations can be summarized as follows:

(1) Considering that the main focus of the program was a comparison between different engine types for high altitude UAVs, more focus on gas turbine engine alternatives would be necessary. For instance, the recuperated open cycle turboshaft and the Coleman engine design features are too dissimilar for a good comparison. In addition, as reported in [3], the current state-of-the-art open cycle is represented by an ICR architecture. This cycle is not investigated in the ERAST analysis, although it represents a more competitive open cycle alternative to the Coleman engine.

(2) Previous research in different engineering environments has shown the five previously listed advantages of semi-closed cycles with respect to open cycles gas turbines. Not enough

elements are available in the report [14] to sufficiently address the question whether these advantages can be extended to UAV and aviation propulsion.

(3) The cycle proposed by ERAST results from a thermodynamic optimal approach. Choices of compressor pressure ratios, engine rotational speed, intercooler and recuperator effectiveness, etc., have been made from an initial parametric study and from scaling approach. Considering the particular engine operating environment, a more detailed analysis is needed to assess the influence of thermodynamic parameters on the engine feasibility. Furthermore, material properties have strong impact on the engine maximal performance, by setting important limitations on functional parameters such as TIT, RIT and engine RPMs. These are not well documented in [14].

(4) Some of the design choices are not fully discussed and it becomes difficult to assess the engine performance. As an example, no clear justification is presented on the selection of the feedback flow ratio (FFR). The impact of the FFR is significant in terms of engine dimensions and performance, and this aspect should be investigated further.

(5) Off-design simplifications have been made. Heat exchangers and combustor constitutional parameters have been kept constant in the off-design analysis. This aspect has been also addressed by the ERAST report [14] as a point of future improvements.

The considerations listed here have been used as starting point to identify key objectives for this project, tailoring the literature review in a manner that can best support the work development. The subsequent paragraphs will retake the points listed here and link them to the objective and the flow diagram of this Master thesis.

1.2 Objectives and Goals

As previously explained, the ERAST program has opened an interesting point on potential benefits of the employment of semi-closed cycles for high altitude UAVs propulsion. However, since most of the recent work has been focused on marine and ground applications, general conclusion on the semi-closed cycle concept for aviation purposes cannot be derived. In conclusion, a fully detailed analysis, considering altitude effects, engine weight and component design issues, that documents design and off-design performance of a semi-closed cycle is missing.

This MSc thesis presents an initial study towards a much deeper understanding of the potential of the semi-closed cycle for aviation. In particular, the work done has been split into two main phases, each one with a particular and predefined objective:

- The first leads to the building of the necessary model for further analysis of semi-closed cycles for aviation purposes.
- The second sees the employment of the created tool to perform a preliminary comparison between promising semi-closed cycle small gas turbines and current state-of-the-art open cycles for high altitude UAV applications.

Initially, the ERAST design case has been used as reference for this analysis, setting altitude, flight Mach number and power requirements. Future work will address the effect of varying operating conditions on the cycle performance and engine size. Detailed discussion on the previously mentioned objectives is provided in the following sections. Finally, the objectives introduced below will be translated into the research questions at the base of this work.

1.2.1 Model objectives

A cycle preliminary study starts from the definition of thermodynamic parameters that allow to find a steady state equilibrium point that satisfies the design requirement. For this project the design requirements will be expressed in terms of altitude, flight Mach number and engine power output, since only the gas turbine section is part of the study. Optimization techniques are required to refine the design choices in order to minimize certain objectives. Minimum SFC and engine weight are considered in this analysis, refer to chapter 5 for more information.

However, it is important to evaluate the impact of thermodynamic choices on the component level. Size effects and manufacturing constraints become significant for small gas turbines typical of UAV propulsion, considerably limiting the maximum performance achievable within a component [15, 16]. Turbomachinery efficiencies are strongly affected by secondary effects associated to complex boundary layer - surface interactions. Clearances and surface roughness become critical aspects in achieving good performance of compressors and turbines. The turbine inlet temperature (TIT) has to be limited to lower values than acceptable for large gas turbines, because the reduced size makes difficult or unpractical to efficiently apply cooling techniques. Furthermore, the presence of the recuperator introduces an additional constraint on the recuperator inlet temperature (RIT), which limits further the TIT. Materials and costs are also affected by RIT admissible values. Higher RPMs are necessary in small machines for the same power output. Hence, high stress levels can be expected, setting a consequent limitation on the design rotational speed.

From a simple thermodynamic analysis all these aspects do not emerge. Therefore, a model is needed which has the capability of including these considerations when selecting fundamental cycle variables. This aspect becomes particularly interesting when an investigation on novel cycles is of interest. Moreover, the thermodynamic optimum might not coincide with a feasible optimum. Therefore, as result of what discussed, a detailed engine model has been created with the following objectives:

(1) Perform the thermodynamic analysis of the selected engine cycle. The tool has to be capable of working with both semi-closed or open cycle architectures. Design and off-design analysis will be considered in the analysis. No transient model is available for this preliminary work. Flexibility in the selection of cycle parameters and operating conditions is needed to assess the cycle response.

(2) Identify component performance variation as function of thermodynamic inputs. Structural and manufacturing issues also have to be considered. This is important not only to properly estimate the impact of particular thermodynamic parameters on component efficiency and performance characteristics, but also to correctly assess the component feasibility.

(3) Identify the effect of thermodynamic choices on engine overall size and weight. This can be assessed through the development of a component based engine weight model, which takes into account the variation of components dimensions as function of thermodynamic values.

The result is a comprehensive model capable of simulating semi-closed cycles as well as conventional open cycles. Component performance behaviors are captured and employed for a realistic design and off-design analysis. Also, component geometrical features can be quickly calculated and employed for an engine weight estimation. Finally, the model created is suitable for an engine optimization, ensuring component feasibility and realistic performance throughout the calculations.

1.2.2 Cycle analysis objectives

The second phase of this project has been performed once the model objectives have been completed. A comparison between different cycle architectures is the scope of this part, with the objective of establishing which propulsion system is more promising for high altitude UAVs. In particular, the semi-closed cycle used in the Coleman engine has been tested against two state-of-the-art open cycles: a simple recuperated turboshaft and an intercooled - recuperated turboshaft. The semi-closed cycle proposed in the HPRTE program [11] has also been tested. The assessment has been carried out at equal engine conditions. Hence, altitude, flight Mach number, engine power output, and engine component arrangement have been kept the same for each cycle type. Moreover, each engine model has been optimized using a multi-objective generic algorithm for minimum SFC and weight. This guarantees to have information on the optimal Pareto front for each engine model; thus, assessing the optimal thermodynamic combination for each gas turbine cycles. Component feasibility and performance variation is ensured by means of the tool output of phase one. The optimized Pareto fronts are further compared between each engine type to assess whether results reported for marine gas turbines are still applicable despite altitude effects. As mentioned, the comparison will be performed for the same operating condition of the ERAST program. Further analysis has to be performed on the impact of altitude and power output change on engine behavior. Changes in technological level should also be addressed in later stages.

1.2.3 Research questions

This section defines the research questions associated to this project, which are derived and justified from the previously set objectives. The main research questions can be expressed as follows: "How can a semi-closed cycle be properly modeled to assess the feasibility of the concept and what advantages would it bring over complex open cycle solutions for UAVs applications?". This main question is comprehensive of both objectives previously treated. The main question can be broken down is a set of secondary questions that have to be considered to efficiently respond to the primary one. As a first step, it is important to find an answer to the following question to proceed:

(1) What is a semi-closed cycle and which benefits could it offer with respect to more conventional and well established solutions?

(2) Which well known open cycle architecture constitutes a valid solution for high altitude UAV applications to be compared with a semi-closed cycle?

(3) What modelling aspects have to be considered when novel thermodynamic cycles are objects of the study, and how might those have an impact on the engine analysis and the results?

(4) What are the effects of altitude and size that have to be properly modelled to correctly assess engines design for high altitude UAVs?

These questions have the scope of introducing the problem and justifying the objectives of the literature review. In particular, the former two questions have the objective of establishing the current status of the knowledge on semi-closed cycles and they have already been partially answered. The latter two are focused on the modelling aspects. In particular, they define the requirements that the model needs to address if a comprehensive analysis and comparison between semi-closed and open cycles for high altitude UAVs has to be made.

The second set of secondary questions are related to the interpretation and analysis of the results. In particular, the focus of these questions is towards the understanding of the semi-closed

cycle capabilities, addressing whether the advantages identified in other engineering applications can be extended to UAV propulsion. Note that no consideration regarding emissions have been made in this project.

(5) Is the design point of the semi-closed cycle better than the most promising open cycle counterpart, in terms of weight and overall performance parameters?

(6) How does the semi-closed cycle behave in part-power off-design situations with respect to the state-of-the-art open cycle?

Finally, the following sub-questions rise spontaneously from items (5) and (6), completing the modelling aspect of this project.

(7) What are the factors that have a major impact on the performance of the selected design point and what is the current best modeling approach?

(8) What is currently available to predict engine component weights and to take into account the major loss sources in the engine component modelling?

(9) How does the efficiency change in the off-design mode and how can this be properly modelled so that a good preliminary estimation of the overall engine performance is obtained, independently form the selection of an open or closed cycle architecture?

To summarize, the main objective of this project can be identified with a preliminary assessment of semi-closed cycles architectures for high altitude UAV environments. As part of the assessment, a comparison with current highly efficient open cycle gas turbine is needed to establish the advantages and disadvantages. Moreover, for the characterization of the cycles, a complete component model is necessary to assess feasibility, engine weight and part power characteristics. The ERAST study is employed to set the flight operating environment and requirements used in the assessment. Further study is recommended to define cycle sensitivity to altitude and design power output change. Suggestions for further work will be made along the project.

1.3 Thesis Outline

This thesis is organized as follows: an introductory part has been presented summarizing the objectives and the reasoning behind this work. Subsequently, a literature review section will be presented, with the scope of analyzing current available knowledge and modeling technique which will help to answer the previously listed research questions. Initially, the literature has been consulted to understand the current status of the knowledge on semi-closed cycles. Moreover, promising open cycle candidates have been identified through this phase. However, most of the literature has been focused on the modelling development purpose. In particular, an understanding was needed on different component modelling techniques that can be used to assess the design and off-design component response to a thermodynamic change. In addition, techniques to predict engine weight as function of thermodynamic design parameters have also been explored. After this section, a deep discussion on the developed model will be presented. Two aspects will be presented: the thermodynamic model built by means of the program NPSS (Numerical Propulsion System Simulation) for semi-closed and open cycles and the component model. This last addresses the way component performance and weight have been defined and used in the analysis. Afterwards, an optimization section will be dedicated to the link between the thermodynamic solver and the component model to identify optimal solutions for each cycle architecture, considering minimum SFC and weight as objective. Finally, results of the analysis

will be presented, showing the modeling capability and the results of the initial study on semi-closed cycles and open cycles for high altitude UAVs. Further recommendation and source of future study will be also discussed here, stressing how the model could be used to identify other aspects not treated in this analysis.

CHAPTER 2

Literature Review

2.1 Introduction

As previously discussed, the literature review has two objectives: establish the current knowledge on semi-closed cycles, and define best practices in modelling component performance and weight as function of thermodynamic inputs. The former objective has been partially treated in the introduction section. It was important to anticipate some of the literature review findings, in particular with respect to the ERAST program to justify and contextualize this work. More information will be presented here with particular focus on the advantages of the semi-closed cycle. Furthermore, possible different semi-closed cycles will also be shown.

The second aspect treated is related to modelling aspects. The effort here has been dedicated to the establishment of modeling techniques capable of correlating main cycle thermodynamic parameters with individual component performance and weight. Different models are available, however their accuracy and complexity strongly depend on the amount of information needed. Therefore, this part of the literature review had the scope of identifying main modeling techniques that would respond to the objectives defined in section 1.2.1 in a simple yet exhaustive way. Consideration toward the particularity of the cycle, the engine size, the operating environment and analysis tasks have been made during the literature assessment.

This literature review module has been organized with an initial general review on the current knowledge on the semi-closed cycle, followed by a detailed discussion on component and weight modelling. Specifically, this last section has been divided according to the main components considered: compressor, turbine, heat exchangers, burners, gearbox and accessories. The weight model will be discussed for each components in a separate section.

2.2 Semi-Closed Cycles

The semi-closed cycle arrangement is a relatively old concept and dates back to 1956 in the so called project "Wolverine*", reported in [11]. Since then, semi-closed cycles have captured the attention of various researchers. As mentioned, most of the currently available knowledge can be found within the marine engineering environment, where semi-closed cycles have been proven valuable (see reference [8]). Subsequent work involving semi-closed cycles, has brought to the practical realization of a prototype to experimentally assess some of the advantages observed with respect to conventional turboshaft engines [10, 11, 17].

*DeWitt, S.H., et al., "Project Wolverine: Submarine Propulsion Unit," Technical Manual No. 1410-C9, V.1, U.S. Navy Contract No. 65-34224, Westinghouse Order WG-56600-T, August 1956. Original report lost as explained in [11].

2.2.1 Cycle Thermodynamics

Semi-closed cycles feature heat exchangers used as intercooler and recuperator. Advantages attributed to conventional ICR open cycles can be observed here as well. However, the main difference is that in a semi-closed cycle, a certain amount of the total mass flow is recirculated within the engine core. To a certain extent, the semi-closed cycle can be seen as a fusion between conventional open and closed Brayton cycles. This becomes particularly clear if the thermodynamic cycle is visualized on a T-s diagram, as reported in Figure 2.1.

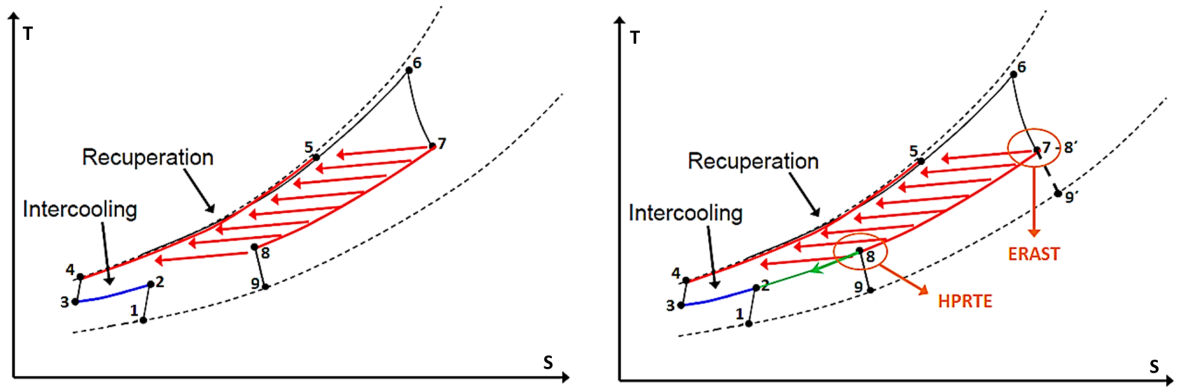

(a) ICR open cycle

(b) Semi-closed cycle

Figure 2.1: Typical T-s diagrams of intercooled-recuperated open and semi-closed cycle architectures*

The similarity between the two cycles in term of thermodynamics is clearly visible from the presented figures. Both cycles features two stages of compression, divided by one or more intercoolers with the function of reducing the amount of power necessary to drive the second compressor block. The flow is then preheated in a recuperator before entering the combustor. Typically, for turboshaft architectures, two turbines are needed to power the compressors and extract useful output work. The difference between the two cycles is between station 8 and 2 of the figure. The semi-closed cycle features a splitter element in 8 which splits the flow into two parts. A portion of the flow will be expanded in turbine as for the ICR open cycle (stage 8-9), while the remaining part will be mixed with the incoming new engine mass flow (stage 8-2). To allow this mixing, the two converging steams have to satisfy the requirement of equal static pressure. From a hardware perspective, the mixing process introduces additional complications in the actual engine realization, as experienced in [11].

2.2.2 Details on Advantages

The flow recirculation introduces noticeable advantages, which has made this cycle extremely interesting. These positive aspects have been already introduced in chapter 1. A more detailed explanation is provided below, showing engine features that contribute to these benefits. More information can be found in references [10, 11] with respect to the HPRTE engine model. Nevertheless, a generalization of these results to any semi-closed cycle model can be reasonably expected from similar observations reported by other cited authors [8, 12, 14, 18].

(a) Reduced inlet mass flow In a conventional open cycle, a high burner exit temperature is beneficial to reduce the total inlet mass flow necessary to produce a certain power. Conse-

*The reported pictures have been adapted from the Aero Engine Technology (AE4238) lecture slides of professor A. Gangoli Rao, year 2016/2017.

quently, the overall engine size and weight also decrease. Therefore, burning at stoichiometric temperatures minimizes the inlet air flow requirements. However, materials and cooling limitations normally prevent to operate the combustor at such high temperatures. On the other hand, the semi-closed cycle operates at far below stoichiometric temperatures, due to the considerable amount of partially reacting feedback gasses. Therefore, only sufficient fresh air has to be supplied to the engine to guarantee the combustion process. To a certain extent, the combustion fresh air to fuel ratio is almost stoichiometric, although the reaction temperature is limited by the recirculated products.

(b) Compactness The semi-closed cycle operates at its optimum at higher overall pressure ratios than a conventional ICR. Because the recuperator is subjected to elevated pressures on both hot an cold sides (due to the recirculation) the overall size of the heat exchanger is decreased. Moreover, the reduced inlet mass flow requirements imply a considerable reduction in the LP compressor and turbine dimensions. Hence, a more compact engine is achieved if a semi-closed cycle is employed.

(c) Flat part power SFC As testified from the analysis reported in the HPRTE program (Figure 2.2), a much flatter specific fuel consumption curve has been observed with respect to conventional open cycles. This aspect has also been confirmed in [18]. Reasons are attributed to the high pressure recirculated loop, which allows the high pressure components to operate at almost constant rotational speed and near optimal temperatures, by changing the low pressure components pressure ratios.

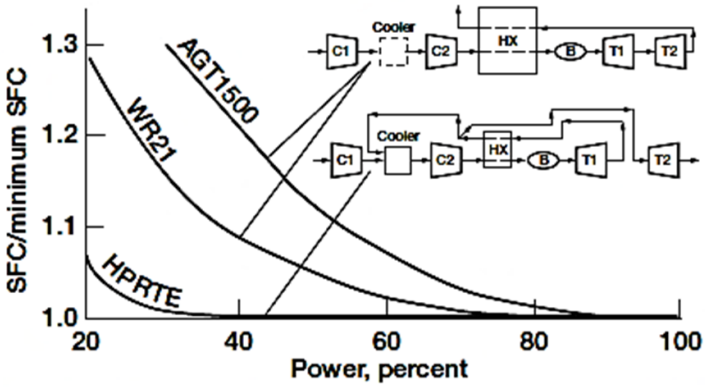

Figure 2.2: Part power SFC curves comparison for open recuperated (AGT1500), intercooler-recuperated (WR21) and semi-closed cycle (HPRTE) turboshaft engines [10].

(d) Reduced emissions Considerable reduction of CO and NO_x has been observed in semi-closed cycle arrangements. Reference [19] provides three important reasons in support:

(1) the semi-closed cycle can recirculate more than two times the engine inlet mass flow, thus, much less exhaust product is released in the environment, limiting CO, NO_x and UHC emissions,

(2) the primary zone chemistry is deeply modified by the presence of the recirculation product. In particular, high concentration of water vapour is injected in the combustor, which dissociates and increases the presence of the free radicals H and OH, reducing flame luminosity and emissions. In addition, a reduction of soot particles is experienced as effect of the recirculation, leading to a reduction of CO,

(3) off-design, the combustion process occurs at near stoichiometric values, with inlet fresh air supplied in sufficient amount only to guarantee the combustion. This reduces the mixture

oxygen concentration and lowers locally the maximum flame temperature. As consequence, NO_x formation is significantly reduced.

(e) Reduced inlet and exhaust ducting This is a consequence of the reduced inlet and outlet mass flow, which has a positive impact on intake and nozzle dimensions.

This list of advantages has been labelled based on currently available documentation on semi-closed cycles. Most of these observations have been made in marine and power generation environments, where more documentation on this cycle is available. It has to be noted that for such applications, additional benefits can be obtained with the employment of water as cooling flow in the intercooler, considerably reducing the size of this element. The interested reader is referred to [12] for more information. Obviously, this possibility is not available for aerospace applications, where air is the only cooling medium available. A possible limiting aspect for UAV application could be identified in the intercooler dimensions (affecting both engine weight and drag), as briefly mentioned in [14].

2.2.3 Cycle Arrangements

After having introduced the currently documented advantages of semi-closed cycle designs, it is important to focus on possible semi-closed cycle arrangements. Mainly two semi-closed cycles models have been documented in literature. The first is the HPRTE disposition reported in Figure 2.3 and the second is the ERAST Coleman engine schematic reported in Figure 2.4. As visible, the only difference between these two arrangements is the way the flow is split after the high pressure turbine. In the HPRTE model, the whole engine mass flow passes through the recuperator before being distributed; in the ERAST case, the splitter element is located between the HP and LP turbines. Only part of the engine mass flow is sent to the recuperator, while the remaining flow is immediately expanded in the LP turbine.

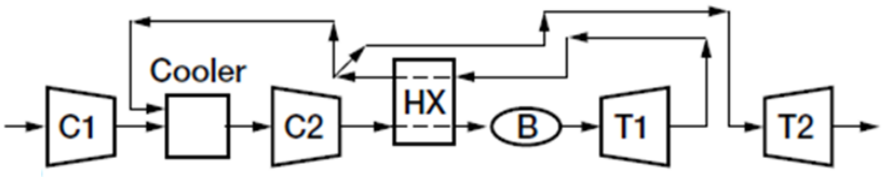

Figure 2.3: HPRTE engine arrangement [10].

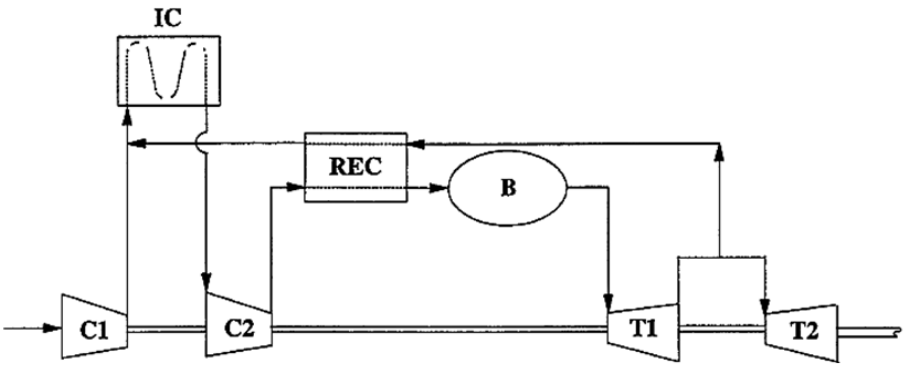

Figure 2.4: ERAST engine arrangement [14].

The thermodynamic representation of the HPRTE cycle can be visually assessed with Figure 2.1(b). The ERAST model can be represented on a T-s diagram in a similar manner, by shifting point 8 and making it coincident with 7. As reported in [12], the HPRTE arrangement is a more efficient solution as more heat is exchanged between hot and cold side in the recuperator. However, because the second expansion in the LP turbine is occurring after the recuperator, less work can be extracted from the cycle than for the ERAST configuration. The choice of the former or the latter architecture is strongly dependent on the mission requirements.

2.3 Component Modeling

This section provides details on existing models that can be used to accurately simulate the engine component response to thermodynamic inputs in design and off-design. The component considered are only the ones associated to the gas turbine section. Therefore a complete modeling discussion will be presented for: compressor, heat exchangers, combustor and turbine. No performance model has been considered for the gearbox and the propeller, as these two elements do not directly affect the engine thermodynamics. Their mechanical impact, however, has been modelled through standard NPSS tools as will be explained later on. For a semi-closed cycle, two additional elements enter in contact with the fluid and have to be considered: a mixer and a splitter. In this section, no explicit mention to these components will be made, as NPSS already provides sufficient tools for a correct assessment of their performance. Inlet and nozzle ducting have been also modelled using standard NPSS tools. More details on NPSS will be presented in chapter 3.

Before proceeding further with the individual models description, it is important to better clarify the reasoning behind this literature research relative to the objectives of this work. From a performance point of view, it is important to track how components behave in response to a certain fundamental thermodynamic setting, in particular, if an optimization has to be performed. For example, in design mode, it is important to correlate the maximum efficiency obtainable from turbomachineries with pressure ratio. In such manner, if the optimizer changes design pressure ratios across compressors and turbines, a realistic component design efficiency is obtained. Therefore, ensuring a high accuracy of the optimization result. Moreover, certain thermodynamic variables have a direct impact on component weight and size. This is particularly evident in the heat exchangers, as will be shown subsequently. In off-design, it becomes useful to characterize how the component design behavior changes in response to the engine off-design demand. Moreover, material and structural limitations have to be included in early design stages, if a feasible output is wanted.

Different models are available in open literature to support this phase of the project. Typically, the level of complexity of the model and the amount of information needed are directly proportional to the accuracy of the model. In a preliminary study, it is thus important to pick the model that provides sufficient and accurate information to satisfy the study objective while not requiring too much computational effort. Later design stages will involve models of much higher complexity, but will certainly benefit from a good and realistic preliminary analysis.

2.3.1 Turbomachinery Modeling

Two main turbomachinery arrangements are available to the designer for compressible fluids applications: axial and radial. The former solution in commonly used in large machines, due to a better ability of dealing with high mass flow rates. On the contrary, radial machines are more suitable for small gas turbine applications, as they are less affected by size effects. A third setup involving a combination of radial and axial machines has also been investigated, showing promising results for small compressor applications [20, 21]. It is difficult to define the border

where a certain turbomachinery type should be employed with respect to another. This becomes particularly true for preliminary design stages, where little knowledge on the engine is available.

Support can be found in the work of Baljé [22, 23], applicable to both compressors and turbines. His treatise is based on the similarity concept which states that only four parameters are needed to completely describe the characteristics of turbomachines handling a compressible medium: operational Mach and Reynolds numbers, specific speed N_s and specific diameter D_s, with these lasts defined as follows:

$$N_s = \frac{N\sqrt{\dot{V}_{1,3}}}{H_{ad}^{3/4}} \tag{2.1}$$

$$D_s = \frac{DH_{ad}^{1/4}}{\sqrt{\dot{V}_{1,3}}} \tag{2.2}$$

where N is the rotational speed, $\dot{V}_{1,3}$ is the volumetric flow rate, respectively 1 represents the volumetric flow at the inlet of the compressor and 3 the volumetric flow at the outlet of the turbine and H_{ad} is the adiabatic head. Since turbomachinery with the same specific speed and same specific diameter are similar in geometry and flow mechanism, it follows that if Reynolds and Mach effects are neglected, similar turbomachines have the same efficiency. As explained in Baljé's paper [22], representing the turbomachinery by means of similarity concepts has the distinct advantage of making it easier to recognize optimum channel geometry and optimal rotational speed. With this new parameterization, it has been possible to derive peak efficiency curves for different turbomachine types as function of specific speed and diameter, allowing for the identification of the most appropriate turbomachine. Two general Baljé's charts have been reported in Figures 2.5 and 2.6, showing the resultant N_sD_s diagram for different turbines and compressors respectively.

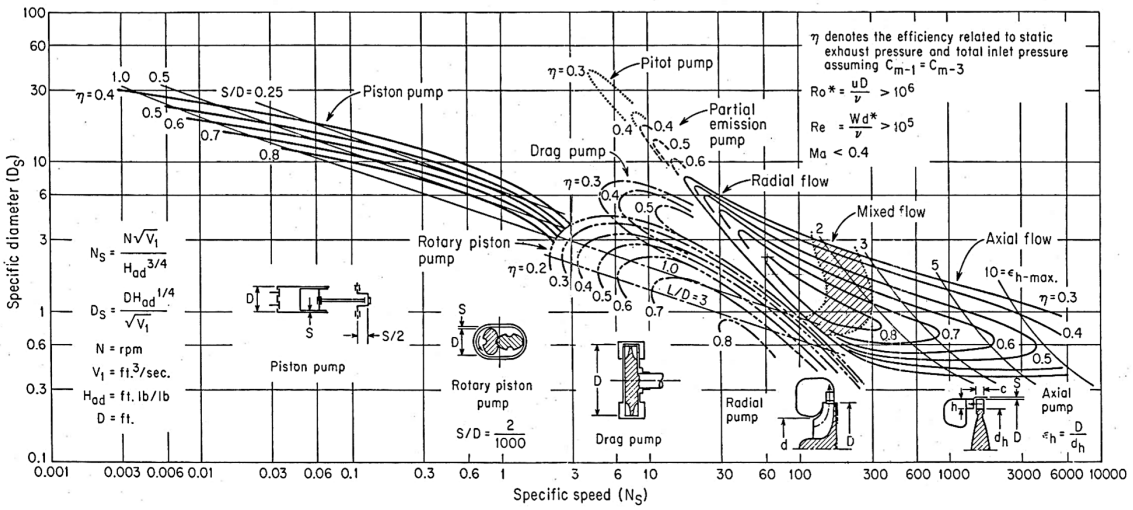

Figure 2.5: N_sD_s diagram for single disk pumps and low pressure ratio compressors [24]

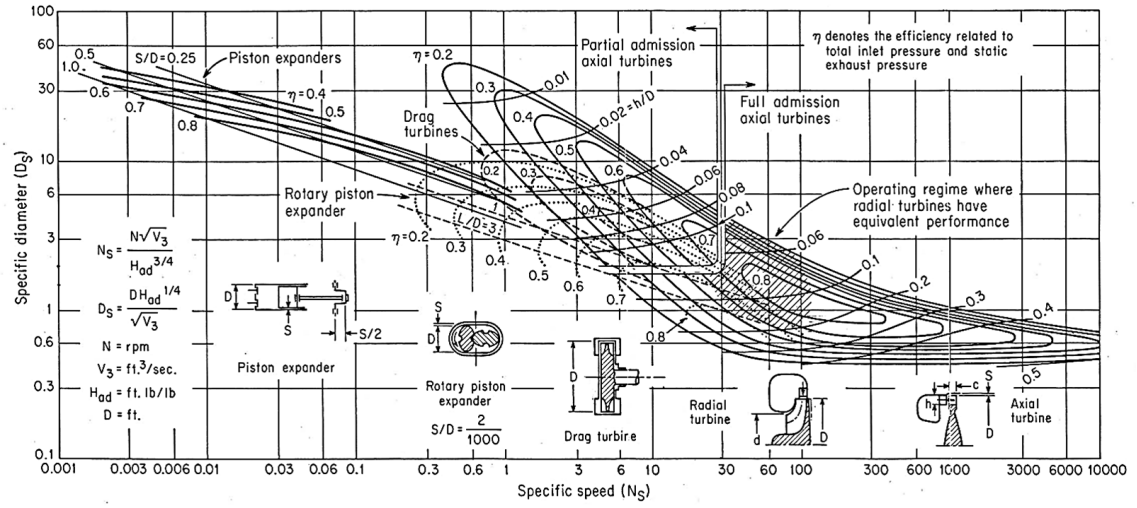

Figure 2.6: $N_s D_s$ diagram for single disk turbines [24]

If Reynolds and Mach effects are taken into account, the similarity principle does not hold fully and the peak efficiency predicted through the Baljé charts has to be corrected. Lower efficiency values must be expected for the same N_s and D_s, as further explained in [22, 23].

For this thesis work, most of the modeling focus has been dedicated to radial turbomachinery. The models presented in the dedicated compressor and turbine paragraphs have validity limited to this environment. This choice has been initially made considering what reported in [25]. At very low mass flow rates, the efficiency of the axial compressor drops sharply, blades are small and difficult to make accurately and the advantage lies with centrifugal compressors. Axial turbines do not suffer from size effects as badly as compressors. However, the most significant advantage of a radial turbine is that it allows a much greater amount of work extraction per stage. Since the second main objective of this work assumes the ERAST operating condition as design case (see Figures 1.3 and 1.5), predicted engine mass flow and dimensions give reason for this approach. Moreover, although the original Coleman engine employs two stages of axial turbines, the power and turbine pressure ratios involved (see reference [14]) allow for the implementation of a single radial turbine stage instead of two axial stages. It has been considered of interest to address this solution and compare the effects with the original case. Nonetheless, the work of Baljé has been taken into account for the verification of the feasibility of the choice in order to ensure that the radial architecture is appropriate for the engine mission and dimension. Further study should address axial and mixed flow turbomachineries as well.

Centrifugal Compressor Model

The scope of this section can be summarized as follows: (1) define state-of-the-art models that allow for a realistic estimation of the compressor design efficiency as function of input pressure ratios, (2) gain sufficient geometrical insight in order to assess component weight variation as function of thermodynamic inputs, and (3) identify techniques to assess the off-design behavior of the compressor.

According to reference [26], a preliminary design can be derived by simply scaling from an existing reference, using appropriate parameter and scaling factors, or by a total redefinition of design requirements which leads to the selection of the best geometry among a set of feasible design solutions. In this second case a more complex aerodynamic design must be carried out, using also more sophisticated techniques to model and analyze the real performance of the final geometry created. Both approaches have been considered in this phase, evaluating advantages and disadvantages. A full mathematical discussion of the selected approach is available in appendix A, here only a brief presentation is made.

Scaling Techniques These models are based on the similarity principle previously discussed (refer to [22, 23, 27]). As stated, if Reynolds and Mach effects are neglected, two machines having same specific speed and diameter will be identical in flow mechanism and efficiency. However, according to [28], several factors can be identified that prevent obtaining a high performing small gas turbine form a highly efficient larger reference:

(1) Large change in Reynolds number, which creates an important increase of viscous losses in small machines.

(2) Considerable heat transfer between hot and cold components, which causes heat losses and significant efficiency penalties. This phenomenon is almost absent in large engines.

(3) Geometrical restrictions related to materials and manufacturing techniques, with consequent loss of accuracy on surface machining.

(4) Secondary losses, in particular tip clearance effects, more dominant in small size machines.

(5) Higher stress level in the rotating components as a small machine, for same power output, needs to rotate faster.

Several models have been proposed to account for some of these effects, producing a more accurate efficiency evaluation for the scaled design. A generalized formula has originally been presented in reference [29] to properly account for Reynolds changes between original and scaled machines. The final formulation has been reported in equation 2.3, accounting for viscous (profile and windage) and non-viscous (mixing and trailing edge) losses, by means of the coefficients a and n.

$$\frac{1-\eta}{1-\eta_{ref}} = a + (1-a)\Big[\frac{Re_{ref}}{Re}\Big]^n \tag{2.3}$$

With Reynolds number defined as:

$$Re = \frac{\rho_1 U_2 D_2}{\mu_1} \tag{2.4}$$

In the previous equations, ρ_1 and μ_1 are the compressor inlet density and dynamic viscosity respectively, U_2 is the impeller exit rotational speed and D_2 the impeller exit diameter. The parameter n denotes the Reynolds ratio exponent and assumes a value between 0.16 and 0.5, depending on the specific compressor [30]. a is the Reynolds independent loss fraction and it has a value between 0.3 and 0.4, according to [31]. A considerable amount of work has been done on equation 2.3 in order to find the best settings for a and n. The Reynolds number definition has also been object of debate, as testified in [30]. More details are available to the interested reader in appendix A.1.

As discussed in [16, 31], it is strongly beneficial to generate high pressure ratio compressor stages to achieve good overall cycle efficiencies. A demand of higher pressure ratio is realized through an increase of the impeller rotational speed, which results in an increment of both rotor inlet and exit Mach numbers. Accurate diffusion and component matching at higher impeller exit Mach numbers becomes harder. Therefore the overall peak stage efficiency will strongly depend on the compressor design aerodynamic quality. In particular for small turbomachines, manufacturing limitations prevent obtaining optimal aerodynamic designs, thus setting a limitation in the maximum compressor efficiencies. Rodgers [16] proposed a relative simple expression to account for efficiency penalties due to Mach and pressure ratio effects (appendix A.1.1). Wilson and Korakianitis [32, 33] present two simple equations (appendix A.1.2) that can be employed as an alternative to the Rodgers's model. Moreover, a fully empirical method has been derived for radial compressors in [34], which accounts for efficiency variation as function of pressure ratio (appendix A.1.2).

Finally, manufacturing processes also affect the performance of small gas turbines, due to limitations on minimum clearance and surface roughness achievable through machining. Rodgers [31] presents a model (equation A.7) to account for efficiency variation due to clearance effects.

An example of usage of scaling techniques is reported in [28, 31], similar approach has been already applied to a UAV gas turbine analysis in [35]. Scaling factors have been derived on the assumption that the gas turbine power output is proportional to the inlet mass flow and/or turbomachinery characteristic diameter squared. Equation 2.6 can be therefore generated from 2.5, as reported in the cited papers.

$$\dot{W} \propto \dot{m}_a \propto D^2 \tag{2.5}$$

$$SF = \frac{\dot{W}}{\dot{W}_{ref}} \propto \frac{\dot{m}_a}{\dot{m}_{a,ref}} \propto \frac{D^2}{D^2_{ref}} \tag{2.6}$$

Once the scaling factor has been defined, it can be inserted in the scaling relations and the resulting efficiency can be calculated. The main advantage of this technique lies in its simplicity and brevity. Disadvantages can be identified as the low accuracy of the predicted efficiency and the little geometrical information that can be derived about the new compressor. In addition, the strong relationship between design pressure ratio and rotational speed cannot be fully captured by means of these techniques. A wrong combination of those two parameters might lead to a compressor design that is not structurally feasible, invalidating also the off-design analysis. There is no clear means to address this issue with such a simplified analysis, leaving the pressure ratio and rotational speed selection fully decoupled.

Meanline Techniques A higher fidelity model that addresses the problems pointed out with the previous method is the meanline method. The behavior of the whole 3D compressor is modeled in terms of overall thermodynamic parameters at the inlet and outlet of each constitutive element. Geometrical information can be addressed by means of a relatively simple mathematical treatise that involves fundamental laws of fluid dynamics applied to turbomachines. Empirical relations are used to characterize the overall performance of the compressor in terms of both efficiency and aerodynamic behavior. Different empirical loss models can be found in literature that allow for a detailed loss estimation. However, three main authors have been commonly mentioned to have collected and organized optimal loss model sets: Galvas [36, 37], Oh [38] and Aungier [39, 40]. These authors have published sets of empirical formulas that can be used to characterize the performance of the impeller and the vaneless/vaned diffuser for design and off-design. The main idea behind those models is to break the overall losses occurred in the compressor flow passages into individual loss contributions that can be independently modelled.

The major source of loss in a well-designed compressor can be identified with the impeller. Impeller loss mechanisms can be classified in internal and external losses. As discussed in [41], external losses are associated to an impeller discharge enthalpy rise without any corresponding pressure rise. Harley et al. [42] report the following table showing, from an impeller perspective, the different loss sources divided into internal and external. In addition Table 2.1 visually explains what loss mechanism can be captured using the different models proposed by the three authors quoted.

Table 2.1: Impeller loss model comparison, adapted from [42]

	Loss	Galvas	Oh	Aungier
External	Recirculation	•	•	•
	Disk Friction	•	•	•
	Leakage		•	•
Internal	Incidence	•	•	•
	Skin Friction	•	•	•
	Blade Loading	•	•	•
	Clearance	•	•	•
	Exit Mixing		•	•
	Shock			•
	Choking			•
	Distortion			•

Regarding the diffuser section, Galvas [36, 37] and Oh [38] both employ the relation developed by Stanitz [43] which defines the diffuser losses from equation 2.16 and 2.17. Aungier [39], developed a model similar to the impeller where vaneless and vaned overall loss contribution can be split into fundamental individual sources for a more complete modeling. Looking at Table 2.1, Aungier's model seems to be the most complete one, however, additional considerations, involving accuracy and computational costs, have to be made before selecting a certain model with respect to another.

Harley [42] analyses the performance of these loss models with respect to test data for three different automotive compressors. The main conclusion derived is that the Galvas loss model is the most robust model because it allows for acceptable performance prediction across the entire map with very good prediction at high tip speeds. In addition, the model uses the least number of equations which simplifies the performance code. Good performance has been observed for Oh's model as well, however, losses in accuracy have been documented at high rotational speed [42, 44]. This aspect is less acceptable in a model as the design point normally sits at high rotational speeds and accurate predictions are wanted in these regions of the compressor map. Aungier's model performs extremely well in only certain regions of the map. All models lack in accuracy close to the surge limits and the peak efficiency is underestimated [42].

Based on these considerations, Galvas's loss model is selected as the most compatible with the goals of this project. Finally, a suitable meanline model had to be identified to provide the geometrical inputs needed to build the Galvas's model. The 1D methodology elaborated in references [26, 41] is perfectly compatible with this task. In addition, sufficient data are also available for the compressor weight model discussed in section 4.5.1. The full meanline approach is discussed in appendix A.2.1. Below, the Galvas loss contributions have been briefly presented.

Galvas loss model The Galvas loss model addresses the following contributions: inducer incidence loss, blade loading loss, skin friction loss, disk friction loss, recirculation loss, vaneless diffuser loss and vaned diffuser loss. Galvas [36, 37] does not report an explicit formulation for clearance losses and shock losses. The author mentioned that the former are considered to be inherent to the impeller losses while the latter have not been included. However, for compressors delivering high pressure ratio, transonic flow and consequently shock losses might be possible. The model proposed by Aungier [39, 40] has been found to be compatible with the current treatise.

Inducer incidence loss The incidence loss is associated with the fact that the flow enters the impeller with a relative flow angle different from the optimal one. This type of losses is minimal for the design point (ideally it is null), since the design blade angle (β_{1m}) is close to the optimal

one (β_{opt}). In off-design, these losses can be significant. The enthalpy loss due to to incidence is calculated by means of:

$$\Delta h_{INC} = \frac{W_L^2}{2} \tag{2.7}$$

with

$$W_L = W_{1m} \sin |\beta_{opt} - \beta_{1m}| \tag{2.8}$$

Blade loading loss The boundary layer growth strongly depends on internal diffusion in the impeller. This has been modeled with equation 2.9, where D_f is the diffusion factor defined in appendix A.2.2. The different diffusion behavior experienced in the presence of splitter blades is embedded in the definition of D_f.

$$\Delta h_{BL} = 0.05 D_f^2 U_2^2 \tag{2.9}$$

Skin friction loss On top of the aerodynamic losses due to the aerodynamic loading of the impeller blades, skin friction losses are experienced by the impeller wetted surfaces. Equation 2.10 has been developed based on fully developed turbulent pipe flows.

$$\Delta h_{SF} = K_{SF} C_f \frac{L/D_2}{D_{hyd}/D_2} \left(\frac{W}{U_2}\right)_{av}^2 U_2^2 \tag{2.10}$$

Where K_{SF} is a coefficient that assumes values of 5.6 and 7.0 for conventional impellers and impellers with splitter blades [36, 37], C_f is the skin friction coefficient calculated as shown in the appendix, L/D_2 is the mean flowpath blade length to diameter ratio and D_{hyd}/D_2 is the mean hydraulic to exit diameter ratio.

Disk friction loss This loss is caused by the friction generated by the flow windage on the backface of the compressor disk [45]. The following relation can be employed to compute the enthalpy losses.

$$\Delta h_{DF} = 0.01356 \frac{\rho_2}{\dot{m} Re_2^{0.2}} U_2^3 D_2^2 \tag{2.11}$$

The Reynolds number in equation 2.11 is defined as function of the impeller exit dimensions and inlet total conditions as reported below.

$$Re_2 = \frac{\rho_{01} U_2 D_2}{\mu_{01}} \tag{2.12}$$

Recirculation loss These losses are caused by the backflow of the working fluid into the impeller due to the pressure difference. Penalties associated to this phenomenon can be estimated from equation 2.13.

$$\Delta h_{RC} = 0.02 \sqrt{\tan \alpha_2} D_f^2 U_2^2 \tag{2.13}$$

Shock loss These losses occurs when the inlet relative Mach number exceeds the inlet critical Mach number (M_{cr_r}). The definition of this last parameter is important and is discussed in detail in appendix A.2.2. The enthalpy loss can be calculated according to equation 2.14.

$$\Delta h_{SH} = 0.2 \left[(M_{1m_r} - M_{cr_r}) \frac{W_{max}}{U_2} \right]^2 U_2^2 \tag{2.14}$$

where

$$W_{max} = \frac{W_1 + W_2 + \Delta W}{2} \tag{2.15}$$

and ΔW is the average blade velocity difference computed from standard irrotational flow relations, as show in appendix.

Vaneless loss The total enthalpy loss in the vaneless section of the diffuser can be calculated from equation 2.16, once the total pressure loss is known. Galvas [36, 37] proposes a methodology to compute the pressure losses from fundamental equation of continuity, equilibrium, heat transfer and fluid state as presented in appendix A.2.2.

$$\Delta h_{VLD} = c_p T_{02} \left[\left(\frac{P_3}{P_{03}} \right)^{\frac{\gamma-1}{\gamma}} - \left(\frac{P_3}{P_{02}} \right)^{\frac{\gamma-1}{\gamma}} \right] \tag{2.16}$$

Vaned loss A similar equation can be used in the vaned section in order to calculate the total enthalpy losses.

$$\Delta h_{VD} = c_p T_{02} \left[\left(\frac{P_4}{P_{04}} \right)^{\frac{\gamma-1}{\gamma}} - \left(\frac{P_4}{P_{03}} \right)^{\frac{\gamma-1}{\gamma}} \right] \tag{2.17}$$

Radial Turbine Model

As discussed, radial turbines have been considered in the current work. In terms of modeling, not much difference can be observed with respect to centrifugal compressors. For this project, the initial design performance modeling can be accomplished by means of scaling techniques or a meanline approach. For the former, equation 2.3 and similar (see appendix B.1.1) can still be used, with a slight modification in the coefficient a and n, as discussed in [28, 30, 31]. According to Rodgers [16], radial turbines do not suffer from significant Mach number and pressure ratio penalties for pressure ratios inferior to 5.0. The paper also provides a simple relation to account for clearance losses in radial turbines stages. Wilson and Korakianitis [32, 33] provide two alternative models to account for size and pressure ratio effects on turbine efficiency that are reported in detail in the appendix. However, similar limitations identified for the compressor case can be also addressed for turbines. For this reasons, a more detailed approach has been performed in the turbine modeling as well, leading to the investigation of a meanline model combined with empirical relation to improve the accuracy of the predictions.

Whitfield and Baines [41, 46] present a relatively simple meanline approach that couples perfectly with the investigated loss models. For radial turbines, two main empirical loss models are available in literature, the first proposed by Rohlik [47, 48] and the second by Glassmann [49, 50]. Both models divide the overall turbine losses the following major contributions: stator and rotor losses. A general model accounts for the overall stator losses, while the rotor losses have been divided in: incidence losses, passage losses, disk friction losses, clearance losses and kinetic energy losses. As for the compressor case, individual relations have been provided to model each loss source. The Glassman model descends directly from Rohlik's model and more details on this model are provided below. Baines [51], has more recently provided a slightly modified version of the Glassman equation for passage and clearance losses. More information on the loss models is available in appendix B.2.2. Moreover, details on the meanline model have also been summarized there.

Glassman loss model As for the Galvas loss model, this section introduces the mathematical relation used to model each loss source. Regarding the stator losses Rohlik and Glassman model

employ similar relations, they slightly differ for the rotor part. A full model description is available in appendix B.2.2.

Stator loss The stator losses can be defined according to equation 2.18.

$$\Delta h_S = e_s (KE)_{id} \tag{2.18}$$

where e_s is the stator loss coefficient defined as shown in appendix, the $(KE)_{id,1}$ is the ideal kinetic energy defined according to equation 2.19 and $(KE)_S$ is the actual kinetic energy defined as: $(KE)_S = C_1^2/2$.

$$(KE)_{id,1} = \frac{(KE)_S}{1 - e_s} \tag{2.19}$$

Incidence loss The incidence losses have been defined according to the following equations. This contribution is minimal or null at design point, however, it can become significant for off-design flow conditions. In the following, i is the incidence angle, defined as: $i = \beta_2 - \beta_{opt}$.

$$\Delta h_{INC} = \frac{1}{2} W_2^2 \sin^2 i \tag{2.20}$$

Passage loss The passage loss contribution can be estimated according to equation 2.21, with i defined as previously shown.

$$\Delta h_P = \frac{1}{2} K_p (W_2^2 \cos^2 i + W_3^2) \tag{2.21}$$

Disk friction loss Disk friction losses can be estimated by means of the following equation. The Reynolds number in equation 2.22 is calculated as: $Re_2 = \rho_2 U_2 r_2 / \mu_2$.

$$\Delta h_{DF} = 0.02125 \frac{\rho_2 U_2^3 r_2^2}{\dot{m} Re_2^{0.2}} \tag{2.22}$$

Clearance loss A simple equation is available for clearance losses, assuming a direct variation of this loss contribution with the average clearance to blade-height ratio (c/h). Δh_y represents the Eulerian work.

$$\Delta h_{CL} = \Delta h_y \left(\frac{c}{h} \right) \tag{2.23}$$

Exit loss The kinetic energy loss associated to the turbine exit velocity (C_3) can be computed according to:

$$\Delta h_{EX} = \frac{C_3^2}{2} \tag{2.24}$$

Cooling consideration Cooling losses cannot be captured with any of the proposed loss models. Typically, small gas turbines tend to be uncooled for manufacturing difficulties and strong mixing efficiency penalties. However, if a better overall cycle thermal efficiency is needed, an increase of TIT is necessary. Rodgers [16] reports that the most practical way of cooling small gas turbines is by impinging the coolant on the rotor rear face and vane tips. In addition, because of the quick mixing that occurs between cold flow and hot free stream, the cooling effectiveness rapidly decreases with distance from the impinging point. Therefore, for an effectiveness (ε) of 30 percent at the rotor tip, it is necessary to employ about 10% of the main flow for cooling

[16]. Similar observations have been reported in [25], where the cooling effectiveness has been defined as:

$$\varepsilon = \frac{T_{01} - (T_m + \Delta T_0)}{T_{01} - (T_{0c} + \Delta T_0)} \tag{2.25}$$

Where, T_{01} is the turbine stagnation inlet temperature, T_{0c} is the coolant temperature, T_m is the rotor metal temperature and ΔT_0 is defined according to equation 2.26.

$$\Delta T_0 = \frac{1}{2}\frac{U_2^2}{c_p} \tag{2.26}$$

Horlock [52], provides a simple expression that associates cooling losses with the coolant fraction parameter (ξ), which assumes the form of equation 2.27. Where ξ is defined as the ratio of the cooling mass flow to the total mass flow, and K is a constant that assumes values of 0.125 for nozzle guide vaned rows, from experimental correlations. These information can be used to derive a simple model, as reported in section 3.4.

$$\frac{\Delta\eta_{stage}}{\eta_{stage}} = -K\xi \tag{2.27}$$

Off-Design Modeling

The turbomachinery off-design analysis consists of finding the compressor-turbine operating point for flow and power conditions that differ from the design ones. Prior knowledge of the design point must be available to perform this analysis. From a compressor and turbine component perspective, off-design literature considerations can be reduced in the identification of techniques to support the generation of the component maps.

Similar to the design case, two techniques are available to generate a full compressor map to be used in the off-design analysis: (1) scaling an existing map to adapt it to the new design point or (2) generating a totally new compressor map of the designed compressor. The former methodology is commonly adopted because it allows for a quick generation of the component maps necessary for a preliminary analysis. The latter employs the same empirical loss models discussed previously to characterize compressor and turbine behavior at different flow condition and fixed geometry. This second method implies full velocity triangles calculation for each off-design condition to recreate the full component map. Although, the accuracy of the second method is certainly improved, the complexity added might not justify the benefits at this stage.

More information on the off-design implementation of the loss models previously treated can be found in [36] and [50], for centrifugal compressors and radial turbines respectively. Below, a brief summary on off-design scaling methodologies will be presented, as this is the approach typically implemented in thermodynamic solvers, NPSS included.

Map scaling approach Traditional scaling techniques can be found in the work done by Sellers and Daniele [53]. In short, the method consists in defining fixed scaling factors to be applied to the reference map in order to adapt it to the new design point. Scaling factors are typically defined for pressure ratio, corrected mass flow and efficiency from information extracted from the reference map and the new turbomachine design point. No scaling factors are traditionally applied to the dimensionless rotational speed [53]. Equations 2.28, 2.29 and 2.30 provide the classical scaling formulation, applicable to both compressors and turbines [53, 54].

$$\Pi = \frac{\Pi_{des} - 1}{\Pi_{map,des} - 1}(\Pi_{map} - 1) + 1 \tag{2.28}$$

$$\dot{m}_c = \frac{\dot{m}_{c,des}}{\dot{m}_{c,map,des}}\dot{m}_{c,map} \tag{2.29}$$

$$\eta = \frac{\eta_{des}}{\eta_{map,des}} \eta_{map} \tag{2.30}$$

The theoretical background behind this approach is once again the similarity principle previously discussed. Therefore, good quality results can be expected for scaling factors as close as possible to the unity, as presented in [53, 54]. Moreover, from the comparison with real data made in reference [53], it has been found that this approach leads to a quite significant error if the value of the scaling factor is far from one. A good number of different compressor maps can be used such that it is always possible to select the best available reference for the specific case. For off-design analysis conducted close to the design operating point, accurate results can still be expected from this method. The further is the operational point from the design one the higher would be the error.

Most of the numerical propulsion software employ similar scaling factors defined through equation 2.28, 2.29 and 2.30. Correction factors can be added to account for Reynolds effects and improve the quality of the scaled maps. References [55, 56] provide additional information. Furthermore, numerous publications are available in literature discussing more advanced and sophisticated techniques with the intent of improving the quality of the resultant scaled maps (refer for example to [54, 57, 58]), however, equations 2.28, 2.29 and 2.30 are still widely used for preliminary analysis.

2.3.2 Heat Exchanger Modeling

As stated previously, the introduction of heat exchangers into the engine becomes essential for increasing the thermal efficiency of conventional gas turbines to values between 30 and 40 percent. For efficiency values close to this last threshold, special materials must be employed, allowing for higher recuperator inlet temperature (RIT) and turbine inlet temperature (TIT) [1, 59], making weight and costs important limiting factors to the maximum performance achieved by the engine. Furthermore, the design of heat exchangers to be employed as intercooler/recuperator in a thermodynamic cycle, cannot be carried out independently from the whole cycle analysis. In fact, the influence of cycle parameters, such as pressure ratios, TIT, etc., on performance and size of the HEXs is important.

This part discusses the literature review performed on heat exchangers modeling techniques. General considerations on heat exchangers design and off-design behavior are initially provided, showing the theoretical background necessary to understand the later modeling choices made. A complex methodology will be introduced to show the influence of geometrical and flow parameters onto the HEX design. Finally, a preliminary methodology will be presented as a more appropriate alternative for this project. Additional focus will be dedicated to off-design modeling techniques that can be used to overcome the simplification made on these components in the ERAST analysis [14].

General consideration

Two important parameters are conventionally used to characterize the heat exchanger behavior in design and off-design: effectiveness (ε) and overall pressure losses ($\Delta P/P$). The former is defined as the ratio of the actual hot to cold fluid heat transfer rate to the maximum heat transfer thermodynamically permitted between the two media (see equation 2.31). Moreover, the effectiveness can be directly associated to fluid and geometrical quantities, considering that: $\dot{q} = U \Delta T_m A$.

$$\varepsilon = \frac{\dot{q}}{\dot{q}_{max}} = \frac{C_h(T_{h,1} - T_{h,2})}{C_{min}(T_{h,1} - T_{c,1})} = \frac{C_c(T_{c,2} - T_{c,1})}{C_{min}(T_{h,1} - T_{c,1})} = \frac{UA}{C_{min}} \frac{\Delta T_m}{\Delta T_{max}} \tag{2.31}$$

where, C_{min} is minimum capacity rate (the smaller between C_c and C_h), ΔT_m is the effective mean temperature defined in [4], A and U are the heat transfer area and the overall heat transfer coefficient respectively.

The overall pressure losses represent the sum of hot and cold side pressure losses [60]. The total pressure drop on each heat exchanger side accounts for the sum of the following contributions: (1) skin friction losses, (2) momentum effects (pressure losses associated to density changing in the HEX core) (3) entrance and exit effects (losses due to sudden contraction and expansion at the inlet and outlet of the HEX) and (4) gravity losses (negligible in many applications).

Hot and cold side pressure losses can be directly correlated to the heat exchanger geometry and flow characteristics by means of equation 2.32, [4, 61].

$$\left(\frac{\Delta P}{P_1}\right)_{h,c} = \frac{G^2}{2\rho_1}\Bigg[\underbrace{(1-\sigma^2+K_c)}_{\text{(Entrance effect)}} + \underbrace{2\left(\frac{\rho_1}{\rho_2}-1\right)}_{\text{(Flow acceleration)}} + \underbrace{f\frac{A}{A_c}\frac{\rho_1}{\rho_m}}_{\text{(Core friction)}} \underbrace{-(1-\sigma^2-K_e)\frac{\rho_1}{\rho_2}}_{\text{(Exit effect)}}\Bigg] \tag{2.32}$$

In the previous equation, K_c and K_e are the contraction and the expansion loss factors that can be approximated as: $K_e = (1-\sigma)^2$ and $K_c = 0.5(1-\sigma)$. Where, σ is the ratio of the free flow area to frontal area and ρ_m is the mean specific density. ε and $\Delta P/P$ are directly related to the heat exchanger geometry and flow arrangement. The definition of these parameters in design is sufficient to completely determine the thermodynamic impact of the component in the cycle. Keys and London [61] provided a complete methodology which can be used to iteratively size the heat exchangers and a similar approach can be used for an off-design analysis [4].

The main limitation of this approach is constituted by the assumption that prior knowledge on HEX type and main geometrical feature is available. Keys and London [61] provide a database of existing heat exchangers geometries and flow data that can be used to apply the methodology. However, it becomes clear from multiple literature examples, that intercooler and recuperator HEXs have to be uniquely designed for the specific application, considering also engine size and constraints before choosing the appropriate configuration [7, 14, 60].

Due to this strong interaction between engine thermodynamic parameters and the aforementioned heat exchangers design issues, the identification of a simpler model in agreement with the scope of this project was needed. Detailed discussion is presented below.

HEX simple model

The scope of this section is to identify a relation that allows to link engine thermodynamic inputs with the heat exchanger constitutional parameters (ε and $\Delta P/P$). Moreover, the effect of the selection of these two design values on HEX size and weight has to be captured. In this manner, the heat exchanger could be modeled as a coherent black box, that behaves as close as possible to a real component.

In agreement to this purpose, Stevens [62, 63] has shown that, for an optimized microchannel recuperator, the optimal ratio between hot and cold side pressure losses is only function of gas turbine proprieties; in particular, it primarily depends on compressor pressure ratios. Moreover, McDonald [2], reports a proportionality relation (equation 2.33) showing the influence of heat exchangers and thermodynamic cycle parameters on the recuperator volume, displaying similar conclusion to Stevens.

$$V \propto \underbrace{\frac{\dot{m}}{\sqrt{\Pi_C}}}_{\text{(Power Parameter)}} \times \underbrace{\left(\frac{\varepsilon}{1-\varepsilon}\frac{1}{\sqrt{\Delta P/P}}\right)}_{\text{(Recuperator Parameters)}} \times \underbrace{\left(\sqrt{\frac{f}{j^3}}\frac{1}{\beta}\right)}_{\text{(Surface Geometry)}} \tag{2.33}$$

Where $\dot{m}$ is the inlet mass flow, f is the Fanning friction factor, j is the Colburn heat transfer factor and β indicates the surface compactness. Similar relations can be found in

references [16, 18, 64], generalizing the treatise to any heat exchangers specialization. Most of the work available in literature has been done on the recuperator side, which exhibits stronger interactions with the cycle thermodynamics than the intercooler. However, the influence of the "Recuperator Parameters" group in equation 2.33 is common to any HEX.

Simple sizing charts are also available for different recuperator types in reference [59, 65–67], showing the impact of effectiveness and pressure drop onto recuperator specific size and weight. An example has been reported in Figure 2.7, that can be used to model the recuperator volume variation as function of target effectiveness or pressure loss for given flow conditions.

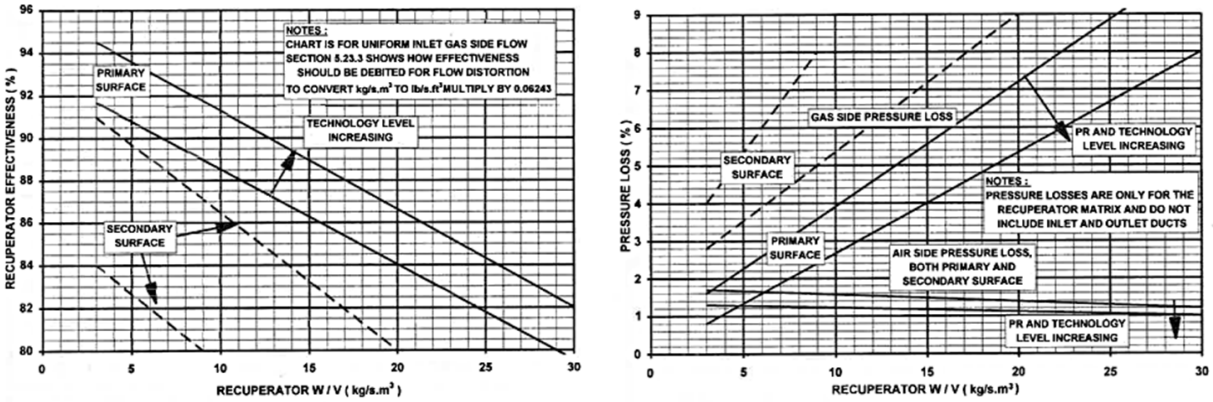

(a) Effectiveness chart

(b) Pressure loss chart

Figure 2.7: Recuperator design point performance as function of mass flow per unit of volume [67]

These charts are useful for both design and off-design. In design, the effect that the selection of a certain effectiveness and pressure loss has on the heat exchanger size can be captured. Great insight is also provided on the recuperator off-design behavior. In part power analysis, the heat exchanger volume is fixed by the design case. Therefore, as the inlet airflow reduces, ε increases and $\Delta P/P$ also decreases (from Figure 2.7). Reference [67] provides equations to model the recuperator effectiveness and pressure loss variation in off-design, respectively equation 2.34 and 2.35.

$$\varepsilon = 1 - \frac{\dot{m}_{1c}}{\dot{m}_{1c,des}}(1 - \varepsilon_{des}) \tag{2.34}$$

As explained in reference [56, 67], this simple relation holds because the downstream capacity is essentially fixed by the HP turbine and it represents a good first order accuracy model for the recuperator. The pressure losses on the recuperator cold side may increase in part power, due to the augmented heat transfer, while, on the hot side, they tend to decrease due to the reduced inlet corrected mass flow. These variation can be captured by means of equations 2.35 and 2.36, [67].

$$\left(\frac{\Delta P}{P}\right)_c = \left(\frac{\Delta P}{P}\right)_{c,des} \cdot \frac{\left[\left(\frac{\dot{m}_{1c}}{P_{01,c}}\right)^2 \cdot \frac{T_{02,c}^{1.55}}{T_{01,c}^{0.55}}\right]}{\left[\left(\frac{\dot{m}_{1c}}{P_{01,c}}\right)^2 \cdot \frac{T_{02,c}^{1.55}}{T_{01,c}^{0.55}}\right]_{des}} \tag{2.35}$$

and

$$\left(\frac{\Delta P}{P}\right)_h = \left(\frac{\Delta P}{P}\right)_{h,des} \cdot \frac{(\dot{m}_{1h}^2 \cdot T_{01,h})}{(\dot{m}_{1h}^2 \cdot T_{01,h})_{des}} \tag{2.36}$$

Equations 2.34, 2.35 and 2.36 are only valid for the recuperator case. Reference [67] provides a similar set of equations for the intercooler off-design modeling. The effectiveness in part power can be assessed by means of equation (2.37). The intercooler effectiveness increases in part power, however, there is a much stronger influence of hot side inlet flow conditions that have to be taken into account.

$$\varepsilon = 1 - \frac{\left(\frac{\dot{m}_{1h}\sqrt{T_{01,h}}}{P_{01,h}}\right)}{\left(\frac{\dot{m}_{1h}\sqrt{T_{01,h}}}{P_{01,h}}\right)_{des}} (1 - \varepsilon_{des}) \tag{2.37}$$

Intercooler hot side pressure ratio losses can be approximated as follows [67]:

$$\left(\frac{\Delta P}{P}\right)_h = \left(\frac{\Delta P}{P}\right)_{h,des} \cdot \frac{\left(\frac{\dot{m}_{1h}^2 T_{01,h}}{P_{01,h}^2}\right)}{\left(\frac{\dot{m}_{1h}^2 T_{01,h}}{P_{01,h}^2}\right)_{des}} \tag{2.38}$$

The heat exchangers off-design behavior can be completely characterized by the previously introduced model. As discussed by McDonald [7], the heat exchanger effectiveness increases with part power except for very low mass flows rates. In this particular condition, longitudinal conduction has a much stronger impact on the effectiveness, which may abruptly decrease. The negative performance effects are strongly dependent on heat exchanger types and materials employed, and, even with the more complete model mentioned, it becomes difficult to properly assess them. For a preliminary study, the simple model proposed by Walsh and Fletcher represents a good approximation, assuming that the off-design analysis is not conducted at extremely low mass flows. In a later design stage, the availability of a full intercooler and recuperator performance maps, such as the one presented in Figure 2.8, can certainly improve the outcome of this study.

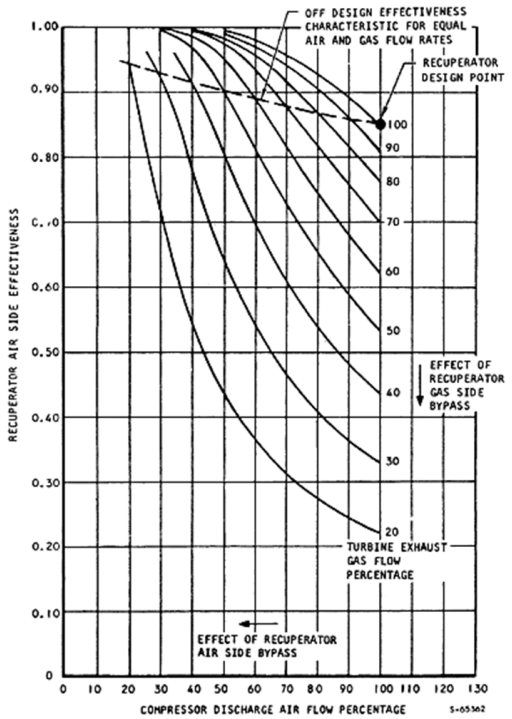

Figure 2.8: Typical recuperator performance map [7]

2.3.3 Combustor Modeling

Complications in the combustor design and off-design model are commonly embedded in the size effects. In fact, according to [68], scaling techniques for small combustors are less defined as result of the following: (1) surface area and volume dramatically changing with size, (2) increased effects of wall quenching, (3) low fuel flow implies a smaller number of injectors and orifice sizing and (4) increased leakage effect and pressure losses.

A simple relation that correlates combustor efficiency with primary zone volume has been presented in [16]. Equation 2.39 accounts for some of the phenomena previously mentioned, and it provides a preliminary base for introducing this treatise.

$$\eta \propto \left(\frac{V \xi \exp(T_3/b)}{\dot{m}_3} T_w \right) \tag{2.39}$$

where V represents the primary combustor volume, ξ is the reaction time, T_w is the wall temperature and b is a constant. Additional complexity has to be accounted for the semi-closed cycle analysis due to the considerable amount of burnt products that enter the combustor. As discussed previously, optimal recirculation ratios (FFR) can be two or three times greater than the inlet air flow. A comprehensive study of the effects of uncooled exhaust gas recirculation on emissions and combustor efficiency has been done in reference [69], using liquid Jet-A as fuel. The experiments were conducted at constant pressure and with an equivalence ratio varying between 0.3 and 1.0. Although more details are available in the reference, main findings are:

- Increasing the recirculation ratio reduces the NO_x and CO emissions up to a certain FFR value. Further increase has little effects on emissions.
- Combustion efficiency rises with the percentage of recirculated flow, in particular for high values of equivalence ratio.
- Equivalence ratio stability range has also augmented, leading to an almost doubled combustor operational range.

These results have been obtained with a combustor designed for a recirculation ratios far below the unity. Although similar trends could be expected for higher recirculation ratios, additional problems have to be accounted in the realization of the combustion chamber. Rodgers [18], identifies the combustor as the key element for the semi-closed cycle success. The author underlines that for high feedback flow ratios, low volumetric heat release ratios are required to ensure sufficient mixing and obtain the desired stability limits. This leads to a primary zone volume per unit of recirculation at least three times larger than a conventional combustor. The LP module weight reduction advantage could be levelled-off by this aspect. Combustor cooling, sufficient pressure drop and clean feedback flow are additional critical aspects to be considered in the design [10, 17, 18].

These aspects prevent using a simplified treatise, based on scaling relations, to acquire sufficient combustor geometrical and performance insight. Therefore, a more sophisticated methodology has been investigated, capable of fulfilling the requirements of this project and addressing common issues encountered in combustor modeling. Sufficient details on the combustor design and off-design performance modeling are subsequently reported. However, the complete design modeling approach is reported in appendix C.

Combustor design

This paragraph discusses a simple formulation based on reference [70], that can be used to assess combustor design dimensions and performance. This methodology has been widely employed in literature [71–74] and is applicable to any combustor type: can, annular or can-annular. For

small gas turbines, it is common practice to use an annular straight or reverse flow configuration [74]. This is because such solutions suffer less from problems associated to the close coupling of compressor, combustor and turbine, and the high rotational speed involved. Reference [75] reports that reverse flow combustors have superior performance than straight flow. However, the characteristic high surface to volume ratio of the first type adds several complications in the liner cooling system. Thus, a straight design is more beneficial from this perspective.

As discussed in [70], not the best combustor design results from the application of the following treatise and further refinement must be addressed. However, reasonable criteria can be derived to size primary areas and features of combustors, such as: casing, liner, diffuser, swirler, etc. Further methodology validation via CFD has been discussed in [76, 77], showing satisfactory results. The design method is essentially composed of the following four steps: (1) combustor type selection, (2) characterization of casing and liner cross-sections, (3) combustor zones sizing, and (4) definition of cooling requirements.

Assuming that the combustor type is already established, the design method starts with the definition of the reference area (A_{ref}), which is typically associated to the case area. Aerodynamic and chemical considerations can be used to define this parameter.

Aerodynamic design Following the discussion in [74], the aerodynamic design of combustors is a primary aspect to be considered. Aerodynamic considerations have a considerable impact on combustor total pressure losses due to the strong mixing between fresh air and burnt products that occurs in each combustor zone. Equation 2.40 has been developed to correlate the reference area to combustor pressure losses and inlet flow data.

$$A_{ref} = \left[\frac{R}{2} \left(\frac{\dot{m}_3 \sqrt{T_{03}}}{P_{03}} \right)^2 \frac{\Delta P_{3-4}}{q_{ref}} \left(\frac{\Delta P_{3-4}}{P_3} \right)^{-1} \right] \tag{2.40}$$

The total pressure loss ($\Delta P_{3-4}/P_3$) depends on combustor type and operating conditions. Its value typically varies between 4% and 8%. The term $\Delta P_{3-4}/q_{ref}$ is the pressure loss factor, which represents the sum of two contributions as shown in equation 2.41: the diffuser pressure drop ($\Delta P_{diff}/q_{ref}$) and the liner pressure drop ($\Delta P_L/q_{ref}$). The former term has to be minimized, since diffuser losses have no contribution in the combustor process. The latter is associated to the liner cooling system sizing and a careful study is needed to quantify this term [74].

$$\frac{\Delta P_{3-4}}{q_{ref}} = \frac{\Delta P_{diff}}{q_{ref}} + \frac{\Delta P_L}{q_{ref}} \tag{2.41}$$

The pressure loss factor, unlike the overall pressure loss, is a fixed property of the combustor which does not depend on operating conditions. Typical values are reported in [70, 74] that can be used for a preliminary evaluation.

Chemical considerations According to references [70, 71], the reference area can obtained from consideration of the chemical processes occurring in the whole combustor, through the definition of the combustor efficiency. For any operating condition, the combustion efficiency can be expressed as function of the correlating parameter θ, defined as:

$$\theta = \frac{P_{03}^{1.75} A_{ref} D_{ref}^{0.75} \exp(T_3/b)}{\dot{m}_3} \tag{2.42}$$

Where, b can be assumed equal to 300 according to [74], or it can be more precisely related to a function of the primary zone equivalence ratio (ϕ_{PZ}) by means of the relations reported below [70, 71].

$$b = 245(1.39 + \ln(\phi_{PZ})) \qquad \text{for} \qquad 0.6<\phi_{PZ}<1.0$$
$$b = 170(2.00 - \ln(\phi_{PZ})) \qquad \text{for} \qquad 1.0<\phi_{PZ}<1.4$$

Reference [70] points out that the majority of combustors have an efficiency close to 100% for a θ-value of $73 \cdot 10^6$. Inserting this value in equation 2.40 allows to compute the reference area value. Figure 2.9 shows visual evidence of what just mentioned.

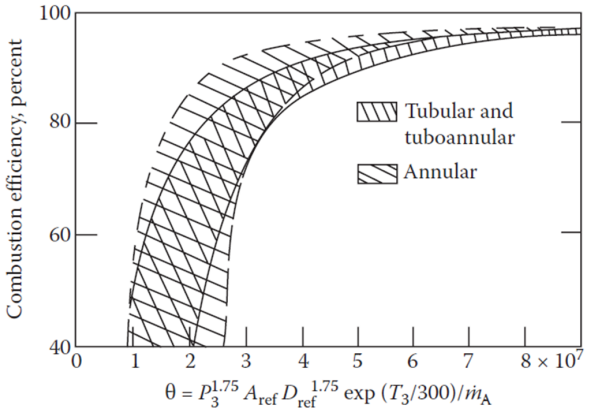

Figure 2.9: θ-parameter correlation for conventional combustor designs [70, 74]

Two different values of the reference area can be computed by means of the aerodynamic and chemical treatise. According to [72] the area calculated using equation 2.40 leads to satisfactory pressure losses, however the expected efficiency will not be high. The chemical treatise provides a value that guarantees good combustor efficiency at the cost of significant pressure losses. Typical choice could be to take the average between the two calculated values. However, most of the references consulted indicate that it is preferable to use equation 2.40 over 2.42 for a preliminary study.

Combustor zone sizing Once the combustor reference area is established, the remaining combustor sizing can be completed for each combustor zone. The full sizing procedure is discussed in appendix C.1. The summary presented here leads to the definition of only the important design parameters that are needed for off-design and weight considerations.

The first step is to calculate the combustor area (A_{ft}), which is related to the liner cross-sectional area. This can be simply done by means of equation 2.43. The value of the constant $\overline{k}$ is normally assumed to 0.7 for can and annular combustors, 0.65-0.67 for can-annular. Reference [72] derives an expression to calculate the optimal value of this constant as function of additional combustor design data.

$$A_{ft} = \overline{k} \cdot A_{ref} \tag{2.43}$$

With this information available, the combustor zones can be preliminary sized. According to Melconian and Modak [70], the length of the primary zone should be set to: $L_{PZ} = 0.75D_{ft}$, while the secondary zone length can be assumed equal to: $L_{SZ} = 0.5D_{ft}$. The dilution zone length is computed following reference [71] from Table 2.2, as function of the pressure loss factor and the pattern factor (PF).

Table 2.2: Dilution zone length estimation table

$\mathbf{\Delta P_{3-4}/q_{ref}}$	$\mathbf{L_{DZ}/D_{ft}}$
15	3.78-6PF
20	3.83-11.83PF+13.4PF^2
30	2.96-9.86PF+13.3PF^2
50	2.718-12.64PF+28.51PF^2

With this information the combustor volume can be estimated, completing the general sizing procedure. Typically, a diffuser is employed to slow down the flow to optimal combustion velocities before entering the primary zone. This section needs to be sized as well before proceeding with the cooling flow calculations. However, the treatise so far presented is enough to gain sufficient insight on the variation of the burner main dimensions as function of thermodynamic and inlet flow requirements. Figure 2.10 is reported to show main combustor parameters employed in the analysis.

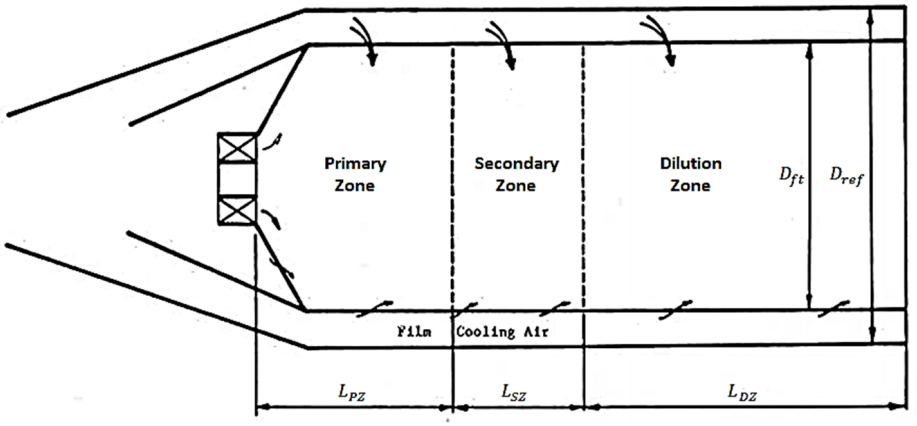

Figure 2.10: Main combustor geometrical parameters, adapted from [70]

Combustor off-design

A simple model to account for combustor efficiency and pressure loss variation as response of off-design flow characteristics is discussed in [55, 56]. It is common to have combustor efficiencies near 100% at design, however, at part load near idle and at very high altitudes, the burner efficiency can deviate noticeably from the design value. A useful parameter that relates efficiency with combustor geometry is the θ-parameter presented in equation 2.42. For the off-design analysis, the two previously mentioned references introduce the so called Ω-parameter (burner loading), whose definition has been reported below.

$$\Omega = \frac{\dot{m}_3}{P_{03}^{1.8} \exp(T_{03}/300) V_{brn}} \tag{2.44}$$

The burner loading represent the inverse of the θ-parameter, although they have been defined in a slightly different manner between the different references. The exact definition used in each cited reference has been reported and used in this treatise. Figure 2.11 reports the combustor efficiency change as function of burner loading for different engine settings.

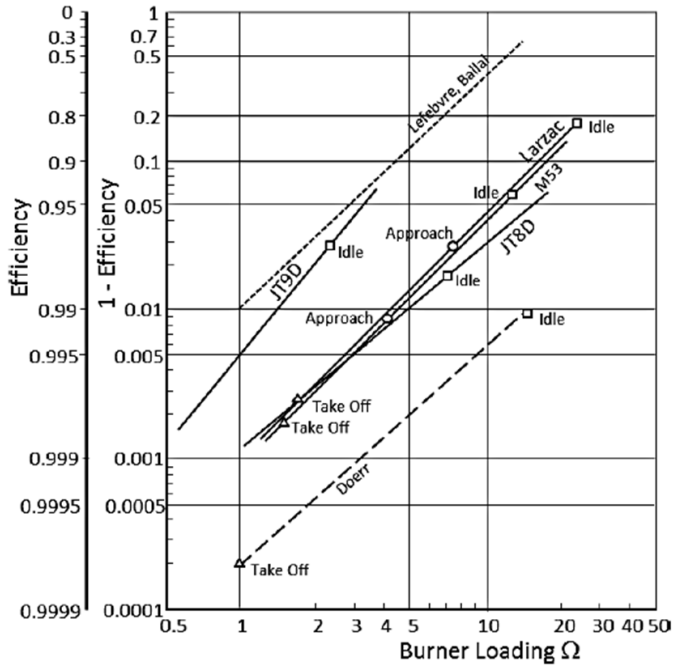

Figure 2.11: Combustor efficiency variation as function of burner loading [56]*

As visible in the figure, a logarithmic relation can well approximate the efficiency variation for different burner loading values. Equation 2.45 has been reported in references [55, 56] to accomplish this task. The part load constant b is normally set to 1.6, however it can be adjusted as shown in [56],

$$\log(1-\eta) = \log(1-\eta_{des}) + b \cdot \log\left(\frac{\Omega}{\Omega_{des}}\right) \tag{2.45}$$

The total pressure losses in combustor systems are caused by two mechanisms: friction losses (cold losses) and heat addiction losses (hot losses). The latter term can be neglected in conventional burners since its influence on the overall pressure losses in considerably less than the cold losses [74]. For this reason, the combustor can be idealized as a duct [55, 56]. Therefore, the overall pressure losses can be associated with the off-design combustor inlet corrected mass flow variation, by means of equation 2.46.

$$\frac{\frac{\Delta P_{3-4}}{P_3}}{\left(\frac{\Delta P_{3-4}}{P_3}\right)_{des}} = \left[\frac{\frac{\dot{m}_3\sqrt{RT_{03}}}{P_{03}}}{\left(\frac{\dot{m}_3\sqrt{RT_{03}}}{P_{03}}\right)_{des}}\right]^2 \tag{2.46}$$

Full combustor loss models are beyond the scope of this work. Nonetheless, complete models can be found in [78, 79]. The impact of hot losses has been properly quantified in the cited papers, giving further justification to the previously presented approach.

2.4 Weight Modeling

The purpose of this section is to identify weight models that are suitable for the scope of this work. According to reference [80], two approaches can be followed to preliminary assess the engine overall weight: a "whole engine based" and a "component based" approach. The former

*Original reference: H.G. Münzberg, J. Kurzke, Gasturbinen - Betriebsverhalten und Optimierung,Springer-Verlag Berlin Heidelberg New York, 1977

leads to the definition of simple weight correlations solely function of main engine parameters such as: mass flow, thrust, OPR and BPR (for turbofan engines), etc. A good summary of the currently available methods that enter this category can be found in [80]. Statistical methods can also be employed for a preliminary overall engine weight assessment [81]. Unfortunately, most of these methods have been developed for turbojet and turbofan engines only, which makes them consequently inapplicable to this case. Head [31] reports a simple relation developed by Berner* and Benguedouar [82], that seems to be more generally applicable to turbo-generators. An adapted version of the original equation to small/micro recuperated gas turbines is also provided.

Advantage of this first approach can be identified in the simplicity of these methods. In fact, a limited amount of data is a priori needed to apply these correlations. However, by means of these models, it becomes difficult to properly assess the effects that different thermodynamic inputs have on engine weight and size. Thus, making this approach unsuitable for the optimization and the objectives of this thesis. Furthermore, these techniques have been developed for conventional cycle architectures. Corrections have to be made to account for the introduction of heat exchangers [31]. Therefore, at the current status, they are certainly not suitable for a semi-closed cycles analysis.

A "component based" weight model represents the solution in agreement with the thesis objectives. The goal of this part of the literature review was to identify component based models that can meet the requirements of this work and that are compatible with the previously discussed component performance models. Detailed discussion on this topic is reported below. Models for compressors, heat exchangers, combustor, turbines, shaft, gearbox and accessories will be treated, showing the reasoning behind the choices made.

2.4.1 Component Based Model

A simplified component weight model has been reported in reference [14]. This model calculates the weight of individual components by means of simple scaling relations from existing reference component data. Scaling relations have been defined in the ERAST design program for all the components investigated in this thesis, and reasonable weight data can be obtained as shown in the reference quoted. However, similar problems discussed for the performance model can be identified here. Additionally, the ERAST models assume the availability of detailed weight reference data, which are absent at this stage.

A detailed component based model has been created by NASA in the 1979 [83], resulting into the computer program called WATE (Weight Analysis of Turbine Engines) applicable to large and small gas turbines. Radial and axial turbomachinery weight can also be assessed by means of this model. Subsequent releases of the program have improved the weight prediction for small gas turbines [84]. More recent component based engine models can be found in reference [80], with particularly focus on turbofan and geared turbofan engines, and reference [85], suitable for micro gas turbines. Both these models are not directly applicable in this thesis work. However, they constitute good references for some component weight estimation.

Below, the overall engine weight is broken down into the individual components analyzed within this work. Detailed information on currently available weight modeling techniques are provided. In this phase, it was important to identify models compatible with the theory developed in the performance sections and capable of satisfying the requirements of this thesis.

*Original reference: J. K. Berner, Space Power Conversion Systems Using a Modified Ericsson Cycle with Turbomachinery, MS Thesis, MIT, 1985

2.4.2 Compressor and Turbine

Typical radial compressor and turbine preliminary weight assessment models relate the overall compressor weight to the impeller characteristic tip dimension (r_2). In the Onat and Klees version of the WATE model [83], the whole turbomachinery weight scales with r_2 by means of a cubic exponent ($W_{C,T} \propto r_2^3$). Different coefficients are used for compressors and turbines to model the typical material employed. Equations 2.47 and 2.48 are valid for titanium centrifugal compressors and steel radial turbines.

$$W_C = \frac{1}{13.1} \cdot r_2^3 \tag{2.47}$$

$$W_T = \frac{1}{5} \cdot r_2^3 \tag{2.48}$$

In the previous equations, the radius value is expressed in inches and the calculated weight in pounds. Rodgers [64], argued that a better weight approximation is given for an exponent of 5/2 or even quadratic, depending on the engine power range under consideration. However, no clear indication is provided on the relation between the exponent value and the power level.

Hale [84], splits compressor and turbine overall weight into the sum of blade, disk and shroud. A diffuser weight model was developed for compressors only. The blade weight has been calculated assuming the flow path to be comprised between two ellipses and a shroud blade thickness (t_{tip}) of 0.076 cm and the hub blade thickness according to equation 2.49, resulting in 15% blockage. The same assumptions have been made for compressor and turbine blade volume calculations.

$$t_{hub} = 0.15 \left(\frac{2\pi r_{1h}}{Z_B} \right) \tag{2.49}$$

The ratio between axial length to radial height (D_A/D_R) is assumed to be equal to 2.0 for compressors and 2.1 for turbines. Figure 2.12 has been added to provide visual explanation of the previously mentioned parameters. In the figure, r_1 has to be substituted by r_3 for the turbine model.

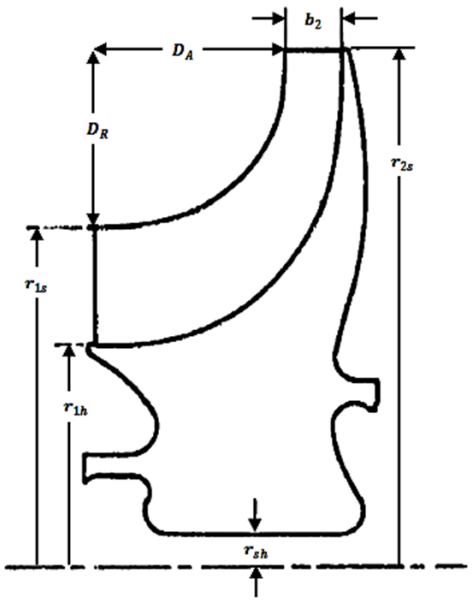

Figure 2.12: Centrifugal compressor - radial turbine impeller schematic [84]

Once the blade volume is available, the blade weight can be computed by multiplying it by the density of the chosen material. The disk volume is sized through a preliminary design iterative

procedure that ensures enough blades support for minimum weight. Just a brief description is provided in [84], which is not sufficient to recreate the whole model. Assumptions will have to be made to consider this aspect. Equations 2.50 and 2.51 are provided to calculate compressor and turbine shroud weight contributions respectively [84].

$$W_{C,sh} = 0.1673\rho \left(\frac{r_{1s} + r_2}{2} \right)^3 \tag{2.50}$$

and

$$W_{T,sh} = 0.1755\rho \left(\frac{r_{3s} + r_2}{2} \right)^3 \tag{2.51}$$

Finally, the compressor diffuser weight can be computed from: $W_{diff} = 0.2845\rho r_2^3$. Reference [83] provides simplified relations to account for centrifugal compressor housing and turbine exit frame. The former weight contribution can be calculated by means of equation 2.52. The latter element is necessary in small turbines to support the turbine bearing and its weight can be computed using equation 2.53. British units have to be used in these equations, hence, L_{ax} and r_2 must be defined in feet.

$$W_{C,case} = 163 \cdot L_{ax} \cdot r_2 \tag{2.52}$$

$$W_{T,frame} = 55.5 \cdot r_2^2 + 6.53 \tag{2.53}$$

2.4.3 Heat Exchangers

The WATE model presents a section dedicated to the heat exchanger weight characterization. The approach presented in references [83, 84] is applicable to rotary and fixed-tube heat exchangers. However, this models assumes sufficient geometrical knowledge which would be unavailable from the performance model illustrated previously. The objective of this section was to identify a model capable of generally linking heat exchanger performance characteristics. As previously explained, specific heat exchangers have to be designed considering mission requirements and engine geometrical constraints. Therefore, at this stage it is not possible to define a more advanced approach than this.

Support can be found in the theory previously presented in section 2.3.2. Distinction has to be made for heat exchangers employed as intercooler or as recuperator. Starting from this last element, McDonald [2] relates the recuperator volume to cycle thermodynamic parameters by means of equation 2.33. Reference [31] employs the previously mentioned relation to develop a preliminary weight scaling relation that can be used without extensive knowledge on heat exchanger geometry. A similar approach has been reported in references [18, 64]. Equation 2.54 can be used to preliminary define a weight trend for the recuperator.

$$W_{RC} = W_{ref} \cdot \left\{ \left[\frac{\dot{m}}{\sqrt{\Pi_C}} \left(\frac{\varepsilon}{1-\varepsilon} \frac{1}{\sqrt{\Delta P/P}} \right) \right] / \left[\frac{\dot{m}_{ref}}{\sqrt{\Pi_{C,ref}}} \left(\frac{\varepsilon_{ref}}{1-\varepsilon_{ref}} \frac{1}{\sqrt{(\Delta P/P)_{ref}}} \right) \right] \right\} \tag{2.54}$$

A similar relation can be derived from [16, 18] for the intercooler (equation 2.55). In the formula, P_{mean} represents the arithmetic mean between hot and cold side heat exchanger inlet pressures.

$$W_{IC} = W_{ref} \cdot \left\{ \left[\frac{\dot{m}}{\sqrt{P_{mean}}} \left(\frac{\varepsilon}{1-\varepsilon} \frac{1}{\sqrt{\Delta P/P}} \right) \right] / \left[\frac{\dot{m}_{ref}}{\sqrt{P_{mean,ref}}} \left(\frac{\varepsilon_{ref}}{1-\varepsilon_{ref}} \frac{1}{\sqrt{(\Delta P/P)_{ref}}} \right) \right] \right\} \tag{2.55}$$

Reference [18], provides sufficient reference data that can be used in equations 2.54 and 2.55 to preliminarily assess the weight of a generic heat exchanger matrix. Table 2.3 summarized the available reference data to get a preliminary numerical value. Bear in mind that the intent of this treatise is not to provide exact absolute weight values, but to reasonably link the thermodynamics to heat exchangers weight trends to perform the weight optimization in a coherent way.

Table 2.3: Intercooler and recuperator reference data from [17]

	$\dot{\mathbf{m}}_{\mathbf{ref}}$	$\mathbf{\Pi}_{C,ref}$	$\mathbf{P}_{\mathbf{mean,ref}}$	$\boldsymbol{\varepsilon}_{ref}$	$(\mathbf{\Delta P/P})_{\mathbf{ref}}$	$\mathbf{W}_{\mathbf{ref}}$
IC	3.6 lb/s	-	29.392 psi	0.80	0.04	190 lb
RC	3.6 lb/s	13.2	-	0.84	0.05	237 lb

2.4.4 Combustor

A suitable combustor weight model has been identified in the treatise presented in reference [83, 84]. In the WATE approach, the overall combustor weight has been split into liner, case and dome contributions. Liner and case are modeled as ducts, while the dome weight is calculated by means of equation 2.58, originally developed in [86] and reported in [83, 84]. Figure 2.13 reports a useful schematic showing important burner parameters used in the weight model.

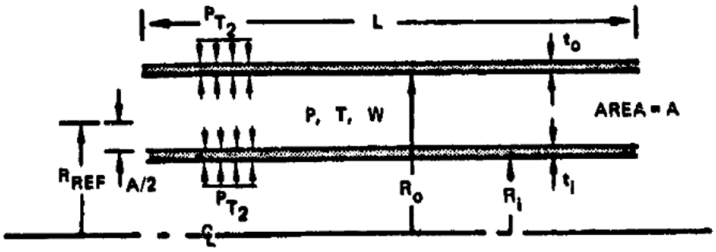

Figure 2.13: Burner duct model schematic [83, 84]

The liner and case wall thickness are determined from the equation for stress in a longitudinal section of a thin cylinder subjected to internal pressure (equation 2.56). The assumed material is stainless steel with an allowable stress level of 483 MPa. With this data, equation 2.56 can be solved for the wall minimum thickness $t_{min,i}$ and $t_{min,o}$. A minimum gage thickness of 0.127 cm is a suggested assumption for the combustor case, while, for the combustor liner 0.140 cm is recommended [84].

$$\sigma = \frac{PD}{2t} \tag{2.56}$$

Equation 2.57 is employed to calculate both liner and case weight; where, D_i and D_o are respectively the combustor inner and outer diameter (see Figure 2.14) and L is the length of the liner or case.

$$W_{B,case-liner} = \rho\pi L\left(D_o t_{min,o} + D_i t_{min,i}\right) \tag{2.57}$$

Finally, the combustor weight can be established by adding the dome weight, estimated according to the following relation. The term W_{dome} is representative of the following individual weight contributions: burner dome, fuel manifold, fuel nozzles and other fuel system components.

$$W_{dome} = 0.0106(R_o^2 - R_i^2) \tag{2.58}$$

Note that in the previous equation the coefficient 0.0106 is expressed in lb/in^3. Units consistency has to be maintained in the employment of equation 2.58. The illustrated combustor

model is compatible with the burner performance modeling technique, presented in section 2.3.3. Moreover, it is applicable to any combustor configuration, because the difference between each type is embedded in the input definition. Figure 2.14 has been added to conclude this section, showing previously discussed inputs referred to a combustor general schematic.

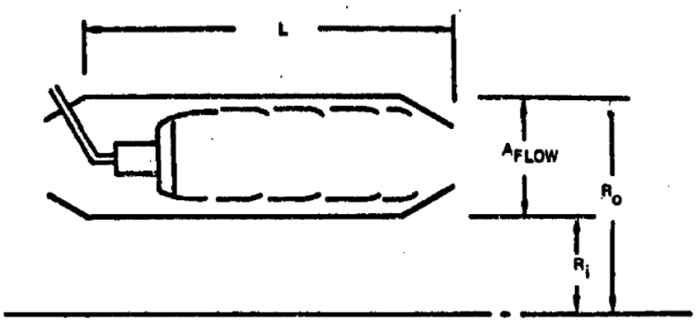

Figure 2.14: Burner wight model parameters schematic [83, 84]

2.4.5 Shafts

The shaft element is the power connection component between compressors, turbines and propeller. For the current project, the preliminary sizing technique introduced in [83, 84] has been found satisfactory. The shaft element is assumed to be a cylinder, with D_i and D_o respectively the inner and outer shaft diameters, as shown in Figure 2.15 reported below.

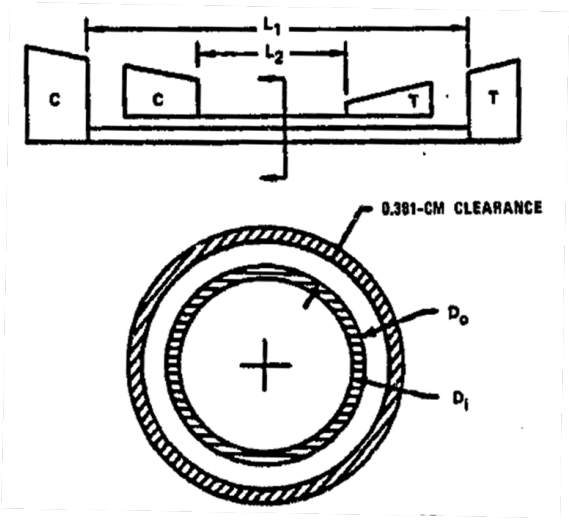

Figure 2.15: Shaft schematic [83, 84]

Shaft dimensions are determined from consideration on the transmitted torque and maximum allowable stress. The torque is calculated from the total power output produced by every turbine element connected to the shaft. The shear stress due to torque load can be calculated by means of equation 2.59, [83, 84]. The following formula can be solved for D_o assuming the shaft material and D_i known.

$$\tau = \frac{16TD_o}{\pi\left(D_o^4 - D_i^4\right)} \tag{2.59}$$

Finally, the overall shaft weight can be calculated by means of the following equation:

$$W_{sh} = \rho \pi L_{sh} \left[\frac{D_o^2}{4} - \frac{D_i^2}{4} \right] \tag{2.60}$$

Concentric multiple shaft configurations can also be sized, assuming a clearance of 0.381 cm between the inner and outer shafts [83, 84]. As pointed out in the references, the calculated shaft weight should be considered as the absolute minimum required. In fact, other considerations, rather than solely torque aspects, normally determine the final shaft sizing. In particular, shaft critical speed and longitudinal stiffness more likely determine the shaft inner and outer diameters. However, these aspects are function of bearing arrangements, mount stiffness and location of the rotating masses, which can only be considered in a detailed design phase. Therefore, the technique discussed so far has been considered appropriated for the current project objectives.

2.4.6 Gearbox and Accessories

The goal of this section is to identify of simple models to predict the weight of gearbox and accessories as function of the relevant thermodynamic parameters. For this project, the gearbox weight includes only the contribution of the reduction element between the main shaft and the thrust element (propeller). The accessories block includes all the remaining weight contributions belonging the gas turbine block, since only this section is object of the study.

Gearbox Different arrangements have been developed for aviation gearboxes. Minimum weight requirements and high reliability are main design requirements, in particular for turboprop engines, where a high reduction ratio is needed [87]. A simple method for estimating the gearbox weight contribution has been proposed by NASA [83], after elaboration of the extensive work presented in [88]. This lead to equation 2.61, generally applicable to the typical gear sets used in aviation.

$$W_{gear} = 324 \left(\frac{SHP}{RPM_{sh}} \right)^{0.80} \tag{2.61}$$

Where SHP is the input shaft power and RPM_{sh} is the input rotational speed. Similar relation can be found in references [14, 84]. Note that equation 2.61 has been developed in British units. Although, the detailed design of a gearbox is outside the scope of this thesis work, equation 2.61 has been found too simplistic. Reference [87] proposes a method applicable in preliminary design stages to estimate the weight of different gear systems that meet the same transmitted power and strength propriety requirements. Spur, helical and planetary gear configurations can be addressed. According to [89], the employment of epicyclic gearbox configuration, with a single output gear and multiple input pinions, ensures the maximum power capacity with minimum size and weight gearboxes. For this reasons planetary gearboxes are commonly used in turboshaft and turboprop engines [80, 90]. Therefore, in the following, more focus is dedicated to this last configuration. Reference [91] presents this methodology applied to all the common aviation gearbox arrangements reported in Figure 2.16.

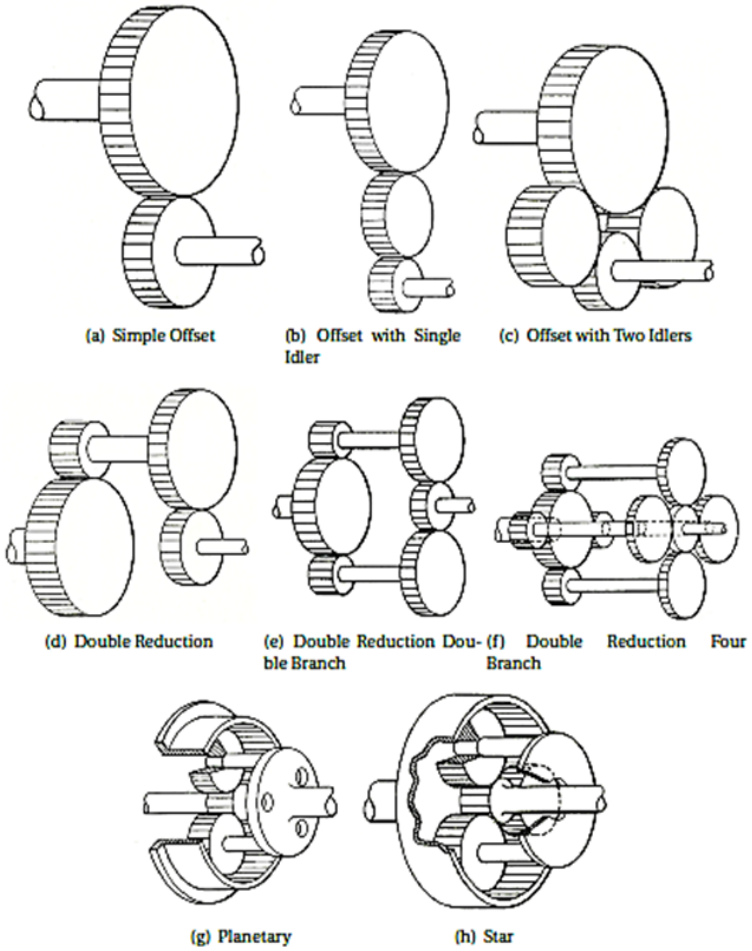

Figure 2.16: Typical aviation gearbox arrangements [91]

As reported in [87], the gearbox weight can be calculated as: $W_{gear} = \rho C M$; where, C is the volume factor, defined according to equation 2.62, and M is the gearbox weight factor, which is function of the gearbox arrangement and relevant design parameters.

$$C = \frac{2T}{K} \tag{2.62}$$

T is the torque transmitted through the gearbox and K is a constant which assumes values between 200 lb/in^3 and 600 lb/in^3. The former value is normally assumed, which leads to more conservative higher mass values [91]. However, reference [80] suggests that correction factor (K) value might have to be adapted according to specific cases. For planetary gearboxes, the weight factor M can be calculated by means of the following relation:

$$M = \frac{1}{b} + \frac{1}{bm_s} + m_s + m_s^2 + \frac{0.4\,(M_0 - 1)^2}{bm_s} + \frac{0.4\,(M_0 - 1)^2}{b} \tag{2.63}$$

Where M_0 is the overall gearbox ratio, b is the number of planets in the epicyclic gearbox system and m_s represents the ratio between planet gears and sun pinion. The following relation holds for planetary gearboxes between M_0 and m_s: $m_s = M_0/2 - 1$. Equation 2.63 can be solved for minimum weight by differentiating with respect to m_s, leading to the following equation:

$$2m_s^3 + m_s^2 = \frac{0.4\,(M_0 - 1)^2 + 1}{b} \tag{2.64}$$

With these equations, the gearbox weight can be calculated for a specified value of b. Lolis [80] reports a relation that can be employed to estimate the optimal number of planets (equation 2.66). As mentioned, similar methodology can be employed for different gearbox types. Specialized definition of the gearbox weight factor can be found in reference [91].

$$b = \frac{16.3677}{3\sin^{-1}\left(\frac{M_0 - 1}{M_0 + 1}\right)1.1736} \tag{2.65}$$

Accessories As reported in reference [84], it is difficult to develop a correlation for individual accessories weight. Therefore, starter/generator, hydraulic pump, oil and fuel pumps have been lumped together into a single correlation. Equation 2.66 can be employed to account for this contribution. If the results of this calculation is less then 10% of the total engine bare weight (W_{bare}), then this last value should be employed instead for a better approximation.

$$W_{acc} = 18.2 + 0.02 * W_{bare} \tag{2.66}$$

For the semi-closed cycle model, a weight model for mixer and splitter elements should be addressed. The WATE model reports a modeling technique for daisy mixer type, which is typical in mixed turbofan configurations. For this work, an individual model for mixer and splitter has not been investigated and their weight has been embedded in the ducting system and characterized within the accessories.

CHAPTER 3

Thermodynamic Cycle

3.1 Introduction

The thermodynamic analysis of a semi-closed cycle represents a particular challenge with respect to conventional open cycles. Several iterations are necessary to solve the thermodynamic cycle in design and off-design. The aid of a computer program is almost necessary to properly perform the analysis. Although numerous software are available to support the thermodynamic engine modeling, their capability of simulating engine arrangements with recirculation has to be verified.

Reference [12] reports a brief summary of commonly employed thermodynamic numerical tools, indicating that NPSS (Numerical Propulsion System Simulation) is suitable for such unconventional analysis. The program allows for an almost complete user customization, giving also the possibility of defining novelty engine concepts such as semi-closed cycles. Hence, NPSS is the selected tool of this project.

This chapter briefly presents NPSS, showing the cycle implementation, the component thermodynamic modeling and solver logic. Subsequently, the focus is dedicated to the numerical implementation of the engine arrangements included in this work, with complete description on the thermodynamic implementation and solver settings.

3.2 NPSS Program Overview

NPSS is an object-oriented environment realized by the NASA Glenn Research Center in cooperation with the U.S. aeropropulsion industry and the Department of Defence. The standard program includes a modified Newton-Raphson solver and a set of standard engine component libraries (Elements), fluid proprieties tables (ThermoPackages) and fluid/shaft linking ports (Fluid/Shaft Ports), built in C++language.

The thermodynamic engine model is created though standard text editors, where the user defines the Elements required to build the engine and their fluid and/or shaft Port links. Moreover, the user has to specify the fluid proprieties and the set of equations that the numerical solver uses to model the engine cycle. Design and off-design steady state as well as transient problems can be defined within the NPSS environment, although only the first two aspects have been considered in this project.

Figure 3.1 has been extracted from the NPSS user guide [92], showing a schematic of a conventional engine model realized within the NPSS logic. Elements, Ports & Links and Solver are the main NPSS building blocks and they will be treated with more detail in the following paragraphs. Since the scope of this section is to provide only a general overview of the program, the reader is referred to [92–95] for more information.

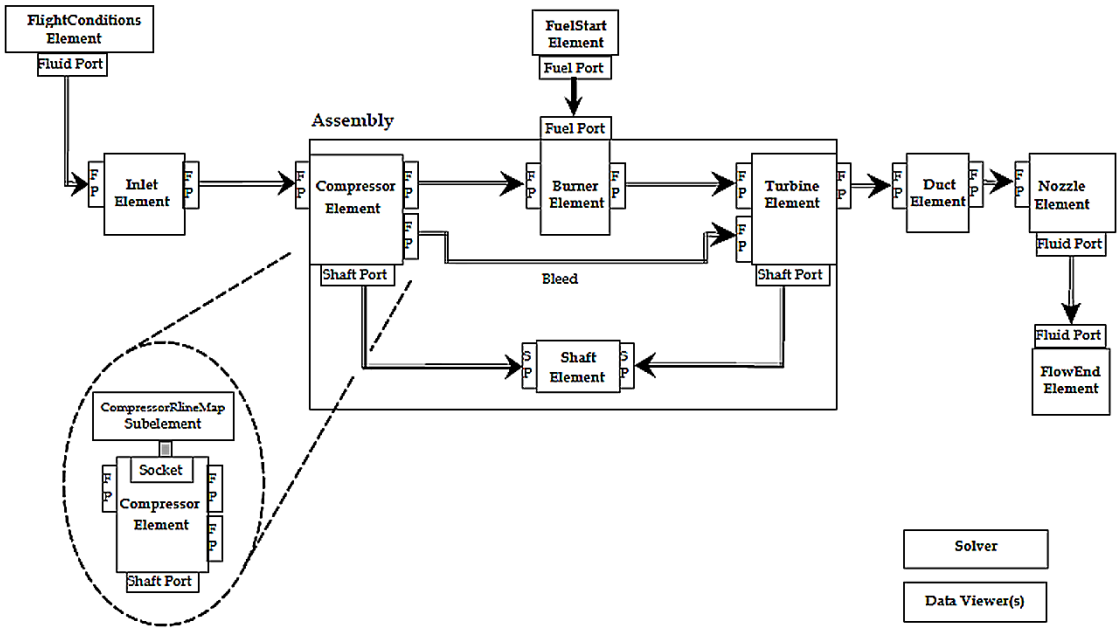

Figure 3.1: Typical NPSS modeling logic of conventional gas turbines [92]

3.2.1 Elements in NPSS

Elements are the main engine cycle building blocks in NPSS. Since the program is an object oriented platform, elements are defined as global classes that the user can use and link to build the desire engine model. Every element has an internal input and output port which is used to automatically pass data from the previous element to the subsequent. Typically fluid data are transmitted between these building blocks such as: mass flow, temperature, pressure, etc, using "Fluid Ports". Some elements are mechanically connected together (compressor, shaft, turbine and propeller elements); in these cases, mechanical proprieties are also provided by means of "Shaft Ports".

External inputs are passed to the corresponding element when the whole cycle model is generated. A complete list of standard elements, with detailed description on necessary input and output for the NPSS version used within this project, is available in the NPSS air breathing reference sheet [93]. Moreover, complex elements such as compressors, turbines, combustors, etc., have the possibility of performing internal calculations using tables, functions or pre-built solvers. The advantage of the component library built in NPSS is the possibility of fully customizing and modifying existing elements, or generating complete new elements. This aspect makes NPSS perfectly suitable for the objectives and the cycle architectures belonging to this thesis work.

The following main NPSS standard building blocks have been used in this project: "Ambient", "FlowStart", "FlowEnd", "Inlet", "Compressor", "Heat Exchanger", "Combustor", "Turbine", "Nozzle", "Propeller" and "Shaft". "Mixer" and "Splitter" elements have been required for the semi-closed cycle arrangement. A brief description of these elements is reported below, showing, where necessary, the modifications and assumptions made to improve the design and off-design performance modeling aspects.

Ambient

Ambient is a standalone element which determines the free stream flow conditions. An internal solver is available to calculate the fluid proprieties at the selected flight operating point. Different atmospheric models are available, including models for humid air. For this project, the international standard atmosphere model has been chosen and dry air has been assumed with

no temperature variations from the standard sea level conditions (dTs = 0). The design flight condition has been set as for the ERAST program [14], see Table 3.1.

Table 3.1: Engine design ambient flight condition

Alt	90000 ft
M	0.40
dTs	0.00

FlowStart - FlowEnd

The FlowStart block is a particular element which features only a flow output port. It is used to define the flow characteristics at the inlet of elements not connected on both sides to others, see Figure 3.1. Three types of FlowStart elements are available in NPSS: "InletStart", "FlowStart" and "FuelStart". InletStart connects elements that require information on the free stream flow conditions calculated within the Ambient element. FlowStart and FuelStart are general block that provide user defined input flow and fuel proprieties to subsequent elements respectively.

The FlowEnd element is used to terminate a flow sequence. It possesses only an input port and it is necessary to tell the solver where to terminate the engine flow sequence. The FlowStart and FlowEnd element combination is extremely important to model the thermodynamics of recuperated engines and semi-closed cycles as will be explained in section 3.3.

Inlet

This element evaluates the performance of a standard inlet component. The user may specify an inlet pressure drop based on ram recovery [93]. Considering the unconventional engine working environment, a complex inlet design might be necessary to provide the engine with the required mass flow with minimal losses in total pressure. Since a detailed inlet model goes beyond the objective of this work, a simplified model has been employed to preliminary estimate a pressure loss value.

Reference [96], reports typical inlet performance maps for different subsonic and supersonic inlet geometries. Pitot inlets are conventionally employed for subsonic flows, exhibiting almost an ideal total pressure recovery along the flight envelope. Experimental data given in [96], which directly correlates the pressure recovery factor with the flight Mach number, have been used for preliminary inlet performance characterization. Figure 3.2 reports a typical subsonic inlet map that has been imported in NPSS. Similar approach has been also followed in reference [97].

Compressor

The compressor element performs complex calculations to ensure proper matching with the turbine element. In design, the block requires information on pressure ratio (Π), total to total stage efficiency (η_s) and design rotational speed (N). The element allows the user to import a compressor reference map for off-design analysis, which is automatically scaled to the given design point by means of equations 2.28, 2.29 and 2.30. Component maps employed within this project are reported in section 4.2.3.

Apart from conventional input and output fluid ports, the compressor element features an output shaft port to ensure the mechanical connection to shaft and turbine elements. In addition, a bleed port is pre-defined in the component for modeling compressor interstage bleeding.

Heat Exchanger

The heat exchanger element performs heat transfer calculations between two working fluid streams for a given total heat flow ($\dot{q}$) or a specified effectiveness (ε), [61]. This second running

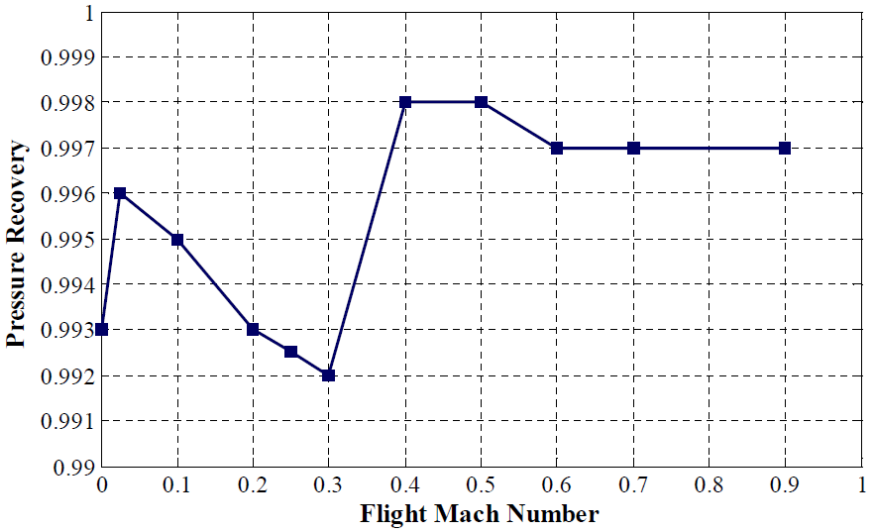

Figure 3.2: Typical subsonic inlet pressure recovery map as function of flight Mach number [96, 97]

option has been preferred, as ε is directly related to HEX performance and size (section 2.3.2). Hot and cold side pressure losses are provided by the user or can be calculated from a given heat exchanger map. Since a component map is not available at this stage, the standard heat exchanger element has been modified to include the off-design modeling relation for intercooler and recuperator effectiveness and pressure losses: equations 2.37 and 2.38, and equations 2.34, 2.35 and 2.36, respectively.

The intercooler cold side mass flow ($\dot{m}_{IC,c}$) has to be a priori defined to perform the heat transfer calculations. This choice has a strong influence not only on the overall intercooler dimensions, but also on the inlet ducting system necessary to supply the required cooling flow, consequently affecting the overall engine drag. Therefore, the selection of $\dot{m}_{IC,c}$ is a trade-off solution between heat transfer performance and HEX size, which is not solely dependent on engine aspects. For this reason, the simplifying assumption of considering the amount of the cold side mass flow rate slightly higher than the hot side (nominally 5% higher) has been used in this project, similarly to the ERAST study [14].

Combustor

The element performs combustion calculations to establish exit gas proprieties from a given fuel and air inlet flows. The combustor element can be run at constant fuel mass flow ($\dot{m}_{fuel}$), fuel to air ratio (FAR) or burner exit temperature, depending on user preferences. A standard input set has to be provided to model the combustor design point and the fuel proprieties. Table 3.2 lists the burner input parameters kept constant in this project, independent of engine arrangement and cycle type.

Table 3.2: Combustor standard input data provided

LHV	18400 BTU/lb
$(\Delta P/P)_B$	0.06
η_B	0.983
$\dot{q}_{loss}$	0.00

Where LHV is the fuel low heat value, set to 18400 BTU/lb (42798.4 kJ/kg) assuming the ASTM-A-1 fuel type [98]. $(\Delta P/P)_B$ is the burner overall pressure losses and the selected value

is indicated for annular combustor geometries [70, 74]. The burner efficiency (η_B) has been assumed from the ERAST program [14]. No parasitic heat losses ($\dot{q}_{loss}$) have been considered for simplicity. Equations 2.45 and 2.46 have been implemented to model the combustor efficiency and pressure loss change in off-design mode.

Finally, the burner exit mixture gas proprieties are defined according to the selected thermodynamic package (ThemoPackage). Different ThemoPackages are available, depending on the modeling accuracy and complexity required by the user. A brief summary is reported below, giving reasoning behind the choice made. Complete NPSS ThermoPackage documentation can be found in [94].

NPSS ThermoPackages The highest fidelity model is represented by the NASA computer program CEA (Chemical Equilibrium with Applications). This ThermoPackage determines thermodynamic and transport proprieties of the product mixture by calculating the chemical equilibrium product concentrations from any set of user specified reactants. The program theoretical background is available in references [99, 100]. As reported in reference [101], significant drawbacks of CEA are constituted by the high computational cost and stability issues. An alternative ThermoPackage is called "Janaf" which, similarly to CEA, solves the chemical equilibrium but with a fixed number of reactants, thus reducing the numerical effort [94].

Alternatively, burner exit fluid proprieties can be gathered using the gas table database available in "GasTbl" or "allFuel" ThemoPackages for minimal computational cost. The former package is indicated for standard mixture of air, water vapour and JP-class fuel, while the latter contains models for other fuel types [94]. Since a detailed combustor chemical study is beyond the scope of this work, this last approach has been employed in this project to improve numerical stability and reduce running time. Hence, the "GasTbl" package has been selected.

GasTbl The gas mixture exit proprieties are calculated with the assumption of complete combustion and ASTM-A-1 as fuel. Conventional NPSS gas tables are based on air composition of 21% oxygen and 79% atmospheric nitrogen, by volume. Using the following combustion reaction, the overall gas proprieties are calculated from the mole weighted average of the individual output species proprieties, considered solely dependent on temperature [94].

$$C_xH_y + \left[x + \frac{y}{4}\right](O_2 + 3.7642N_2) \longrightarrow xCO_2 + \frac{y}{2}H_2O + 3.7642\left[x + \frac{y}{4}\right]N_2 \tag{3.1}$$

As reported in reference [94], chemical dissociation is very likely to occur for gas temperatures above 2000°R (∼1110K). Hence, the simple combustion model based on equation 3.1 cannot be as accurate. NPSS includes an improved set of tables which results from a more accurate description of the air composition (78.0840% N_2, 20.9476% O_2, 0.9340% A_r, 0.0314% CO_2 and 0.0030% N_e, by volume) and considers only the most common product species: N_2, H_2O, O_2, CO_2, A_r, N_e, H, O, OH and CO [94]. This model represents a good and quicker alternative to "Janaf" and it has been used in this project.

Turbine

The turbine element behaves similarly to the compressor. It requires the definition of the component total to total efficiency and rotational speed. The solver must ensure the compressor-turbine power matching by typically varying the pressure drop across this element. The reader is referred to the solver setup section for more information (section 3.2.3). A component map has to be provided for off-design calculations. The program automatically scales the given map using similar equation to the compressor case. Section 4.3.3 reports the baseline turbine maps employed within this study.

Beside a standard fluid input/output port, the turbine features a Shaft port for modeling the the mechanical connection with the compressor. In addition, a pre-built interstage bleed

port to model the turbine cooling flow is available. More information are provided in the Ports & Links section.

Nozzle

The nozzle element allows for the performance evaluation of simply convergent or convergent-divergent nozzles. The element requires information on free flow stream static pressure, given by "Ambient", and, the design nozzle pressure ratio has to be specified to size the nozzle. A simply convergent nozzle has been selected and modeled as ideal with fixed geometry.

Propeller

NPSS provides a simple built-in propeller element, which calculates propeller performance, size and gear ratio for a given design input shaft power ($\dot{W}_{des}$), design power load ($\dot{W}_{load,des}$) and design tip rotational speed ($U_{tip,des}$). The element allows the implementation of maps to assess the propeller performance in off-design condition.

During the ERAST program [14], a detailed propeller design has been necessary to establish baseline propeller models suitable for the particular engine operating environment. However, since the focus of this work is concentrated only on the gas turbine block, the propeller has been simplified and modeled as a pure load element. In design, the gearbox ratio has been calculated assuming the ERAST baseline propeller data and using the standard NPSS propeller element. The design propeller data employed are tabulated in Table 3.3. In off-design, the propeller entirely absorbs the engine power output without losses or consideration on the aircraft thrust requirements. The part power analysis is conducted for an engine output power ($\dot{W}$) of 75%, 50% and 25% of the design power output.

Table 3.3: List of NPSS input propeller data used in this project [14]

$\dot{W}_{des}$	300 hp (223.7 kW)
$\dot{W}_{load,des}$	1.35 hp/ft^2 ($\sim$10.8 kW/m^2)
$U_{tip,des}$	785 ft/s (239.3 m/s)
$\dot{W}$	$\dot{W}_{des} \cdot [0.75, 0.50, 0.25]$

Shaft

The shaft element defines the mechanical connection between the rotating elements, ensuring the power balance between all the connected components. A single shaft architecture has been selected for every cycle arrangement to minimize the overall engine complexity and weight, ensuring an equivalent cycle comparison with the Coleman engine model presented in [14].

Mixer

The mixer element is used in the semi-closed cycle architectures to model the mixing between the primary flow and the feedback flow rate. Conservation of energy, continuity and momentum is used in the NPSS mixer model [93]. The user has to define the Mach number of the mixer primary stream ($M_{1,mix}$) which is used, in design, to calculate the main stream entrance area. The secondary flow area is obtained from the element internal solver, which iteratively modifies the second stream inlet Mach number ($M_{2,mix}$) until the static pressure matches at the element inlet. From continuity, the outlet area is calculated. In off-design, the determined design flow areas are held constant (constant area mixer). The static pressure matching has to be ensured from an external solver, while the matching Mach number is calculated within the mixer element. The off-design mixer solver settings are discussed in section 3.3.2.

Splitter

The splitter elements allows for the separation of the main stream into two sub-streams with equal characteristics. Pressure losses can be applied independently on each output fluid port. This element is used in combination with the mixer element to entirely model the semi-closed cycle recirculation. The splitter bypass ratio (BPR) variable is defined as:

$$BPR = \frac{\dot{m}_{2,split}}{\dot{m}_{1,split}} \tag{3.2}$$

where $\dot{m}_{1,split}$ and $\dot{m}_{2,split}$ are the first and second splitter output streams respectively. For this project, the $\dot{m}_{2,split}$ is the amount of mass flow recirculated in closed loop of the semi-closed cycle, while, $\dot{m}_{1,split}$ is the amount of air exhausted. Leading to the definition of the feedback flow ratio as: $BPR = FFR$, in agreement with reference [14]. A constant pressure drop of 2% has been imposed on the splitter output steams to account for losses due to the additional plumbing system not present in the conventional open cycle arrangement [14].

3.2.2 Ports & Links

As explained previously, three port types are available in NPSS: Fluid, Shaft and Bleed ports. Every main element used in this project, with the exception of "Ambient", possesses at least one fluid port. Built-in NPSS functions are used to define the flow path between each element, starting with a FlowStart element type and terminating with a FlowEnd. Similarly, elements that are mechanically connected by means of a shaft, possess mechanical ports that have to be linked together. Since a single shaft model has been employed here, compressors, turbines and propeller are connected together via ports to a single shaft element.

More delicate considerations are needed regarding the bleed ports, since this aspect has been used to model the turbine cooling requirements and to construct a simple turbine cooling model in NPSS. The following paragraph explains in detail the Bleed ports settings for compressors and turbines, while information on the loss model is reported in section 3.4.

Bleed Ports

The bleed ports considered in this work are the interstage bleed port available in the compressor and turbine element. Starting from the compressor element, this component bleed port allows to extract a certain fraction of the compressed flow ($\xi = \dot{m}_{bld}/\dot{m}$) at a specified total pressure rise fraction (ζ_C) defined as:

$$\zeta_C = \frac{P_{0,bld} - P_{01}}{P_{04} - P_{01}} \tag{3.3}$$

where $P_{0,bld}$ is the total pressure at the bleed extraction point. From equation 3.3 results that if $\zeta_C = 0$ the bleed air is extracted at the compressor inlet, else if $\zeta_C = 1$ at the outlet.

The turbine possesses a similar interstage bleed port which allows for the cooling flow modeling. The turbine bleed inlet point location is established by means of ζ_T, defined according to equation 3.4. A value of 1 implies that the flow is introduced at the turbine inlet, 0 at the turbine outlet.

$$\zeta_T = \frac{P_{0,bld} - P_{03}}{P_{00} - P_{03}} \tag{3.4}$$

The bleed flow coupling between compressor and turbine is made using standard NPSS fluid linking functions as for a normal element to element connection. More information can be found in references [92, 93].

3.2.3 NPSS Numerical Solver

The NPSS solver is responsible of the engine model convergence, by solving the set equations provided by the user. The NPSS solver is based on modified Newton-Raphson method, which iteratively solves the given equations until a pre-defined tolerance is satisfied.

Detailed mathematical aspects on the numerical solver are beyond the scope of this section. A brief explanation is hereby provided with focus on those aspects directly related to the project implementation. More details on NPSS numerical aspects can be found in references [12, 92, 97].

Solver Description

The equations are defined in NPSS by means of the so called *Dependent* variables. A dependent variable is constituted by two main parameters which define the left and the right hand sides of the equation: Eq_{lhs} and Eq_{rhs} respectively. These terms must yield to a real number and are used to define the solver iteration error in fractional term as follows:

$$Error = \frac{Eq_{lhs} - Eq_{rhs}}{Eq_{ref}} \tag{3.5}$$

where Eq_{ref} is the equation reference variable. The solver requires an equal number of *Independent* variables that are iteratively modified to reduce the *Dependent* variable error to a certain tolerance, which has been set to 10^{-6} for design point calculations and 10^{-4} for off-design, due to the augmented complexity of the problem. An initial guess is embedded within the independent variable to start the iteration. The remaining solver settings that can be defined throughout these variables have been left as default [92].

NPSS features a function called *autoSolverSetup()* which automatically adds *Dependent* and *Independent* variables to the solver, as function of the elements employed in the engine model to ensure the turbomachinery mechanical matching in design and off-design analysis. Due to the complexity of the engine models treated in this project, additional equations must be added manually to the solver, to properly model the engine. This aspect is treated in detail for each engine arrangement in section 3.3.

In addition, NPSS allows for the definition of constraints which can be used to affect the solver independent variable change during the iterations. *Constraints* are defined similarly to *Dependent* and have to be manually added to the solver [92].

The default maximum number of iterations allowed before reaching convergence has been modified with respect to default settings. In particular, more iterations have been found necessary to solve the thermodynamics of semi-closed cycles, having negative impact on algorithm speed. A maximum number of iterations of 1000 and a maximum Jacobian generation of 500 has been used in this analysis.

Solver Output

As observed in reference [97], there are mainly two reasons that can negatively affect the solver convergence: (1) No feasible solution can be obtained for the given flight conditions and independent variable guessing points, and (2) the solver fails to achieve the tolerance provided, getting stuck into an infinite loop as results of discontinuities, such as those generated in the discrete definition of the component performance maps.

This second aspect becomes particularly critical if NPSS is coupled with an external optimizer, since it prevents the algorithm to continue the optimization. Moreover, due to the random nature of the generic algorithm, it is virtually impossible to track the design vector combination that causes this phenomenon to occur in the NPSS solver. It has been observed that perturbing the guessing values defined within the *Independent* variables by a small amount, might be sufficient to avoid the infinite loop problem. Therefore, an algorithm has been built

in Matlab to improve the NPSS convergence problems during the optimization, based on the suggestions given in reference [97]. A detailed explanation will be given in section 5.4.4.

Alternatively, if a converging solution has been found, a complete output file, showing in detail the engine solved thermodynamics is given using the so called "Data Viewer(s)" block visible in Figure 3.1. Modification has been made to the standard NPSS output file to include the unconventional characteristics given by the semi-closed cycle.

3.3 Cycle Modeling

This part presents in detail the engine models created in NPSS for this project. Each engine arrangement is constituted of four files: a .mdl file, which includes the engine fluid and mechanical model, a .case file, providing all the solver settings for design and off-design analysis, a .inp file, used to define the external input data required by the model and a .run file, necessary to perform the whole cycle analysis.

The objective here is to show how the different NPSS elements presented in the previous section have been linked together to build conventional open cycle and semi-closed cycle models. Details on the solver setup are also given to facilitate the model replication for future studies. Moreover, the thermodynamic variables that will be used in the engine optimization are hereby introduced. Note, all the engine variables subsequently introduced are defined according to the standard NPSS notation for a better model understanding.

3.3.1 Open Cycle Models

Recuperated and intercooled-recuperated open cycles have been implemented in NPSS. The model schematic is reported in Figure 3.3 as defined in the .mdl file. To switch between the simple recuperated and the intercooled-recuperated cycle is sufficient to set the heat flux in the intercooler to null. Since a reasonable comparison between the different architectures is desired, the open cycle engine model has to feature similar components and solver settings to the ERAST model [14]. Therefore, the turbomachinery block has been modeled by means of a pair of compressor and turbine elements connected with a single spool to the propeller element.

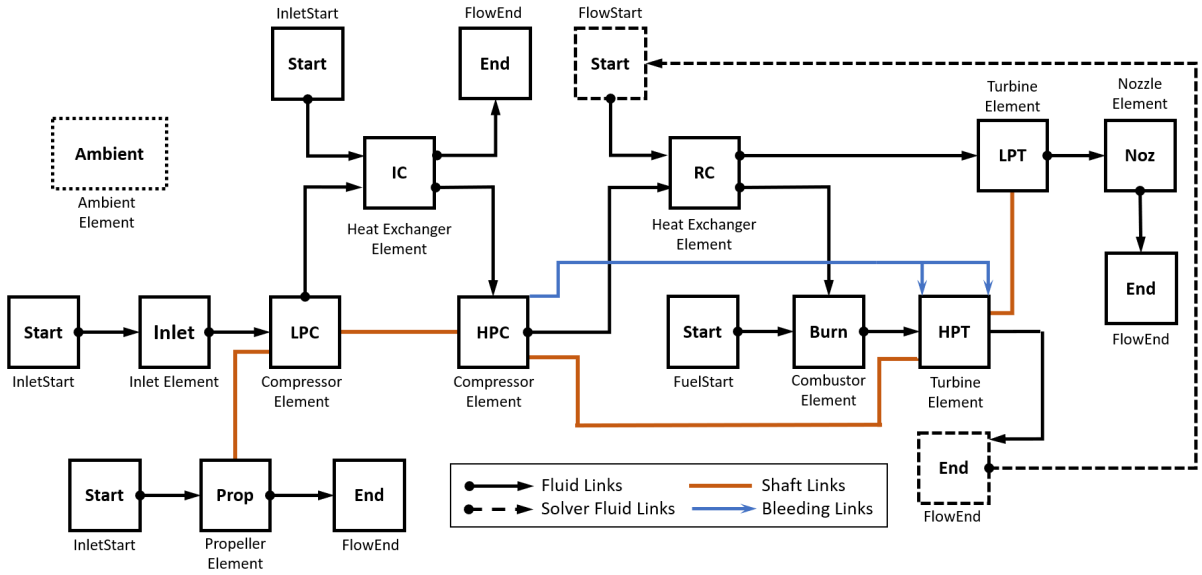

Figure 3.3: RC/ICR engine schematic as realized in NPSS (.mdl file)

The previous figure shows how the conventional open cycle thermodynamic model has been generated in NPSS using the previously discussed program features (Elements, Ports Links, Solver). Since the NPSS solver needs to pre-process the whole engine model to define flow path and stations from the inlet to the exhaust elements, each building block has to be initialized when the solver passes through it [12]. In particular, the inlet flow conditions of the currently analyzed element have to be known to allow the solver to calculate the exit conditions. Therefore, elements that are not directly linked with a preceding one, necessitate a FlowStart element to start the calculations. Similarly, a FlowEnd element is used to terminate the flow from a solver perspective.

In traditional open cycle models, where recuperators are not used, the solver logically passes throughout each element and no additional modeling considerations have to be made. However, with the introduction of the recuperator, the solver expects this element to be fully initialized when stepping through. Because the recuperator hot side is defined only after the HPT (see Figure 3.3), this prevents the solver to complete its preliminary analysis, thus, precluding the model correct execution.

Similarly to reference [12], this issue has been solved by using a FlowStart element to a priori define the recuperator hot side inlet conditions. However, since the HPT flow exit properties have to be identical to the recuperator hot side inlet, a numerical iteration has to be made to satisfy this constraint. By means of a FlowEnd element at the end of the HPT and by defining a particular set of *Dependent* and *Independent* variables, the solver ensures the flow matching. Complete details on the solver setup for the RC/ICR engine are reported in the following paragraph.

Finally, the shaft and bleed links have been presented in Figure 3.3 as well. Once the mechanical link is defined, *autoSolverSetup()* ensures the proper solver settings for the design and off-design mechanical coupling.

Solver Setup

Two similar sets of equations have to be provided to the NPSS solver to correctly model the thermodynamic behavior of the engine in design and off-design. The objective of the gas turbine is to produce a specified power output, given as input to the load/propeller element. The solver acts on the provided *Independent* variables to ensure engine feasibility and power requirements, by solving given *Dependent* conditions. The solver setup for design and off-design is presented in the following paragraphs.

Design equations Starting from the cycle design modeling, the primary set of equations has to ensure the engine mechanical and power consistency. In particular, the power produced by the two turbines must be sufficient to satisfy the compressors and the propeller demand. *autoSolverSetup()* automatically defines a dependent condition on the shaft net torque (trqNet) and uses as independent variable the turbine pressure ratio (S_map.ind_PRbase).

Since two turbines are built on a single shaft, an additional equation has to be defined to match the number of independent variables generated by the *autoSolverSetup()* function. A condition of the turbine power split has been manually added to the solver, based on the exit HPT total pressure (HPT.Fl_O.Pt). In particular, HPT.Fl_O.Pt has been set equal to a certain percentage of the LPC exit pressure (HPT_Pt $*$ LPC.Fl_O.Pt), where HPT_Pt is the percentage value, given as external input (see Tables 3.4 and 3.5).

Additionally, the fuel to air ratio has been changed to match a given turbine inlet temperature (dep_TITmax). As reported in [102], the nozzle pressure ratio (Noz.PR) must be specified to determine the relative size of the engine core. As independent, the inlet mass flow (InletStart.W_in) is modified by the solver to satisfy the power demand. The remaining equation list is related to the recuperator flow matching and it is separately discussed below.

Recuperator equations The initial conditions given to the recuperator hot stream using the FlowStart element are: total temperature (RC_HotStart.Tt), total pressure (RC_HotStart.Pt), inlet mass flow (RC_HotStart.W) and fuel to air ratio (RC_HotStart.FAR). These parameters are sufficient to fully define the flow station and must be equal to the calculated ones at the HPT outlet. The whole set of equations used to define the solver design model is presented in Table 3.4 for *Dependent* and Table 3.5 for *Independent* variables, using the NPSS object oriented dot notation [92, 93].

Table 3.4: RC/ICR solver dependent variables list in design mode

Dependent Name	**Dependent Eq$_{lhs}$**	**Dependent Eq$_{rhs}$**
Shaft.integrate_Nmech	trqNet	0.000
dep_PowerSplit	HPT.Fl_O.Pt	HPT_Pt $*$ LPC.Fl_O.Pt
dep_TITmax	Burn.Fl_O.Tt	T_max
dep_Noz_PR	Noz.PR	NozPR
depR_Pt	RC_HotStart.Pt	HPTFlowEnd.Pt
depR_Tt	RC_HotStart.Tt	HPTFlowEnd.Tt
depR_W	RC_HotStart.W	HPTFlowEnd.W
depR_FAR	RC_HotStart.FAR	HPTFlowEnd.FAR

where T_max and NozPR are the target variables for turbine inlet temperature and nozzle pressure ratio provided by means of the .inp file as external inputs. The correspondent independent variables list is reported below. "Independent varName" refers to the model variable that has to be iteratively changed and "Independent indepRef" is a guess value given through the .inp file or automatically set by the *autoSolverSetup()* function. A complete explanation of the reference values is reported in a dedicated section later on.

Table 3.5: RC/ICR solver independent variables list in design mode

Independent Name	**Independent varName**	**Independent indepRef**
HPT.S_map.ind_PRbase	PRbase	PR_HPT
LPT.S_map.ind_PRbase	PRbase	PR_LPT
ind_FAR_Burn	Burn.FAR	FAR
ind_WairIn	InletStart.W_in	Wair
indR_Pt	RC_HotStart.Pt	Pt_RC_hot
indR_Tt	RC_HotStart.Tt	Tt_RC_hot
indR_W	RC_HotStart.W	Win_RC_hot
indR_FAR	RC_HotStart.FAR	FAR

Off-Design equations During off-design calculations, *autoSolverSetup()* generates all the necessary equations to match compressors and turbines. In particular, the solver modifies the compressor map running line (S_map.ind_RlineMap), the shaft rotational speed (ind_Nmech) and the turbine pressure ratio (S_map.ind_PRbase) to match the compressor and turbine corrected inlet mass flow (Wc and Wp respectively) with the one calculated from the component maps (WcCalc and WpCalc), and to obtain a null shaft net torque (as for design). Moreover, since during the design the nozzle area has been sized, the calculated flow effective area (WqAE) must match the value defined in design (WqAEdem). The engine inlet mass flow is used as independent (InletStart.W_in).

Since a singe shaft arrangement has been chosen in this work, an additional dependent and independent correlation has to be added to define the power split between the two turbines, as for the design case. Assuming a fixed turbine geometry, a constant turbine work split defined

in terms of enthalpy drop percentage ($\%\Delta h$) has been used as suggested in [14]. $\%\Delta h$ has been defined according to the following relation.

$$\%\Delta h = \frac{\Delta h_{HPT}}{\Delta h_{HPT} + \Delta h_{LPT}} \tag{3.6}$$

Equation 3.6 is used in design to calculate the enthalpy drop percentage (dHdes) and in off-design to define iteratively the actual enthalpy drop percentage (dH). The solver modifies independently the fuel to air ratio (FARind) to make sure that the turbine power split off-design dependent condition is satisfied (dep_dHper). Finally, the recuperator equations have to be maintained unchanged in the off-design as well. Tables 3.6 and 3.7 summarize the entire off-design dependent and independent variable list respectively.

Table 3.6: RC/ICR solver dependent variables list in off-design mode

Dependent Name	**Dependent Eq$_{lhs}$**	**Dependent Eq$_{rhs}$**
LPC.S_map.dep_errWc	Wc	WcCalc
HPC.S_map.dep_errWc	Wc	WcCalc
Shaft.integrate_Nmech	trqNet	0.000
HPT.S_map.dep_errWp	Wp	WpCalc
LPT.S_map.dep_errWp	Wp	WpCalc
Noz.dep_Area	WqAE	WqAEdem
dep_dHper	dH	dHdes
depR_Pt	RC_HotStart.Pt	HPTFlowEnd.Pt
depR_Tt	RC_HotStart.Tt	HPTFlowEnd.Tt
depR_W	RC_HotStart.W	HPTFlowEnd.W
depR_FAR	RC_HotStart.FAR	HPTFlowEnd.FAR

A complete description of the standard NPSS "Independent indepRef" variables reported in the following table is available in the program user guides, refer in particular to [92, 93]. User defined variables specifically created for this project will be explained in the following paragraph.

Table 3.7: RC/ICR solver independent variables list in off-design mode

Independent Name	**Independent varName**	**Independent indepRef**
LPC.S_map.ind_RlineMap	RlineMap	RlineMapDes
HPC.S_map.ind_RlineMap	RlineMap	RlineMapDes
Shaft.ind_Nmech	Nmech	Ndes
HPT.S_map.ind_PRbase	PRbase	PR_HPT
LPT.S_map.ind_PRbase	PRbase	PR_LPT
InletStart.ind_W	InletStart.W_in	Wair
FARind	Burn.FAR	FAR
indR_Pt	RC_HotStart.Pt	Pt_RC_hot
indR_Tt	RC_HotStart.Tt	Tt_RC_hot
indR_W	RC_HotStart.W	Win_RC_hot
indR_FAR	RC_HotStart.FAR	FAR

Constraints equations The off-design analysis has been internally constrained in NPSS to set a limitation on the calculated turbine inlet temperature (Burn.Fl_O.Tt) and recuperator hot side inlet temperature (RC.Fl_I2.Tt), dependent on the component materials employed. In design, there is no need for these constraints since the optimizer already ensures their satisfaction.

Table 3.8: RC/ICR solver constraints variables list applied in off-design calculations

Dependent Name	**Dependent Eq$_{lhs}$**	**Dependent Eq$_{rhs}$**
TITmax	Burn.Fl_O.Tt	T_max
RITmax	RC.Fl_I2.Tt	TRC_max

NPSS Inputs

Table 3.9 presents the full list of inputs needed by NPSS to perform the design and off-design analysis of the recuperated and the intercooled - recuperated gas turbine. Inputs are provided from the .inp file which is used as a link between NPSS and the optimizer in Matlab. The following table reports the NPSS nomenclature used ("NPSS Input Name") and the corresponding mathematical symbol ("Input Symbol"), explaining what defined in previous tables. The column named "Input Origin" defines the variable characteristics by classifying them as: "Fixed", "Guessed", "Calculated" or "Optimized". The first refers to variables that are kept constant throughout the optimization, the second identifies the independent guessing values specifically created for the NPSS model and affected by the repairing algorithm (section 5.4.4). "Calculated" refers to every variables that is given by the component models, while, "Optimized" to those given as design variable by the optimizer (section 5.3.1).

Table 3.9: RC/ICR complete input variables list used in NPSS (.inp file)

NPSS Input Name	**Input Symbol**	**Input Origin**
Wair	$\dot{m}$	Guessed
Alt	Alt	Fixed
dTs	ΔT_s	Fixed
M	M	Fixed
- Flight Data -		
PR_LPC	Π_{LPC}	Optimized
LPC.effDes	η_{LPC}	Calculated
PR_HPC	Π_{HPC}	Optimized
HPC.effDes	η_{HPC}	Calculated
- Compressor Data -		
IC.W_in	$\dot{m}_{IC,c}$	Guessed
IC.dPqP2	$(\Delta P/P)_{IC,h}$	Optimized
IC.effect	ε_{IC}	Optimized
- Intercooler Data (ICR) -		
RC_HotStart.Pt	$P_{01,h}$	Guessed
RC_HotStart.Tt	$T_{01,h}$	Guessed
RC_HotStart.W	$\dot{m}_{01,h}$	Guessed
RC.dPqP1	$(\Delta P/P)_{RC,c}$	Optimized
RC.dPqP2	$(\Delta P/P)_{RC,h}$	Optimized
RC.effect	ε_{RC}	Optimized
RC.FL_I2.Tt	RIT	Fixed
- Recuperator Data -		
FuelStart.LHV	LHV	Fixed
Burn.dPqP_dmd	$(\Delta P/P)_B$	Fixed
Burn.effBase	η_B	Fixed
Burn.Qhx	$\dot{q}_{loss}$	Fixed
Burn.FAR	FAR	Guessed
Burn.FL_O.Tt	TIT	Optimized

Continue on next page

Continue from previous page

- Combustor Data -		
PR_HPT	Π_{HPT}	Guessed
HPT.effDes	η_{HPT}	Calculated
HPT_Pt	$\%P_{04,LPC}$	Optimized
PR_LPT	Π_{LPT}	Guessed
LPT.effDes	η_{LPT}	Calculated
- Turbine Data -		
NozPR	Π_{Noz}	Optimized
- Nozzle Data -		
Prop.pwr	$\dot{W}$	Fixed
Prop.pwrLoadDes	$\dot{W}_{load,des}$	Fixed
Prop.UtipDes	$U_{tip,des}$	Fixed
- Propeller Data -		
Shaft.Nmech	N	Optimized
- Shaft Data -		

3.3.2 Semi-Closed Cycles

Semi-closed cycle NPSS modeling represents an additional challenge with respect to the conventional open cycles previously introduced. In fact, due to the flow recirculation, the solver has to perform further iterations to match the static pressure of the two streams in the mixer. As a consequence, augmented running time and convergence issues have been experienced for the semi-closed cycle analysis.

Furthermore, the mixer feedback flow side has to be a priori initialized to allow the solver model pre-processing phase, as for the recuperator case. Thus, an additional FlowStart/FlowEnd element combination has to be employed in the engine model for a proper semi-closed cycle representation in NPSS. Figure 3.4 illustrates the NPSS cycle model of the ERAST Coleman engine arrangement given in Figure 2.4.

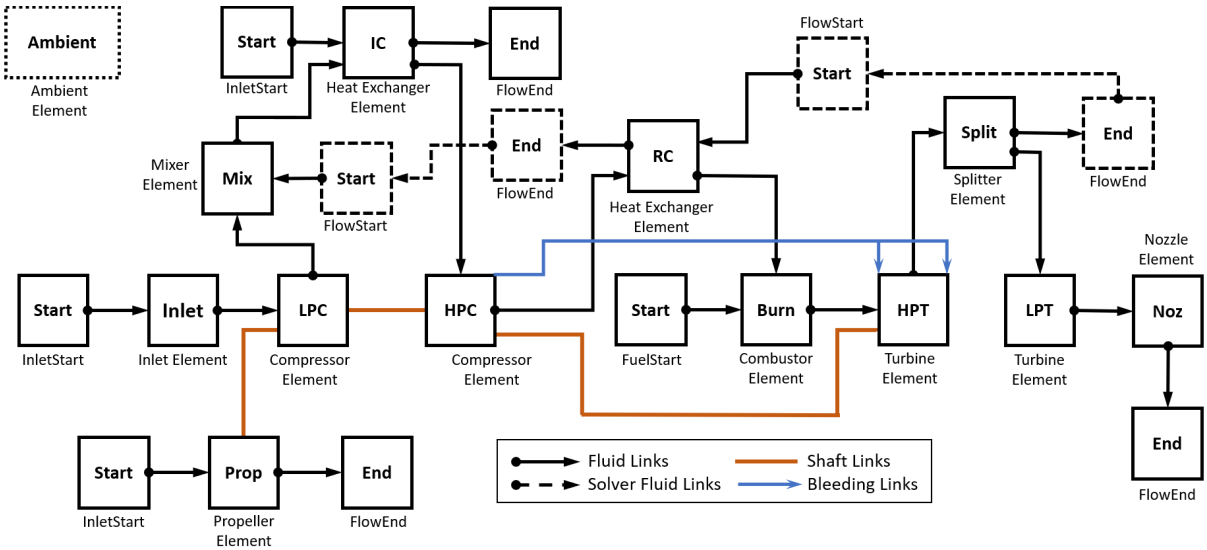

Figure 3.4: ERAST engine schematic as realized in NPSS (.mdl file)

As visible in Figure 2.3, the only difference between the ERAST and HPRTE semi-closed cycle versions lays in the location of the flow splitting element. Figure 3.5 presents the HPRTE

thermodynamic model realized in NPSS, showing the similar FlowStart/FlowEnd solver linking made to initialize the whole model. As for the open cycle case, a pair of compressor and turbine elements running on a single shaft have been used in this work, minimizing the overall UAV engine complexity.

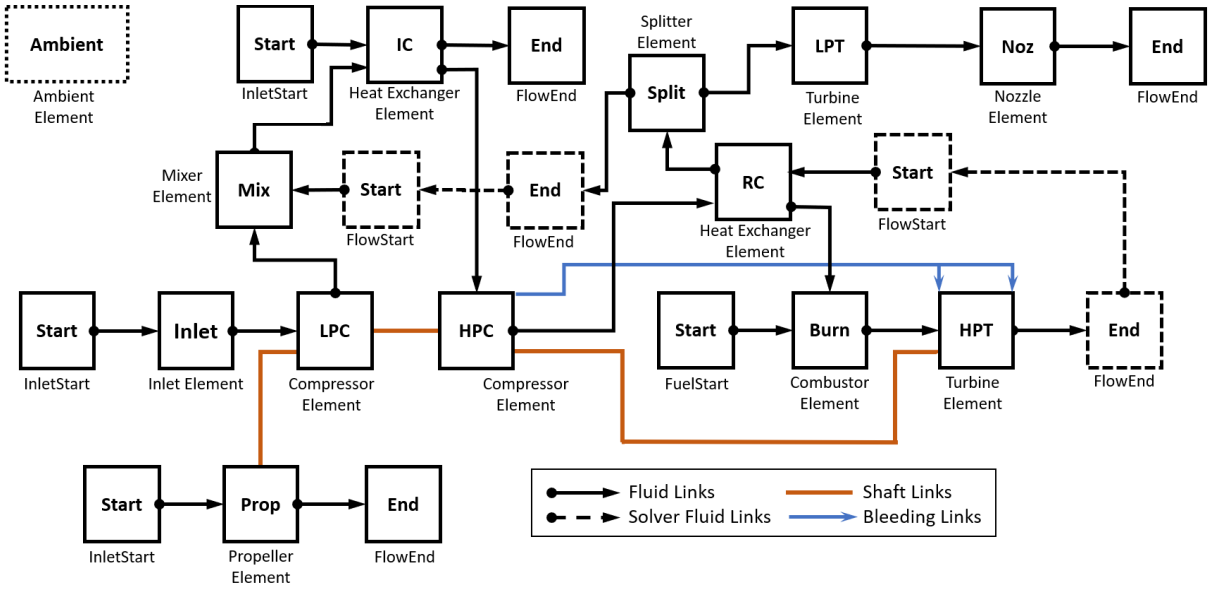

Figure 3.5: HPRTE engine schematic as realized in NPSS (.mdl file)

Solver Setup

Solver settings have a certain similarity with the open cycle models, at least with respect to the recuperator handling. Common aspects are not discussed again here, and only unique solver dependent and independent relations are explained in detail for design and off-design mode. Only slight differences are present between the ERAST and the HPRTE semi-closed cycles due to the dissimilar location of splitter element. However, from a conceptual perspective, similar assumptions and modeling features have been used. As for the open cycles, the complete set of dependent and independent relations are tabulated in separate paragraphs for design and off-design analysis.

Design equations Table 3.10 provides the list of *Dependent* and *Independent* variables in common between the ERAST and the HPRTE engine models. Important difference with the single shaft open cycle is that the turbine power split is defined to ensure the mixer static pressure match. From an NPSS modeling perspective, the open cycle dependent variable called "dep_PowerSplit" have been replaced by "dep_MixPressure", which imposes the condition of equal total pressure between the two mixer inlet streams.

Reference [103] has shown that the condition for minimum mixer total pressure loss occurs for an inlet cold stream total pressure (Mixer.Fl_I1.Pt) slightly higher than the hot one (Mixer.Fl_I2.Pt). However, since an adiabatic mixing processes has been considered, the equal total pressure condition has been set to facilitate mixer internal solver settings and convergence.

According to [14], the design feedback flow ratio has been established by fixing the combustion FAR to be 90% of the stoichiometric value (FARst), calculated with respect to the engine inlet fresh air. Unfortunately, the ERAST report does not provide a clear explanation on the reasons behind the selection of this value. Other authors [10, 19] have confirmed that the semi-closed cycle operates at nearly stoichiometric combustion, but no precise indication can be derived.

Hence, this aspect has been further investigated by introducing an additional condition on the fuel to air ratio (dep_BurnFAR) in NPSS, which influences the FFR independent variable (ind_FFR), similarly to [14]. However, the fuel to fresh air equivalence ratio ("phi_st") has been defined as external variable controlled by the optimizer, instead of fixing it to 90%. The remaining engine equations have been set as for the open cycle case (Table 3.4).

Table 3.10: ERAST/HPRTE design solver dependent/independent variables list

Dependent Name	**Dependent Eq$_{lhs}$**	**Dependent Eq$_{rhs}$**
Shaft.integrate_Nmech	trqNet	0.000
dep_MixPressure	Mixer.Fl_I1.Pt	Mixer.Fl_I2.Pt
dep_TITmax	Burn.Fl_O.Tt	T_max
dep_Noz_PR	Noz.PR	NozPR
dep_BurnFAR	Burn.FAR	phi_st $*$ FARst
Independent Name	**Independent varName**	**Independent indepRef**
HPT.S_map.ind_PRbase	PRbase	PR_HPT
LPT.S_map.ind_PRbase	PRbase	PR_LPT
ind_FAR_Burn	Burn.FAR	FAR
ind_WairIn	InletStart.W_in	Wair
ind_FFR	Split.BPRdes	FFR

Recuperator equations The recuperator equations are defined similarly to the open cycle. Separate tables are below reported for the ERAST and the HPRTE engines due to the different nomenclature used depending on the splitter location in the models.

Table 3.11: ERAST design recuperator dependent/independent variables list

Dependent Name	**Dependent Eq$_{lhs}$**	**Dependent Eq$_{rhs}$**
depR_Pt	RC_HotStart.Pt	Split_FlowEnd.Pt
depR_Tt	RC_HotStart.Tt	Split_FlowEnd.Tt
depR_W	RC_HotStart.W	Split_FlowEnd.W
depR_FAR	RC_HotStart.FAR	Split_FlowEnd.FAR
Independent Name	**Independent varName**	**Independent indepRef**
indR_Pt	RC_HotStart.Pt	Pt_RC_hot
indR_Tt	RC_HotStart.Tt	Tt_RC_hot
indR_W	RC_HotStart.W	Win_RC_hot
indR_FAR	RC_HotStart.FAR	FAR

Table 3.12: HPRTE design recuperator dependent/independent variables list

Dependent Name	**Dependent Eq$_{lhs}$**	**Dependent Eq$_{rhs}$**
depR_Pt	RC_HotStart.Pt	HPTFlowEnd.Pt
depR_Tt	RC_HotStart.Tt	HPTFlowEnd.Tt
depR_W	RC_HotStart.W	HPTFlowEnd.W
depR_FAR	RC_HotStart.FAR	HPTFlowEnd.FAR
Independent Name	**Independent varName**	**Independent indepRef**
indR_Pt	RC_HotStart.Pt	Pt_RC_hot
indR_Tt	RC_HotStart.Tt	Tt_RC_hot
indR_W	RC_HotStart.W	Win_RC_hot
indR_FAR	RC_HotStart.FAR	FAR

Mixer equations Additional dependent and independent relations have to be added for the mixer modeling, similarly to what was done for the recuperator case. Solver flow continuity is ensured by providing a FlowStart/FlowEnd solver link between the recuperator and the mixer, in the ERAST model, and between splitter and mixer in the HPRTE. Tables 3.13 and 3.14 give the variable list for the ERAST and the HPRTE respectively.

Table 3.13: ERAST mixer dependent/independent variables list

Dependent Name	**Dependent Eq$_{lhs}$**	**Dependent Eq$_{rhs}$**
depM_Pt	Mix_HotStart.Pt	RC_HotEnd.Pt
depM_Tt	Mix_HotStart.Tt	RC_HotEnd.Tt
depM_W	Mix_HotStart.W	RC_HotEnd.W
depM_FAR	Mix_HotStart.FAR	RC_HotEnd.FAR
Independent Name	**Independent varName**	**Independent indepRef**
indR_Pt	Mix_HotStart.Pt	Pt_mix
indR_Tt	Mix_HotStart.Tt	Tt_mix
indR_W	Mix_HotStart.W	W_mix
indR_FAR	Mix_HotStart.FAR	FAR

Table 3.14: HPRTE mixer dependent/independent variables list

Dependent Name	**Dependent Eq$_{lhs}$**	**Dependent Eq$_{rhs}$**
depM_Pt	Mix_HotStart.Pt	Split_FlowEnd.Pt
depM_Tt	Mix_HotStart.Tt	Split_FlowEnd.Tt
depM_W	Mix_HotStart.W	Split_FlowEnd.W
depM_FAR	Mix_HotStart.FAR	Split_FlowEnd.FAR
Independent Name	**Independent varName**	**Independent indepRef**
indR_Pt	Mix_HotStart.Pt	Pt_mix
indR_Tt	Mix_HotStart.Tt	Tt_mix
indR_W	Mix_HotStart.W	W_mix
indR_FAR	Mix_HotStart.FAR	FAR

Off-Design equations In the off-design analysis, *autoSolverSetup()* already defines all the main required equations. In addition to what was used for the open cycle off-design analysis, a further dependent relation is automatically defined to ensure the static pressure matching in the mixer element (Mix.dep_errPs). As independent, the splitter feedback flow ratio is used (Split.ind_BPR). Similarly, the single shaft off-design analysis has been conducted by fixing the enthalpy drop percentage, given by equation 3.6, equal to the design one. Flow continuity in recuperator and in the mixer has been ensured by means of the dependent/independent relations defined in Tables 3.11 and 3.13 for the ERAST model and Tables 3.12 and 3.14 for the HPRTE respectively. The remaining semi-closed cycle common off-design variables are reported in Table 3.15.

Table 3.15: ERAST/HPRTE off-design solver dependent/independent variables list

Dependent Name	**Dependent Eq$_{lhs}$**	**Dependent Eq$_{rhs}$**
LPC.S_map.dep_errWc	Wc	WcCalc
HPC.S_map.dep_errWc	Wc	WcCalc
Shaft.integrate_Nmech	trqNet	0.000
HPT.S_map.dep_errWp	Wp	WpCalc

Continue on next page

Continue from previous page

LPT.S_map.dep_errWp	Wp	WpCalc
Noz.dep_Area	WqAE	WqAEdem
dep_dHper	dH	dHdes
Mix.dep_errPs	Mix.Fl_I1.Ps	Mix.Fl_I2.Ps
Independent Name	**Independent varName**	**Independent indepRef**
LPC.S_map.ind_RlineMap	RlineMap	RlineMapDes
HPC.S_map.ind_RlineMap	RlineMap	RlineMapDes
Shaft.ind_Nmech	Nmech	Ndes
HPT.S_map.ind_PRbase	PRbase	PR_HPT
LPT.S_map.ind_PRbase	PRbase	PR_LPT
InletStart.ind_W	InletStart.W_in	Wair
FARind	Burn.FAR	FAR
Split.ind_BPR	Split.BPR	Split.BPRdes

The constraints applied in the open cycle modeling and defined in Table 3.8 have been employed in the off-design analysis of semi-closed cycles as well.

NPSS Inputs

Same input settings are given for the ERAST and the HPRTE engine models. In addition to the open cycle input variables given in Table 3.9, splitter and mixer necessitate further information. The complete set of input data used for the NPSS semi-closed cycle modeling has been provided in Table 3.16. The same convention applied to the open cycle is maintained here.

Table 3.16: ERAST/HPRTE complete input variables list used in NPSS (.inp file)

NPSS Input Name	**Input Symbol**	**Input Origin**
Wair	$\dot{m}$	Guessed
Alt	Alt	Fixed
dTs	ΔT_s	Fixed
M	M	Fixed
- Flight Data -		
PR_LPC	Π_{LPC}	Optimized
LPC.effDes	η_{LPC}	Calculated
PR_HPC	Π_{HPC}	Optimized
HPC.effDes	η_{HPC}	Calculated
- Compressor Data -		
IC.W_in	$\dot{m}_{IC,c}$	Guessed
IC.dPqP2	$(\Delta P/P)_{IC,h}$	Optimized
IC.effect	ε_{IC}	Optimized
- Intercooler Data (ICR) -		
RC_HotStart.Pt	$P_{01,h}$	Guessed
RC_HotStart.Tt	$T_{01,h}$	Guessed
RC_HotStart.W	$\dot{m}_{01,h}$	Guessed
RC.dPqP1	$(\Delta P/P)_{RC,c}$	Optimized
RC.dPqP2	$(\Delta P/P)_{RC,h}$	Optimized
RC.effect	ε_{RC}	Optimized
RC.FL_I2.Tt	RIT	Fixed
- Recuperator Data -		

Continue on next page

Continue from previous page

FuelStart.LHV	LHV	Fixed
Burn.dPqP_dmd	$(\Delta P/P)_B$	Fixed
Burn.effBase	η_B	Fixed
Burn.Qhx	$\dot{q}_{loss}$	Fixed
Burn.FAR	FAR	Guessed
Burn.FL_O.Tt	TIT	Optimized
Phi_st	ϕ_{st}	Optimized
- Combustor Data -		
PR_HPT	Π_{HPT}	Guessed
HPT.effDes	η_{HPT}	Calculated
PR_LPT	Π_{LPT}	Guessed
LPT.effDes	η_{LPT}	Calculated
- Turbine Data -		
NozPR	Π_{Noz}	Optimized
- Nozzle Data -		
Prop.pwr	$\dot{W}$	Fixed
Prop.pwrLoadDes	$\dot{W}_{load,des}$	Fixed
Prop.UtipDes	$U_{tip,des}$	Fixed
- Propeller Data -		
Shaft.Nmech	N	Optimized
- Shaft Data -		
Mix_HotStart.Pt	$P_{0,mix}$	Guessed
Mix_HotStart.Tt	$T_{0,mix}$	Guessed
Mix_HotStart.W	$\dot{m}_{mix}$	Guessed
Mix.Fl_I1_MN	$M_{1,mix}$	Optimized
Mix.Fl_I2_MN	$M_{2,mix}$	Guessed
- Mixer Data -		
Split.dPqP1	$(\Delta P/P)_{1,split}$	Fixed
Split.dPqP2	$(\Delta P/P)_{2,split}$	Fixed
Split.BPRdes	BPR	Guessed
- Splitter Data -		

where $M_{1,mix}$ is the low pressure compressor design exit Mach number and $M_{2,mix}$ represents the recirculation mixer side guessed inlet Mach number. It is used in the mixer element as a guess to start the internal mixer solver. $(\Delta P/P)_{1,split}$ and $(\Delta P/P)_{2,split}$ are the splitter user defined pressure losses, fixed to 2% in both sides to model plumbing losses [14].

3.4 Bleed/Cooling Modeling

The advantages of using higher turbine inlet temperatures on cycle efficiency and specific power are well known for conventional Brayton cycles. Limitations on the maximum TIT achievable are due to the current technological level and materials in use [25].

Reference [104] discusses ongoing studies to develop ceramic materials for radial turbine applications capable of operating with inlet temperatures up to 2500°F (∼1644K) uncooled. Since no additional evidence on the current status of this research is available, such high TIT values are considered out of reach in this project, if not by means of cooling techniques. Reference [105] has indicated that for TITs greater than 1250K, cooling should be employed to avoid a significant decrease of the component life. Therefore, this value has been used here to define the cooling need threshold.

According to [104], radial turbines have the advantage of a reduced amount of coolant for the same inlet temperature. In fact, due to the higher work extraction per stage, considerably less number of parts (blades and stages) require cooling. Moreover, the rotor relative temperature is reduced by the high tip speed involved, positively affecting the cooling flow needs. However, the high complexity associated with an efficient cooling design offsets the benefits previously indicated. Although examples of sophisticated turbine cooling systems are available in literature [106, 107], film cooling still represents the most practical and cost effective method to employ [16, 25].

From a cycle modeling perspective, it is of interest to determine: (1) the amount of cooling flow necessary, which is not participating to the turbine output power, for a given TIT, and (2) the impact that cooling losses have on the uncooled turbine efficiency.

A simple model has been built in NPSS using the flow information obtained from compressor and turbine bleed ports. The model has been implemented for each engine arrangement analyzed. The turbine cooling model description is given in the next paragraph, while the NPSS implementation is discussed subsequently.

3.4.1 Model Description

A simple formula to preliminarily assess the amount of cooling flow necessary as function of the cooling effectiveness (ε_{cool}) has been reported below as given in references [52, 108, 109].

$$\xi = \frac{\dot{m}_{cool}}{\dot{m}} = K \frac{\varepsilon_{cool}}{1 - \varepsilon_{cool}} \tag{3.7}$$

where the cooling effectiveness (ε) is given by equation 3.8 and K is a constant which is adjusted depending on the model. Typically assumed values are between 0.02 and 0.06 for stator and rotor cooling [109]. Equation 3.7 has been applied to model axial turbine cooling system, however, the applicability to radial turbines has not to be excluded, since the model has been originally derived to describe convection and film cooling in general, as shown in [110].

$$\varepsilon_{cool} = \frac{T_{gas} - T_w}{T_{gas} - T_{cool}} \tag{3.8}$$

T_{gas} and T_{cool} are the inlet hot gas and the coolant gas temperatures respectively, and T_w is the turbine wall temperature. Since both stator and rotor require cooling, equations 3.7 and 3.8 have to be specialized to establish the cooling flow requirements of these two turbine sections.

Once the total turbine cooling flow requirements has been established, equation 2.27 can be employed to quantify the turbine cooling losses and penalize the input turbine efficiency.

3.4.2 Model Implementation

The equations previously presented are suitable for the implementation in NPSS, using the interstage bleed ports and standard *preBleed()* and *preexecute()* functions defined within the program. These functions allow to set external variables used in the cycle analysis, but not directly calculated by the main thermodynamic solver (refer to [92] for more information).

The bleeding flow is assumed to be extracted from the HPC exit, by setting ζ_C equal to the unity for both rotor and stator turbine cooling. This assumption has been made to ensure that sufficient pressure is available at the high pressure turbine inlet to push the coolant through despite cooling channels pressure losses. On the other hand, two turbine bleed inlet points have been defined to model stator and rotor cooling respectively. The stator flow ($\zeta_T = 1$) is assumed to participate in the turbine work extraction, while no contribution is given by the rotor cooling flow ($\zeta_T = 0$).

Stator Cooling The stator cooling effectiveness is calculated from equation 3.8, using the burner exit temperature (Burn.Fl_O.Tt) as T_{gas} and the high pressure compressor exit condition (HPC.Fl_O.Tt) as coolant temperature (T_{cool}). The wall temperature (T_w) has been set to 1250K, the maximum allowed for uncooled blades.

Finally, the stator cooling fraction (ξ_N) is calculated from equation 3.7, using a value of 0.05 for the parameter K, as suggested in [52, 108]. The calculated ξ is given as bleed fraction input to the compressor bleed port in NPSS. If $T_{gas} \leqslant 1250K$ no cooling is assumed.

Rotor Cooling The rotor cooling effectiveness is calculated from equation 2.25 assuming $(T_w + \Delta T_0)$ equal to 1250K and $(T_{0c} + \Delta T_0)$ to the compressor exit temperature (HPC.Fl_O.Tt). Since the stator cooling air mixes with the main flow, the rotor inlet temperature is lower than the burner exit temperature. Reference [108] approximates this phenomenon by setting the gas temperature equal to 90% of the burner exit temperature. The same assumption was kept here.

As presented in section 2.3.1, using approximately 10% of the primary flow as coolant is sufficient to ensure an effectiveness of 0.30 at the turbine rotor tip [16]. With this consideration, the rotor cooling fraction (ξ_R) is calculated from equation 3.7, with the parameter K set to 0.2.

With ξ_N and ξ_R the overall cooling fraction (ξ) is calculated in the turbine element and the input turbine efficiency is consequently updated. This model has been implemented in all the NPSS cycle models as visible from the engine schematics of Figures 3.3, 3.4 and 3.5. For a better turbine efficiency penalty due to cooling losses, more advanced models should be employed. However, the model here presented has been found satisfactory for this preliminary analysis.

CHAPTER 4

Component Modelling

4.1 Introduction

This chapter discusses the implementation and validation of the component performance and weight models created in Matlab. Complex performance models have been defined for compressors, turbines and combustor. Further justification of the implementation of these higher fidelity models is provided here, by weighing advantages and disadvantages with respect to more simplified modeling thechniques.

Relations to estimate the individual component weight contributions have been defined for all the main gas turbine building blocks used in NPSS. Since a detailed design of the propeller is beyond the scope of this work, no weight model has been built for this element. Complete discussion on the implemented weight model is provided at the end of the chapter.

4.2 Compressor Performance Modeling

The compressor performance model has the objective of defining the component design efficiency as function of known inlet flow conditions, design pressure ratio and rotational speed. Thus, providing NPSS with an accurate estimation of previously discussed LPC.effDes and HPC.effDes parameters to perform a more accurate design cycle analysis. Moreover, these values are used by the program to scale the component map provided for off-design analysis.

As presented in section 2.3.1, different preliminary performance tools are available. However, since accuracy and complexity of the methods are strongly related, additional considerations, with respect to the thesis main objectives, have to be made before selecting the final model. Furthermore, sufficient compressor geometrical insight has to be gained to estimate the component weight. Therefore, this aspect is also influencing the selection of the performance model.

In the following paragraphs, the implementation and validation of the highest fidelity model considered in this work will be briefly presented, discussing necessary inputs and aerodynamic feasibility aspects. Subsequently, a comparison between the different models discussed in section 2.3.1 is presented, giving reasons for the ultimately selected model. Moreover the off-design performance are discussed in section 4.2.3.

4.2.1 Detailed Design Performance Model

Since no work is done on the flow by the compressor diffuser, the total power absorbed by the compressor can be determined by the flow conditions at the inlet and outlet of the impeller element [111]. Therefore, the entire compressor behavior can be assessed by means of the turbomachinery fundamental equation [41], which relates the compressor main geometry with pressure ratio and rotational speed as follows:

$$\Pi_C^{(\gamma-1)/\gamma} = 1 + (\gamma - 1)\eta_s \lambda M_{u2}^2 \tag{4.1}$$

where M_{u2} is the dimensionless rotational speed and λ is the work factor, defined as function of the slip factor (σ), the impeller exit flow angle (α_2) and blade angle (β_2) as:

$$\lambda = \frac{C_{\theta 2}}{U_2} = \frac{\sigma}{1 - \tan\beta_{B2}/\tan\alpha_2} \tag{4.2}$$

Typically, the compressor is designed for a given pressure ratio (Π_C). Assuming the stage total to total efficiency (η_S) and λ known, equation 4.1 allows to calculate the impeller exit radius (r_2) for a specified rotational speed and vice versa, since $U_2 = (2\pi r_2 N)/60$. Starting from here, a detailed meanline procedure has been presented in appendix A to characterize the compressor geometry, assumed constituted by: impeller, vaneless diffuser and vaned diffuser. The mathematical description of the model is given in section A.2, while the actual model implementation is explained in section A.3.

The resultant compressor geometrical tool has been coupled with the Galvas loss model [36, 37] to calculate impeller and stage total to total efficiencies: η_I and η_S, needed for the geometrical calculations. A value of 0.9 and 0.8 has been respectively assumed to generate the initial geometrical data, as suggested in references [26, 41]. Subsequent iterations refine the compressor geometry until a pre-defined tolerance has been reached for both η_I and η_S. Figure 4.1 illustrates the compressor design model realized in Matlab; references to specific section of the appendix are provided for a more complete understanding of the model.

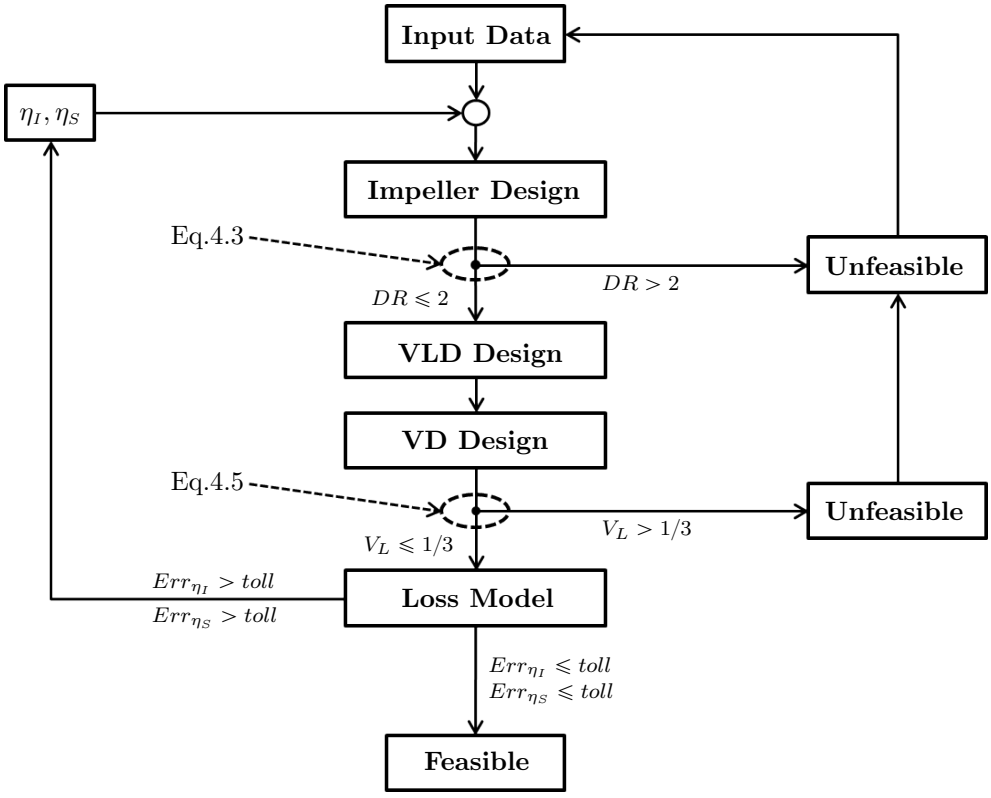

Figure 4.1: Compressor performance whole diagram

Err_{η_I} and Err_{η_S} represent the relative error between the previous and current impeller and stator efficiency evaluation. *toll* is the tolerance value set to 0.05 for both impeller and stage efficiencies. The resultant impeller and diffuser designs have to be checked to ensure their aerodynamic feasibility. According to [26, 41], an important impeller parameter has been identified with the diffusion ratio (DR), defined as equation 4.3. Many authors have associated

high diffusion rates with the inception of the impeller stall. Rodgers [112] showed diffusion ratios around 1.9 and 2.0 at surge flow rates, while, Harley [42] uses a value of 2.4 to model the beginning of surge in his study, treating the impeller as the only element responsible for surge conditions. A more conservative value of 2.0 has been used in this study to define the impeller aerodynamic feasibility range.

$$DR = \frac{W_{1s}}{W_2} = \frac{r_{1s}/r_2}{(1 - 2\lambda + \lambda^2/\sin^2\alpha_2)^{1/2}\sin\beta_{1s}} \tag{4.3}$$

Moreover, references [26, 41] provide indications of optimum specific speed (n_s) from maximum compressor efficiency. It has been observed that n_s increases with the blade backward sweep angle (β_2) and decreases for a given blade angle with the pressure ratio rise. Galvas [37] shows that optimal specific speed ranges for backswept impellers should be expected between 0.705 and 1.018 for maximum efficiency. Since this range cannot be considered applicable to every design pressure ratio [41], this aspect has been treated mainly as an indication rather than a strict requirement. The definition of n_s has been developed into equation 4.4 reported in [26], showing better its direct dependence on compressor geometrical parameters.

$$n_s = \frac{\omega\sqrt{\dot{V}}}{\Delta h_{0s}^{3/4}} = \frac{(r_{1s}/r_2)^{3/2}(\pi/\tan\beta_{1s})^{1/2}(1-\nu^2)^{1/2}}{(\lambda\eta_s)^{3/4}} \tag{4.4}$$

From extensive test data, Aungier* suggests two vaned diffuser feasibility criteria. The first is associated to the equivalent divergence angle ($2\theta_c \leqslant 11^\circ$) and the second to the vane loading parameter ($V_L \leqslant 1/3$), given by equation 4.5. According to references [113, 114], these constraints ensure to avoid diffuser stall and achieve maximum static pressure recovery.

$$V_L = \frac{2\pi(r_3 C_{\theta 3} - r_4 C_{\theta 4})}{Z_{VD} L_v (C_3 - C_4)} \tag{4.5}$$

In the previous equation, r represents the vaned diffuser radius, C and C_θ are respectively the absolute and tangential velocity components, Z_{VD} is the number of vanes and L_v is the vane length. Since θ_c is given as compressor input variable, only the vane loading check is performed within the compressor design, as visible in Figure 4.1. The compressor design standard input setting is summarized by the following list of variables: {$\dot{m}$, γ, R, P_{01}, T_{01}, Π_C, N or r_2, ν, α_2, β_2, θ_c, Z_{FB}, Z_{SB}}. By specifying this input data, the compressor design is conducted with the objective of minimizing impeller inlet relative and exit absolute Mach numbers, which, according to references [26, 41], reduces incidence and friction losses, diminishing also the diffusion requirements. The diffuser system is sized for a VLD exit Mach number less than 0.8 and a VD exit Mach of 0.2, as recommended in reference [37].

Alternatively, it is possible to specify a value for the absolute Mach numbers of each compressor flow station (M_1, M_2, M_3 and M_4). The design tool attempts to design the compressor respecting the user defined input Mach numbers. If successful the geometry and the predicted efficiency is normally calculated, otherwise an error is returned. This option has been implemented to ensure the cycle component matching during the thermodynamic analysis, as it will be explained in section 5.3.2, and to facilitate the compressor model validation. In addition, the user can specify a value of the root mean square surface roughness (e_{rms}) to better approximate the skin friction coefficient calculation (see Figure A.11 of appendix A.2.2). Since no indications have been found in literature for a reasonable estimation of the e_{rms} value, the skin friction has been calculated assuming a smooth blade channel.

*R. Aungier. Design of centrifugal compressor stage for enhanced operating range and head rise. Internal Report, 1997 (cited by Kim et al. [113]).

Model Validation

The compressor design model has been validated using reference compressor data available in literature. The initial challenge was constituted by the identification of compressor documentation with sufficient performance and geometrical data to properly replicate and compare the reference design with the constructed numerical model. References [45, 115–117] contain detailed information on compressor features, such as: design data, velocity triangles, predicted impeller and stage efficiencies, etc., to perform a reliable validation study.

High accuracy on the predicted compressor total to total efficiency for a given inlet mass flow, pressure ratio and rotational speed is important, since NPSS uses these inputs to perform the cycle analysis. Therefore, a maximum error of 5% between the calculated efficiency and the reference data has been considered acceptable for this project. Table 4.1 summarizes the main outcome of this validation phase.

Table 4.1: Validation main outcome with detailed reference data (compressor)

Reference	$\dot{\mathbf{m}}$ **(kg/s)**	**N (RPM)**	$\boldsymbol{\Pi_C}$	$\boldsymbol{\eta_I}$	$\boldsymbol{\eta_{I,ref}}$	$\boldsymbol{\eta_S}$	$\boldsymbol{\eta_{S,ref}}$
Japikse and Baines [45]	5.320	14000	2.05	0.9191	0.9200	0.8699	0.8700
NASA-TN-D-5761 [115]*	0.278	38500	2.43	0.9108	0.8960	0.8216	0.8130
NASA-TM-X-3552 [116]	0.996	68840	5.93	0.8770	0.8710	0.7833	0.7800
ASME-GT-2002-30394 [117]†	2.550	50000	5.10	0.8280	0.8400	0.8180	0.8000

Good agreement with the reference data is visible form the table. The compressor efficiency is predicted well within the accuracy requested. Moreover, the calculated compressor geometry, flow angles and velocity triangles match quite well with the reference ones. Hence, the compressor model has been considered successfully validated, since the predictions are sufficiently accurate for all the four case study.

4.2.2 Model Comparison

As presented in section 2.3.1 and appendix A.1, different models have been identified in literature to estimate the compressor design performance. Scaling methodologies are certainly the most commonly adopted approach in preliminary design stage to select a reasonable value for the compressor efficiency in the cycle analysis. Subsequent studies have improved the original formulation, increasing the overall accuracy of the method [30]. Since scaling factors are defined as function of the Reynolds number ratio (Re_{ref}/Re), or from parameters that still depend on it, it is difficult to correctly employ these techniques within this project.

A set of additional methods have been presented in appendix A.1.2 as alternative to the higher fidelity method previously discussed. These methods are typically used for preliminary cycle calculations to quickly assess the compressor performance variation as function of thermodynamic input. The accuracy of these relations has been compared in Table 4.2, together with the detailed model treated in the previous section. The ERAST Coleman engine data, reported in Figure 1.3, have been used as reference for compressor efficiencies and flow conditions.

Table 4.2: Different models output efficiency comparison (compressor)

	$\boldsymbol{\eta_K}$	$\boldsymbol{\eta_W}$	$\boldsymbol{\eta_M}$	$\boldsymbol{\eta_G}$	$\boldsymbol{\eta_{ref}}$
LPC	0.8641	0.7885	0.7953	0.7019	0.7220
HPC	0.8640	0.8200	0.7952	0.7432	0.7550

*Additional data available at: NASA-TM-X-1622 [118] and NASA-CR-54368 [119].

†Additional data available at: ASME-95-GT-079 [120], ASME-98-GT-024 [121] and ASME-99-GT-446 [122].

where $\eta_{\mathbf{K}}$ indicates the efficiency calculated from equation A.8, reference [32], η_W using equation A.9 provided in [33], and η_M from equation A.10 of reference [34]. η_G is the efficiency value calculated using the Galvas loss model [36, 37] and η_{ref} is the ERAST reference value [14]. All the efficiencies reported in Table 4.2 are expressed as adiabatic total to total. Appropriate conversion has been made to transform the polytropic efficiency given by equations A.8 and A.9 into the correct form.

Table 4.2 justifies the implementation of a higher fidelity model for this study. In fact, models which depend exclusively on pressure ratio are not reliable for this semi-closed cycle study, since the effect of inlet mass flow variation cannot be detected. Although, the approach proposed by Wilson and Korakianitis [33] properly models the efficiency trend, it is still quite inaccurate in terms of absolute values. η_G has been obtained for a flow angle (α_2) of 65°, a blade angle (β_2) of -20° and assuming an impeller blade number (Z_{FB}) of 20. The efficiency reported in Table 4.2 varies slightly for different values of these parameters, even though still maintaining a good matching with the reference data.

Hence, since the application of scaling factor is impractical and less accurate, the detailed loss model implemented has been used during the engine optimization to provide NPSS with an accurate efficiency value for the thermodynamic analysis. However, since the compressor efficiency value not only depends on thermodynamic and inlet flow data, but also on input geometrical parameters ($N, r_2, \nu, \alpha_2, \beta_2, \theta_c, Z_{FB}, Z_{SB}$), these variables have been properly considered in the optimization of each cycle arrangement (see chapter 5).

4.2.3 Off-Design Performance

The loss model equations used for the design efficiency calculation, can be adjusted to define complete compressor performance maps, as shown in reference [36]. From comparison with test data, Galvas's loss model has been proven to be satisfactory in assessing the overall compressor off-design performance. The most significant errors have been detected around the surge line [42] and in predicting choking weight flow at certain speed lines. This is because strictly one-dimensional correlations are not able to accurately approximate such complex multi-dimensional phenomena [36]. Since a much longer development time was needed to build and validate this off-design model, its implementation has been suggested as future work.

As mentioned in section 3.2.1, centrifugal compressor maps have been gathered from existing references and imported in NPSS. Reference maps have been chosen from considerations on pressure ratio ranges and feature similarities with the ERAST compressors data [14]. The ASME-89-GT-112 [123] has been finally selected for this project, since it is representative of a typical impeller-vaneless/vaned diffuser configuration. The correspondent compressor map has been plotted in the following paragraph.

ASME-89-GT-112

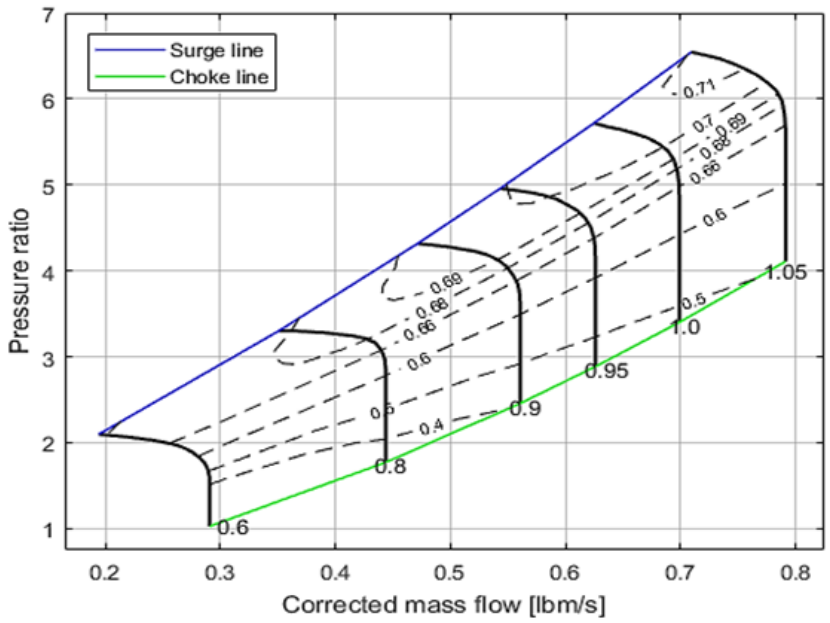

Figure 4.2: ASME-89-GT-112 centrifugal compressor map [123]

4.3 Turbine Performance Modeling

Similarly to the compressor block, the turbine performance model provides NPSS with an accurate estimation of the design component efficiency (HPT.effDes and LPT.effDes) for given inlet flow conditions, rotational speed and turbine power output. Different level of fidelity models are available in literature to accomplish the turbine geometric and aerodynamic modeling. The same reasoning used for the compressor has been applied for selection of the turbine performance model. The ultimate choice has been based on trade-off considerations between high accuracy and reduced computational effort. Furthermore, since the turbine weight model requires a similar set of inputs (see section 2.4.2), the obtained geometrical data must be sufficient to allow for the weight calculations.

This section illustrates the implementation and validation of the detailed turbine performance model, comparing the accuracy of the efficiency prediction with lower fidelity methods. Moreover, the performance of the three turbine loss models presented in section 2.3.1 is further discussed in this part of the document. Finally, off-design turbine performance details are given at the end of this section, showing the component maps imported in the NPSS environment.

4.3.1 Detailed Design Performance Model

As mentioned, the turbine package designs the component from a specified power output ($\dot{W}_T$), inlet flow conditions and rotor inlet radius (r_2) or rotational speed (N). In addition, the inlet Mach number (M_0) or the nozzle radius ratio (r_0/r_1) has to be provided to size the turbine nozzle section.

The code starts with an assumed turbine nozzle ($\eta_{N_{ts}}$) and stage ($\eta_{S_{ts}}$) total to static efficiency value to estimate stator and rotor geometry. A nozzle-rotor interspace has been also included to ensure sufficient nozzle wake mixing and circumferentially uniform flow conditions at the rotor inlet [41]. The initially set efficiency values are then iteratively updated using one of the implemented loss model, as shown in Figure 4.3.

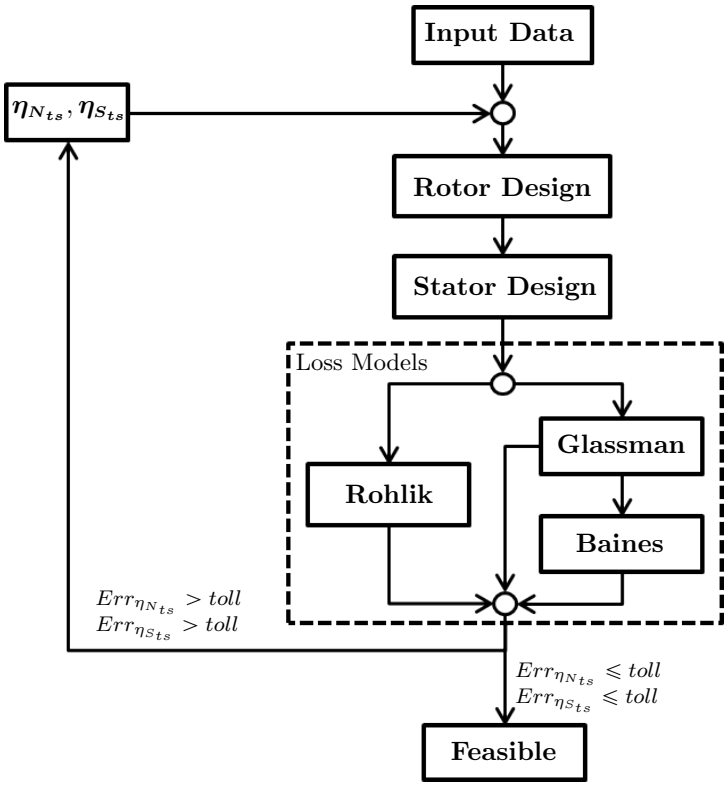

Figure 4.3: Turbine performance whole diagram

where $Err_{\eta_{N_{ts}}}$ and $Err_{\eta_{S_{ts}}}$ represent the relative error between the previous and current nozzle and stage efficiency evaluation. No feasibility constraints have been defined in references [41, 46] on the turbine rotor aerodynamic design. However, indications have been provided on specific speed (n_s) and specific diameter (d_s) to achieve maximum efficiency, which can be summarized by means of Figure 4.4. The definition of these parameters is given by equation 4.6 and 4.7 respectively, as discussed in reference [41].

$$n_s = \frac{\omega\sqrt{\dot{V}}}{\Delta h_{0s}^{3/4}} = \frac{D_{3,M}}{D_2}\left(\frac{\eta_s}{\lambda}\right)\left[2\pi k\left(\frac{1-\nu^2}{1+\nu^2}\right)\right]^{1/2} \tag{4.6}$$

where η_s is the total to total stage efficiency and k is the discharge velocity ratio (C_{m3}/U_2). This last parameter is fundamental to model the radial turbine rotor, as extensively discussed in appendix B.2.1. Optimal values of k are around 0.25 which corresponds to a n_s value of about 0.6 [41]. The specific diameter is given by:

$$d_s = \frac{D_2\Delta h_{0s}^{1/4}}{\sqrt{\dot{V}}} = \frac{D_2}{D_{3,M}}\left(\frac{\lambda}{\eta_s}\right)\left[\frac{\pi}{2}k\left(\frac{1-\nu^2}{1+\nu^2}\right)\right]^{-1/2} \tag{4.7}$$

Similarly, optimal specific diameters have been indicated around 3.5 [41]. The typical radial turbine $n_s d_s$ map has been reported below, showing attainable efficiency values for a given specific speed and specific diameter. The line representing the product $n_s d_s = 2$ is the theoretical maximum efficiency line discussed in [41].

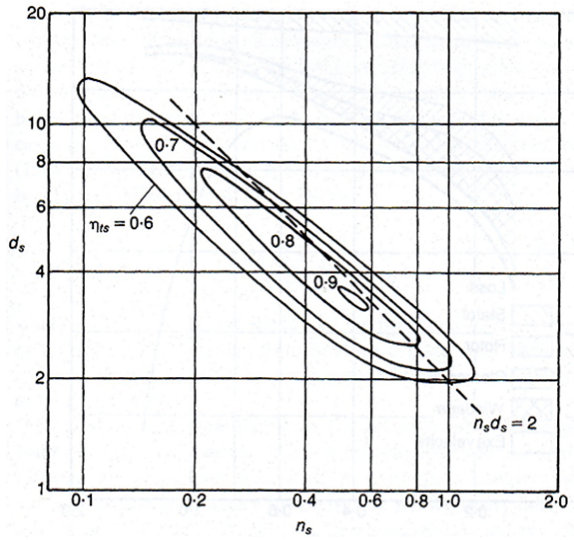

Figure 4.4: Radial turbine $n_s d_s$ diagram [41]

Aungier [124] reports a set of guidelines gathered from literature for a good turbine design. Dissimilar recommendations have been given by the different authors cited, making difficult to derive consolidated rules. Therefore, these suggestions have been only evaluated in the rotor design, without resulting into strong aerodynamic design constaints (see appendix B.3).

The radial turbine design performance model requires the following set of standard input data: $\{\dot{m}, \gamma, R, P_{00}, T_{00}, \dot{W}_T, N$ or $r_2, \nu, \beta_{3s}, M_0$ or $r_0/r_1\}$. Using these settings, the rotor design procedure discussed by Whitfield and Baines [41] for minimum rotor inlet Mach number is attempted, for given power demand and rotational speed. While, the nozzle design is conducted for a specified radius ratio (r_0/r_1) and the inlet Mach number (M_0) is calculated. Any unconverged or unfeasible resultant design is dealt by the optimizer, as shown in section 5.4.

Additional input settings have been created, allowing for user defined absolute axial (c_2) and radial (c_3) clearances to calculate the associated losses. Rohlik [47] suggested to define c_2 and c_3 as percentage of D_2 and D_{3s} (see appendix B.2.2). Instead Rodgers [16] discusses a limiting values of 0.015in (0.0381cm) for small turbine rotors, due to machining limitation. This approach has been preferred since Rohlik's approach might result in manufacturing impossibilities for too small D_2 and D_{3s} values. Thus, the assumption of best clearance gap possible has been made.

Finally, the possibility of specifying different rotor inlet Mach number M_2 and an inlet blade angle (β_2) has been implemented in the code to facilitate the validation phase. Checks have been made to ensure the feasibility of the resultant design for not standard input settings. Refer to appendix B.3 for a complete description of the turbine performance model. The mathematical treatise is given in appendix B.2.

Model Validation

The turbine validation has been conducted similarly to the compressor case. References [125–127] provide sufficient data for a good replication of the radial turbine designs presented in the papers. The model objective is to achieve an efficiency prediction within a 5% error with respect to the reference value. Table 4.3 reports the results of the radial turbine validation study. All efficiency data reported in the table are the stage total to static adiabatic efficiency, unless otherwise specified.

Table 4.3: Validation main outcome with detailed reference data (turbine)

Reference	$\dot{\mathbf{m}}$ **(kg/s)**	$\mathbf{N}$ **(RPM)**	$\dot{\mathbf{W}}_{\mathbf{T}}$ **(W)**	$\boldsymbol{\eta}_{\mathbf{R}}$	$\boldsymbol{\eta}_{\mathbf{G}}$	$\boldsymbol{\eta}_{\mathbf{B}}$	η_{ref}
Khader's thesis [125]*	0.0800	130000	18020	0.8289	0.8397	0.8134	0.8380
Ventura et al. [126]	0.2271	38500	22371	0.8252	0.7836	0.8078	0.7900
NASA-TP-1730 [127]	0.8918	70000	305620	0.8228	0.8388	0.8029	0.8340

where η_R, η_G and η_B are the efficiencies calculated using Rohlik, Glassman and Baines' loss models presented in detail in appendix B.2.2. As visible from Table 4.3, the entire set of loss models meets the requirements previously stated. However, the precision of the models differs from case to case. For example, Baines's formulation results in the most pessimistic prediction, since the impact of clearance losses and passage losses is much greater than for the conventional Glassman loss model. On the other hand, Rohlik's approach leads to the greatest error in the second case study. The Glassman loss model gives on average the most accurate efficiency estimations. Hence, it has been preferred, among the whole set of higher fidelity models implemented, for the turbine analyses of this project.

4.3.2 Model Comparison

The applicability of scaling relations is complicated by the lack of reliable references and by the difficulty explained in correctly estimating the Reynolds number ratio. Thus, the performance of the simplified empirical models, presented in appendix B.1.2, has been evaluated as an alternative to the more computationally expensive method treated previously. Table 4.4 presents a comparison between the whole set of "simple" models efficiency prediction and the Glassman loss model. Differently from section 4.2.2, the ERAST Coleman engine data (Figure 1.3) have not be employed in this study, since they are not representative of a radial machine. Thus, the analysis has been conducted using data from reference [127].

Table 4.4: Different models output efficiency comparison (turbine)

Π_T	$\Pi_{T,ts}$	D_{3h} **(mm)**	$\boldsymbol{\eta}_{\mathbf{K}}$	$\boldsymbol{\eta}_{\mathbf{W}}$	$\boldsymbol{\eta}_{\mathbf{G}}$	$\boldsymbol{\eta}_{\mathbf{ref}}$
2.793	2.997	116.13	0.8582	0.8710	0.8388	0.8340

where $\eta_{\mathbf{K}}$ indicates the efficiency calculated from equation B.2, reference [32] and η_W using equation B.3 provided in reference [33]. All efficiency values have been expressed as total to static. These data are sufficient to show the advantage of the higher fidelity model implemented for the radial turbine analysis, which leads to a much more reliable efficiency estimation.

4.3.3 Off-Design Performance

Radial turbine off-design performance modeling has been accomplished through map scaling, as for the centrifugal compressor. Future work should address the implementation of the turbine loss models employed in this work to generate full component maps, starting from the so far obtained design geometrical data. The radial turbine map given in the ASME-92-GT-93 [128] have been imported in NPSS. Similar considerations on pressure ratio ranges have been used here to select the turbine map, as for the compressor.

*The efficiencies reported here are expressed as total to total adiabatic [125].

ASME-92-GT-93

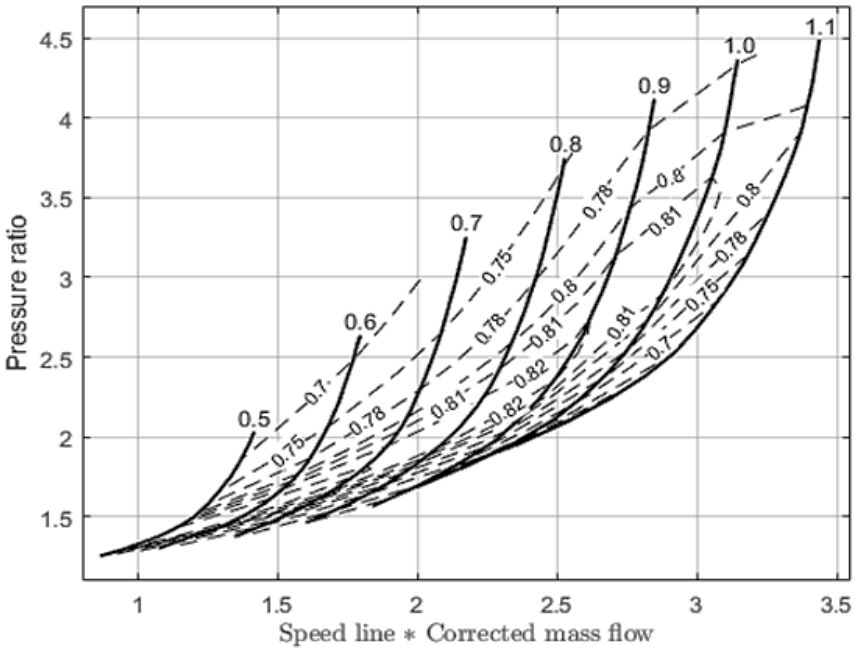

Figure 4.5: ASME-92-GT-93 radial turbine map [128]

4.4 Combustor Performance Modeling

According to reference [18], the combustor element constitutes the most crucial aspect in determining the success of the semi-closed cycle, since extremely high recirculation rates are employed by this cycle arrangement. Reference [69] represents the only example found in literature which addresses in detail the effects of the introduction of recirculated products inside the burner. The general conclusion derived in the paper, and summarized at the beginning of section 2.3.3, has been obtained for significantly lower recirculation ratios than those commonly used in semi-closed cycles [10]. In addition, the semi-closed cycle combustor is exposed to considerably high inlet pressures and temperatures, which has the subsequent effect of diminishing the burner loading (equation 2.44). Therefore, not only the design and off-design efficiency is augmented with respect to conventional open cycles, but also the burner size can be reduced [14].

A relatively simple combustor model has been created in this project to address some of the observations previously mentioned. In particular, this model has the objective of tracking performance and size differences between similar burner concepts applied to open cycles or semi-closed cycles. Thus, partially improving the simplified combustor analysis of the ERAST study [14]. Moreover, since the combustor inlet temperature is relatively high due to the recuperator presence, liner cooling aspects might constitute an issue. A preliminary tool has been developed to include this consideration within the model. Complete modeling description can be found in appendix C, while a brief summary is provided here.

4.4.1 Model Description

Since accurate design combustor efficiency and pressure losses cannot be estimated at this stage, in particular for the semi-closed cycle arrangements, the data reported in Table 3.2 have been assumed for the design analysis of each engine model. As discussed, the simple off-design combustor model, presented in section 2.3.3, has been implemented in NPSS to capture the

combustor efficiency variation as function of the burner loading parameter.

With the given burner design data, the combustor chemistry can be solved by NPSS, providing information on inlet and outlet flow conditions and fuel requirements. These additional parameters have been used to implement the combustor sizing procedure of Melconian and Modak [70], which allows to derive sufficient geometrical insight to estimate the combustor weight. Moreover, preliminary indications of how to distribute the overall inlet mass flow between primary, secondary and dilution zone have been given such that sufficient cooling air is available for the liner.

Once the geometrical and flow sizing has been computed, a preliminary heat transfer analysis is conducted to establish, from the calculated liner inner and outer wall temperatures, whether liner cooling is required. A maximum wall temperature of 1300K has been set as cooling threshold [70]. If any combustor zone registers a wall temperature higher than this value, the procedure discussed in in appendix C.3 is used to verify whether the available coolant flow is sufficient to ensure proper liner cooling. Since the combustor sizing has been conducted following the standard guidelines reported in [70], a failing in the cooling design does not necessarily mean that the combustor is not realizable. Therefore, the optimization has not been directly affected in such cases, although more combustor development has been recommended.

The following diagram reports the logic used in the implementation of the combustor model. The calculations made until the first circular node are employed to define the geometrical parameters used in the weight model (Figure 4.6). The second section then addresses the cooling aspects previously discussed. The block called "Flame" allows for a preliminary estimation of the flame temperature, information used by both "Wall" and "Cooling" blocks.

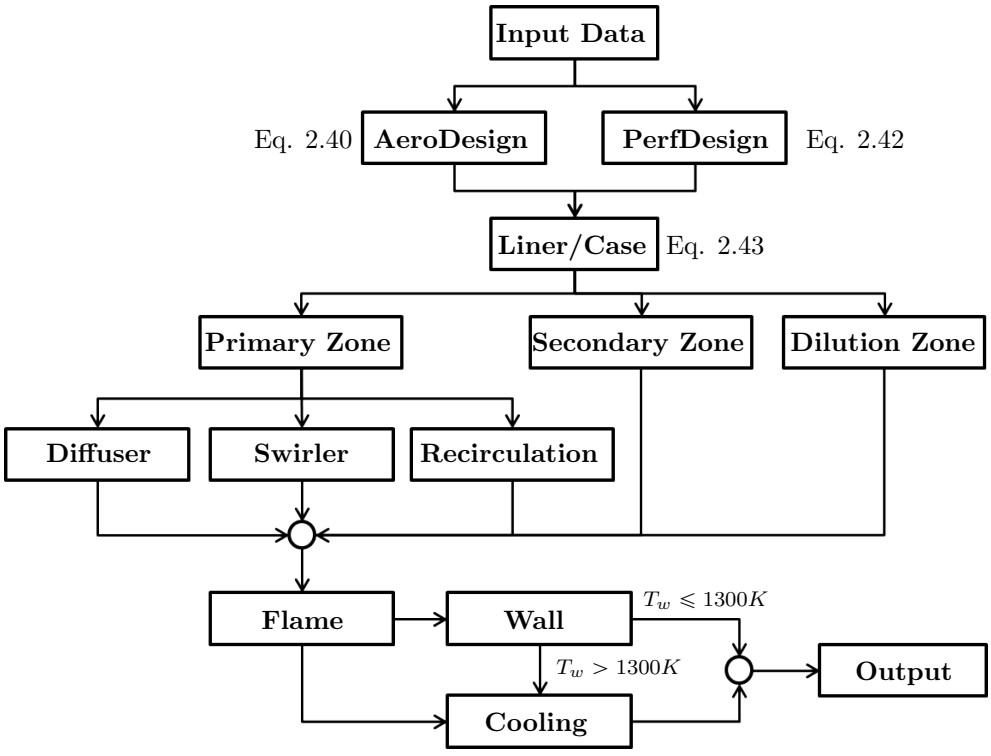

Figure 4.6: Combustor performance model diagram

A standard set of inputs are needed by the combustor model to perform the element sizing. The following general combustion flow and fuel data are provided by the NPSS combustor element, once cycle convergence has been reached: $\{\dot{m}_3, \dot{m}_f, R, P_{03}, T_{03}, P_3, (\Delta P/P)_B, FAR_{st}\}$. Furthermore, depending on the combustor type specified, the can number (N_b) or the inner diameter (D_{in}) have to be given for tubular and annular combustor respectively. As mentioned, this last option has been assumed in this project. The combustion inlet area (A_3) has to be set

to allow for the diffuser sizing. This parameter is important to ensure also reasonable matching with the previous engine component.

Model Validation

Validation of the presented methodology has been done by other authors with more advanced CFD tools as well as experiments [72, 76, 77, 129]. Therefore, the correctness of the model implementation has been tested throughout the replication of some case study reported in the previously cited references and in reference [70].

Semi-Closed Cycle Remarks

The combustor design methodology here presented has been successfully applied to different design cases available in literature. Although, this technique does not represent the most advanced combustor design approach and much more sophisticated tools are needed, it allows for a geometrical definition capable of withstanding the given gas turbine operating conditions [71]. The applicability of this methodology to the open cycle analysis is certainly not a concern. Since no further studies on semi-closed cycle combustion chambers have been performed, the validity of this model to such case has been reasonably assumed for this preliminary assessment.

Furthermore, an additional modeling assumption has been made to ensure the correct coupling between the NPSS burner analysis and the combustor performance modeling tool built in Matlab. In particular, the NPSS combustor solver automatically assumes that only the fresh air portion of the whole burner inlet mass flow is participating at the combustion process. Therefore, the recirculated flow presence is ignored in the estimation of the burner exit flow proprieties.

Since a low oxygen concentration is present in the recirculated products, the NPSS solver assumption is acceptable at this stage. However, the combustor sizing procedure must consider the whole amount of gasses entering the system to ensure the correct estimation of combustor dimensions. As a consequence, the whole inlet mass flow ($\dot{m}_3$) has been modeled as fresh air for the semi-closed cycle analysis, allowing for proper geometrical characterization.

4.5 Weight Modeling

Since early studies discussed that the semi-closed cycle arrangement allows for a considerable weight reduction with respect to conventional ICR open cycles [10], it is of interest of this project to investigate this aspect in more depth. As seen from section 2.4, a component based models have the advantage of better capturing the weight variation as function of primary cycle thermodynamic parameters, making this approach in line with this project goals.

Most of the recent focus has been dedicated to the implementation of models for large turbofan engines [80], which mainly feature axial turbomachinery stages. The sole model applicable to the small gas turbine architectures defined in this thesis project, is constituted by the NASA WATE model [83, 84]. A modern release of this program, suitable for the coupling with NPSS, has been made available on the NASA software download webpage*. Up to the current project date, the software release is limited to the U.S. Hence, the implementation of a similar modeling approach, based on the available references, has been necessary to accomplish the thesis objectives.

The difficulty associated with the implementation of highly accurate component based weight models is due to the lack of reference data to calibrate and validate the resultant methodology. Therefore, the accuracy of this method is not expected to be high. However, the ultimate objective here is to define component weight trends that allow proper optimization of the engine thermodynamics. Thus, considering the effects that the modification of a certain global variable

*U.S. software release available at: https://software.nasa.gov/software/LEW-19687-1

has not only on component performance, but also on its overall weight. The overall engine weight (W_{eng}) has been calculated considering the following contributions:

$$W_{eng} = W_C + W_{IC} + W_{RC} + W_B + W_T + W_{sh} + W_{gear} + W_{acc} \tag{4.8}$$

where: W_C is overall compressor weight, W_{IC} and W_{RC} are weight of the heat exchangers, W_B represents the combustor and W_T the turbines overall weight. W_{sh} is the overall shaft weight, W_{gear} and W_{acc} are the gearbox weight and the accessories weight respectively.

The weight calculations have been accomplished via the implementation of the equations presented in the literature review chapter (see section 2.4). This section provides more details on those components that have not been modeled using exclusively the information available in references [83, 84], such as: heat exchangers, gearbox, compressors and turbines. Validation and calibration aspects related to these components are also briefly mentioned here. More information on the actual model implementation has been given in appendix D.

4.5.1 Weight Modeling Details

Most of the component weight models have been taken from references [83, 84], with the exceptions of the heat exchangers and the gearbox. The HEXs weight has been calculated using the approach discussed in section 2.4.3, since a complete intercooler and/or recuperator design has not been performed for reasons explained. The estimated weight trends have been compared with detailed design data published in references [60, 130], showing good agreement of the model in terms of weight dependence on effectiveness and pressure loss. The gearbox weight has been assessed using the methodology suggested in references [87, 91], assuming planetary gearbox and a value of 400 lb/in^3 for the constant K of equation 2.62, set according to data published in reference [89].

The remaining component weight contributions of equation 4.8 have been estimated using equations reported in references [83, 84]. However, since the papers do not provide detailed indication on disk and blade sizing for radial turbomachinery, a methodology has been developed to fill this gap in the WATE weight model, involving material and structural consideration. The complete model explanation is reported in appendix D.1 and D.2 for compressor and turbine respectively, while, only a short summary is given here.

Centrifugal Compressor Weight

The implemented compressor weight model logic has been summarized by the diagram reported in Figure 4.7. The program requires geometrical information gathered previously from the performance model. In particular, the impeller inlet and outlet compressor radii (r_{1h}, r_{1s} and r_2), passage width (b_1 and b_2), exit blade angle (β_2), exit rotation speed (U_2) and total temperature (T_{02}) are needed. In addition, the compressor material must be a priori selected among a list of commonly employed materials (see appendix, Table **??**). Considering the compressor temperature ranges of the ERAST Coleman engine [14], a titanium alloy (Ti-6Al-4V) has been initially assumed.

With this data settings, a preliminary structural analysis based on reference [131, 132] is performed to establish whether the given rotational speed (U_2) does not lead to excessive stresses in the compressor blades and disk. For such unfeasible cases, an attempt of identifying alternative more robust materials among the list of available materials is made. If successful, the material properties are updated, otherwise, the compressor design results in a structural infeasibility and the optimizer will deal with it as shown in section 5.4. The weight of any feasible solution is calculated as sum of disk, blades, diffuser and case.

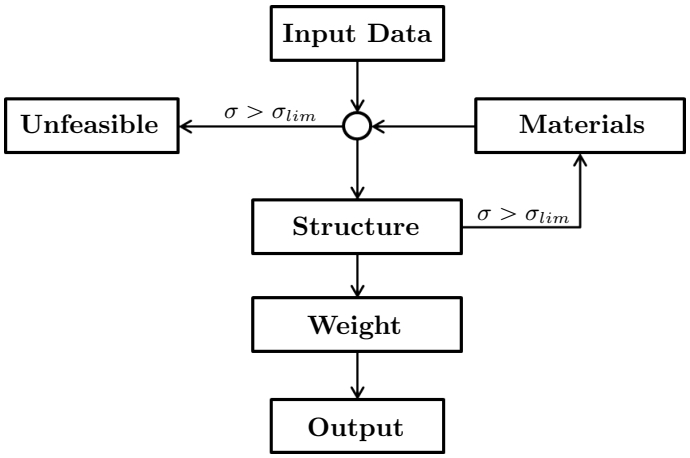

Figure 4.7: Compressor weight model diagram

As presented in appendix D.1, a procedure has been developed to produce a reasonable estimation of the impeller weight, given essentially by the contribution of disk and blades. Since no detailed references are available to calibrate the model, the simple models reported in references [64, 83] have been used as target reference. In such way, the general centrifugal compressor weight trends defined in literature have been respected by the current model.

Reference [133], provides a set of empirical information to support the preliminary design phase of industrial impellers. A population of sixteen ASTM A564 stainless steel unshrouded impellers has been used for weight considerations. Strong relation between weight and impeller diameter has been shown, and a general correlation is derived from the figure reported below.

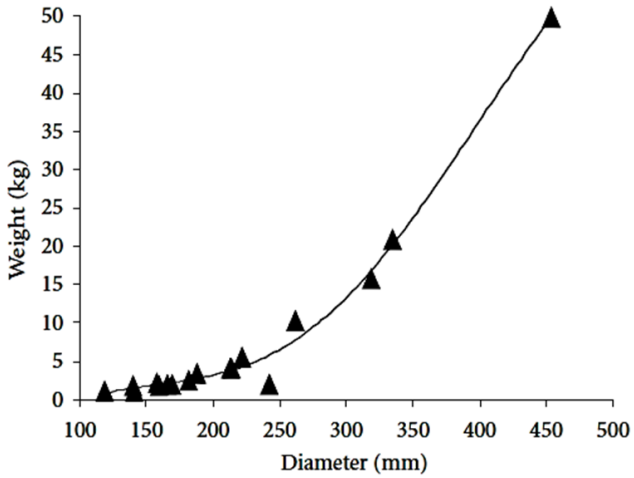

Figure 4.8: Industrial impeller weight with diameter correlation [133]

Since the reference impeller population of Figure 4.8 has been taken from industrial applications and no additional design data have been published, this weight trend cannot be comfortably used for the model calibration in the current project. Therefore, the approach discussed previously has been preferred. More details regarding the model calibration are given in appendix D.1.

Radial Turbine Weight

The weight of the radial turbine has been calculated in a similar manner to the compressor. Complete description of the model is reported in appendix D.2. Figure 4.7 remains representative of the turbine weight model, with the exception of the structural section. In fact, according to references [131, 132], the radial turbine stresses distribution is far more complicated than the

compressor one, due to the high operating temperatures involved. The application of a simple theory such as the one employed for the compressor to define maximum allowed stresses might not possible due to uneven temperature and stress distribution. Cooling aspects further increase the model complexity.

Reference [132] suggests to select the material based on TIT considerations. High temperature and strength materials have been investigated, capable of withstanding the temperature limitation of 1250K set for the cooling system. Nickel and Cobalt alloys have been assumed for the weight estimation (see appendix D.2.1). Rotational speed limitation are set according to the compressor stress analysis, assuming that the turbine material is capable of handling it. Although, more sophisticated tools are needed to properly define the stress distributions in the component and assess the design feasibility, the assumptions made here are acceptable for this preliminary analysis.

Model calibration has been performed in agreement with what done for the compressor using reference trends data available in reference [64, 83]. Since even less reference data are available to support the assessment of the radial turbine weight model, the approach followed here is the most reasonable, considering project objectives and deadlines.

4.5.2 Final Considerations

The original WATE model has been developed for small gas turbines with an accuracy of $\pm 10\%$ with respect to reference component data provided by the Garrett engine manufacturer [83, 84]. Although most of the equations have been taken form the originally developed model, such high accuracy in not expected here. The lack of complete engine data, which allows to properly replicate the given case study with the current model, makes extremely difficult to quantify the developed model error in absolute terms.

The ERAST document [14] reports a preliminary estimation of component weights, obtained by scaling reference weight data. Although exact replication of the Coleman engine cycle has not been possible with the available information and tools, it has been possible to derive general conclusion on the developed weight model. The following observation have been made:

(a) The most significant error should be expected in the turbomachinery weight calculations.

(b) The heat exchanger weight model acceptably approximates standard intercooler and recuperator configurations.

(c) The influence of the remaining components on the overall engine weight is significantly lower than the previous ones.

These conclusions have been derived by replicating, where possible, the ERAST Coleman engine cycle conditions of Figure 1.3 with the component performance and weight models created. The calculated weight of compressors and heat exchangers have been compared with the estimated reference data in the paper [14].

Model Outcome Discussion

The low and high pressure compressor overall weight is overestimated with respect to the ERAST data. Similar output is observed even using the simple models from reference [83]. This outcome is expected since these models compute the weight of the machine as function of the cubic exponent of r_2. Hence, the calculated weight of the relatively large radial turbomachines used in the Coleman engine (Figure 1.5) will be over predicted. Same conclusions can be applied to the turbine model.

The calculated heat exchangers weight matches well with the ERAST data for conventional configurations. In fact, the weight of the plate-fin intercooler, used in the Coleman Engine,

matches the calculated value from the model. On the other hand, the recuperator weight is underestimated. Since the ERAST recuperator has a specifically designed arrangement, described in reference [14], and the overall predicted model weight trend agrees with conventional recuperator data [60, 130], this has not been considered a concern.

To summarize, the currently employed weight model has been focused on establishing general component weight trends as function of global cycle thermodynamic variables. High accuracy cannot be ensured at this stage, unless a complete weight model is rebuilt from scratch. Future work should address improvements to the current weight model, focusing in particular on radial turbomachineries, since major discrepancies with reference [14] have been observed here. This would involve more detailed aerodynamic and stress calculations and is, as such, considered to fall outside the scope of the current project.

CHAPTER 5

Optimization

5.1 Introduction

An effective way to ensure a reasonable performance comparison between the different cycles, is to optimize each engine for the same objectives and compare the results. Since early studies on semi-closed cycles have shown promising improvements in terms of part power specific fuel consumption and weight with respect to conventional solutions (section 2.2.2), it is of interest here to verify the applicability of these observation to the current case study. As mentioned, emission aspects have not been considered at this stage.

The performance and weight models explained in the previous chapters allow for the complete characterization of the engine thermodynamics. In particular, component efficiency, feasibility and size as function of given cycle and flow data are properly considered. Therefore, it is possible now to optimize each engine arrangement for minimum weight and minimum SFC_{av}. Where SFC_{av} is the average specific fuel consumption defined as:

$$SFC_{av} = \frac{SFC_{des} + SFC_{75\%} + SFC_{50\%} + SFC_{25\%}}{4} \tag{5.1}$$

Equation 5.1 equally accounts for design and off-design SFC variation as function of the different propeller cruise power demands (Table 3.3). Since two clearly distinct objectives can be identified for the current analysis, the multi-objective optimization approach represents the most appropriate way of dealing with competing objective problems [134]. Although a complete discussion on optimization theory is beyond the scope of this chapter, sufficient details are provided on the chosen optimization algorithm to give the reader a more complete understanding on how the problem has been formulated and solved.

Moreover, the integration of the so far discussed component performance and weight models with the cycle thermodynamic analysis is explained for each cycle arrangement, showing also how feasibility aspects have been taken into account in the optimization settings. Results and conclusions derived from this study are separately presented in the following chapter.

5.2 Optimization Theory

A multi-objective optimization problem can be mathematically formulated as [134]:

$$min[J_1(x), J_2(x), \cdots, J_i(x), \cdots, J_n(x)]$$

subjected to

$$g(x) \leqslant 0$$

$$h(x) = 0$$

and

$$x_l \leqslant x \leqslant x_u$$

where J_i represents the generic objective function, n is the number of objectives used in the problem, x is the design vector, $g(x)$ and $h(x)$ are the inequality and the equality constraints respectively, x_l and x_u define the lower and upper bounds applied to the design space. The solution of a multi-objective optimization problem is given by the so called Pareto optimality, which is representative of those design variables that lead to a non-simultaneous improvement of all the objectives [134].

5.2.1 Optimization Algorithms

Different algorithms have been developed to find the Pareto optimality of a multi-objective optimization problems. Reference [135] presents a complete list of currently available methods, dividing the treatise into: classical methods (CMs) and evolutionary algorithms (EAs). The first class includes mainly those algorithms that convert the multiple objective optimization into a single objective one, by combining the different objectives together through weighed average procedures. Since standard weighed average algorithms struggle to solve non-convex problems, a set of improved procedures have been developed [135]. However, they involve the specification of user defined parameters that are difficult to set for any given problem. According to reference [134, 135], EAs have several advantages over classical methods:

- The algorithms work with populations of solutions, instead of single solutions per iteration, giving the possibility of capturing multiple optimal points per generation.
- Because of their stochastic nature, a much grated design space is considered by the algorithm, increasing the probability of finding global optimum solutions.
- Since gradient information is not used by the algorithms, EAs are able to work with non-smooth or discontinuous objective functions.
- Due to the non deterministic nature of the algorithms, EAs are applicable to more arbitrary and unstructured optimization problems.

Main disadvantages are associated to the need for an increased number of function evaluations, which considerably rises the optimization running time compared to conventional CMs. Considering the nature and the objectives of the current thesis problem, evolutionary algorithms represent the best choice.

Matlab implements a particular type of EAs, which is based on a controlled elitist generic algorithm formulation [136], where individuals from the previous population survive in the next one depending on a rank based system. Since a detailed mathematical treatise of the algorithm is outside the scope of this work, only a practical description of the method is provided in the following section. The algorithm theoretical background is given in reference [135], for the interested reader.

5.2.2 The Matlab Algorithm

The algorithm is implemented under the function called: *gamultiobj*. The algorithm starts with an initial population which is defined within the bounds given, but not necessarily respectful of linear and non linear constraints. It is important at this stage to specify a reasonable number of initial elements that allows to produce a sufficiently distributed Pareto frontier at an acceptable computational effort. Reference [137] provides a rule of thumb to select the initial population number (N_p) valid for many applications. In particular, it is recommended to use a population size of at least ten times the length of the design vector (x). Gotshall and Rylander [138] report

a study, conducted on three different problems, to identify the optimal initial population size for a given problem. Equation 5.2 has been experimentally derived.

$$N_p = 267.43 \ln x - 293.21 \tag{5.2}$$

The applicability of this equation to different problems might hold, according to the paper, but it has to be verified.

Once the initial population has been defined, the algorithm selects the parent variables that will be kept in the subsequent generation (elite child), according to the best fitness values ($Rank = 1$), and creates child objects, using crossover and mutation techniques (Figure 5.1).

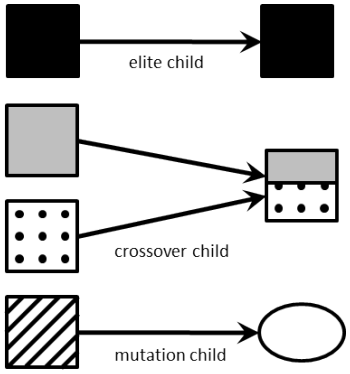

Figure 5.1: Children generation schematic in the *gamultiobj* algorithm, adapted from [136]

Crossover This technique takes a parent individual and randomly exchanges a certain number of bits with a second member, generating consequently a child which shares with each parents only a certain amounts of bits [134].

Mutation A particularly chosen parent randomly inverts a certain amount of bits, generating a completely different child. Only a single parent is required in this procedure, which occurs according to specifically defined probabilistic laws within the code.

A rank is then given to the child objects by evaluating their corresponding objective function values, which are subsequently used in the following iteration. The process is repeated until one of the algorithm stopping criteria has been satisfied. For standard applications, basic stopping criteria ensures that the average relative change in the Pareto optimally is less than a given tolerance or are based on an admissible maximum number of generations. More detail on the optimization algorithm are given in the Matlab global optimization toolbox user guide [136].

5.3 Problem Formulation

Each engine cycle arrangement has been optimized for minimum average specific fuel consumption (equation 5.1) and minimum engine weight (equation 4.8). The design vector (x) has been composed not only by primary thermodynamic variables, which slightly differ depending on the engine configuration, but also by compressor and turbine parameters. No external constraints have been applied to the problem, with the exception of the ones defined in NPSS, that have no influence on the Matlab optimization algorithm.

In this way, the number of function evaluations needed to perform the optimization has been significantly reduced. Lower and upper bounds have been defined to limit the optimizer search path within a feasible region. The criteria employed to set these bounds has been justified from common practices discussed in literature as well as from preliminary feasibility studies.

The problem under investigation can be mathematically described as a double multi-objective optimization. Equation 5.3 specializes the general formulation reported in section 5.2 to the actual optimization objectives.

$$min[\bar{J}(x)] = min \begin{bmatrix} J_1(x) \\ J_2(x) \end{bmatrix} = min \begin{bmatrix} SFC_{av}(x) \\ W_{eng}(x) \end{bmatrix} \tag{5.3}$$

subjected to

$$x_l \leqslant x \leqslant x_u$$

This section discusses the system of design variables used for the optimization of each engine, together with related lower and upper bounds used. In particular, the thermodynamic parameters are initially explained for recuperated, intercooled-recuperated and ERAST/HPRTE semi-closed engine configurations. Subsequently, the geometrical characteristics of compressors and turbines used as design vector are discussed. Final considerations on the *gamultiobj* settings and on the initial population will be given in the last paragraph of this section.

5.3.1 Thermodynamic Design Variables

From a thermodynamic point of view, a similar set of characteristic variables can be defined for semi-closed cycles and open cycles, since they share most of the engine components in a similar arrangement. Common engine cycle parameters that impact both objectives of equation 5.3 are: compressor pressure ratios, heat exchangers effectiveness and pressure loss, turbine inlet temperature, nozzle pressure ratio and shaft rotational speed. Additional cycle variables have been specifically defined for each cycle configuration, as shown in section 3.3. More information is given below on the optimization preliminary settings of each engine model.

Recuperated Cycle

Table 5.1 presents the whole set of thermodynamic variables used for the recuperated open cycle arrangement. The column named "Reference" reports, where applicable, the literature documentation used to specify the correspondent lower and upper bounds. These design data are passed to NPSS, together with other input parameters (see Table 3.9), through the .inp file previously discussed. In this way, the thermodynamic analysis is performed for each design vector modification defined by the Matlab system optimizer (*gamultiobj*).

Table 5.1: RC optimization design variables and relative bounds

$\mathbf{x}$	$\mathbf{x_l}$	$\mathbf{x_u}$	**Reference**
Π_{LPC}	2.000	5.000	-
Π_{HPC}	3.000	6.000	-
$(\Delta P/P)_{RC,c}$	0.020	0.050	[14, 60, 130]
$(\Delta P/P)_{RC,h}$	0.020	0.050	[14, 60, 130]
ε_{RC}	0.650	0.950	[14, 130]
TIT	1200K	1650K	[14]
$\%P_{04,LPC}$	0.850	1.150	-
Π_{Noz}	1.050	1.250	[102, 139, 140]
N	8500	13500	-

The compressor pressure ratios (Π_{LPC} and Π_{HPC}) and the design rotation speed (N) bounds have been set from a preliminary study conducted to identify a design feasible region for compressors and turbines. In fact, since the selection of the rotational speed strongly affects turbomachinery aerodynamics and structures, it was important to constrain the algorithm search space

of N within the feasible zone. Thus, helping *gamultiobj* to find the correct initial population to start with.

Similarly the $\%P_{04,LPC}$ bounds have been set after a preliminary study conducted with NPSS. In particular, it has been observed, from an initial cycle sensitivity study focused on specific fuel consumption and specific power, that the optimal turbine power split lays in solutions where LP and HP compressors are entirely driven by the HPT, while the LPT powers part of the propeller and ensures the demanded nozzle pressure ratio. Since the $\%P_{04,LPC}$ variable defines the amount of power extracted by the HPT, a value of approximately one ensures that the previous condition is met.

The turbine inlet temperature upper bound has been set from the ERAST report [14]. Since higher TITs have the effect of reducing both specific fuel consumption and overall engine weight, a limitation on the maximum TIT value depends on other aspects, such as: turbine materials and cooling, combustor liner cooling and recuperator materials.

A value of 2500°F (∼1644.3K) was assumed for the Coleman engine, resulting, from Figure 1.3, in a RIT of 1641.1°F (∼1167.1K), which already implies special high temperature alloys or even ceramic materials [7, 141, 142]. Therefore, this TIT value, rounded to 1650K, has been used as upper bound, while material feasibility checks have been implemented within the objective function, as explained section 5.4.

Recuperator and nozzle lower and upper bounds have been defined from common practices discussed in the references given in Table 5.1. For identical design variables used in the remaining cycle arrangements, similar reasoning has been applied to define their bounds. Therefore, only the different settings will be explained.

Intercooled-Recuperated Cycle

Table 5.2 shows the list of design variables used for the intercooled-recuperated open cycle. In addition to the recuperated engine parameters only two intercooler performance variables are considered. Similar criteria have been used to set the associated bounds.

Table 5.2: ICR optimization design variables and relative bounds

$\mathbf{x}$	$\mathbf{x_l}$	$\mathbf{x_u}$	**Reference**
Π_{LPC}	2.000	5.000	-
Π_{HPC}	3.000	6.000	-
$(\Delta P/P)_{IC,h}$	0.020	0.050	-
ε_{IC}	0.650	0.950	-
$(\Delta P/P)_{RC,c}$	0.020	0.050	[14, 60, 130]
$(\Delta P/P)_{RC,h}$	0.020	0.050	[14, 60, 130]
ε_{RC}	0.650	0.950	[14, 130]
TIT	1200K	1650K	[14]
$\%P_{04,LPC}$	0.850	1.150	-
Π_{Noz}	1.050	1.250	[102, 139, 140]
N	8500	13500	-

Semi-Closed Cycle

The semi-closed cycle design vector is reported in Table 5.3 for both ERAST and HPRTE engine models. Since the HPT exit pressure is dictated by the mixer total pressure condition (section 3.3.2), there is no need to define the turbine power split variable ($\%P_{04,LPC}$) as for the open cycle cases. Instead, the stoichiometric combustor ratio parameter (ϕ_{st}) has been defined as design variable. Because semi-closed cycles operate at near stoichiometric FAR [10, 14, 19], assessing the effect of this parameter on the cycle performance is of interest.

Considering that the selected NPSS ThemoPackage does not allow for rich or near stoichiometric ratios, the upper bound has been conservatively set according to [94]. The lower bound has been selected from a preliminary cycle study in NPSS to ensure the correct search space for the optimizer initial population, as optimal values of ϕ_{st} lays around 0.90 as indicated in [14].

Similar considerations applied to open cycles have been used here to define the optimal algorithm search path for rotational speed. It has been observed that feasible N values for the semi-closed cycle arrangements are almost double of those of the open cycles. This consideration matches with the design rotational speed assumed for the Coleman engine in the ERAST study [14]. Moreover, the LPC and HPC pressure ratio upper bounds have been slightly increased, since optimal cycle solutions lay at high overall pressure ratios [14].

Table 5.3: ERAST/HPRTE optimization design variables and relative bounds

$\mathbf{x}$	$\mathbf{x_l}$	$\mathbf{x_u}$	**Reference**
Π_{LPC}	2.000	6.500	[14]
Π_{HPC}	3.000	6.500	[14]
$(\Delta P/P)_{IC,h}$	0.020	0.050	-
ε_{IC}	0.650	0.950	-
$(\Delta P/P)_{RC,c}$	0.020	0.050	[14, 60, 130]
$(\Delta P/P)_{RC,h}$	0.020	0.050	[14, 60, 130]
ε_{RC}	0.650	0.950	[14, 130]
TIT	1200K	1650K	[14]
ϕ_{st}	0.850	0.950	[14, 94]
Π_{Noz}	1.050	1.250	[102, 139, 140]
N	18500	23500	[14]

5.3.2 Turbomachinery Design Variables

An additional set of design variables related to the turbomachinery component has been provided to the optimizer. In this way, the solver defines criteria for highly efficient compressors and turbines, still ensuring that aerodynamic and structural feasibility are respected. Tables 5.4 and 5.5 give design variables and relative bounds for compressor and turbine respectively. Since two pairs of compressors and turbines have been used in this project, the same data presented in the tables have been applied to both low and high pressure machines.

Table 5.4: Compressor optimization design variables and relative bounds

$\mathbf{x}$	$\mathbf{x_l}$	$\mathbf{x_u}$	**Reference**
ν	0.300	0.700	[37, 41, 143, 144]
α_2	60°	70°	[26, 41]
β_2	-40°	0°	[26, 41]
$2\theta_c$	7°	11°	[39]

According to references [41, 143], the selection of the impeller inlet hub to tip radius ratio (ν) mainly dependents on structural considerations. Sufficient space is also needed to accommodate the blades and ensure the correct mass flow passage. A value of 0.4 has been used in the cited papers for their study. It has been observed that smaller values lead to the reduction the inlet Mach number for a given mass flow, with the related benefit of increasing the impeller efficiency [143]. Galvas [37] recommends the range given in Table 5.4, although examples of ν values higher than 0.7 have been investigated in literature for unconventional machines [144].

The remaining parameters have been set according to common practices discussed in the references provided in Table 5.4. The compressor blade number has not been included in the

optimization and a value of 20 blades (no splitter blades) has been assumed as suggested in [145]. More information on the blade number selection is reported in appendix A.3.1.

The radial turbine design vector is reported in the following table. Again, the optimization bounds have been specified as suggested in the references given within the table.

Table 5.5: Turbine optimization design variables and relative bounds

$\mathbf{x}$	$\mathbf{x_l}$	$\mathbf{x_u}$	**Reference**
r_0/r_1	1.100	1.700	[124]
ν	0.300	0.700	[47, 146]
β_{3s}	-70°	-50°	[41, 46]

Special Variable

An additional variable has been created to ensure correct flow matching between the low pressure compressor and the subsequent element. In particular, the design LPC exit Mach number ($M_{4,LPC}$) is an important variables for semi-closed cycle arrangements, since it dictates the mixer area sizing in NPSS. In the simple recuperated open cycle, on the other hand, the LPC exit Mach number has a strong impact on the HPC overall performance. Furthermore, in the intercooled-recuperated configuration, it influences the intercooler coupling.

As seen in section 4.2.1, the standard compressor sizing methodology assumes an exit Mach number equal to 0.2, which has been recommended for a good combustor matching by [37]. Since this value might not be optimal for the compressor matching with the subsequent non-combustor element, the control of this variable has been left to the optimizer. The parameter bounds have been assumed as shown in Table 5.6.

Table 5.6: LPC exit Mach number design variable and relative bounds

$\mathbf{x}$	$\mathbf{x_l}$	$\mathbf{x_u}$	**Reference**
$M_{4,LPC}$	0.200	0.500	-

5.3.3 Optimization Settings

The Matlab *gamultiobj* default settings has been applied to each engine model, being consistent with the problem formulation and objective of this work. The definition of the initial population number has been performed according to reference [137], which results in an acceptable Pareto optimality for the current problem. Equation 5.2 led to a significantly high number of variables, which almost doubles the computational effort. For this reason, N_p has been calculated according to: $N_p = 10 \cdot N_{var}$. The real number of variables has been augmented by one for the the initial population characterization to ensure a resultant smoother Pareto frontier. A summary of the optimization preliminary settings is given in the table below for each engine model.

Table 5.7: Summary of the optimization initial settings per engine arrangement

	$\mathbf{N_{var}}$	$\mathbf{N_p}$
RC	24	250
ICR	26	270
ERAST	26	270
HPRTE	26	270

5.4 Objective Function Setup

The objective function $\bar{J}(x)$, used in the optimization framework, is composed by two main parts. The first one defines engine design performance and component weights. Component efficiencies and feasibility aspects are also accounted during this phase, using the component modeling techniques discussed in chapter 4. Feasible design data are subsequently employed in the second part of the objective function characterization, where the off-design analysis is performed to calculate the part power SFCs.

A strong coupling between NPSS and the component model is necessary to properly define the objective function for each design vector provided by the optimizer. Therefore, an iterative process has been set up to ensure consistency between the thermodynamic analysis and the component characterizing tools.

This process slightly differs between the different engine arrangements, becoming quite articulated for semi-closed cycles. Therefore, this section has been entirely dedicated to the explanation of the objective function definition. The treatise has been divided according to the cycles considered in this project, showing how the NPSS-Matlab coupling has been made, together with relative assumptions. A final section has been dedicated to the NPSS running method and the repairing algorithm mentioned in section 3.2.3.

5.4.1 Recuperated Cycle

Figure 5.2 summarizes the implementation of the objective function methodology for the recuperated open cycle engine, showing the NPSS integration with the component models. The system optimizer specifies a new design vector (x), which combined with additional flight and cycle data (Table 3.9), allows to perform the first cycle calculation with NPSS. At this stage, compressor and turbine efficiencies have to be assumed. With these inputs, NPSS is run and checked for convergence. If successful, the program outputs the flow station data at the inlet and outlet of each engine component (pressures, temperatures, mass flow, etc.).

These data are then used to size each component. Since the efficiency of the turbomachines changes as function of the different inlet flow conditions, iterations are needed to progressively update the NPSS thermodynamic model, using the efficiency values calculated by the turbomachinery performance model. Throughout these iterations, the components are sized, checked for feasibility and their weight is estimated. Once this phase has been completed, the whole set of design performance data is organized for a final NPSS analysis which defines the desired design and off-design SFC values, allowing for the definition of the objective function $\bar{J}(x)$.

Since flow continuity between engine components is ensured by NPSS, flow consistency between elements has to be maintained to produce a reasonable design performance prediction. This means that the outlet flow station or geometrical data of every component has to be considered in the performance and geometrical characterization of the subsequent component. More details have been provided on compressor, recuperator and combustor matching. The remaining components have been sized using NPSS output data, and checked following the description given in previous chapters and in appendix.

LP-HP Compressors The compressor model requires mainly inlet flow and the design variables of Table 5.5 to build the full model (section 4.2.1). However, since the compressor standard model generates the design for minimum relative inlet mach number, a LPC exit mach number of 0.2 might not be reasonable for the component matching with the HPC. Therefore, the variable $M_{4,LPC}$ has been created to define the inlet flow of the second compressor as consequence of the design choices of the first one. Hence, the calculated efficiency also accounts for the LPC and HPC relative coupling effects.

Recuperator - Burner The annular combustor model necessitates information on the inlet flow area and the inner diameter to perform the sizing procedure (section 4.4.1). Since a detailed geometrical model has not been built for the heat exchanger, no velocity information is available at the recuperator exit to estimate the combustor inlet area. Therefore, the assumption of equal HEX inlet and exit flow area has been used to calculate the recuperator exit velocity from the known inlet velocity. Thus, iteratively obtaining the combustor inlet area. The combustor inlet diameter is calculated assuming a 5% clearance from the shaft outlet diameter.

RIT considerations The calculated RIT from NPSS has to be checked with the user defined *RIT* value (Table 3.9) to account for HEX material limitations. McDonald [7] reports a general guideline for recuperator materials selection. The author indicates that a value of 900°C (1173.15K) is the maximum threshold for high temperature metal alloys, above this value only ceramic material can be employed. Thus, since costs have not been considered in the optimization, this value has been set as maximum admissible RIT for the recuperator. Checks are performed throughout the optimization to ensure that this condition is satisfied for any given design vector. The same limitations are applied to the other cycle models.

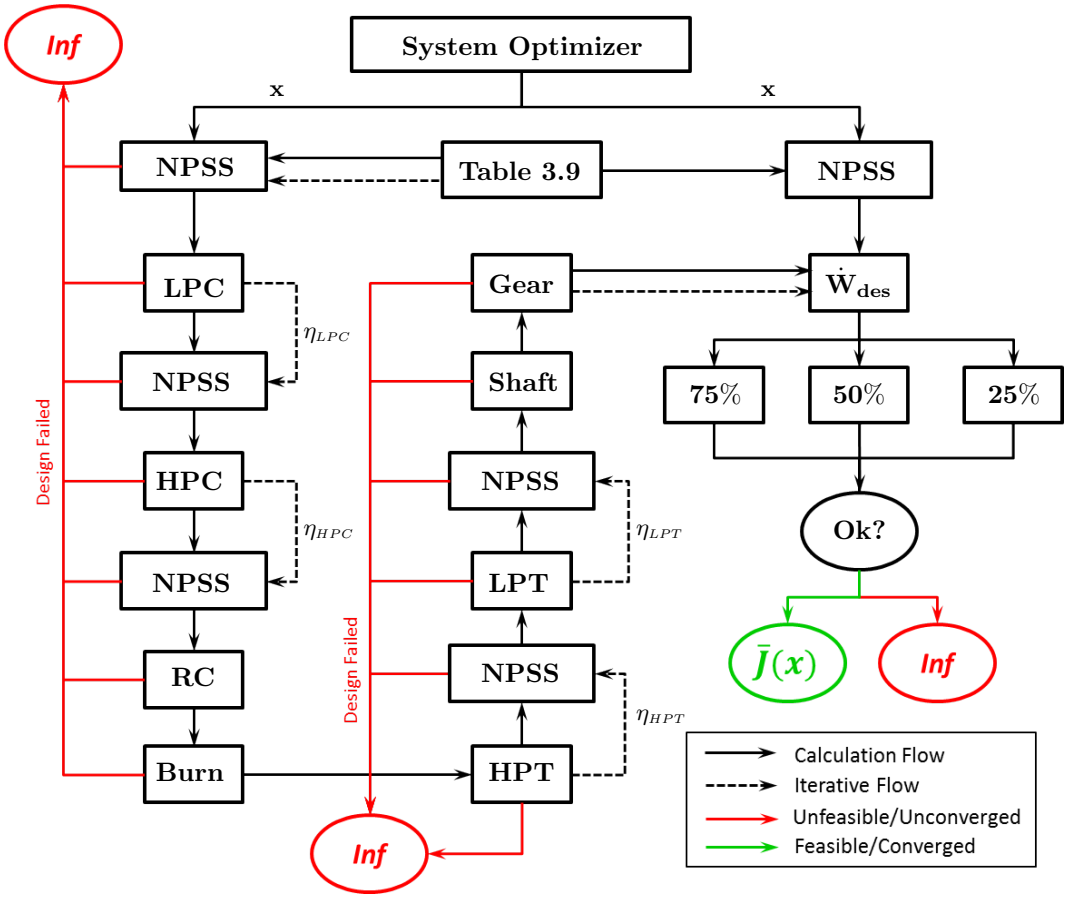

Figure 5.2: RC objective function schematic

Any design vector combination resulting into component infeasibility, inconsistency or NPSS convergence failure, has been sent back to the optimizer with the worst rank possible (Inf). In this way, the optimizer takes into account these aspects in defining the new generation.

5.4.2 Intercooled-Recuperated Cycle

The objective function of the intercooled-recuperated open cycle has been reported in Figure 5.3. The same reasoning applied to the RC case has been used in the engine performance and weight characterization. The introduction of the intercooler adds an additional complication in the component matching between LPC, intercooler and HPC. Once again the LPC exit Mach number variable ($M_{4,LPC}$) has been used to model this interaction.

Intercooler-HPC The intercooler element has been modeled in the same way as the recuperator. A constant inlet and outlet area assumption has been maintained here as well to calculate the flow velocity at the heat exchanger exit, thus determining the HPC inlet flow Mach number for the compressor sizing and efficiency calculations.

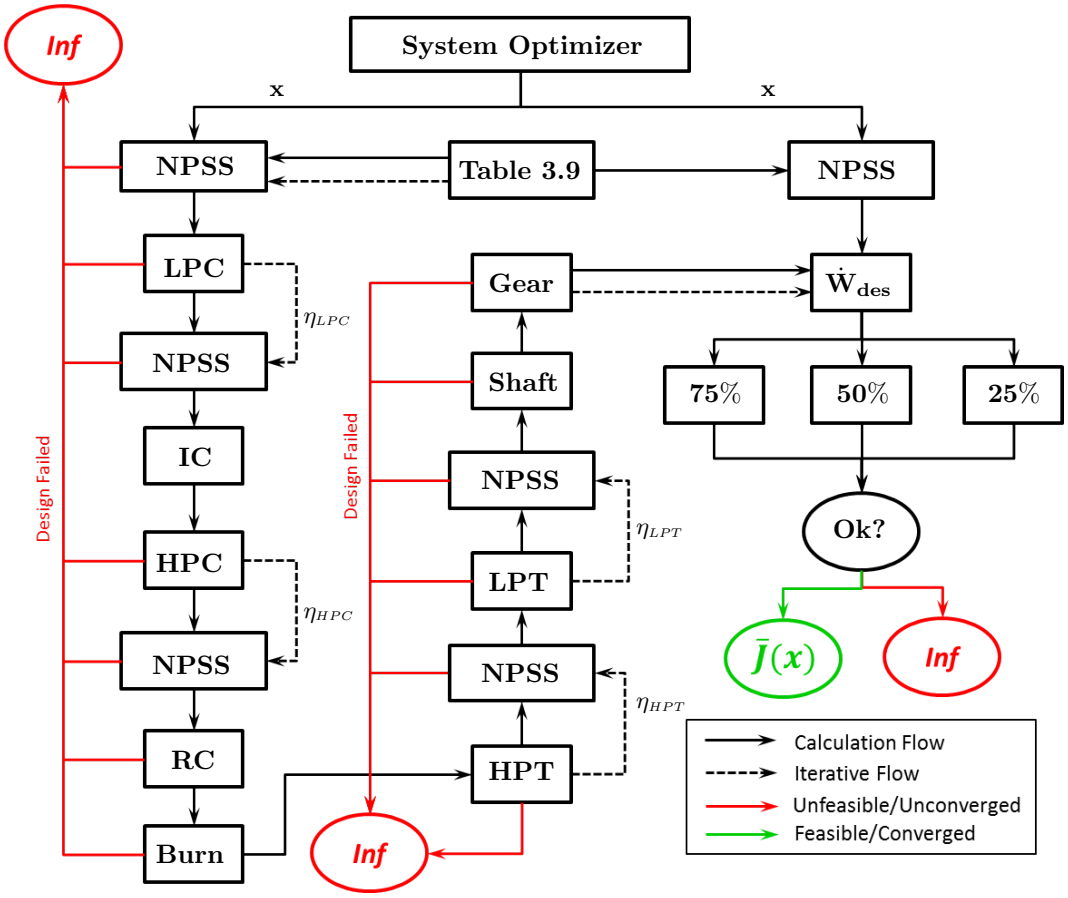

Figure 5.3: ICR objective function schematic

5.4.3 Semi-Closed Cycles

The semi-closed cycle objective function is identical for the ERAST and the HPRTE engine models, since the only differences lay in the NPSS model and solver settings (see section 3.3.2). Figure 5.4 presents the semi-closed cycles objective function setup schematic, similarly to what was done for the open cycle cases. Due to the flow recirculation, each efficiency change to the downstream engine components (HPT), strongly affects the recirculated mass flow, which has a direct impact on HPC efficiency, recuperator heat transfer and combustor dimensions. Therefore further iterations are needed to properly characterize the elements within the feedback loop.

The inner loop iteration has been stopped when the relative error between the HPT power output at the current iteration, calculated by the last NPSS block in the inner loop of Figure

5.4, and the one at the previous iteration is less than a predefined tolerance. This ensures that consistency is respected by the model. Additional difference with respect to the open cycle arrangements is determined by the addition of the mixer element. Consistency has to also be ensured between LPC, mixer, intercooler and HPC. The following paragraph briefly discusses this aspect.

LPC-Mixer As explained in section 3.2.1, the mixer requires the definition of the inlet Mach number of one stream to perform the element sizing. The LPC stream has been chosen in this case and the mixer inlet Mach is defined within the compressor element. Once more, the variable $M_{4,LPC}$ has been used for these components linking. With this information, NPSS sizes the mixer and provides the static quantities at the mixer outlet. Using this additional flow data, the intercooler inlet velocity can be determined. Finally, the heat exchanger and compressor matching has been performed as previously discussed for the ICR case.

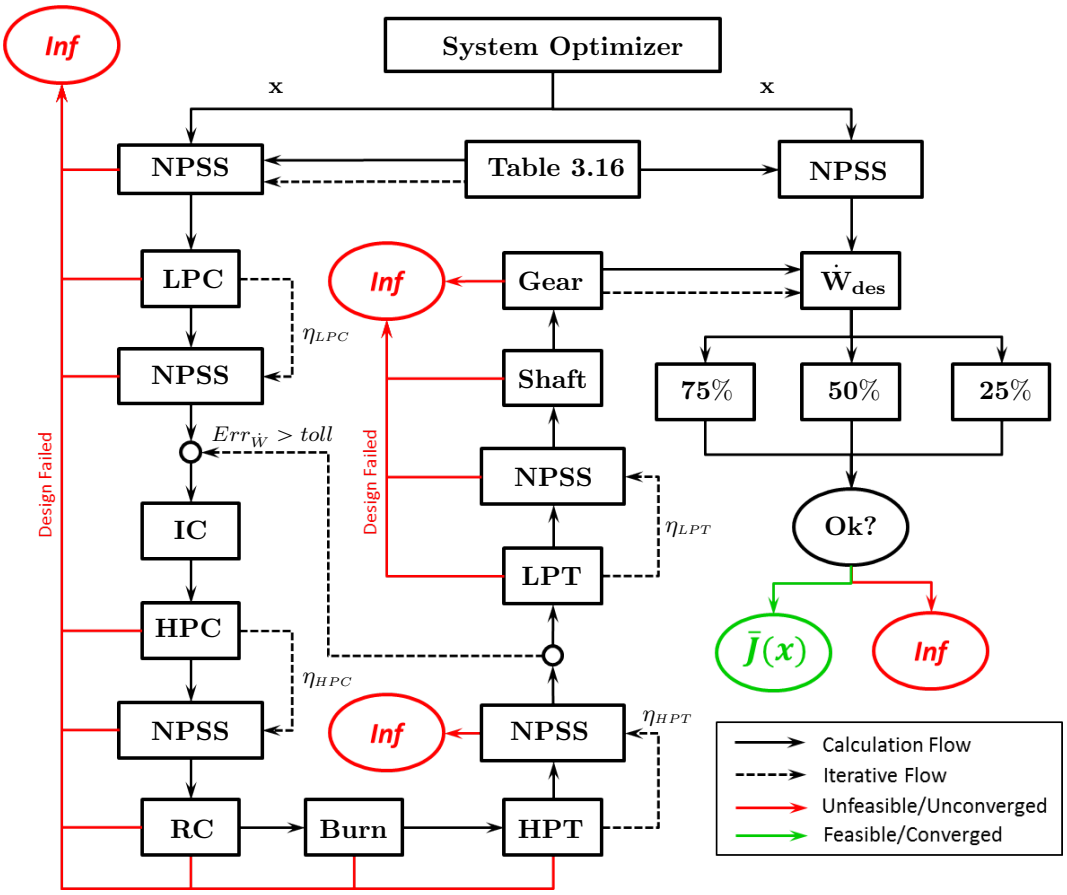

Figure 5.4: ERAST/HPRTE objective function schematic

5.4.4 NPSS Repairing Algorithm

Since NPSS has to be called multiple times during the objective function evaluation, the infinite loop problem discussed in section 3.2.3 is likely to occur throughout the optimization. The selection of good guessing points to start the iterations inside NPSS helps to solve this problem. However, due to the random nature of the algorithm chosen for the optimization, it is extremely difficult to ensure the correct NPSS initialization for every given design vector.

The repairing algorithm has been embedded within every Matlab to NPSS call. For each design vector given by the optimizer, Matlab creates the related NPSS .inp file, adding all the necessary guessing variables, depending on the engine arrangement (see Tables 3.9 and 3.16).

The guessing points have been defined, based on a preliminary cycle study conducted with NPSS, and kept constant throughout the optimization.

Once NPSS has completed the calculations, it outputs a general file that Matlab is able to detect. If the file is not generated within an acceptable time, it means than NPSS is stuck in the infinite loop. Therefore, Matlab terminates the NPSS job and starts to randomly modify the input guessed variables. This operations continues for a certain amount of time until the correct guessing value has been found or the maximum amount of attempts allowed has been reached. In this last event, the design vector is considered not feasible from the optimizer perspective. Thus, only the actual design vectors that lead to unfeasible or unconverged NPSS solutions are actually discarded. While variables that only cause numerical problems are further assessed, leading to a much more consistent optimization.

CHAPTER 6

Results and Conclusions

6.1 Introduction

This chapter discusses the results of the optimization. In particular, the Pareto optimal solutions are presented for the four engine arrangements analyzed, showing the variation of average specific fuel consumption (SFC_{av}) and engine weight (W_{eng}) as function of the design vector. The treatise has been organized with an initial focus on the overall engine results, showing general differences between the semi-closed cycles and the open cycles. Subsequently, the recuperated and the intercooled-recuperated open cycle results are discussed in detail, showing the influence of main thermodynamic variables on the Pareto frontier (sections 6.3.1 and 6.3.2). Similar considerations are then presented for the ERAST (section 6.4.1) and the HPRTE (section 6.4.2) semi-closed cycle engines, displaying similarities and differences in the impact that cycle variables have on the final solution. A final section has been included to summarize the project findings and to suggest future improvements (section 6.5).

6.2 General Considerations

Since only two objectives have been specified in the optimization, the resulting Pareto optimality can be easily visualized onto a single 2D plot, showing the minimum average specific fuel consumption and minimum weight solutions. Figure 6.1 reports the Pareto frontier of the simple recuperated and the intercooled-recuperated gas turbine, while Figure 6.2 shows the Pareto frontier of the ERAST and the HPRTE semi-closed cycle models respectively.

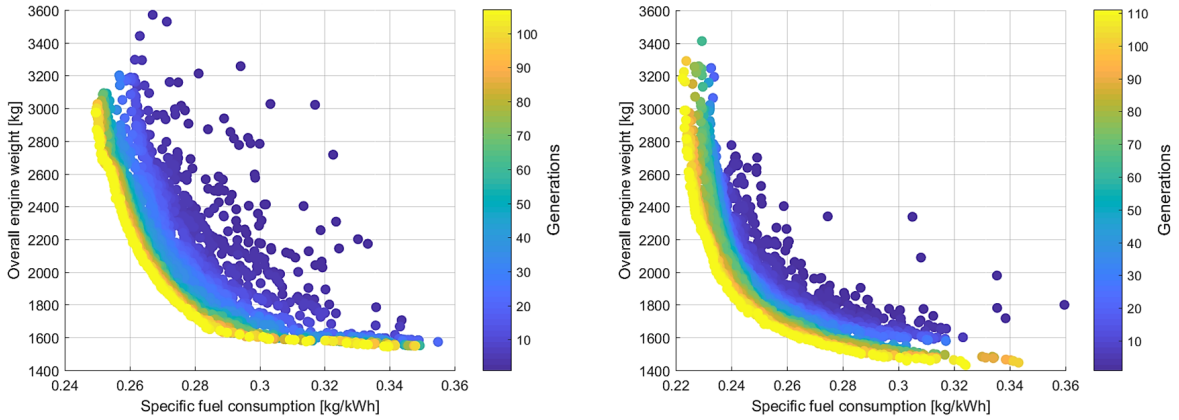

(a) Simple recuperated engine

(b) Intercooled-recuperated engine

Figure 6.1: Open cycles Pareto optimality solutions

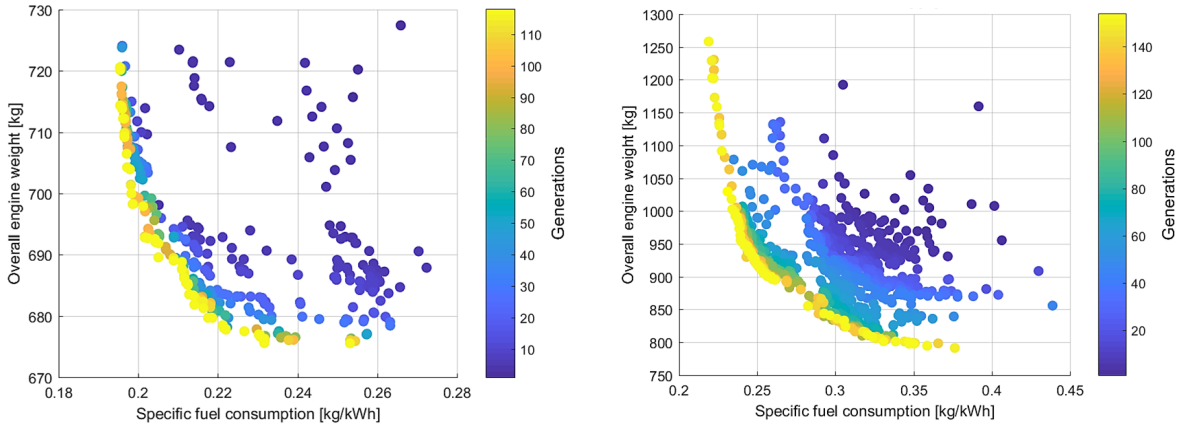

(a) ERAST intercooled-recuperated engine

(b) HPRTE intercooled-recuperated engine

Figure 6.2: Semi-closed cycles Pareto optimality solutions

Although a far more difficult Pareto optimality convergence has been observed with the semi-closed cycle models, some of the advantages outlined in section 2.2.2 can be appreciated from the presented figures, in particular regarding engine compactness and efficiency. These aspects are briefly treated in the following paragraphs. A detailed explanation of the optimization results is reported in the following sections for each engine, giving further evidence to some of the concepts discussed here as well.

Weight Discussion

Open Cycles Figure 6.1 shows that for the same power output and SFC_{av}, the calculated recuperated engine weight is compatible with the intercooled-recuperated one. As will be explained in the following sections, thanks to the intercooler presence, a relatively higher overall pressure ratio (OPR) can be achieved in the ICR engine with respect to the RC model.

A higher OPR implies a significant reduction of the mass flow required to produce the same design power output, improving the engine specific power and, consequently, reducing the overall turbomachinery size and weight. Similarly, the weight of the remaining components is decreased, resulting in a significant engine size reduction which offsets the weight added by the intercooler in the ICR configuration.

Semi-Closed Cycles The semi-closed cycle architectures lead to a much more compact engine solution with respect to the open cycles analyzed. In fact, Figure 6.2 shows that for the same average specific fuel consumption, an overall weight reduction of more than half of the equivalent RC or ICR configurations can be achieved with the employment of the ERAST or the HPRTE engine architectures.

This weight reduction is mostly attributed to the reduced inlet mass flow requirements for producing the same engine power output in semi-closed cycle configurations. This leads to a significant reduction of the overall turbomachinery weight, thus increasing the overall machine compactness. Furthermore, as will be presented later on, the semi-closed cycles exhibits their optimum solutions at much higher overall pressure ratios, which contributes to reduce the recuperator weight (equation 2.33).

A further weight reduction is experienced in the remaining engine components, although their impact on the overall engine weight is far less important than the heat exchanger and the turbomachinery contributions. However, since a considerable amount of flow is recirculated within the engine, the intercooler weight remains the most significant aspect, even for semi-closed cycle solutions.

The weight difference between the ERAST and the HPRTE semi-closed cycles is in part due to the different feedback flow splitter position (Figures 2.3 and 2.4). Since a smaller mass flow enters the recuperator hot side in the ERAST model, a further reduction of the overall heat exchanger weight is registered. Moreover, in the HPRTE solution, because the whole mass flow is used in the recuperator, a smaller enthalpy jump is possible throughout the LPT. Therefore, the remaining power demand has to be accomplished by the HPT, increasing significantly the size of this last.

SFC Discussion

As expected, the recuperated open cycle arrangement leads to the greatest values of average specific fuel consumption. The addiction of the intercooler only improves the engine performance a little with respect to the recuperated open cycle solution, leading to lower SFC_{av} values in the Pareto frontier. However, no significant amelioration is noticeable in the optimized SFC_{av} values between the semi-closed cycles and the ICR configuration, although slightly lower SFC solutions have been found for the ERAST Coleman engine.

These differences in terms of average specific fuel consumption behavior between the ERAST and the HPRTE engines can be attributed to the dissimilar feedback flow splitting point. In fact, because in the ERAST model more power can be extracted from the LPT, the optimizer balances the engines such that the maximum temperature difference between recuperator hot and cold side is achieved, reducing the amount of fuel necessary to reach the same TIT.

In the HPRTE arrangement, the optimizer tries the same approach. However, since the whole flow passes through the heat exchanger for the same power output, the recuperator hot side exit temperature cannot be too low, otherwise no sufficient power can be extracted from the LPT. Because the LPC and the HPT pressure ratios are constrained by the mixer, which imposes the equal total pressure conditions on each flow side, the optimizer has to limit the maximum recuperator effectiveness for a given OPR to meet the engine power demand.

For these reasons, a slightly greater inlet mass flow is necessary for the HPRTE configuration to function with respect to the ERAST engine. As almost the same total mass flow is needed for the ERAST and the HPRTE models to produce same design shaft power, a lower feedback flow ratio is observed in the HPRTE engine configuration. Since NPSS considers that only the inlet fresh air participates to the combustion process, a higher fuel flow is consequently necessary in the HPRTE configuration for the same equivalence ratio. Thus leading to a slight increase in SFC_{av}.

Part Power Behavior Reference [10] has shown a much flatter SFC curve for the HPRTE engine configuration during part power operating conditions (Figure 2.6). This aspect has been investigated here as well, assessing eventual differences between the off-design performance of the two semi-closed cycle engines and the open cycle ones.

Figure 6.3 shows the part power behavior of the four gas turbine arrangements analyzed in this project. The chart has been obtained by selecting a common SFC_{av} point ($\sim$0.253 kg/kWh) from the final Pareto frontier of each engine and plotting the resultant SFC individual terms at 100%, 75%, 50% and 25% of the design power output. The SFC data have been normalized with respect to the design SFC value to make them more independent from the engine thermodynamic optimum.

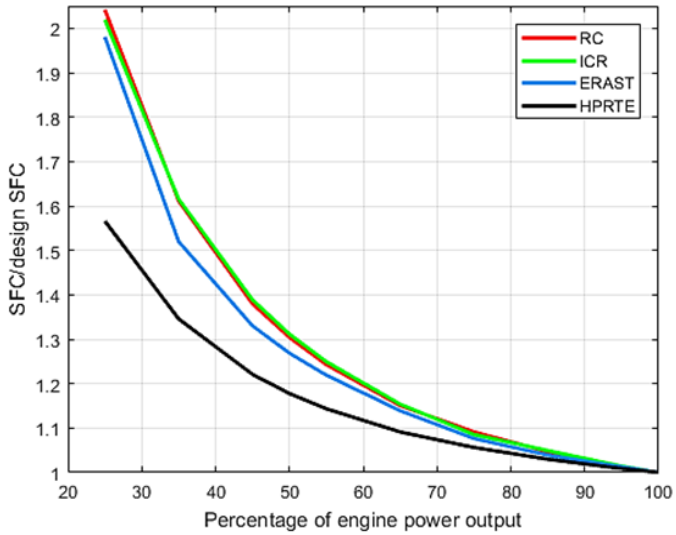

Figure 6.3: Part-power specific fuel consumption comparison

A much flatter off-design SFC curve can be observed for the HPRTE semi-closed cycle arrangement with respect to the conventional open cycles. Slightly improved part power performance can be achieved with the ERAST Coleman engine as well, even though, no significant difference can be appreciated with respect to the open cycles at low output power demand.

The explanation given in reference [10] for the HPRTE part power characteristics has been confirmed by the NPSS output data. In particular, the high pressure recirculation loop allows the HP cycle components to operate around their maximum efficiency point for far larger power ranges than for the open cycles. The strong off-design performance differences with respect to the ERAST can be completely attributed to the dissimilar feedback flow ratio splitting point. In fact, since a far greater recirculated mass flow processed by the recuperator, the heat transfer between the hot and cold side streams in the HPRTE engine becomes almost double that of the ERAST one at really low engine power demand.

As discussed, this aspect becomes a limitation in design, since for the same power output a slightly greater fresh mass flow is needed. However, in off-design the recirculation ratio can be better controlled to ensure a much more effective recuperator heat transfer. Therefore, for the same SFC_{av}, the ERAST configuration shows a lower SFC at high power outputs, while, the HPRTE maintains a relatively flat SFC curve which becomes significantly competitive from approximately 50% of the design power on (Figure 6.3).

6.3 Open Cycle Results

This section discusses the design vector results for the recuperated and intercooled-recuperated open cycle models. Although the influence of the design variables considered here is quite conventional and expected, it is important to provide a detailed explanation for facilitating the understanding of the semi-closed cycle behavior.

In fact, most of the trends observed for open cycle arrangements have been followed by the semi-closed cycles as well. However, since there are no constraints on the LPC and HPT exit pressures, the open cycle components can be optimized considering their pure impact on engine thermodynamics and weight. Therefore, for a given output power, far less trade-offs between individual component performance variables are needed here with respect to the ERAST or the HPRTE configurations.

6.3.1 Recuperated Engine

The optimized recuperated design vector is presented in detail here. Focus is separately given to the thermodynamic and the turbomachinery optimum solutions, showing, where significant, how the design vector modification affects the minimum weight and SFC optimal results. Before moving forward with the explanation of the results, it is important to underline a key aspect of the developed methodology, which is also applicable to every engine model treated within this thesis project.

Because the component model defines the turbomachinery efficiencies from the calculated inlet flow conditions, the optimization procedure is much more sensitive to the effect that a certain design variable has on the overall cycle performance. Hence, the optimized design vectors account for all those performance and feasibility aspects discussed so far in this document.

Thermodynamic Optimality

The thermodynamic design variables (Table 5.1) contribution to weight and specific fuel consumption is individually presented in this section. The treatise has been developed by grouping the design variables associated to the main components together into common paragraphs. Therefore, this paragraph has been divided according to turbomachinery, combustor, heat exchangers and additional parameters.

The first discusses the influence of compressor pressure ratios and rotational speed onto the design objectives. The second explains the influence of the turbine inlet temperature, while, the third one reports the impact of recuperator effectiveness and pressure losses. Finally, the last group presents the effects of nozzle pressure ratio and turbine power split on the cycle optimality. A similar approach has been kept for the remaining engine models.

Turbomachinery Figure 6.4 presents the effects of overall pressure ratio and rotational speed onto the resultant RC engine Pareto frontier, by means of a four variables 2D scatter plot. Where, the OPR influence on weight and specific fuel consumption are identified by the color scale, while, the rotational speed effects throughout the different size of the plotted bubble.

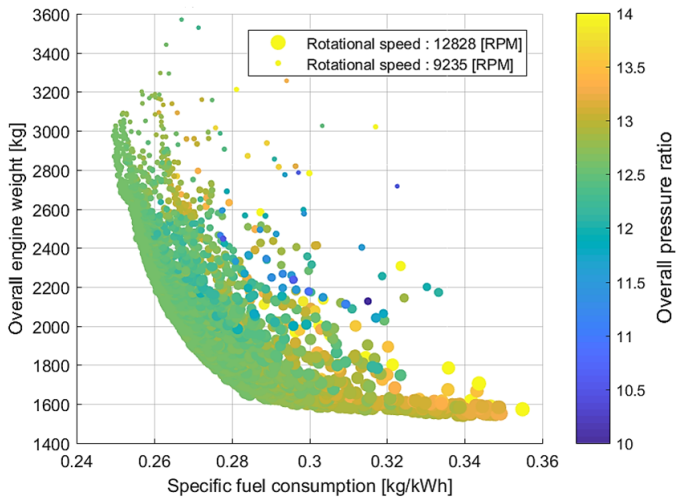

Figure 6.4: Effects of pressure ratio and rotational speed on the RC Pareto frontier

Approximately the same overall pressure ratio is optimal for both optimization objectives, with an almost equal split between low and high pressure compressors (about 3.0 for the LPC and 4.0 for the HPC). Since an increase in OPR corresponds to a reduction of the inlet mass flow required for the same power output, the optimizer tries to maximize this parameter to reduce the overall engine weight and the improve the thermal effciency. However, because of the

recuperator presence, the maximum OPR has to be limited to avoid offsetting the heat exchanger performance. For this reason, a slightly higher OPR is visible in Figure 6.4 for minimum weight solutions.

On the other hand, increasing the turbomachinery rotational speed has a quite significant effect on the relative size of these components. Hence, a clear trend towards higher N for minimum weight solutions is visible from the figure. On the contrary, reducing the size of the rotating components too much causes a considerable drop in their efficiency, since secondary and shock losses become important. As a consequence, the same overall pressure ratio is achieved with a slightly bigger turbomachinery section, which ensures that the maximum compressor and turbine efficiency is obtained for the given inlet flow conditions.

Combustor A high turbine inlet temperature is beneficial for the minimization of both objectives, because it contributes to reduce the inlet mass flow requirements, improving the engine thermal efficiency and specific power. However, the maximum turbine inlet temperature is limited by the technological level of turbines, combustor and recuperator. In particular, the limiting condition set on the RIT, prevents the optimizer to push the TIT close to the upper bound defined in Table 5.1, levelling the TIT to approximately 1520K. These observations are summarized by Figure 6.5.

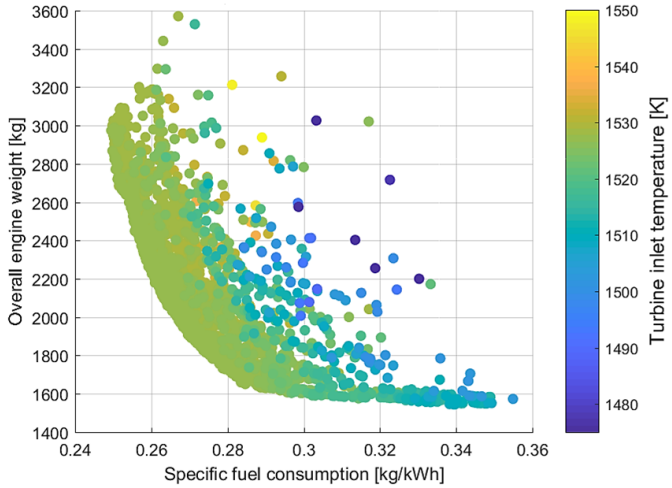

Figure 6.5: Effects of turbine inlet temperature on the RC Pareto frontier

Heat Exchangers Figure 6.6 (a) shows the effect of recuperator effectiveness and total pressure losses on the objective function, with these lasts given as the sum of recuperator hot and cold side contributions. As expected, a clear trend towards high effectiveness and minimal pressure drops belongs to minimum SFC solutions. On the other hand, ε_{RC} and $(\Delta P/P)_{RC,c}$ have a strong impact on the recuperator volume and weight (equation (2.3)), hence, the opposite trend is evident for minimum weight solutions.

Figure 6.6 (b) similarly shows the impact of hot and cold side pressure losses on the optimized solutions, displaying more clearly what was just discussed. By looking at the NPSS optimized raw data, it becomes more evident that minimum SFC solutions admit the lowest pressure losses on the hot side, vice versa for the minimum weight case. This is in agreement to what presented in [62], since the recuperator hot side has a much stronger impact on the overall engine performance. This effect becomes less significant at high effectiveness solutions, as exemplified also by the output data.

The bounds set on the recuperator design variables are not entirely reached during the optimization, as a consequence of the complex component model created. In fact, the optimizer weighs the advantages that a further improvement in effectiveness or pressure losses causes on

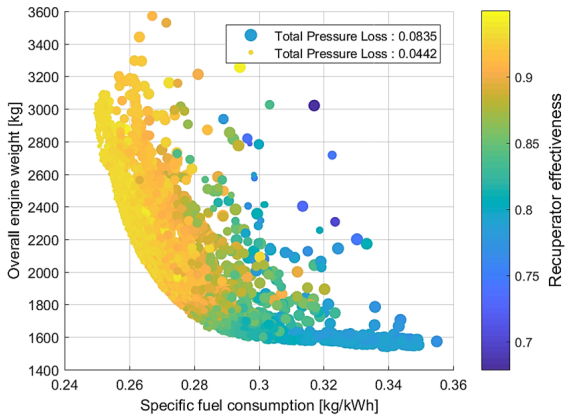

(a) Effectiveness and total pressure loss

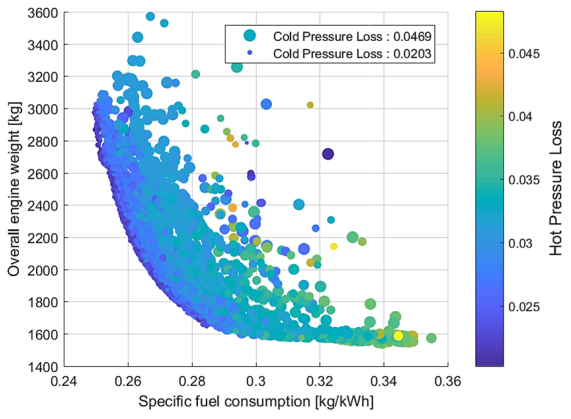

(b) Hot and cold side pressure loss

Figure 6.6: Effect of recuperator performance parameters on the RC Pareto frontier

performance and size of the remaining components. For example, the maximum turbomachinery efficiency significantly depends on inlet flow conditions and mass flow rate. Hence, the optimizer has a much stronger consideration on component mutual effects when performing the analysis and selecting optimal thermodynamic values.

Additional Parameters The effects of turbine power split and nozzle pressure ratio on SFC_{av} and W_{eng} are documented in Figure 6.7 (a). The turbine power split is established such that most of the power is extracted from the HPT, which allows for the greatest enthalpy jump. However, the optimal HPT exit total pressure is set to avoid levelling off the effect of the recuperator, allowing for a sufficient hot to cold side temperature difference to ensure an acceptable heat transfer.

The nozzle pressure ratio (Figure 6.7 (b)) has a direct impact on the overall mass flow required by the engine, thus, a reduction of this variable becomes beneficial for both objectives. Since at part power conditions Π_{Noz} is dramatically reduced with the engine mass flow, the optimizer sets the nozzle design pressure ratio to ensure that a feasible off-design performance is achieved. Hence, a slightly higher value is observed for minimum weight solutions to ensure that Π_{Noz} remains above unity at low power settings.

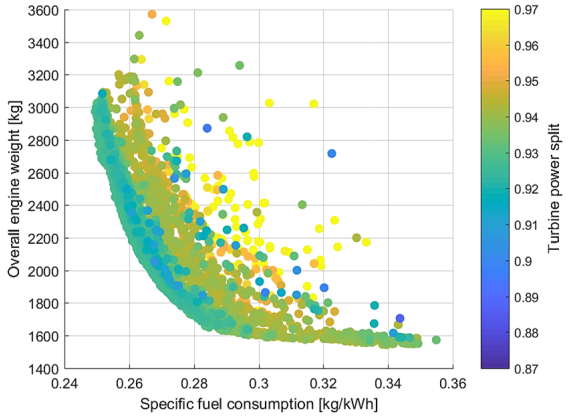

(a) Effects of turbine power split

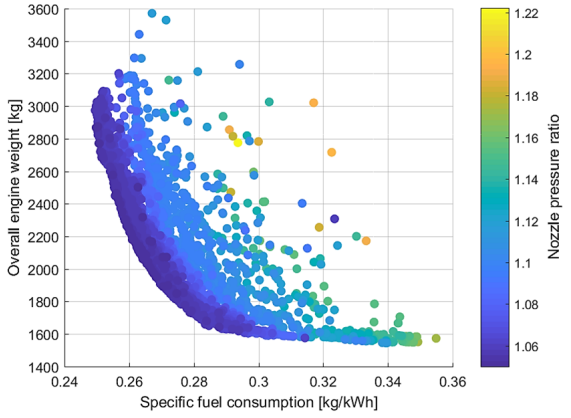

(b) Effects nozzle pressure ratio

Figure 6.7: Effects of turbine and nozzle parameters on the RC Pareto frontier

Turbomachinery Optimal Solutions

As previously discussed, the shaft rotational speed has a strong impact on the relative size of the turbomachinery block and, consequently on its efficiency. However, having high compressor and turbine efficiencies positively affects both optimization objectives, since a reduced power demand is needed across the rotating components for the same engine settings.

Therefore, the optimizer modifies the turbomachinery design vector (Tables 5.4 and 5.5) to maximize the component efficiency for given inlet flow conditions. In addition, the component feasibility is guaranteed during the optimization throughout the proper definition of these turbomachinery design characteristics.

Compressors Tables 6.1 and 6.2 summarize the LPC and HPC design vectors for the minimum average specific fuel consumption and minimum weight respectively. No significant differences can be detected between the LP and HP compressor solutions for the two optimization objectives.

Table 6.1: Compressors design vector for minimum average SFC (RC engine)

	$\boldsymbol{\nu}$	$\boldsymbol{\alpha_2}$	$\boldsymbol{\beta_2}$	$\boldsymbol{2\theta_c}$	$\boldsymbol{\eta_s}$
LPC	0.387	61.753	-21.790	8.477	0.767
HPC	0.411	65.589	-7.592	8.225	0.773

Table 6.2: Compressors design vector for minimum weight (RC engine)

	$\boldsymbol{\nu}$	$\boldsymbol{\alpha_2}$	$\boldsymbol{\beta_2}$	$\boldsymbol{2\theta_c}$	$\boldsymbol{\eta_s}$
LPC	0.378	62.059	-26.530	8.169	0.717
HPC	0.434	64.967	-8.722	8.108	0.770

Since a reduction of the hub to tip radius ratio diminishes the inlet absolute Mach number, improving the compressor efficiency [143], ν assumes the lowest value possible for the given inlet mass flow. A slightly higher value can be observed from Tables 6.1 and 6.2 for the HPC case, as a consequence of different inlet flow conditions.

The combination α_2 and β_2 is opportunely set to ensure minimal losses in the impeller channels with an acceptable diffusion ratio. Differences between the LPC and HPC results are due to the significant density change at the inlet of the two components. Since a much higher θ-parameter (equation A.11) results for the LPC, a relatively high impeller tip to exit radius ratio (equation A.19) is expected. For this reason, a far greater diffusion ratio is registered in the LPC, which forces the optimizer to reduce α_2 and increase β_2 (Figure A.13).

On the other hand, the augmented density at the HPC inlet is such to define α_2 closer to the optimal value suggested in references [26, 41]. β_2 is consequently adjusted to allow for good diffusion ratio and reduced blade stresses. Finally, θ_c is similarly set to ensure good diffusion in the compressor vaned section and to produce an acceptable vane loading.

A LPC/HPC matching Mach number of 0.3504 and 0.3394 has been calculated for minimum SFC_{av} and W_{eng} respectively.

Turbines Tables 6.3 and 6.4 provide the HPT and LPT optimized variables for the minimum SFC_{av} and W_{eng} respectively. The radius ratio is selected to provide the turbine rotor with the correct inlet Mach number and mass flow for the given inlet flow conditions. Similarly, ν is defined from considerations on mass flow and efficiency. A lower value is registered for minimum SFC solutions, since it improves the overall turbine efficiency [143]. The calculated β_{3s} are in agreement with the data reported in Figure B.5 and with the theory reported in references [41, 46].

Table 6.3: Turbines design vector for minimum average SFC (RC engine)

	$\mathbf{r_0/r_1}$	$\boldsymbol{\nu}$	$\boldsymbol{\beta_{3s}}$	$\boldsymbol{\eta_S}$
HPT	1.282	0.377	-59.981	0.889
LPT	1.375	0.361	-60.598	0.807

Table 6.4: Turbines design vector for minimum weight (RC engine)

	$\mathbf{r_0/r_1}$	$\boldsymbol{\nu}$	$\boldsymbol{\beta_{3s}}$	$\boldsymbol{\eta_S}$
HPT	1.373	0.411	-59.872	0.883
LPT	1.439	0.592	-61.869	0.688

As shown in Table 6.4, the LPT efficiency drops sharply for the minimum weight solution, in agreement with the radial turbine theory presented in appendix A.2. In fact, since a relatively high mass flow is needed to compensate for the reduced recuperator performance, and a higher rotational speed is used to decrease the turbomachinery weight, far more significant exit losses occur in the LPT.

As further proof, the calculated turbine specific speed (n_s) at the minimum weight solution is about 1.3, which is close to the limit of applicability for radial turbines [41]. The resultant η_S value is in agreement with the observations made in reference [47] (see Figure A.7). Considering the given n_s value, an improvement in performance for minimum weight solutions could be expected with the employment of axial or even mixed flow turbines, although their impact on weight has to be verified.

6.3.2 Intercooled-Recuperated Engine

The addition of the intercooler significantly improves the minimum average specific fuel consumption with respect to the recuperated open cycle. Moreover, the intercooler reduces the amount of work required by the compressors to produce a certain pressure ratio for the same output power. This can be directly translated into the possibility of considerably increasing the cycle OPR, allowing for a reduction of the engine mass flow with positive effects on turbomachinery and recuperator sizes. For this reason, the overall engine weight becomes comparable with the recuperated engine case for the same specific fuel consumption, in spite of the intercooler presence.

This section presents the thermodynamic and turbomachinery optimized design vector for the intercooled-recuperated cycle. Considerations made on the simple recuperated results can be extended here for some of the components. Hence, a detailed description is presented for those aspects that strongly differ from the previous case. As obvious, many more similarities with the semi-closed cycles behavior can be expected for this engine model.

Thermodynamic Optimality

The thermodynamic design vector reported in Table 5.2 is hereby presented, dividing the treatise according to turbomachinery, combustor, heat exchanges and additional parameters, as previously done.

Turbomachinery Figure 6.8 (a) reports the Pareto optimality considering the effects of overall pressure ratio and rotational speed onto the cycle optimal solutions. What was briefly summarized in the introduction of this section is proven here by the output data. The intercooler allows for a significantly greater overall cycle pressure ratio with respect to the RC case, which

improves the minimum average specific fuel consumption. For these solutions, the optimal pressure ratio split between LPC and HPC lays between 3.0 and 5.2 respectively (Figure 6.8 (b)), for a total pressure ratio of about 15.6, with respect to 12.0 of the RC design case.

Differently, the minimum weight behavior is much more similar to the simple recuperated case in terms of OPR and pressure split between compressors. This is understandable since most of the weight reduction is obtained through a decrease of the heat exchangers effectiveness (Figures 6.10 and 6.11). Hence, the intercooler influence on the cycle thermodynamics is strongly reduced, causing the engine to behave more similarly to the RC model (Figures 6.4 and 6.8 (a)).

The effects of rotational speed on both optimization objectives are well in line with what was observed for the previous engine example, as proven from the reported figures.

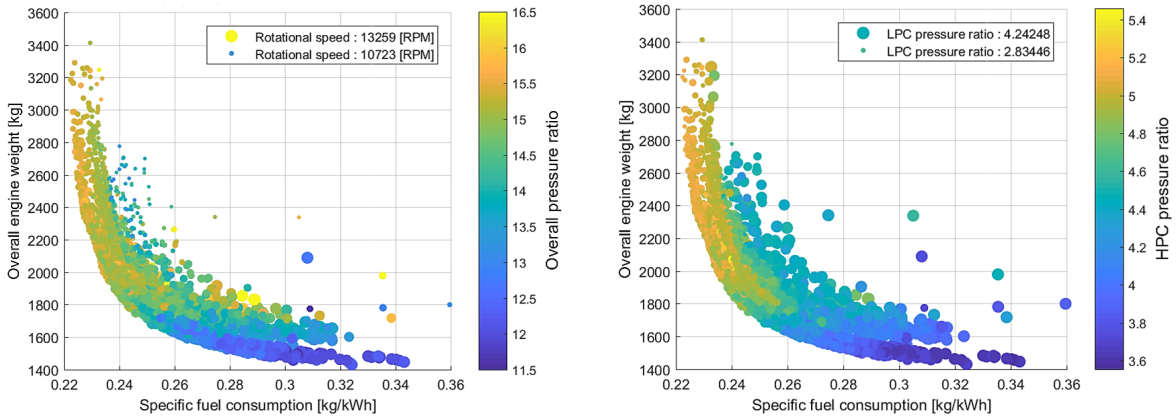

(a) Effects of OPR and rotational speed

(b) Effects of compressors pressure split

Figure 6.8: Effects of turbomachinery variables on the ICR Pareto optimality

Combustor A slightly higher TIT is achieved by the intercooled-recuperated open cycle for minimum SFC solutions. In fact, because of the higher overall pressure ratio, the optimizer balances the engine such that more power is extracted from the HPT, obtaining a turbine exit temperature that does not compromise the recuperator structural integrity. In this way, the TIT can be slightly increased to around 1570K, which significantly improves the cycle thermal efficiency. However, for low weight solutions, since the OPR is reduced to a value comparable to the simple recuperated analysis, such a high TIT can no longer be reached, fixing the engine at around 1540K.

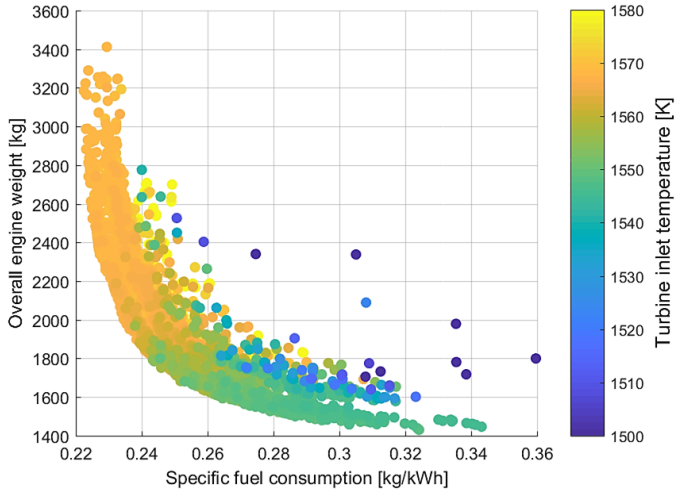

Figure 6.9: Effects of turbine inlet temperature on the ICR Pareto frontier

Heat Exchangers The intercooler effectiveness and hot side pressure loss contribution onto minimum SFC_{av} and W_{eng} is summarized in Figure 6.10. As expected, high effectiveness and low pressure loss characteristics belong to high thermal efficiency cycle solutions, while the other way around is found for minimum weight optimal points.

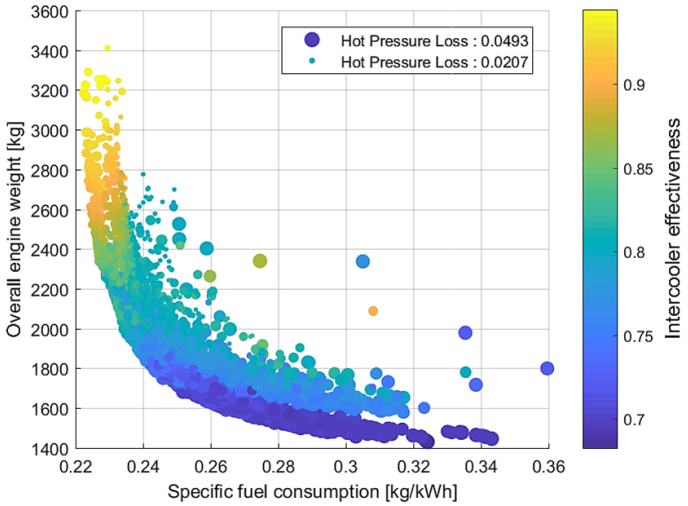

Figure 6.10: Effects of the intercooler parameters on the ICR Pareto frontier

The recuperator effects on the cycle thermodynamics are equivalent to what was presented for the simple recuperated engine. Figure 6.11 summarizes the recuperator results for the ICR configuration. The considerations reported in reference [62] regarding the recuperator optimal hot and cold side pressure losses have been verified for the ICR case as well. Higher thermal efficiency solutions have the greatest pressure loss located at the heat exchanger cold stream.

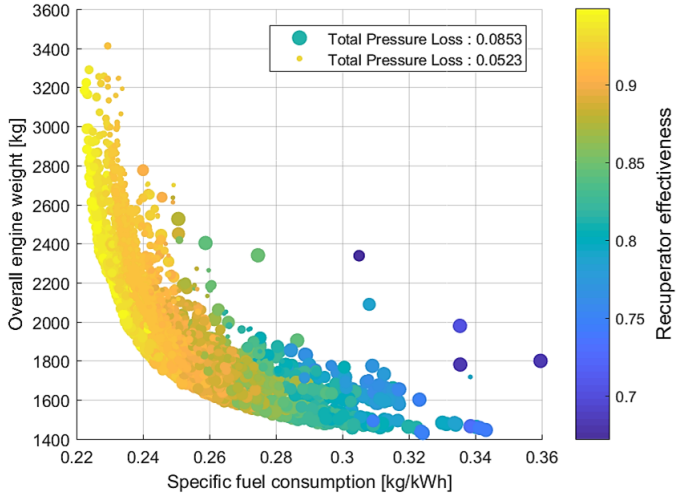

Figure 6.11: Effects of the recuperator effectiveness and total pressure on the ICR Pareto frontier

Additional Parameters The optimized turbine power split is similar to the simple recuperated engine. Both objectives are minimized for a power split which ensures that most of the power extraction occurs in the HPT turbine. The HPT exit pressure is controlled to guarantee that the RIT maximum value condition is respected and that a satisfactory heat transfer is achieved in the recuperator channels (Figure 6.12 (a)).

The nozzle pressure ratio is kept as small as possible to limit the amount of engine mass flow rate required, ensuring that a sufficient part power nozzle performance behavior is achieved.

Similar to the RC model, a higher nozzle pressure ratio has been found for minimum weight optimal solutions (Figure 6.12 (b)).

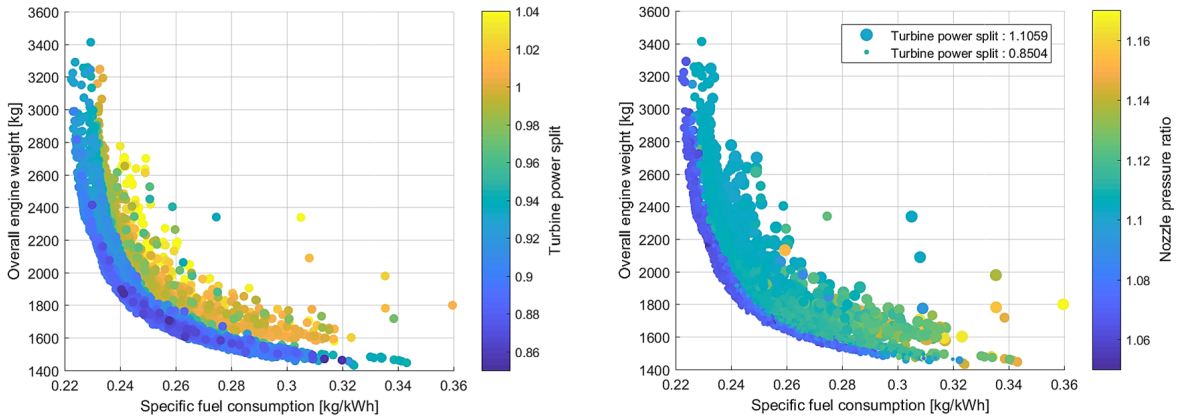

(a) Effects of turbine power split

(b) Effects nozzle pressure ratio

Figure 6.12: Effects of turbine and nozzle parameters on the ICR Pareto frontier

Turbomachinery Optimal Solutions

The turbomachinery optimal solutions for minimum weight and SFC are presented in this paragraph. The optimization philosophy applied to the RC engine turbomachinery variables remains unaltered for the ICR configuration. The design vector is still modified with the objective of maximizing the efficiency for the given flow conditions. However, the influence of the intercooler is visible in the relative variation that the optimal compressor and turbine design vector assumes in comparison with the simple recuperated gas turbine.

In fact, because of the intercooler presence, the thermodynamic cycle finds its optimum at greater overall pressure ratios than in the simple recuperated case for the same engine power output. Although this leads to an overall improvement of the cycle performance, generally, the maximum attainable turbomachinery efficiency is slightly penalized due to the relatively higher rotational speed and lower engine mass flow involved. Hence, compressors and turbines constitutional parameters exhibit a different trend in the attempt of improving the component efficiencies. More details are provided below for compressors and turbines.

Compressors Tables 6.5 and 6.6 present the compressor results for minimum SFC and minimum weight solutions respectively. As visible, the optimizer copes with the reduced inlet mass flow by diminishing the ν value to accommodate the given mass flow and improve the overall compressor efficiency [143]. The impeller exit Mach number (M_2) is dropped by rising the magnitude of exit flow and blade angles for both optimization objectives. A slightly higher $2\theta_c$ is finally selected to properly control the vane loading parameter.

Table 6.5: Compressors design vector for minimum average SFC (ICR engine)

	ν	α_2	β_2	$2\theta_c$	η_s
LPC	0.347	63.059	-22.405	8.750	0.763
HPC	0.359	66.924	-12.607	9.372	0.766

Table 6.6: Compressors design vector for minimum weight (ICR engine)

	ν	α_2	β_2	$2\theta_c$	η_s
LPC	0.344	62.193	-25.142	8.328	0.726
HPC	0.389	66.024	-13.491	9.341	0.777

No significant differences have been observed for the LP compressor exit Mach number used to match this component with the intercooler as explained in section 5.4.2. The output optimal values for minimum average specific fuel consumption and weight are: 0.3782 and 0.3343 respectively.

Turbines The turbine design vector results for minimum SFC and weight are reported in Tables 6.7 and 6.8 respectively. Slightly different optimal turbine design parameters can be detected with the corresponding simple recuperated tables to better accommodate the change in mass flow and rotational speed.

Table 6.7: Turbines design vector for minimum average SFC (ICR engine)

	r_0/r_1	ν	β_{3s}	η_s
HPT	1.444	0.437	-58.005	0.881
LPT	1.449	0.340	-56.295	0.779

Table 6.8: Turbines design vector for minimum weight (ICR engine)

	r_0/r_1	ν	β_{3s}	η_s
HPT	1.438	0.314	-56.379	0.886
LPT	1.419	0.415	-56.862	0.739

6.4 Semi-Closed Cycle Results

This section discusses in detail the optimization results for the two semi-closed cycles configurations analyzed in this project, focusing on the effects that the different recirculated flow splitting point has on the optimal design vector. As already anticipated in section 6.2, a significantly better design performance can be obtained with the ERAST engine, while the HPRTE is superior in off-design. Evidence of this aspect will be also given from the different cycle optimization outputs.

Because of the different engine arrangement, a slightly dissimilar optimal behavior is visible for the ERAST and the HPRTE configurations. The typical trends observed in the open cycles for turbomachines and heat exchangers main parameters are also experienced here. However, since the semi-closed cycles operates at far greater OPRs the optimal solutions are far more dependent on trade-off between individual component performance.

6.4.1 ERAST Coleman Engine

The ERAST Coleman engine represents a greater improvement in terms of engine compactness, with respect to any of the other engine architectures considered in this work. Because the feedback flow rate can be opportunely adjusted, the engine inlet fresh air is only sufficient to guarantee that the combustion takes place, thus reducing the turbomachinery impact on weight for the same power output.

Moreover, the combination of intercooler and mixer allows the engine to operate at far greater overall pressure ratios than any conventional open cycle, improving the overall thermal

efficiency and reducing the recuperator size. The intercooler element still constitutes one of the biggest weight sources in the engine, as for the equivalent open cycle. Future design stages have to identify opportune heat exchanger arrangements to cope with this common disadvantage. Nonetheless, this architecture is promising.

Thermodynamic Optimality

The thermodynamic optimality is discussed in this paragraph, which has been organized similarly to the open cycle cases. As mentioned, due to the recirculated nature of the engine, the mutual interaction between component performance parameters and cycle overall behavior is more significant than for the ICR open cycle case. The optimizer finds the optimal balance between the different design variables to ensure the minimization of the objective function.

Turbomachinery Figure 6.13 shows the overall pressure ratio and the rotational speed effects on minimum SFC and weight solutions. As visible, an almost double OPR has been identified by the optimizer as optimal for the semi-closed cycle with respect to the ICR engine output (Figure 6.8). The optimal pressure ratio split between LPC and HPC sees a higher value for the first component (about 5.8 for the LPC and 4.7 for the HPC), for a total pressure ratio of approximately 27.3 for both optimization objectives.

Since a much lower inlet mass flow is used by the LP components, a greater pressure ratio can be obtained by the LPC for almost half of the turbine power required by an open cycle configuration. Moreover, thanks to the intercooler, a quite important pressure rise is also achieved through the HPC, despite the great mass addition in the mixer.

The effects of rotational speed are identical to the previous engines, with the highest RPMs located at minimum SFC solutions. As a consequence of the almost doubled OPR, the shaft rotational speed has to be increased. On the one hand, this contributes to reduce the size of the turbomachinery block considerably, leading to a much more compact gas turbine also for minimum SFC solutions. On the other hand, the compressors and turbines maximum efficiency is lower than the equivalent open cycle components, due to the augmented size effects. Hence, the remaining thermodynamic parameters are modified by the optimizer to account for this turbomachinery deficit as well.

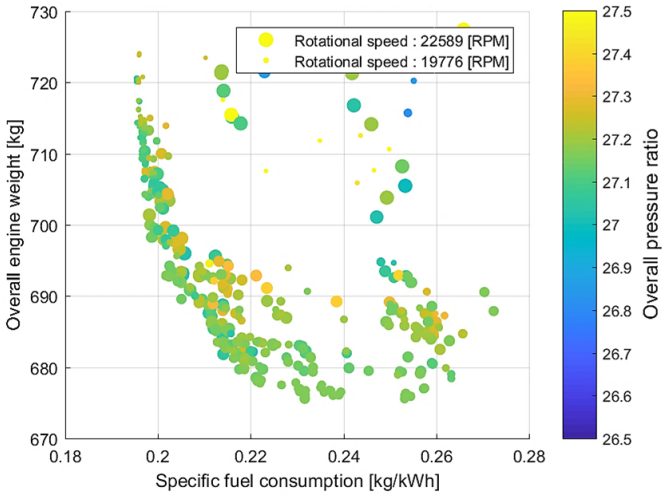

Figure 6.13: Effects of pressure ratio and rotational speed on the ERAST Pareto frontier

Combustor The effect of the turbine inlet temperature on the overall cycle performance is identical to that experienced for conventional open cycle configurations (Figure 6.13). The optimizer maximizes the TIT to improve both engine thermal efficiency and specific power, considering the limitation imposed by the RIT and the turbine materials.

Of a far greater importance is the equivalence ratio parameter (ϕ_{st}), which, as discussed in section 3.3.2, directly influences the design feedback flow ratio. Figure 6.14 shows that minimum SFC solutions correspond to equivalence ratios close to the upper bound, while, a lower ϕ_{st} value leads to a weight reduction.

Increasing the equivalence ratio leads to a reduction of the inlet fresh air necessary to perform the combustion [10], thus, diminishing the fuel required to reach the given TIT. The desired power output is achieved by increasing the engine recirculation ratio, which becomes slightly more than three times the inlet fresh air at the minimum SFC point.

Because an augmented feedback flow rate has a strong impact on the overall turbomachinery weight, ϕ_{st} is reduced to approximately 0.88 for the minimum weight solution, which implies a recirculation ratio of about 2.6. A further lowering of the equivalence ratio is not beneficial, because the weight of the LP components starts to become more significant. Figure 6.14 represents the discussed trend.

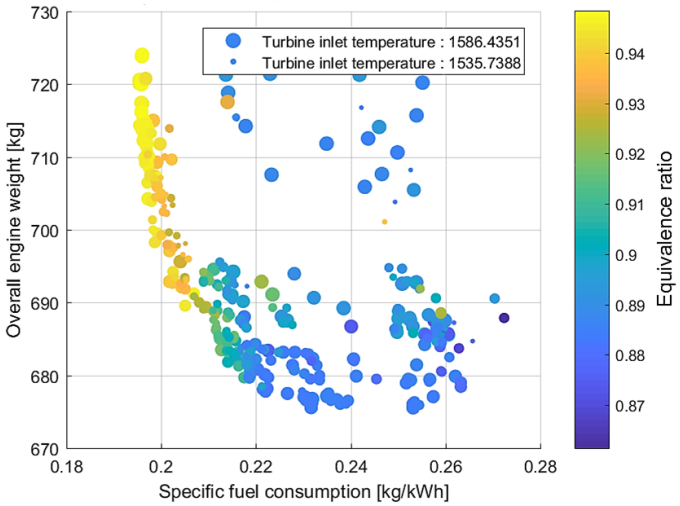

Figure 6.14: Effects of turbine inlet temperature and equivalence ratio on the ERAST Pareto frontier

Heat Exchangers A much stronger interaction between the intercooler/recuperator performance parameters and the cycle thermodynamics has been found in the ERAST engine arrangement more than in any other configuration analyzed. In particular the impact of the intercooler effectiveness is far less significant than in any other configuration, while the recuperator has a much stronger impact on the cycle performance. Similar observations have been derived for minimum SFC as well as minimum weight solutions.

For a fixed design power output and TIT, improving the intercooler effectiveness leads to a reduction of the HPC required power for a given pressure ratio. Because the HPT exit pressure is fixed by the mixer, the power split between the two turbines is consequently constrained, meaning that a higher HPT exit temperature is reached for a higher ε_{IC}. Since the RIT is limited by the mechanical properties of the recuperator, there is a further constraint on the maximum HPT exit temperature.

Few options are available to the optimizer to accommodate this. The LPC-HPC pressure ratio split could be modified for the same OPR, reducing the LPC pressure rise which allows for a greater expansion in the HPT. However, this causes a reduction of the LPT inlet temperature, which implies the need for a greater engine inlet mass flow to accommodate the power demand. Furthermore, as a consequence of the higher HPC pressure ratio the efficiency of the HP components drops sharply, penalizing both SFC and weight.

In addition, the TIT could be slightly reduced to decrease the RIT, with the negative effect of decreasing overall thermal efficiency and specific power. Alternatively, the heat exchanger

effectiveness can be reduced. Because the recuperator has a strong influence on the overall engine performance, the optimizer keeps this value high, also for minimum weight solution (see Figure 6.15). While the intercooler effectiveness is dropped to approximately 0.7. This value was also originally selected for the ERAST Coleman engine model [14].

Because the recuperator is placed in a high pressure loop, this operation becomes beneficial also for minimum weight, and its effectiveness has been only slightly decreased for this last case. From a pressure loss perspective, the semi-closed cycle HEX optimality appears similar to the ICR, where minimum pressure losses are associated to minimum SFC solutions and vice versa.

Anagnostis [12] has observed that the influence of intercooler pressure loss on cycle thermal efficiency is not extremely significant, while the HPC effciency is far more important. A similar outcome has been observed in this project as well, where the impact of the cycle flow stations on turbomachinery performance has been better captured by the detailed component model created. In fact, the optimizer allows for a slightly greater $(\Delta P/P)_h$ in the intercooler with respect to the ICR case, leading to a relatively higher recirculated mass flow rate, which allows for a light improvement of the HPC efficiency.

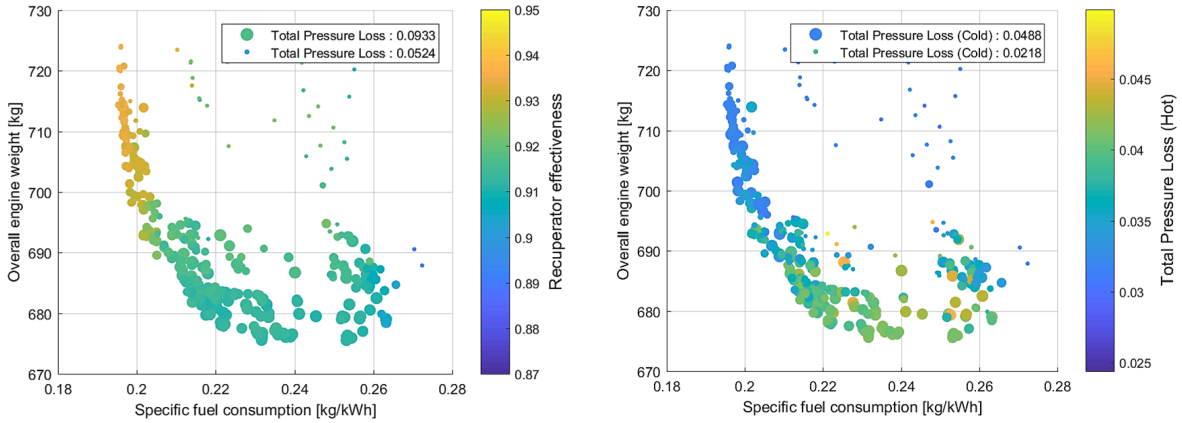

(a) Effectiveness and total pressure loss

(b) Hot and cold side pressure loss

Figure 6.15: Effect of recuperator performance parameters on the ERAST Pareto frontier

Additional Parameters The trend observed for the ICR open cycle gas turbine has been found here for the nozzle pressure ratio variable. A slightly higher Π_{Noz} value has been detected for ERAST engine configuration with respect to the open cycle arrangements. This can be explained by looking at the NPSS optimized raw data. In particular, since the turbomachinery efficiency is highly sensitive to mass flow, a relatively higher nozzle pressure produces a small increment in the whole engine mass flow, which positively affects the rotating component efficiencies. The different nozzle settings for minimum weight solutions are explained in a similar way of the open cycles, looking at the off-design performance. Figure 6.16 summarizes the optimization output data.

Turbomachinery Optimal Solutions

The turbomachinery output data for minimum average specific fuel consumption and weight are provided in this paragraph for the ERAST engine. Although some similarities can be observed with respect to the intercooled-recuperated open cycles, the far greater overall pressure ratios and rotational speed have an impact on compressor and turbine parameters for maximum efficiencies.

In particular, due to the smaller size of the LP compressor and the higher pressure ratios involved, the maximum attainable efficiency is significantly reduced compared to the open cycle architectures. Less important size effects have been observed for the high pressure components, where the addition of the feedback flow makes the efficiency only slightly reduced with respect

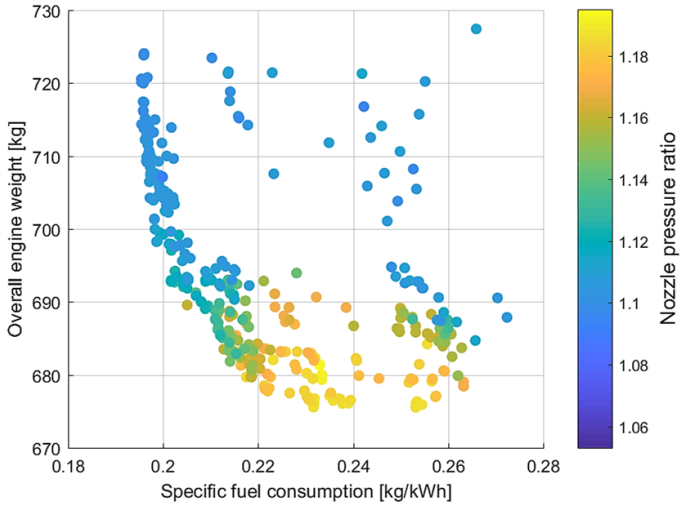

Figure 6.16: Effects of nozzle pressure ratio on the ERAST Pareto frontier

to conventional arrangements. On the other hand, the smaller mass flow employed in the LPT, reduces the turbine exit losses improving the efficiency of this component with respect to the open cycles and proving that radial configuration is a good solution for the semi-closed arrangement.

Compressors Compressor data for minimum SFC and minimum weight are summarized in Tables 6.9 and 6.10. The higher pressure ratio is achieved with a greater impeller flow angle, while the blade angle is used to control the diffusion ratio and ensure the structural integrity of the compressor. The remaining parameters have been set to accommodate the different inlet flow conditions and to limit the vane loading.

Table 6.9: Compressors design vector for minimum average SFC (ERAST engine)

	ν	α_2	β_2	$2\theta_c$	η_s
LPC	0.404	66.765	-12.963	9.448	0.738
HPC	0.347	65.786	-10.804	8.799	0.768

Table 6.10: Compressors design vector for minimum weight (ERAST engine)

	ν	α_2	β_2	$2\theta_c$	η_s
LPC	0.397	66.619	-12.784	8.453	0.733
HPC	0.349	65.918	-10.212	9.566	0.764

A slightly higher LPC/mixer matching Mach number has been found optimal for the ERAST model: 0.4215 for the minimum SFC solutions and 0.4142 for minimum weight.

Turbines Similarly, turbine parameters have been given in Tables 6.11 and 6.12. The slight differences with the open cycles turbines can be entirely attributed to the dissimilar amount of mass flow handled by the HPT and LPT elements.

Table 6.11: Turbines design vector for minimum average SFC (ERAST engine)

	r_0/r_1	ν	β_{3s}	η_s
HPT	1.320	0.452	-56.799	0.872
LPT	1.411	0.494	-60.208	0.849

Table 6.12: Turbines design vector for minimum weight (ERAST engine)

	r_0/r_1	ν	β_{3s}	η_s
HPT	1.367	0.331	-56.534	0.877
LPT	1.419	0.336	-59.732	0.856

6.4.2 HPRTE Engine

The HPRTE semi-closed cycle arrangement shares some of the design features with the ERAST model. However the different feedback flow ratio splitting point position introduces significant differences in the multi-objective optimization outcome of certain variables. As a consequence, the HPRTE engine possesses far better part power performance than any other configuration discussed in this work, as shown in section 6.2. The HPRTE optimized design vector is presented in the following paragraphs, discussing differences and similarities with the ERAST model.

Thermodynamic Optimality

The HPRTE thermodynamic optimality is presented here. The cycle operates at far greater pressure ratios than the conventional intercooled-recuperated open cycle, as for the ERAST case. However, the splitter element located after the heat exchanger offers a better control of the recirculation ratio in part power, leading to superior cycle performance at low engine power demand. Furthermore, the selection of optimal HEX parameters is also much less influenced by the RIT than for the ERAST model.

Turbomachinery The effects of overall pressure ratio and rotational speed are perfectly in agreement with what was displayed for the ERAST engine. A relatively higher OPR has been observed for the HPRTE, with a pressure ratio split of about 6.2 on the LPC and 5.0 on the HPC, for a total OPR of approximately 31.0 for minimum SFC and weight solutions (Figure 6.17).

Because the recuperator operates with the total engine mass flow, the heat transfer across the heat exchanger is far less affected by a higher OPR than in the ERAST model. Hence, the optimizer can further increase the overall pressure ratio, improving the cycle thermal efficiency and specific power.

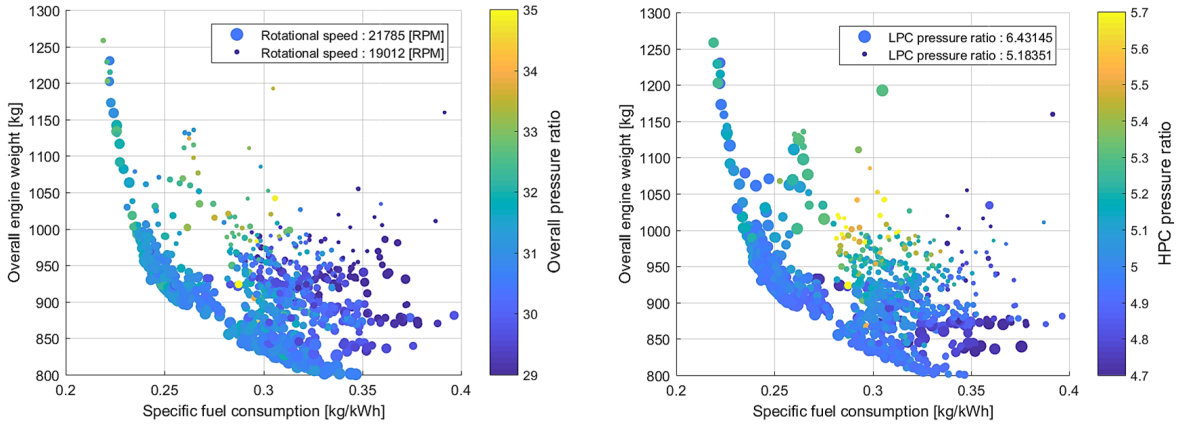

(a) Effects of OPR and rotational speed

(b) Effects of compressor pressure split

Figure 6.17: Effect of turbomachinery variables on the HPRTE Pareto frontier

Combustor The influence of TIT on the optimization objectives is in agreement with the trend observed for the other cycles. The optimizer maximizes the turbine inlet temperature, within

the feasibility range, to improve thermal efficiency and specific power. A value of approximately 1565K has been set by the optimizer for minimum SFC and weight solutions (Figure 6.18 (a)).

The equivalence ratio parameter shows a trend similar to the ERAST model, where a lower ϕ_{st} value has been found optimal to primarily diminish the HP components weight, through the reduction of the recirculated flow rate. While, a higher equivalence ratio has been registered for minimum SFC_{av} solutions (Figure 6.18 (b)).

However, the ERAST engine shows a more stoichiometric combustion for the minimum average specific fuel consumption points than the HPRTE configuration. This is understandable, considering the different recuperator effectiveness behavior discussed in section 6.2. Because the HPRTE has the recuperator hot side exit temperature limited by LPT, more fresh air is needed in the combustor to reach the given TIT.

A smaller design equivalence ratio allows to introduce more fresh air into the engine, reducing the feedback flow ratio for the same output power. Consequently, the optimizer sets the ϕ_{st} design value to about 0.91 for minimum SFC, with respect to the approximately 0.95 of the ERAST engine.

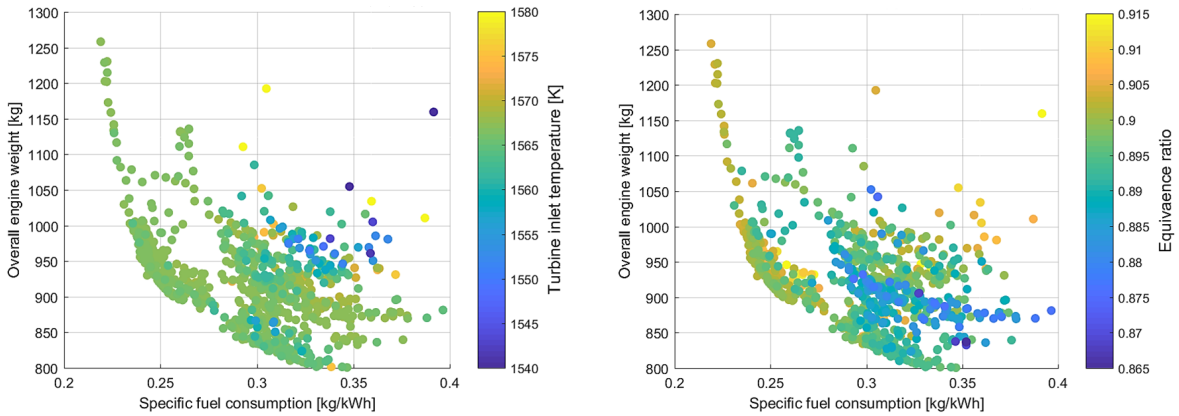

(a) Effects of turbine inlet temperature

(b) Effects of equivalence ratio

Figure 6.18: Effect of combustor variables on the HPRTE Pareto frontier

Heat Exchangers A different heat exchanger optimal behavior has been observed for the HPRTE engine with respect to the ERAST arrangement. The importance of the intercooler is much more significant here, as shown in Figure 6.19. This can be explained by considering different cycle arrangements between HPRTE and ERAST, Figures 2.3 and 2.4 respectively.

In design, the HPRTE recuperator hot side exit temperature is strongly influenced by the LPT performance and power demand. In fact, because the splitter is located after the recuperator (Figure 2.3), the maximum heat transfer across the HEX has to be limited, which results in a mixer core side inlet temperature significantly higher than in the ERAST case.

Therefore, a more effective intercooler becomes essential not only for an improvement in SFC, but also in weight, since it significantly reduces the HPC inlet temperature, thus dropping the compressor power demand. As a consequence, the HPRTE intercooler effectiveness range goes from 0.77, for minimum weight, up to 0.92, for minimum SFC (Figure 6.19).

The intercooler hot side pressure loss behavior is similar to the ERAST engine. The cycle sensitivity to intercooler pressure loss variation is far less significant than for the ICR open cycle, as already observed in [12].

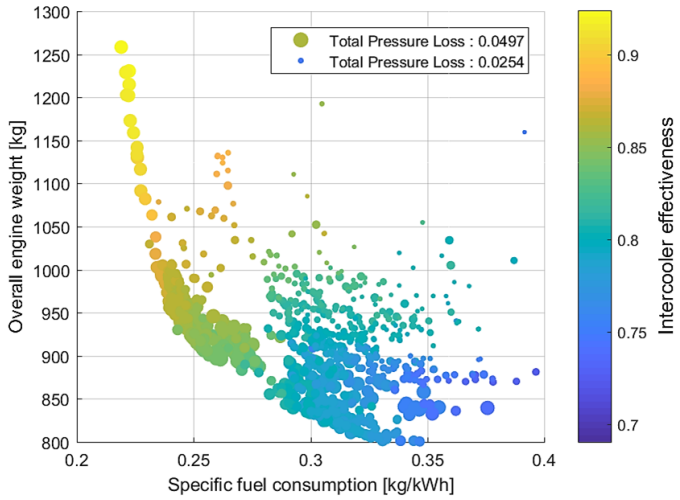

Figure 6.19: Effects of the intercooler parameters on the HPRTE Pareto frontier

The recuperator parameters trend, presented in Figure 6.20, is in agreement with the ERAST output data. A higher effectiveness and low pressure drop is characteristic of minimum SFC solutions and vice versa. As mentioned, the maximum effectiveness achieved by the HPRTE configuration is slightly lower than the ERAST case to accommodate the power demand of the LPT. The greater HEX pressure losses are located at the recuperator cold side, in agreement with previous observations made for the other engines (Figure 6.20 (b)).

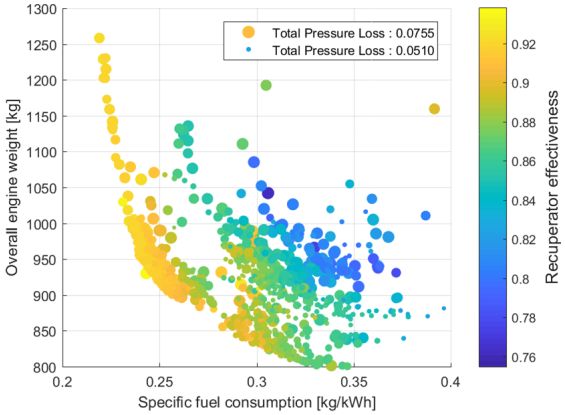

(a) Effectiveness and total pressure loss

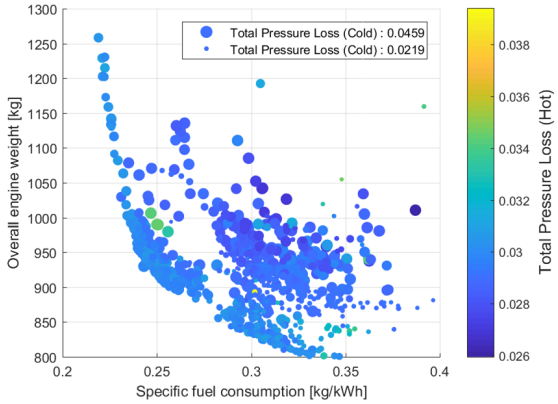

(b) Hot and cold side pressure loss

Figure 6.20: Effect of recuperator performance parameters on the HPRTE Pareto frontier

Additional Parameters The effects of nozzle pressure ratio on the whole cycle performance resemble the observation made for the ERAST engine. A slightly higher design Π_{Noz} value is visible in the NPSS output data with respect to the open cycles, which implies a small improvement in the turbomachinery performance, as stated previously.

Turbomachinery Optimal Solutions

Consideration made for the ERAST turbomachinery optimized design parameters can be applied here. Due to the high rotational speed and low mass flow rate, the maximum efficiency level of compressors and turbines are generally reduced compared to the open cycles. This is particularly true for the LPC and the HP turbomachinery where the component deficiencies behave as for the ERAST model. Slightly lower values than the ERAST engine have been observed for the LPT, due to the higher amount of fresh air used by the engine. Since semi-closed cycles have been

proven to be quite sensitive to the turbomachinery efficiency, as already observed by Anagnostis [12], the optimizer properly modifies the turbomachinery variables to ensure that maximum efficiency has been obtained for the given inlet flow conditions.

Compressors Tables 6.13 and 6.14 summarizes the optimal compressor design vector for the minimum SFC and weight Pareto frontier solutions respectively.

Table 6.13: Compressors design vector for minimum average SFC (HPRTE engine)

	ν	α_2	β_2	$2\theta_c$	η_s
LPC	0.406	65.822	-9.090	8.555	0.738
HPC	0.340	64.615	-7.686	8.962	0.760

Table 6.14: Compressors design vector for minimum weight (HPRTE engine)

	ν	α_2	β_2	$2\theta_c$	η_s
LPC	0.3795	65.5602	-9.2765	8.282	0.723
HPC	0.3301	64.6395	-9.2144	9.414	0.740

The LPC matching mach number is 0.4352 and 0.4156 for minimum SFC_{av} and W_{eng} of the HPRTE engine. Similarity with the ERAST optimal solutions can be found here, showing that the impact of the mixer is equivalent in both engines.

Turbines Tables 6.15 and 6.16 similarly display the turbine results.

Table 6.15: Turbines design vector for minimum average SFC (HPRTE engine)

	r_0/r_1	ν	β_{3s}	η_s
HPT	1.552	0.458	-57.739	0.878
LPT	1.533	0.434	-59.988	0.842

Table 6.16: Turbines design vector for minimum weight (HPRTE engine)

	r_0/r_1	ν	β_{3s}	η_s
HPT	1.568	0.385	-57.654	0.872
LPT	1.455	0.519	-58.476	0.813

6.5 Conclusions

The different objectives discussed in section 1.2 have been entirely addressed throughout this thesis work. A detailed component performance and weight model has been built, with the objective of better characterizing the impact that individual thermodynamic parameters have on the whole cycle behavior. Limiting aspects of the commonly employed turbomachinery performance tools have been discussed, giving reasons for the more advanced methodology implemented with respect to the objective of this work.

The developed tool has been subsequently coupled with a multi-objective algorithm to establish optimal engine settings for a simple recuperated and an intercooled-recuperated open cycle, together with the two intercooled-recuperated semi-closed cycle architectures: the ERAST Coleman engine [14] and the HPRTE configuration [10, 11]. The cycles have been built using the same component arrangements, and the optimization study has been performed with the minimization of SFC_{av} and W_{eng} as common target.

The primary objective of the analysis has been the study of the cycle design performance to identify whether the semi-closed cycle positive features, underlined in other engineering studies, could be applicable to UAV gas turbines designed for high altitude missions. The part power study has been included in the analysis to compare the engine response to off-design flow characteristics and assess differences with conventional state-of-the-art open cycles, establishing whether future research on semi-closed cycles should be addressed.

6.5.1 Results Summary

The main outcomes of this thesis work can be summarized by the following points:

- Despite the presence of intercooler and recuperator, the semi-closed cycle arrangements lead to a significant engine weight reduction for the same average SFC with respect to any of the open cycles analyzed. This is primarily due to the recirculated nature of the engine, which allows to achieve higher pressure ratios, further reducing the engine inlet mass flow requirement for the same power output. Consequently, the turbomachinery and heat exchangers becomes more compact, leading to an overall weight reduction factor greater than two.
- Among the semi-closed cycles analyzed here, the ERAST configuration allows for the greatest weight reduction. This is entirely associated to the different feedback splitting point location, which leads to a further reduction of the inlet mass flow rate needed by the engine. Hence, if weight is a concern, the ERAST configuration should be employed.
- The semi-closed cycle arrangements show advantages also in terms of average specific fuel consumption, since a slightly lower minimum SFC_{av} has been obtained during the optimization. The ERAST model leads to lower SFC values, since this configuration can be better adjusted by the optimizer to cope with the feasibility constraints set on the engine.
- For the same average specific fuel consumption, the different position of the splitter element between ERAST and HPRTE engines results in a complete different performance behavior. The ERAST engine shows superior response at design flow conditions, while the HPRTE presents improved performance at low engine power demand. Therefore, for applications that require the engine to run at low power for a significant part of its mission, the HPRTE configuration is preferred.

6.5.2 Future Work

Certain improvements have been suggested throughout the development of this document regarding the created model and the analysis performed here. Primary key improvements that have been left as future work are summarized in this section, dividing the treatise according to model and analysis amelioration. The first refers directly to the component performance and weight model, while the second to the performed analysis.

Model Improvements

The following suggestions have been indicated as future work to improve the current model capabilities for a more detailed study of semi-closed cycles:

- The radial turbomachinery off-design model should be improved through the employment of the hereby obtained design geometry and loss models to derive component maps. This ensures a better off-design efficiency estimation for compressors and turbines, increasing the accuracy of the predictions with respect to the common scaling approach.

- During the optimization specific speed and specific diameters have been monitored to ensure the feasibility of using radial turbomachinery for the current analysis. It has been observed that the calculated n_s and d_s are within the range where axial and radial solutions could be of interest. This is particularly true for the turbine block. Hence, it would be beneficial to investigate the implementation of an equivalent performance and weight model for axial stages, comparing the resultant optimized performance and weight with the one currently gathered.

- A single shaft architecture has been employed in this analysis to reduce the engine complexity, as typically done for UAV applications. However, it would be of interest to perform a similar study with a twin shaft configurations, which allows more control on the turbomachinery rotational speed, consequently potentially improving the peak efficiency of this last.

Analysis Improvements

The following ameliorations have been identified for future semi-closed cycle analysis, that can be realized with the implemented model:

- The effects of reduced engine size, altitude variation and a more cost effective technological level should be addressed in future work. This helps to evaluate whether the semi-closed cycle solution remains competitive with more conventional solutions.

- Considerations on take-off performance have not been included in this preliminary work. It was more of interest here to evaluate design and part power engine behavior at the design altitude, assessing whether a semi-closed cycle small gas turbine could represent an interesting alternative to conventional open cycle configurations. Thus, identifying whether advantages discussed in literature for naval and ground applications could be applicable here.

- Including a take-off study in the current optimization analysis implies a significant effort for the optimizer to find a geometry capable of satisfying all the requirements defined here. The extremely high altitude used in this project makes this approach even more sophisticated for the solver. A more effective methodology has been presented in reference [97], which could be included in the model to improve the performance of the algorithm, before the optimization takes place. In particular, the author discusses a multi-design point approach built entirely in NPSS, which allows to obtain thermodynamic design data capable of satisfying multiple performance requirements of numerous design and off-design points simultaneously. This approach could be investigated to improve the multi-objectives optimization algorithm search path and better define the optimization bounds to include the take-off study.

6.5.3 Recommendations

The combustor has been identified in different publications [10, 11, 14, 17, 18] as the most critical aspect and parameter of success of semi-closed cycles. As observed also in this work, a significant amount of burnt product is introduced in the combustor, which improves the cycle thermal efficiency and the engine compactness. Burner cooling represents the first challenge, which could be solved through a detailed combustor design phase.

More important are the effects that burnt products have on combustion performance in design and off-design. The only detailed experimental work has been discussed in reference [69], with a recirculation ratio that is small in comparison with what is identified here to be optimal. Similar semi-closed cycles advantages on emissions have been found in [10, 11, 17, 19]

for greater recirculation ratios, with combustor adapted and not fully optimized. Hence, a far greater combustion research has been recommended here in a separate section, to stress out the importance of this component on the successful realization of semi-closed cycles.

Bibliography

[1] Colin F. McDonald. Heat Recovery Exchangers Technology for Very Small Gas Turbines. *International Journal of Turbo and Jet Engines*, 13(4):239–261, 1996.

[2] Colin F. McDonald. Low-cost compact primary surface recuperator concept for microturbines. *Applied Thermal Engineering*, 20(5):471–497, 2000.

[3] M. Malkamaki, Ahti Jaatinen-Varri, J. Honkatukia, J. Backman, and J. Larjola. A High Efficiency Microturbine Concept. In *11th European Conference on Turbomachinery Fluid Dynamics and Thermodynamics, ETC 2015*, pages 1–12, Madrid, Spain, 2015.

[4] Ramesh K. Shah and Dusan P. Sekulic. *Fundamentals of Heat Exchanger Design*. 2003.

[5] R. K. Shah. Compact Heat Exchangers for Microturbines. In *International Conference of Enhanced, Compact and Ultra-Compact Heat Exchangers: Science, Engineering and Technology*, pages 247–257, Indianapolis, Indiana, USA, 2005.

[6] June Kee, Min Ji, Hwan Jeong, and Man Yeong. High temperature heat exchanger studies for applications to gas turbines. *Heat Mass Transfer*, pages 175–186, 2009.

[7] Colin F. McDonald. Recuperator considerations for future higher efficiency microturbines. *Applied Thermal Engineering*, 23:1463–1487, 2003.

[8] Nebojsa Gasparovic. The Advantage of Semi-Closed Cycle Gas Turbines for Naval Ship Propulsion. *Naval Engineers Journal*, 1968.

[9] S. H. Dewitt and W. B. Boyum. Internally Fired Semi-Closed Cycle Gas Turbine Plant for Naval Propulsion. In *Gas Turbine Power Conference*. ASME, 1956.

[10] Peter L. Meitner, Anthony L. Laganelli, Paul F. Senick, and William E. Lear. Demonstration of a Semi-Closed Cycle, Turboshaft Gas Turbine Engine, 2000.

[11] W. E. Lear and A. L. Laganelli. High Pressure Regenerative Turbine Engine: 21st Century Propulsion. Technical report, NASA Glenn Research Center, 2001.

[12] George Anagnostis. Design Point Analysis of the High Pressure Regenerative Turbine Engine Cycle for High-Speed Marine Applications, 2007.

[13] Todd S. Nemec and William E. Lear. Thermodynamic Design Point Study of a Semi-Closed Recuperated Intercooled Gas Turbine Combined With a Rankine Bottoming Cycle. In *International Gas Turbine and Aeroextgine Congress & Exhibition*, Birmingham, UK, 1996. ASME.

[14] James L. Bettner, Craig S. Blandford, and J. Rezy. Propulsion System Assessment for Very High Altitude UAV Under ERAST. Technical report, Allison Engine Company, Indianapolis, Indiana, USA, 1995.

[15] C. Rodgers. Some Effects of Size on the Performances of Small Gas Turbines. In *ASME TURBO EXPO*, pages 1–10, Atlanta, Georgia, USA, 2003. ASME.

[16] C. Rodgers. A Cycle Analysis Technique for Small Gas Turbines. In *Proceedings of the Institution of Mechanical Engineers*, volume 183, pages 37–49, 1969.

[17] C. Rodgers. Design, Fabrication, and Testing of a Semi-Closed Cycle Gas Turbine Engine. In *ASME TURBO EXPO 2001*, New Orleans, Louisiana,USA, 2001. ASME.

[18] C. Rodgers. 300 kW Class, Semi-Closed Cycle Gas Turbine Engine Design Considerations. In *International Gas Turbine & Aeroengine Congress & Exhibition*, Indianapolis, Indiana, USA, 1999. ASME.

[19] A. L. Laganelli, C. Rodgers, W. E. Lear, and P. L. Meitner. Semi-Closed Gas Turbine Cycles: An Ecological Solution. In *ASME TURBO EXPO 2001*, New Orleans, Louisiana,USA, 2001. NASA Glenn Research Center, ASME.

[20] Mert Çevik. Design and Optimization of a Mixed Flow Compressor Impeller Using Robust Design Methods, 2009.

[21] Fumikata Kano, Yoshiteru Fukao, and Takafumi Shirakami. Development of High Specific Speed Mixed Flow Compressors. *Turbomachinery and Pump Symposia*, pages 139–148, 1984.

[22] E. Balje. Study on Design Criteria and Matching of Turbomachines: Part A - Similarity Relations and Design Criteria of Turbines. *Journal of Engineering for Power*, pages 83–102, 1962.

[23] E. Balje. A Study on Design Criteria and Matching of Turbomachines: Part B - Compressor and Pump Performance and Matching of Turbocomponents. *Journal of Engineering for Power*, pages 103–114, 1962.

[24] E. Keneth and P. E. Nichols. How to Select Turbomachinery For Your Application.

[25] S. L. Dixon and C. A. Hall. *Fluid Mechanics and Thermodynamics of Turbomachinery*. Elsevier, seventh edition, 2014.

[26] A. Whitfield. Preliminary Design and Performance Prediction Techniques for Centrifugal Compressors. *Proceedings of the Institution of Mechanical Engineers*, 204(1):131–144, 1990.

[27] E. Balje. *Turbomachines: A Guide to Design, Selection, and Theory*. John Wiley & Sons, 1981.

[28] Adam Joseph Head. Conceptual Design and Simulation of a Microturbine; An Electric Car Range Extender Application, 2004.

[29] D. E. Holeski and S. M. Futral. Experimental Performance Evaluation of a 6.02-Inch Radial-Inflow Turbine Over a Range of Reynolds Number. Technical report, NASA Lewis Research Center, Cleveland, Ohio, USA, 1967.

[30] Lunnan Kjersti. Altitude Effects on the Performance of Small Radial Turbomachinery, 2014.

[31] Adam Joseph Head and W. P. J. Visser. Scaling 3-36kW Microturbines. In *ASME TURBO EXPO*, pages 1–9, Copenhagen, Denmark, 2012. ASME.

[32] Theodosios Korakianitis and David Gordon Wilson. Models for Predicting the Performance of Brayton-cycle Engines. In *International Gas Turbine and Aeroengine Congress and Exposition*, Cologne, Germany, 1992. ASME.

[33] David Gordon Wilson and Theodosios Korakianitis. *The Design of High-Efficiency Turbomachinery and Gas Turbines*. Pearson ed edition, 1998.

[34] R. Monig, K. D. Broichhausen, and H. E. Gallus. Application of Highly Loaded Single-Stage Mixed-Flow Compressors in Small Jet-Engines. In *AGARD Conference Proceedings, Advanced Technology for Aero Gas Turbine Components*, number 421, Paris, France, 1987. AGARD.

[35] Anna Marcellan. An exploration into the potential of microturbine based propulsion systems for civil Unmanned Aerial Vehicles, 2015.

[36] Michael R. Galvas. Fortran Program for Predicting Off-Design Performance of Centrifugal Compressors. Technical report, NASA Lewis Research Center and U.S. Army Air Mobility R&D Laboratory, Cleveland, Ohio, USA, 1973.

[37] Michael R. Galvas. Analytical Correlation of Centrifugal Compressor Design Geometry for Maximum Efficiency with Specific Speed. Technical report, NASA Lewis Research Center, Cleveland, Ohio, USA, 1972.

[38] H. W. Oh, E. S. Yoon, and M. K. Chung. An optimum set of loss models for performance prediction of centrifugal compressors. *Proceedings of the Institution of Mechanical Engineers, Part A: Journal of Power and Energy*, 211(4):331–338, 1997.

[39] R. H. Aungier. *Centrifugal Compressors: A Strategy for Aerodynamic Design and Analysis*. ASME, 2000.

[40] R. H. Aungier. Mean Streamline Aerodynamic Performance Analysis of Centrifugal Compressors. 117:360–366, 1995.

[41] A. Whitfield and N.C. Baines. *Design of Radial Turbomachines*. Pearson Education, 1990.

[42] P. Harley, S. Spence, J. Early, D. Filsinger, and M. Dietrich. An evaluation of 1D loss model collections for the off-design performance prediction of automotive turbocharger compressors. In *6th International Conference on Pumps and Fans with Compressors and Wind Turbines*. IOP, 2013.

[43] John D. Stanitz. One-Dimensional Compressible Flow in Vaneless Diffusers of Radial- and Mixed-Flow Centrifugal Compressors, Including Effects Of Friction, Heat Transfer and Area Change. Technical report, NASA Lewis Flight Propulsion Laboratory, Cleveland, Ohio, USA, 1952.

[44] Pei-yuan Li, Chu-wei Gu, and Yin Song. A New Optimization Method for Centrifugal Compressors Based on 1D Calculations and Analyses. *Energies*, 8:4317–4334, 2015.

[45] David Japikse and N.C. Baines. *Introduction to Turbomachinery*. 1997.

[46] A. Whitfield. The Preliminary Design of Radial Inflow Turbines. *Journal of Turbomachinery*, 112(1):50–57, 1989.

[47] H. E. Rohlik. Analytical Determination of Radial Inflow Turbines Design Geometry for Maximum Efficiency. Technical report, NASA Lewis Research Center, Cleveland, Ohio, USA, 1968.

[48] Arthur J. Glassman. *Turbine Design and Application (3 volumes)*. National Aeronautical and Space Administration, Washington D.C., USA, 1973.

[49] Arthur J. Glassman. Computer Program for Design Analysis of Radial-Inflow Turbines. Technical report, NASA Lewis Research Center, Cleveland, Ohio, USA, 1976.

[50] Charles A. Wasserbauer and Arthur J. Glassman. Fortran program for predicting off-design performance of radial-inflow turbines. Technical report, NASA Lewis Research Center, Cleveland, Ohio, USA, 1975.

[51] N. C. Baines. A meanline prediction method for radial turbine efficiency. In *Sixth International Conference on Turbocharging and Air Management Systems*, volume 1998, pages 45–56, 1998.

[52] J. H. Horlock, D. T. Watson, and T. V. Jones. Limitations on Gas Turbine Performance Imposed by Large Turbine Cooling Flows. *Journal of Engineering for Gas Turbines and Power*, 123(3):487, 2001.

[53] J. F Sellers and C. J. Daniele. Dyngen - A Program for Calculating Steady-State and Transient Performance of Turbojet and Turbofan Engines. Technical report, NASA Lewis Research Center, Cleveland, Ohio, USA, 1975.

[54] Changduk Kong, Jayoung Ki, and Myoungcheol Kang. A New Scaling Method for Component Maps of Gas Turbine Using System Identification. In *ASME TURBO EXPO*, pages 1–8, Amsterdam, The Netherlands, 2002. ASME.

[55] L. Zafer. An investigation into performance modeling of a small gas turbine engine. Technical report, Australian Government Department of Defence, 2012.

[56] Gasturb Gmbh. GasTurb 13 Design and Off-Design Performance of Gas Turbines, 2017.

[57] B. Ernst, J. Kammeyer, and J. R. Seume. Improved Map Scaling Methods for Small Turbocharger Compressors. In *ASME TURBO EXPO*, pages 1–12, Vancouver, British Columbia, Canada, 2011. ASME.

[58] Joachim Kurzke and Claus Riegler. A New Compressor Map Scaling Procedure for Preliminary Conceptional Design of Gas Turbines. In *ASME IGTI*, pages 1–8, Munich, Germany, 2000. ASME.

[59] Colin F. Mcdonald and David Gordon Wilsont. The Utilization of Recuperated and Regenerated Engine Cycles for High-Efficiency Gas Turbines in the 21st Century. *Applied Thermal Engineering*, 16, 1996.

[60] Colin F. McDonald. Study of a Lightweight Integral Regenerative Gas Turbine for High Performance. Technical report, The Garret Corporation AiResearch Manufacturing Company, Los Angeles, California, USA, 1970.

[61] M. W. Kays and A. L. London. *Compact Heat Exchangers*. Third edit edition, 1998.

[62] T. Stevens, F. Verplaetsen, and M. Baelmans. Requirements for Recuperators in Micro Gas Turbines. In *International workshop on micro and nanotechnlogy for power generation and energy conservation application*, pages 96–99, Kyoto, Japan, 2004.

[63] Tine Stevens and Martine Baelmans. Optimal Pressure Drop Ratio for Micro Recuperators in Small Sized Gas Turbines. *Applied Thermal Engineering*, 28(17-18):2353–2359, 2008.

[64] Colin Rodgers. Thermodynamic and Economic Trade Studies for a 3000 kW Gas Turbine. In *ASME COGEN*, 1995.

[65] Colin F. Mcdonald, Aristide F. Massardo, Colin Rodgers, and Aubrey Stone. Recuperated Gas Turbine Aeroengines, Part II: Engine Design Studies Following Early Development Testing. Technical report, 2008.

[66] Colin F. Mcdonald. Gas Turbine Recuperator Renaissance. *Heat Recovery Systems & CIP*, 10(I):1–30, 1990.

[67] P. P. Walsh and P. Fletcher. *Gas Turbine Performance*. Blackwell, second edition, 2004.

[68] Anne-Marie Borbely and Jan F. Kreider. *Distributed Generation: the Power Paradigm for the New Millennium*. 2001.

[69] Cecil J. Marek and Robert R. Tacina. Effect of Exhaust Gas Recirculation on Emissions from a Flame-Tube Combustor Using Liquid Jet A Fuel. Technical report, NASA Lewis Research Center, Cleveland, Ohio, USA, 1976.

[70] Jerry O. Melconian and Ashok T. Modak. Combustor Design, in Sawyer's Gas Turbine Engineering Handbook. *Turbomachinery International Publications*, 1, 1985.

[71] Ana Costa Conrado, Pedro Teixeira Lacava, Alberto Carlos Pereira Filho, and Milton de Souza Sanches. Basic Design Principles for Gas Turbine Combustor. In *Brazillian Congress of Thermal Sciences and Engineering*, Rio de Janeiro, Brazil, 2004.

[72] Digvijay B. Kulshreshtha and S. A. Channiwala. Simplified Design of Combustion Chamber for Small Gas Turbine Applications. In *ASME International Mechanical Engineering Congress and Exposition*, pages 1–6, Orlando, Florida USA, 2005. ASME.

[73] A. H. Lefebvre and E. R. Norster. The Design of Tubular Gas Turbine Combustion Chambers for Optimum Mixing Performance. In *Proceedings of Institution of Mechanical Engineers*, volume 183, pages 150–155, 1969.

[74] A. H. Lefebvre and D. R. Ballal. *Gas Turbine Combustion: Alternative Fuels and Emissions*. Third edit edition, 2010.

[75] P. Arunachalanl. Selection of a Suitable Combustion System for a Small Gas Turbine Engine. *Defence Science Journal*, 38(4):381–396, 1988.

[76] K. V. Chaudhari, D. B. K. Ulshreshtha, and S.A. Channiwala. Design and CFD Simulation of Annular Combustion Chamber with Kerosene as Fuel for 20 kW Gas Turbine Engine. *International Journal of Engineering Research and Applications (IJERA)*, 2(6):1641–1645, 2012.

[77] C. Priyant Mark and A. Selwyn. Design and analysis of annular combustion chamber of a low bypass turbofan engine in a jet trainer aircraft. *Propulsion and Power Research*, 5 (2):97–107, 2016.

[78] Robert R. Tacina and Jack Grobman. Analysis of Total-Pressure Loss and Airflow Distribution for Annular Gas Turbine Combustors. Technical report, NASA Lewis Research Center, Cleveland, Ohio, USA, 1969.

[79] A. Knight and R. B. Walker. The Component Pressure Losses in Combustion Chambers. Technical report, Aeronautical Research Council, 1953.

[80] Periklis Lolis. *Development of a Preliminary Weight Estimation Method for Advanced Turbofan Engines*. PhD thesis, Cranfield University, 2014.

[81] Robert P. Gerend and John P. Roundhill. Correlation of Gas Turbine Engine Weight and Dimensions. In *AIAA 6th Propulsion Joint Specialist Conference*, San Diego, California, USA, 1970.

[82] Ammar Benguedouar. Types of Turbomachinery Best Suited for Space Missions Requiring Power Outputs in the Range of Few Kw to 1 Mw, 1988.

[83] E. Onat and W. G. Klees. A Method to Estimate Weight and Dimensions of Large and Small Gas Turbine Engines. Technical report, NASA Lewis Research Center, 1979.

[84] P. L. Hale. A Method to Estimate Weight and Dimensions of Small aircraft Propulsion Gas Turbine Engines. Technical report, NASA Lewis Research Center, 1982.

[85] Michal Czarnecki. Mass Model of Microgasturbine Single Spool Turbojet Engine. *Journal of KONES Powertrain and Transport*, 20(1):49–54, 2013.

[86] G. W. Klees. Aircraft Engine Weight Estimation Method. In *Thirty seventh Annual Conference of the Society of Allied Weight Engineers*, Munich, West Germany, 1978.

[87] E. Rejman and M. Rejman. Gears Weight Equation - Gear Chain Weight Calculation Methodology. *MTMVirtual Journals*, (2):18–21, 2011.

[88] A. H. Schmidt. A Method for Estimating the Weight of Aircrfat Transmissions. In *35th Annual Conference of the Society of Allied Weight Engineers*, Philadelphi, Pennsylvania, USA, 1976.

[89] D. W. Dudley. *Handbook of Practical Gear Desing.* 1994.

[90] Andrew T. Bellocchio. Drive System Design Methodology for a Single Main Rotor Heavy Lift Helicopter, 2005.

[91] Rohan H. Glover. Free Turbine Design of Micro Gas Turbine Engines, 2013.

[92] NPSS Consortium. NPSS^{TM} User's Guide, 2016.

[93] NPSS Consortium. NPSS User Guide Reference Sheets, 2016.

[94] NPSS Consortium. NPSS^{TM} Thermo Guide, 2016.

[95] NPSS Consortium. NPSS Fluid Network Thermo Guide, 2016.

[96] Edward J. Kowaiski and Robert A. Atkins. A Computer Code for Estimating Installed Performance of Aircraft Gas Turbine Engines. Technical report, Advanced Airplane Branch Boeing Military Airplane Company, Seattle, Washington, USA, 1979.

[97] Jeffrey Scott Schutte. *Simultaneous Multi-Design Point Approach to Gas Turbine On-Design Cycle Analysis for Aircraft Engines.* PhD thesis, Georgia Institute of Technology, 2009.

[98] Coordinating Research Council Inc. *Handbook of Aviation Fuel Proprieties.* 1983.

[99] Sanford Gordon and Bonnie J. McBride. Computer Program for Calculation of Complex Chemical Equilibrium Compositions and Applications - I. Analysis. Technical report, NASA, 1994.

[100] Bonnie J. McBride and Sanford Gordon. Computer Program for Calculation of Complex Chemical Equilibrium Compositions and Applications - II. Users Manual and Program Description. Technical report, NASA, 1996.

[101] Scott M. Jones. An Introduction to Thermodynamic Performance Analysis of Aircraft Gas Turbine Engine Cycles Using the Numerical Propulsion System Simulation Code. Technical report, NASA Glenn Research Center, Cleveland, Ohio, USA, 2007.

[102] Eric S. Hendricks. Development of an Open Rotor Cycle Model in NPSS Using a Multi-Design Point Approach. Technical report, NASA Glenn Research Center, Cleveland, Ohio, USA, 2011.

[103] B. S. Stratford and J. G. Williams. A Simplified Treatment of Losses for One-Dimensional Mixing Between Hot and Cold Gas Streams at Constant Pressure and Low Velocity. Technical report, Ministry of Aviation Aeronautical Research Council, 1963.

[104] Richard J. Roelke. Radial Turbine Cooling. Technical report, NASA Lewis Research Center, Cleveland, Ohio, USA, 1992.

[105] Ganesh N. Kumar and Russell G. DeAnna. Development of a Thermal and Structural Analysis Procedure for Cooled Radial Turbines. In *33rd International Gas Turbine and Aeroengine Congress and Exposition*, Amsterdam, The Netherlands, 1988. ASME.

[106] Philip H. Snyder. Cooled High-Temperature Radial Turbine Program. Technical report, Allison Gas Turbine Division General Motors Corporation, 1992.

[107] J. M. Lane. Cooled Radial In-Flow Turbines for Advanced Gas Turbine Engines. In *Gas Turbine Conference & Products Show*, pages 1–9, Houston, Texas, USA, 1981. ASME.

[108] Joachim Kurzke. Achieving maximum thermal efficiency with the simple gas turbine cycle. Technical report, MTU Aero Engines, 2018.

[109] Joachim Kurzke. Aero-Engine Design: A State of the Art, 2003.

[110] M. A. El-Masri. GASCAN - an Interactive Code for Thermal Analysis of Gas Turbine Systems. 110:201–209, 1988.

[111] H. I. H. Saravanamuttoo, G. F. C. Rogers, H. Cohen, P. V. Straznicky, and A. C. Nix. *Gas Turbine Theory*. Pearson, 7th edition, 2017.

[112] C. Rodgers. Impeller Stalling as Influenced by Diffusion Limitations. *Journal of Fluids Engineering*, pages 84–93, 1977.

[113] Y. Kim, A. Engeda, R. Aungier, and N. Amineni. A centrifugal compressor stage with wide ow range vaned diffusers and different inlet con gurations. *Journal Power and Energy*, 216:307–320, 2002.

[114] Waleed Al-busaidi and Pericles Pilidis. Techno-Economic Optimization of Diffuser Configuration Effect on Centrifugal Compressor Performance. *American Journal of Energy Research*, 3(2):37–48, 2015.

[115] Laurence J Heidelberg, Calvin L Bull, and Carl Weigel. Effect Of Reynolds Number on Overall Performance of a 6-inch Radial Bladed Centrifugal Compressor. Technical report, NASA Lewis Research Center, Cleveland, Ohio, USA, 1970.

[116] Hugh A. Klassen, Jerry R. Wood, and Lawrence F. Schummann. Experimental Performance of a 16.10-Centimeter-Tip-Diameter Sweptback Centrifugal Compressor Designed for a 6:1 Pressure Ratio. Technical report, NASA Lewis Research Center and U.S. Army Air Mobility R&D Laboratory, Cleveland, Ohio, USA, 1977.

[117] Gernot Eisenlohr, Hartmut Krain, Franz-Arno Richter, and Valentin Tiede. Investigations of the Flow Through a High Pressure Ratio Centrifugal Impeller. In *ASME Turbo Expo*, pages 1–9, Amsterdam, The Netherlands, 2002. ASME.

[118] Edward R. Tysl, C. L. Ball, Carl Weigel, and Laurence J. Heidelberg. Overall Performance in Argon of a 6-Inch Radial-Bladed Centrifugal Compressor. Technical report, NASA Lewis Research Center, Cleveland, Ohio, USA, 1968.

[119] AiResearch Manufacturing Company of Arizona. Design and Fabrication of a High-Performance Brayton-Cycle Compressor Research Package. Technical report, Garrett Corporation, Phoenix, Arizona, USA, 1965.

[120] Hartmut Krain, B. Hoffmann, and H. Pak. Aerodynamics of a Centrifugal Compressor Impeller with Transonic Inlet Conditions. In *International Gas Turbine & Aeroengine Congress & Exhibition*, pages 1–9, Houston, Texas, USA, 1995. ASME.

[121] Gernot Eisenlohr, Peter Dalbert, Hartmut Krain, Hartwig Proll, Franz-Arno Richter, and Karl-Heinz Rohne. Analysis of the Transonic Flow at the Inlet of a High Pressure Ratio Centrifugal Impeller. In *International Gas Turbine & Aeroengine Congress & Exhibition*, pages 1–11, Stockholm, Sweden, 1998. ASME.

[122] Chunill Hah and Hartmut Krain. Analysis of Transonic Flow Fields Inside a High Pressure Ratio Centrifugal Compressor at Design and Off Design Conditions. In *International Gas Turbine & Aeroengine Congress & Exhibition*, pages 1–15, Indianapolis, Indiana, USA, 1999. ASME.

[123] Tsukasa Yoshinaka, R. G. Thompson, and Jean Letourneau. The Performance Prediction and Demonstration of a Centrifugal Compressor for the Multiple Purpose Small Power Unit (MPSPU). In *Gas Turbine and Aeroengine Congress and Exposition*, Totonto, Ontario, Canada, 1989. ASME.

[124] Ronald H. Aungier. *Turbine Aerodynamics, Axial-Flow and Radial-Inflow Turbine Design and Analysis*. ASME Press, New York, 2005.

[125] Mahmoud Khader. Optimised Radial Turbine Design D1.8, 2014.

[126] Carlos A. M. Ventura, Peter A. Jacobs, Andrew S. Rowlands, Paul Petrie-repar, and Emilie Sauret. Preliminary Design and Performance Estimation of Radial Inflow Turbines : An Automated Approach. 134:1–13, 2012.

[127] Kerry L. McLallin and Jeffrey E. Haas. Experimental Performance and Analysis of 15.04-Centimeter-Tip-Diameter, Radial-Inflow Turbine with Work Factor of 1.126 and Thick Blading. Technical report, NASA Lewis Research Center, Cleveland, Ohio, USA, 1980.

[128] K. R. Pullen, N. C. Baines, and S. H. Hill. The Design and Evaluation of a High Pressure Ratio Radial Turbine. In *International Gas Turbine & Aeroengine Congress & Exhibition*, pages 1–7, Cologne, Germany, 1992. ASME.

[129] Digvijay B. Kulshreshtha and S. A. Channiwala. Hydrogen Fuelled Micro Gas Turbine Combustion Chamber. *The Hong Kong Institution of Engineers Transactions*, 18:19–25, 2010.

[130] R. W. Tameo, P. W. Vinson, and R. E. Neitzel. Regenerative Engine Analysis. Technical report, General Electric Company, 1980.

[131] W. D. Marscher. Structural Design and Analysis of Modern Turbomachinery Systems, in Sawyer's Gas Turbine Engineering Handbook. *Turbomachinery International Publications*, 1, 1985.

[132] E. Robert Dundas. Mechnaical Design of Gas Turbine, in Sawyer's Gas Turbine Engineering Handbook. *Turbomachinery International Publications*, 1, 1985.

[133] Cheng Xu and Ryoichi S. Amano. Empirical Design Considerations for Industrial Centrifugal Compressors. *International Journal of Rotating Machinery*, pages 1–15, 2012.

[134] Achille Messac. *Optimization in Practice with MATLAB®: For Engineering Students and Professionals*. Cambridge University Press, 2015.

[135] Kalyanmoy Deb. *Multi-Objective Optimization using Evolutionary Algorithms*. John Wiley & Sons, 2001.

[136] Mathworks. Global Optimization Toolbox User 's Guide, 2018.

[137] Rainer Storn. On the Usage of Differential Evolution for Function Optimization, 1996.

[138] Stanley Gotshall and Bart Rylander. Optimal Population Size and the Genetic Algorithm, 1992.

[139] Thomas Row, Elliot Bicker, Alex Carnoali, Antonio Schoneich, Austin Tuggle, Christopher Bynum, Cody Hill, Juan Castro, and Elizabeth Stoops. SF-1600: A Next Generation High Efficiency Turboprop for Single-Engine Aircraft. Technical report, The University of Kansas, 2017. AIAA 2016-2017 Undergraduate Team - Engine Design Competition.

[140] Zhang Yingao, Wen Mengyang, and Wang Haonan. WJ-25 Design Proposal. Technical report, Beihang University, 2017. AIAA 2016-2017 Undergraduate Team - Engine Design Competition.

[141] David P. Stinton and Michael A. Karnitz. Microturbine Materials Program. Technical report, Oak Ridge National Laboratory, 1999.

[142] Bruce A. Pint, Sebastien Dryepondt, Michael P. Brady, and Yukinori Yamamoto. Evaluation of Commercial and Next Generation Alumina-Forming Austenitic Foil for Advanced Recuperators. In *ASME TURBO EXPO*, pages 1–8, San Antonio, Texas, USA, 2013. ASME.

[143] A. Whitfield. Conceptual Design of a Centrifugal Compressor Including Consideration of the Effect of Inlet Prewhirl. In *International Gas Turbine and Aeroengine Congress and Exposition*, Cologne, Germany, 1992. ASME.

[144] F. G. Groh, G. M. Wood, R. S. Kulp, and D. P. Kenny. Evaluation of a High Hub/Tip Ratio Centrifugal Compressor. *Journal of Basic Engineering*, pages 419–428, 1970.

[145] Colin Rodgers. Effects of Blade Number on the Efficiency of Centrifugal Compressor Impellers. In *ASME TURBO EXPO 2000*, pages 1–8. ASME, 2000.

[146] Antonio Perdichizzi and Giovanni Lozza. Design Criteria and Efficiency Prediction for Radial Inflow Turbines. In *Gas Turbine Conference and Exhibition*, pages 1–9, Anaheim, California, USA, 1987. ASME.

[147] C. Rodgers. The Efficiencies of Single-Stage Centrifugal Compressors for Aircraft Applications. In *International Gas Turbine and Aeroengine Congress and Exposition*, Orlando, Florida USA, 1991.

[148] Carl Weigel and C. L. Ball. Reynolds Number Effect on Overall Performance of a 10.8-centimeter (4.25-in.) Sweptback-bladed Centrifugal Compressor. Technical report, NASA Lewis Research Center, Cleveland, Ohio, USA, 1972.

[149] F. J. Wiesner. A New Appraisal of Reynolds Number Effects on Centrifugal Compressor Performance. *Journal of Engineering for Gas Turbines and Power*, 101:384–392, 1979.

[150] H. Simon and A. Bulskamper. On the Evaluation of Reynolds Number and Relative Surface Roughness Effects on Centrifugal Compressor Performance Based on Systematic Experimental Investigations. *Journal of Engineering for Gas Turbines and Power*, 106: 489–498, 1984.

[151] R. A. Strub, L. Bonciani, C. J. Borer, M. V. Casey, S. L. Cole, S. L. Cook, J. Kotzur, H. Simon, and M. A. Strite. Influence of the Reynolds Number on the Performance of Centrifugal Compressors. *Journal of Turbomachinery*, 109:541–544, 1987.

[152] M. V. Casey. The Effects of Reynolds Number on the Efficiency of Centrifugal Compressor Stages. *Journal of Engineering for Gas Turbines and Power*, 107:541–548, 1985.

[153] Fabian Dietmann and Michael Casey. The Effects of Reynolds Number and Roughness on Compressor Performance. In *Proceedings of 10thEuropean Conference on Turbomachinery Fluid dynamics & Thermodynamics*, pages 1–11, Lappeenranta, Finland, 2013.

[154] N. A. Cumpsty. *Compressor Aerodynamics*. Krieger Publishing Company, 2004.

[155] A. Whitfield. Non-Dimensional Aerodynamic Design of a Centrifugal Compressor Impeller. *Proceedings of the Institution of Mechanical Engineers*, 205:257–268, 1991.

[156] Colin Rodgers. Typical Performance Characteristics of Gas Turbine Radial Compressors. *Journal ol Engineering for Power*, 1964.

[157] John D. Stanitz. Design Considerations for Mixed-Flow Centrifugal Compressors with High Weight-Flow Rates per Unit Frontal Area. Technical report, Lewis Flight Performance Laboratory, Cleveland, Ohio, USA, 1953.

[158] R. C. Pampreen. A Blockage Model for Centrifugal Compressor Impellers. *Journal of Engineering for Power*, 103:698–707, 1981.

[159] F. J. Wiesner. A Review of Slip Factors for Centrifugal Impellers. *Journal of Engineering for Power*, pages 558–572, 1967.

[160] M. Zangeneh. On 3D Inverse Design of Centrifugal Compressor Impellers with Splitter Blades. In *International Gas Turbine & Aeroengine Congress & Exhibition*, Stockholm, Sweden, 1998.

[161] Alfred F. Stahler. The Slip Factor of a Radial Bladed Centrifugal Compressor. *Journal of Engineering for Power*, pages 181–188, 1965.

[162] David Japikse. *Centrifugal Compressor Design and Performance*. Concepts ETI Inc., 1996.

[163] Michael Casey and Daniel Rusch. The Matching of a Vaned Diffuser with a Radial Compressor Impeller and its Effect on the Stage Performance. In *Proceedings of ASME Turbo Expo 2014: Turbine Technical Conference and Exposition*, pages 1–14, Düsseldorf, Germany, 2014.

[164] J. E. Coppage, F. Dallenbach, H. P. Eichenberger, G. E. Hlavaka, E. M. Knoernschild, and N. Van Le. Study of Supersonic Radial Compressor for Refrigeration and Pressurization Systems. Technical report, Wright Air Development Center, Wright-Patterson Air Force Base, Ohio, USA, 1957.

[165] Xiaoyang Gong and Rui Chen. Total Pressure Loss Mechanism of Centrifugal Compressors. *Mechanical Engineering Research*, 4(2):45–59, 2014.

[166] S Abolfazl Moussavi, Ali Hajilouy Benisi, and Mohammad Durali. Effect of Splitter Leading Edge Location on Performance of an Automotive Turbocharger Compressor. *Energy*, 123:511–520, 2017.

[167] C. Rodgers. Performance of a High- Efficiency Radial / Axial Turbine. 109:151–154, 1987.

[168] I. Watanabe, I. Ariga, and T. Mashimo. Effect of Dimensional Parameters of Impellers on Performance Characteristics of a Radial-Inflow Turbine. *Journal of Engineering for Power*, pages 81–102, 1971.

[169] Homer J. Wood. Current Technology of Radial-Inflow Turbines for Compressible Fluids. In *Gas Turbine Power Conference and Exhibit*, Huston, Texas, USA, 1962. ASME.

[170] Ramon Silva. Preliminary Design of a Combustion Chamber for Microturbine Based in an Automotive Turbocharger. (November), 2013.

[171] P. Gosselin, A. de Champlain, and D. Kretschmer. Prediction Of Wall Heat Transfer For a Gas Turbine Combustor. *IMeche*, 213(A05998):169–180, 1999.

[172] A. H. Lefebvre and M. V. Herbert. Heat-Transfer Processes in Gas-Turbine Combustion Chambers. *Proceedings of the Institution of Mechanical Engineers*, 174:463–478, 1960.

[173] D. Kretschmer and J. Odgers. A Simple Method for the Prediction of Wall Temperatures in Gas Turbines. In *Gas Turbine Conference & Products Show*, London, England, 1978. ASME.

[174] A. H. Lefebvre. Influence of Fuel Properties on Gas Turbine Combustion Performance. Technical report, 1985.

[175] David J. Poferl, Roger A. Suehla, and Kenneth Lewandowski. Thermodynamic and Transport Properties of Air and the Combustion Products of Natural Gas and of ASTM-A-1 Fuel With Air. Technical report, NASA Lewis Research Center, Cleveland, Ohio, USA, 1969.

[176] Nikhil Sharma. Heat Transfer Analysis for Preliminary Design of Gas Turbine Combustion Chamber Liners, 2015.

[177] T. L. Gall, H. E. Boyer, and American Society for Metals. *Metals Handbook*. American Society for Metals, desk edition, 1984.

[178] C. Osborne, P. W. Runstadler, and W. Stacy. Aerodynamic and Mechanical Design of an 8:1 Pressure Ratio Centrifugal Compressor. Technical report, NASA Lewis Research Center, Cleveland, Ohio, USA, 1975.

[179] Peter M. Schoonmaker. Preliminary Experience with an Expert System Providing Initial Centrifugal Compressor Sizing for Performance Prediction and Analysis. In *International Gas Turbine and Aeroengine Congress and Exposition*, Orlando, Florida USA, 1991. ASME.

[180] V. Zurita-Ugalde, J. C. Gómez-Mancilla, and F. García-Cristiano. A Simple Method for Geometry Definition of Radial Compressors. *International Journal of Turbo and Jet Engines*, 18(1):31–36, 2001.

[181] D. J. L. Smith and H. Merryweather. The Use of Analytic Surfaces for the Design of Centrifugal Impellers by Computer Graphics. *International Journal for Numerical Methods in Engineering*, 7(2):137–154, 1973.

[182] Sanju Kumar, Rashmi Rao, and B. A. Rajeevalochanam. Current Practices in Structural Analysis and Testing of Aero-Engine Main Shafts. *Procedia Engineering*, 55:499–509, 2013.

Appendix

APPENDIX A

Centrifugal Compressor

This appendix contains all the information related to the compressor model developed in this thesis. Initially, additional information on current modeling techniques investigated within the literature review section will be provided, completing what just briefly presented in section 2.3.1. Evidence of limiting aspects in the employment of scaling factors (section A.1.1) or lower fidelity models (section A.1.2) will be further discussed within the objectives of this work. Moreover, a complete description of the theoretical background of the higher fidelity methodology implemented finds sufficient explanation in the following sections. Specific details will be provided on the meanline approach (section A.2.1) and the Galvas loss model (section A.2.2), just briefly mentioned in the main body of this document. Finally, a complete description of the model implementation is provided in section A.3.

A.1 Simple Models

Different simple models have been developed to quickly estimate the centrifugal compressor design performance with no or little knowledge on the actual geometry. These models are typically employed in preliminary thermodynamic analysis to have a realistic prediction of the compressor efficiency as function of fundamental cycle parameters such as: mass flow, pressure ratio, etc. As discussed, scaling techniques are commonly used to produce, from existing reference data, an equivalent machine of a different size, according to the similarity principle [22, 23]. Theoretically, ignoring Reynolds and Mach effects, two compressor having in common specific speed and diameter are similar, thus, exhibit same flow mechanism and efficiency. Efficiency correction have been developed to account for penalties due to size effects.

As discussed by Rodgers [16, 147], scaling effects are not the only phenomena that prevent to obtain high efficiency machine from a good performing reference. Manufacturing and technological aspects have a significant impact on the peak efficiency of a small scale centrifugal compressor. Models have been developed to include clearance and pressure ratio penalties due to manufacturing limitations into the scaling methodology, improving the efficiency prediction of the method. Alternatively, empirical formulations are available to derive the centrifugal compressor efficiency only as function of thermodynamic cycle data. All these aspects are discussed with more details in the following.

A.1.1 Compressor Scaling Technique

As stated, scaling techniques are commonly employed for preliminary performance analysis. They are similarly defined for compressors and turbines, allowing for satisfactory efficiency predictions of the turbomachinery block without entering into much detail on the actual geometry. Being this approach theoretically based on the similarity principle [22, 23, 27], the more the ref-

erence and the scaled machine are similar, the better the accuracy of the method. As discussed in [15, 31], not only Reynolds and Mach effects, but also heat transfer between hot and cold components, secondary losses and manufacturing limitations prevent from obtaining efficient small gas turbines form highly performing references. Therefore, several relations have been developed to model these phenomena in the efficiency evaluation of the scaled machine.

Size effects

The open literature provides different set of expressions that allow to scale down from an existing reference and to account for Reynolds or size effects. Equation A.1 originally proposed by C. Pfleiderer in 1946, and reported in [30], expresses the efficiency of the scaled compressor (η) as function of the reference efficiency (η_{ref}) and the ratio between the reference Reynolds number (Re_{ref}) and the new Reynolds number (Re). Note that within the Reynolds number definition is included the effect of the geometrical scale embedded in the impeller tip diameter (D_2).

$$\frac{1-\eta}{1-\eta_{ref}} = \Big[\frac{Re_{ref}}{Re}\Big]^n \tag{A.1}$$

Reynolds number is defined as:

$$Re = \frac{\rho_1 U_2 D_2}{\mu_1} \tag{A.2}$$

The parameter n denotes the Reynolds ratio exponent and assumes value between 0.16 and 0.5, depending on compressors, as reported in [30]. Equation A.1 measures to what extent the similarity principle holds. In fact, two perfectly similar machines show common flow characteristics, thus, have same efficiency. The Reynolds ratio in equation A.1 measures the geometry and flow dissimilarity between reference and the scaled machine, which prevents from having similar performance [30].

A lot of experimental work has been conducted by NASA in order to find the best data fitting for the Reynolds ratio exponent, as discussed in the technical reports [115, 148] and summarized in [30]. Rodgers [16] proposed a similar relation where the dependency on the impeller tip diameter is directly visible. This is only valid if the reference and derived design Reynolds number are defined at the same flow conditions and rotational speed. In such case, equation A.1 can be rewritten as:

$$\frac{1-\eta}{1-\eta_{ref}} = \Big[\frac{D_{ref}}{D}\Big]^n \tag{A.3}$$

For rotor diameters smaller than 5in (12.7cm), Rodgers [16] suggests to replace D_{ref} with 5 in (12.7 cm). To be precise, equation A.3 assumes that the Reynolds effects are only dependent on the geometrical scaling. If strong differences between the reference and the scaled compressor Reynolds number are present, equation A.3 cannot be employed.

A more generalized formula has been originally formulated by NASA [29] and reported by many authors. The overall Reynolds effects have been divided into losses associated to viscous (profile and windage) and non-viscous (mixing or trailing edge) losses. Equation A.1 has been rearranged into equation A.4 introducing the constant a. a is the Reynolds independent loss fraction and it assumes values between 0.3 and 0.4, according to [31].

$$\frac{1-\eta}{1-\eta_{ref}} = a + (1-a)\Big[\frac{Re_{ref}}{Re}\Big]^n \tag{A.4}$$

A considerable amount of work has been performed on equation A.4 to find the best settings for a and n. Wiesner [149] suggests that the parameter n should be expressed as direct function of Reynolds number to improve the empirical correlation. Moreover, as reported in [30], equation A.4, has been further rearranged by Simon and Bülskämper [150] and Strub et al. [151], replacing the Reynolds number ratio with the pipe flow friction factor C_f. This eliminates the equation

A.4 dependence on the parameter n. The final form of the proposed equation is below reported for reference as discussed in [30, 152].

$$\frac{1-\eta}{1-\eta_{ref}} = a + (1-a)\Big[\frac{C_f}{C_{f,ref}}\Big] \tag{A.5}$$

C_f and $C_{f,ref}$ can be obtained from Colebrook's equations or from their visual representation by means of the so called Moody chart [30]. Despite the effort of determining a better form for equations A.1 and A.4, Casey [152] pointed out that no universal validity can be assumed for the previously discussed methodologies. This has to be attributed to the dependency of the equations on the coefficients a and n, which cannot be globally defined for every compressor case. The latest formulation proposed (equation A.5) removes the reliance on n, however, the specific selection of a is still needed for high fidelity predictions.

Casey [152] presents a completely new formulation for a single-stage compressor which is based on the observation that the friction losses of a compressor stage are similar to the one experienced in a fully turbulent pipe flow. The paper also mentions that the optimal definition of the Reynolds number for estimating the friction losses is in accordance with equation A.2. The proposed approach has the advantage of removing any dependence on empirical constants, with the benefit of having a more universally valid method. The complete model of Casey is discussed in [152, 153].

Pressure ratio effects

The scaling effects are not the only source of loss that has to be accounted to predict the efficiency of a new compressor. As discussed by Rodgers in [16], it is strongly beneficial to generate high pressure ratios compressor stages to achieve good overall cycle efficiencies. A demand of higher pressure ratio is realized through an increase of the impeller rotational speed, which it is translated in an increment of both rotor inlet and exit Mach numbers. Accurate diffusion and component matching at higher impeller exit Mach numbers becomes harder. Therefore the overall peak stage efficiency will strongly be dependent on the compressor design aerodynamic quality. In particular for small turbomachines, manufacturing limitations prevents from obtaining optimal aerodynamic designs, thus setting a limitation in the maximum compressor efficiencies. Rodgers [16] proposed a relative simple expression (equation A.6) to account for efficiency penalties due to Mach and pressure ratio effects.

$$\Delta\eta_c = \frac{C}{\sqrt{\gamma R}}\Big(\frac{P_{04}}{P_{01}} - 2.0\Big) \tag{A.6}$$

where, C is a constant that can be set to 0.13 for current small compressors with zero prewhirl, and the efficiency penalty ($\Delta\eta_c$) is expressed as adiabatic total to total.

Manufacturing considerations

In the preliminary analysis, it might be of interest to track the additional efficiency penalties that are associated to manufacturing limitations. In particular, for small gas turbines, the component efficiency is affected in a more significant way by clearance and surface roughness, both defined by the machining process. while the last can partially be captured through the size effect theory discussed previously, the first needs a more dedicated formulation. Rodgers [16], discussed a straightforward relation to model the tip clearance losses. This can be done using equation A.7 and assuming a value of the clearance to blade height parameter (C_c/h_c).

$$\Delta\eta_c = 0.20\Big(\frac{C_c}{h_c} - 0.02\Big) \tag{A.7}$$

Extensive development on small gas turbines has shown that is difficult to maintain compressor tip clearance below than 0.007in ($\sim$0.018cm), see Rodgers [16].

With these information, the efficiency prediction of simple scaling methods can be made more accurate, including loss source models for main flow phenomena and manufacturing aspects. Rodgers [147] reports a similar set of equations as well as a baseline reference data to properly employ this methodology.

Although, the already discussed advantages of the scaling approach are evident here, a reliable efficiency predictions can only be made for design cases that obey as close as possible to the similarity principle. Otherwise, the application of equation A.4 or similar might lead to considerable error.

A.1.2 Empirical Relations

An alternative solution to account for efficiency variation as function of purely thermodynamic parameters is represented by empirical relations. Simple models are available in literature that can be used for a preliminary cycle analysis. Korakianitis and Wilson [32] introduce equation A.8 to characterize the compressor efficiency decrease with the increase of pressure ratio. This model has been applied to simple, recuperated, intercooled-recuperated shaft-power and jet-propulsion cycles.

$$\eta_{poly} = 0.91 - \frac{\Pi_c - 1}{300} \tag{A.8}$$

Note that η_{poly} represents the total to total polytropic efficiency. No differentiation between the turbomachinery arrangement is made in reference [32], nor limit of applicability have been indicated. Hence, this model can be used only for preliminary calculations, independently on compressor type and number of stages. Limited accuracy and reliability have to be accounted in the employment of this treatise.

Reference [33], proposed an updated version of the previously discussed model, specializing it for axial and radial machines and including size effects as well. Equation A.9 can be used for centrifugal compressors. Note that the component efficiency is expressed in total to static polytropic efficiency ($\eta_{poly,ts}$) and Π_{ts} represents the total to static pressure ratio.

$$\eta_{poly,ts} = 0.878 + 0.030 \ln(\dot{m}) - 0.0037\, \Pi_{c,ts} \tag{A.9}$$

As reported in [33], equation A.9 can be employed for centrifugal compressors with an inlet mass flow rate ($\dot{m}$) not exceeding 90kg/s. Size effects are modelled by means of the inlet mass flow term and pressure ratio effects can be captured with the last block of the equation.

Finally, a fully empirical relation has been discussed in [34]. Equation A.10 represents the empirical data fitting of a range of published transonic axial and radial compressors stages data. The compressor total to total adiabatic efficiency variation as function of pressure ratio can easily calculated from:

$$\eta_c = 1 - c_1(c_2 + \sqrt{c_2^2 + (\Pi_c - c_3)/c_4} \tag{A.10}$$

where:

$$\begin{aligned} c_1 &= 0.120 \qquad & c_2 &= 0.901 \\ c_3 &= 7.236 \qquad & c_4 &= 7.521 \end{aligned}$$

A.2 Advanced Models

As discussed in section 4.2, the requirements of this thesis project cannot be properly satisfied throughout the employment of the simple expressions previously introduced. More accurate performance and weight predictions as function of the cycle thermodynamics can only be made by means of higher fidelity models. As seen, empirical loss and weight models have been identified

as the optimal solution for this analysis. Sufficient geometrical knowledge is a priori needed to employ these methods. Meanline design thechniques can provide the necessary geometrical insight required.

At the base of these methodologies there is a relatively simple mathematical treatise that involves fundamental laws of fluid dynamics applied to turbomachines. This allow to estimate main compressor dimensions and flow mechanisms from known inlet flow conditions and design requirements. Multiple meanline procedures have been discussed in literature. The complexity of these methods increases depending on the level of details required by the designer. Since the objective here is not to fully design the compressor, only preliminary geometrical information are needed. Therefore, a relatively simple technique had to be identified that matches with the loss and weight models employed.

The following treatise addresses the centrifugal compressor modeling aspects identified as suitable for this thesis work. A detailed discussion regarding the compressor geometrical characterization is presented in section A.2.1, while performance aspects are treated in section A.2.2.

A.2.1 Compressor Meanline Method

Normally, centrifugal compressors are composed by the following sub-elements: impeller, vaneless and/or vaned diffuser. The main static pressure rise is given by the combination of impeller and diffuser. In most applications, the solely vaneless diffuser is sufficient to achieve the desired pressure ratio. However, this might require a long flow path not easily reducible, since a sufficient radius ratio is necessary to gain pressure rise from the conservation of the angular momentum [41, 43]. Therefore, a vaned diffuser could be introduced where significant pressure rise is needed to contain the compressor size. Lower efficiencies are normally experienced for off-design flow conditions.

For industrial compressor and turbocharger applications further pressure rise is achieved in the volute. For a well design volute system, the efficiency loss introduced is in the order of 2% to 5%, which makes their employed uncommon in aerospace compressors [154]. Therefore, volute modeling has not been addressed.

Impeller considerations

Most of the modeling effort has been dedicate to the characterization of the impeller due to the importance that this element has on the whole compressor performance. Since no energy is absorbed by the diffuser section, the entire power demand is determined by the flow conditions across the impeller. Moreover, as this element constitutes the major efficiency loss source [37]. Hence, most of the geometrical knowledge needed to employ empirical loss models belong to this element.

References [26, 41, 155] present an interesting meanline technique that provides sufficient design geometrical data for the successful employment of the Galvas loss model [36, 37]. The treatise is based on a general dimensionless analysis, derived from fundamental turbomachinery principles, that can be specialize to the particular case of interest, using known inlet flow data. Assuming inlet mass flow and stagnation conditions known, two assumptions hold in this method:

1. The working fluid is modeled as ideal gas.
2. No degree of prewhirl has been assumed ($\alpha_1 = 0$).

Two dimensionless group have to be defined before introducing the full methodology: the θ-parameter and dimensionless rotational speed (M_{u2}). The former represents the compressor non-dimensional mass flow rate, which can be expressed as function of the impeller inlet hub to tip ratio ($\nu = r_{1h}/r_{1s}$) and the impeller inlet tip/shroud to exit radius ratio (r_{1s}/r_2), as shown in [41].

$$\theta = \frac{\dot{m}}{\pi r_2^2 \rho_{01} a_{01}} = \frac{r_{1s}^2}{r_2^2}(1-\nu^2)\frac{\rho_1}{\rho_{01}}\frac{C_{1s}}{a_{01}} \tag{A.11}$$

The latter parameter is the impeller dimensionless rotational speed defined as: $M_{u2} = U_2/a_{01}$. Euler's turbomachinery equation expresses the compressor power per unit of mass flow as direct function of the velocity triangle, as shown by equation A.12.

$$\frac{\dot{W}}{\dot{m}} = (U_2 C_{\theta 2} - U_1 C_{\theta 1}) \tag{A.12}$$

From thermodynamic considerations, equation A.12 can be rewritten as:

$$\frac{T_{02}}{T_{01}} = 1 + \frac{\gamma - 1}{\gamma R T_{01}}(U_2 C_{\theta 2} - U_1 C_{\theta 1}) \tag{A.13}$$

The impeller total-to-total isentropic efficiency definition reported below can be further rearranged as explicit function of the impeller pressure rise (equation A.14).

$$\eta_I = \frac{h_{02_{id}} - h_{01}}{h_{02} - h_{01}} = \frac{(P_{02}/P_{01})^{(\gamma-1)/\gamma} - 1}{T_{02}/T_{01} - 1} \tag{A.14}$$

By combining equation A.13 with equation A.14, equation A.15 is obtained. This final form directly relates the impeller total-to-total pressure rise to the velocity triangle and the impeller efficiency parameter η_I.

$$\left(\frac{P_{02}}{P_{01}}\right)^{(\gamma-1)/\gamma} = 1 + \frac{\gamma - 1}{\gamma R T_{01}}\eta_I(U_2 C_{\theta 2} - U_1 C_{\theta 1}) \tag{A.15}$$

By replacing the impeller efficiency in equation A.15 with the overall total-to-total compressor efficiency (η_S), it is possible to compute the compressor stage pressure rise (Π_c). Hence, equation A.15 includes all the elements necessary to fully characterize the compressor behavior because it relates the thermodynamic of the machine with its aerodynamic design through the inlet/outlet velocity distribution. The complexity associated to the application of this relation lays on the determination of the efficiency and the tangential velocity components.

As discussed in detail by Whitfield and Baines [26, 41], major impeller loss sources can be identified with skin friction and tip clearance effects. The first is proportional to the square of the relative velocity and the flow path length, the second, depends on tip clearance gap to blade height ratio. Therefore, a procedure has been developed in reference [41] which defines the requirements for the impeller inducer and discharge elements with the intent of minimizing these two loss mechanisms.

Inducer design According to [41], the inducer has to guarantee that the required mass flow is entering the impeller with the lowest possible relative Mach number. This minimizes the design incidence losses. In addition, Rodgers [156] observed that the minimization of the inlet relative Mach number is also beneficial for obtaining stable operating conditions between choke and stall; as the stability range decreases with the increase of the relative inlet velocity.

For zero degree of prewhirl, the inlet velocity triangle can be expressed as follows:

$$W_{1s}^2 = C_{m1s}^2 + U_{1s}^2 \tag{A.16}$$

This relation can be algebraically rearranged in terms of Mach numbers into the final form given in equation A.17 [41]. The inducer relative Mach number (M_{1s_r}) is explicitly function of the dimensionless parameters introduced previously, ν and the absolute inlet Mach number (M_{1s}).

$$M_{1s_r}^2 = M_{1s}^2 + \frac{\theta M_{u2}^2}{(1-\nu^2)}\frac{1}{M_{1s}}\left(1 + \frac{\gamma - 1}{2}M_{1s}^2\right)^{\frac{3\gamma-1}{2(\gamma-1)}} \tag{A.17}$$

The graphical representation of equation A.17 has been reported in Figure A.1 as function of $\theta M_{u2}^2/(1-\nu^2)$. As displayed, the typical minimum inlet relative Mach number occurs for flow angles (β_{1s}) between -56 and -64 degrees.

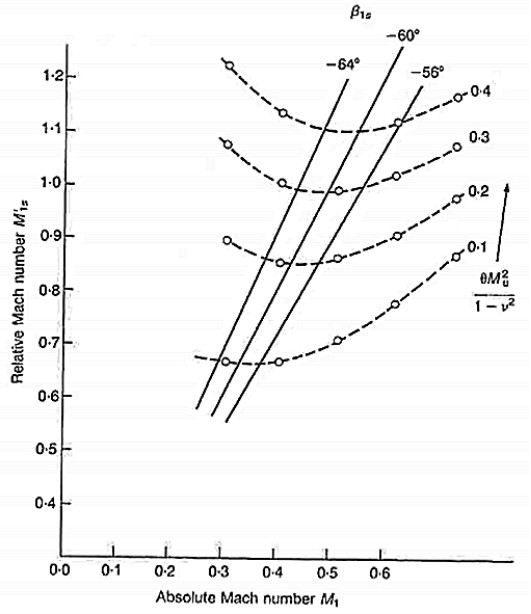

Figure A.1: Relative Mach number as a function of inducer absolute Mach number and $\theta M_{u2}^2/(1-\nu^2)$ [26]

To get the minimum relative Mach number for a given mass flow rate is possible to maximize the flow rate for a given relative Mach [41]. Stanitz [157] provides a methodology that allows to obtain the optimal flow angle (β_{1s}) to achieve the objective mentioned. By rewriting equation A.17 as explicit function of the flow angle, considering that $M_{1s} = M_{1s_r}\cos\beta_{1s}$, and by differentiating it with respect to β_{1s}, equation A.18 can be derived. The whole derivation is presented in [157] and summarized in [41], only the final form of the equation is below presented.

$$\cos^2\beta_{1s} = \frac{3+\gamma M_{1s_r}^2}{2M_{1s_r}^2}\left\{1-\left[1-\frac{4M_{1s_r}^2}{(3+\gamma M_{1s_r}^2)^2}\right]^{1/2}\right\} \tag{A.18}$$

The graphical result of equation A.18 is reported in reference [26, 41], showing the line of optimal β_{1s} on Figure A.1. Further discussion on the inducer design is reported in reference [155], showing the influence of the remaining impeller main design parameters onto M_{1s_r}.

By rearranging equation A.11, is possible to explicit the inlet tip to exit radius ratio as function of the θ-parameter and inlet Mach number (equation A.19). By combining this equation with equation A.17 is possible to calculate the value of r_{1s}/r_2 that ensures minimum relative Mach number for the given the mass flow, hence, concluding the inducer design.

$$\frac{r_{1s}}{r_2} = \left[\frac{\theta}{(1-\nu^2)M_{1s}(1+\frac{\gamma-1}{2}M_{1s}^2)^{-\frac{\gamma+1}{2(\gamma-1)}}}\right]^{1/2} \tag{A.19}$$

The link between inducer and discharge design is created by means of the dimensionless parameters, which ensures that continuity is respected. It has to be noted that all the geometrical quantities obtained so far have been expressed as fractions, leaving this approach perfectly adaptable to any impeller flow inputs.

Discharge design Equation A.15 can be rewritten into a form that depends only on dimensionless quantities and flow/blade angles. With the assumption of zero prewhirl and applying the isentropic speed of sound definition ($a_{01} = \sqrt{\gamma R T_{01}}$), equation A.15 becomes:

$$\Pi_c^{(\gamma-1)/\gamma} = 1 + (\gamma - 1)\eta_s \lambda M_{u2}^2 \tag{A.20}$$

This equation directly relates the stage total-to-total pressure ratio (Π_c) to the compressor velocity triangle via the work factor definition ($\lambda = C_{\theta 2}/U_2$). As shown in equation A.21, the work input coefficient is directly function of the impeller exit flow angle (α_2), the impeller exit blade angle (β_{B2}) and the slip factor (σ).

$$C_{\theta 2} = \frac{\sigma U_2}{1 - \tan\beta_{B2}/\tan\alpha_2} = \lambda U_2 \tag{A.21}$$

In a fully radial machine, due to the air inertia, the air trapped between the impeller vanes is reluctant to move around with the impeller, this effect implies a higher static pressure on the leading face of a vane than on the trailing face. For this reason, the air cannot acquire a whirl component which is equal to the machine rotational speed [111].

The coefficient σ in equation A.22 is employed to model this phenomenon called slip effect. A graphical explanation is also reported in Figure A.2 for purely radial and backswept impellers showing how the exit velocity triangle is affected by the slip effect.

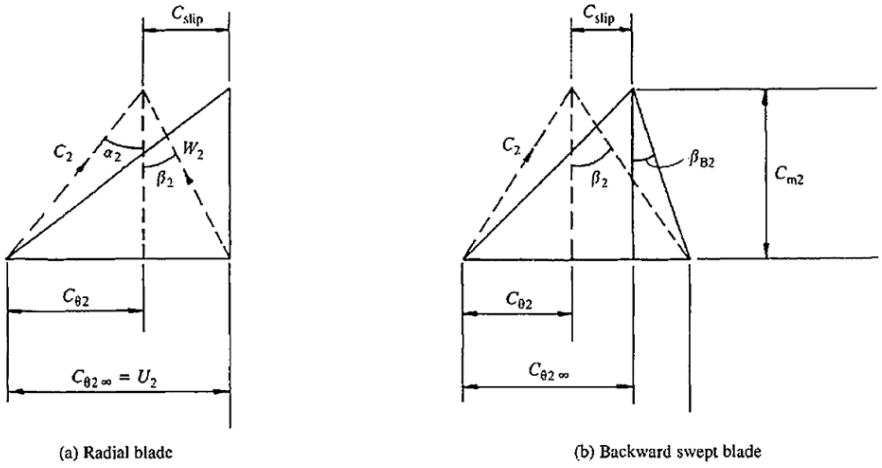

Figure A.2: Slip effect on impeller exit velocity triangle ($\sigma = 1 - C_{slip}/U_2$) [26]

As seen, the slip factor (σ) is a limiting feature of the work capacity of the compressor and it should be maximized. Different models are available in literature to accurately predict the value of σ. A detailed presentation of the slip factor empirical models is reported in the following paragraph. It can be anticipated here that the overall blade number parameter (Z_B) has an important influence on its value. In particular, increasing the vane number leads to a higher slip factor coefficient, with the drawback of augmenting losses due to friction.

Combining the definition of the exit absolute Mach number ($M_2 = C_2/a_2$) with equation A.21, equation A.22 can be obtained as shown in [41].

$$M_2 = \frac{M_{u2}\lambda/\sin\alpha_2}{\left\{1 + (\gamma - 1)M_{u2}^2\lambda[1 - (0.5\lambda/\sin^2\alpha_2)]\right\}^{1/2}} \tag{A.22}$$

The inlet shroud tip rotational speed (U_{1s}) is also related to the impeller inlet tip/shroud to exit radius ratio through the following relation:

$$\frac{U_{1s}}{a_{01}} = \frac{U_2 r_{1s}}{a_{01} r_2} \tag{A.23}$$

From the inlet velocity triangle (Figure A.2), equation A.24 can be derived to calculate the inlet relative Mach number or to verify that the minimum relative Mach number predicted with equations A.17 and A.18 is consistent.

$$M_{1s_r} = \frac{(U_{1s}/a_{01})/\sin\beta_{1s}}{1-[(\gamma-1)/2](U_{1s}/a_{01})^2/\tan^2\beta_{1s}} \tag{A.24}$$

Finally, from the application of the continuity equation, the discharge flow area can be expressed in terms of impeller flow and geometrical parameters as shown in [26, 41]. Further elaboration leads to equation A.25 which allows to compute the impeller channel exit width to radius ratio (b_2/r_2), thus, finalizing the impeller design procedure.

$$\frac{2b_2B_2}{r_2} = \frac{\rho_1}{\rho_2}\frac{r_{1s}^2}{r_2^2}(1-\nu^2)\frac{C_{m1}a_{01}}{a_{01}C_{m2}} \tag{A.25}$$

As previously done, equation A.25 can be rewritten in terms of the dimensionless parameters presented and the absolute exit Mach number. The final expression, given in equation A.26, is hereby presented without derivation for brevity. It can be obtained combining equations A.11 and A.14 with equation A.25, and applying the isentropic flow definition to transform the static densities into total ones: $\rho_0 = \rho(1+((\gamma-1)/2)M^2)^{(\gamma/(\gamma-1)}$.

$$\frac{b_2}{r_2} = \frac{\theta}{2M_2B_2}\frac{1}{\cos\alpha_2}\left(1+\frac{\gamma-1}{2}M_2^2\right)^{\frac{\gamma+1}{2(\gamma-1)}}\left[\frac{\eta_I}{\eta_S}(\Pi_c^{\frac{\gamma-1}{\gamma}}-1)+1\right]^{-\frac{\gamma}{\gamma-1}}\left(\frac{\Pi_c^{\frac{\gamma-1}{\gamma}}-1}{\eta_S}+1\right)^{1/2} \tag{A.26}$$

To employ equation A.25 or A.26, it is necessary to define the discharge blockage factor (B_2). According to Aungier [39], little guidance is available on literature to properly set this parameter, however, the following conclusions has been derived by the author: (1) the blockage factor is directly dependent on skin friction losses for impellers with a low flow coefficient, (2) rising the velocity diffusion head (ρW^2) from the blade throat to the blade discharge augments the blockage factor, (3) increasing the blade aspect ratio (b_2/L_B) proportionally affects the blockage coefficient and (4) B_2 grows with the blade clearance, in particular in open impellers.

Similar consideration have been derived also by Pampreen in [158]. In particular, it has been shown that the blockage factor depends equally on: flowpath and blade curvatures, diffusion, and the Coriolis acceleration up to the axial-radial bend of the flowpath. However, in the radial portion of the impeller, the further increment of B_2 can be efficiently correlated with the Richardson number ($Rn = \omega B/W_{min}$). Charts have been reported in [158], showing the variation of the impeller blockage coefficient as function of impeller meridional distance and rotational speed.

Aungier [40] proposes an empirical tip blockage factor correlation for a practical estimation of B_2. A similar form of the below presented equation is also available in [39].

$$B_2 = (\Delta q_{SF}+\Delta q_{HS})\frac{U_2^2}{W_2^2} + \left[0.3+\frac{b_2^2}{L_B^2}\right]\frac{A_R^2\rho_2 b_2}{\rho_1 L_B} + \frac{s_{CL}}{2b_2} \tag{A.27}$$

Δq_{SF} and Δq_{SF} are respectively the skin friction and the hub-to-shroud distortion loss coefficients ($\Delta q = \Delta h/U_2^2$), reported in [40]. s_{CL} is the clearance gap width and A_R is the area ratio defined in terms of the throat blade angle (β_{th}) as: $A_R = A_2\sin\beta_2/A_1\sin\beta_{th}$.

Before moving to the vaneless and vaned diffuser modeling, a graphical representation of the compressor performance behavior as function of the impeller parameters has been subsequently reported in Figures A.3 and A.4.

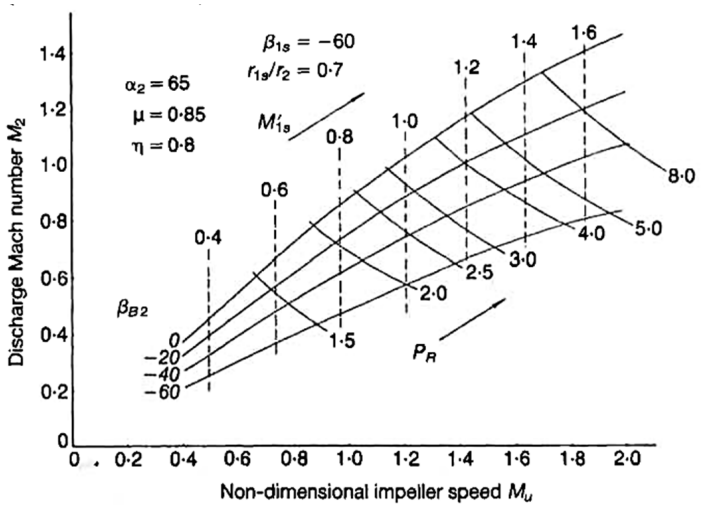

Figure A.3: Blade angle and pressure ratio influence on inlet relative Mach number, for a given inlet blade angle, exit flow angle, compressor total-to-total efficiency, slip factor and inlet tip/shroud to exit radius ratio [26, 41]

Figure A.3 can be obtained from equation A.20 and equation A.22 combined with the λ definition (equation A.21). The value of the remaining parameter is indicated in the plot for exact replication. The graph clearly shows one of the advantages of a negative backsweep angle which can be summarized as follows [41]: (a) reduction of discharge Mach number (M_2) with additional positive effect of decreasing the amount of diffusion required in the diffuser part, (b) increase of compressor stability range for a given mass flow and pressure ratio and (c) higher streamline curvature in the blade to blade plane, which causes a reduction of the pressure gradient between the blades with the associated decrease of secondary losses.

A major disadvantage of backswept configurations is also visible in Figure A.3. For the same compressor pressure ratio, the dimensionless rotational speed is significantly augmented. This is immediately translated into higher blades and disk centrifugal stress. Moreover the blades can no longer be constructed with purely radial fibers, which leads to significantly greater bending stresses, as reported in [41].

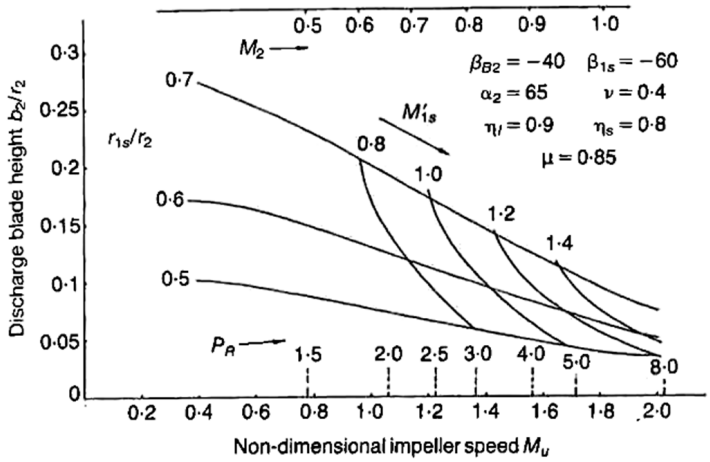

Figure A.4: Discharge blade height variation as function of r_{1s}/r_2 [26, 41]

Equations A.24 and A.26 are employed in realizing Figure A.4. The chart displays that to reduce the inlet relative Mach number, b_2/r_2 has to decrease considerably. As visible, for high pressure ratio compressors, two design options are available to minimize the losses from the

minimization of M_{1s_r}. The first implies a reduction of the radius ratio (r_{1s}/r_2), producing a long narrow impeller which leads to important skin friction losses. The second uses transonic inlet flows to contain the overall compressor dimensions with the disadvantage of increasing shock losses [41]. Hence, a trade-off solution must be found.

Slip factor As briefly mentioned, slip effects constitute a limitation on the work capacity of the impeller. Different models are available in literature to estimate the slip factor coefficient for a preliminary assessment. An extensive summary is reported in reference [159]. On of the simplest relation has been developed by Stanitz, which correlates the slip factor coefficient to the total blade number according to equation A.28.

$$\sigma = 1 - \frac{0.63\pi}{Z_B} \tag{A.28}$$

According to [26] this equation is satisfactory for a blade angle in the range $-45^\circ < \beta_{B2} < 45^\circ$. Wiesner [159] proposed a correlation (equation A.29) which well fits empirical results for conventionally used blade angles and blade number up to a certain limiting inlet to exit radius ratio factor (ε_{limit}).

$$\sigma = 1 - \frac{\sqrt{\cos\beta_{B_2}}}{Z_B^{0.7}} \tag{A.29}$$

Furthermore, the author proposed a relation for approximating the slip factor coefficient for solutions beyond this limiting radius ratio ($\varepsilon > \varepsilon_{limit}$), which is defined according to the following relation.

$$\varepsilon_{limit} = \frac{r_1}{r_2} \cong \exp\left(-8.16\frac{\cos\beta_{B2}}{Z_B}\right) \tag{A.30}$$

Finally the corrected slip factor can be calculated according to equation A.31. Evidence of good agreement between the presented treatise and empirical data is available in reference [159], in particular for conventional blade angle and blade number values.

$$\sigma_{cor} = \sigma\left[1 - \left(\frac{\varepsilon - \varepsilon_{limit}}{1 - \varepsilon_{limit}}\right)^3\right] \tag{A.31}$$

Aungier [39, 40] proposes a slightly modified version of equations A.30 and A.31, ensuring a better approximation of the empirical data reported in [159], however, not detailed evidence has been reported within these references. Equations A.32 and A.33 represents the slip factor model derived by the author.

$$\varepsilon_{limit} = \frac{\sigma - \sigma^*}{1 - \sigma^*} \tag{A.32}$$

Where, σ is the slip factor coefficient defined from equation A.29 and σ^* is a coefficient calculated from: $\sigma^* = \sin(19^\circ + 0.2 \cdot (90^\circ - \beta_{B2}))$. This relation has been made consistent with the definition of the blade angle used in this project. Same reasoning has been applied to equation A.33.

$$\sigma_{cor} = \sigma\left[1 - \left(\frac{\varepsilon - \varepsilon_{limit}}{1 - \varepsilon_{limit}}\right)^{\sqrt{\frac{90^\circ - \beta_{B2}}{10}}}\right] \tag{A.33}$$

According to Aungier [39], compressors designed for high rotational Mach numbers normally features splitter blades. Their purpose is to ensure that an acceptable blade solidity is maintained for a reduced blade blockage factor. In case splitter blades have been employed, the author

suggest to define the equivalent blade number according to equation A.34. With this definition, the theory presented so far is still applicable.

$$Z_B = Z_{FB} + Z_{SB}\frac{L_{SB}}{L_{FB}} \tag{A.34}$$

L represents the meridional blade length. It is common practice to use same blade shapes for full and splitter blades and place this lasts at mid-pitch location. As shown in [160], moving the splitter blade leading edge position have strong impact on the overall compressor performance.

Stahler [161] has indicated from experimental results that modeling the slip factor coefficient only as function of the blade number and exit blade angle does not lead to accurate results. A dependence from weight flow, rotational speed and impeller tip-diameter has also been identified by the author. A relation has been proposed in [161], which, however, cannot be generalized to any impeller. Hence, for the purpose of this thesis, the simplified models hereby presented have been considered sufficient for a preliminary slip factor estimation.

Diffuser considerations

The diffuser consists of a non-rotating channel with an increased flow area in the flow direction. This ensures the reduction of the absolute velocity leaving the impeller that is immediately translated into static pressure rise [25]. As seen, the diffusion system is usually composed by the sole vaneless diffuser or a combination of the former and a vaned section.

Regardless of the final diffusion architecture employed, a reasonable requirement for diffusers can be identified in the minimization of the overall losses for the same pressure rise. However, this condition is not sufficient to ensure a good overall centrifugal compressor design, especially for cases where the employment of vaned diffusers is necessary [42, 162]. In fact, as reported in [44, 163], to ensure promising stage performance, a good matching between the impeller and the vaneless/vaned diffuser is necessary.

Casey and Rusch [163] pointed out that highly efficient compressors can be realized if impeller and diffuser operate at their peak efficiency and they both have the same choke margin. In addition, the author derived a relation that provides the theoretical impeller-diffuser throat area ratio at which the optimal component matching can be achieved. The final form of this equation, valid for vaned diffusers, has been reported below.

$$\left(\frac{A_d^*}{A_i^*}\right)_{design} = \chi\frac{\left[1+\frac{\gamma-1}{2}\left(\frac{D_1}{D_2}\right)^2 M_{u2}^2\right]^{\frac{\gamma+1}{2(\gamma-1)}}}{\left[1+(\gamma-1)\lambda M_{u2}^2\right]^{\frac{n+1}{2(n-1)}}} \tag{A.35}$$

Where χ is the matching coefficient and n is the polytropic exponent. A χ value higher than one means that choking occurs first in the impeller section and vice versa. According to [163], the compressor should be designed with a χ value as close to the unity as possible. Moreover, the reference emphasizes that also compressor surge and stall behavior can be affected from an inaccurate component matching. Reference [44], reports an optimization procedure that involves the 1D theory briefly introduced in redesigning a diffuser system that better matches with the impeller. Benefit in overall compressor efficiency and stage pressure ratio have been documented.

In the following paragraphs, a quite detailed preliminary methodology is presented to model vaneless and vaned diffuser. Component matching aspects have been partially covered in this thesis, due to the complexity of the flow phenomena involved. Future work should address these aspects in more detail.

Vaneless diffuser Whitfield and Baines [41] provide a simplified method to quickly generate main geometrical data of the vaneless diffusion element. This approach is based on the ap-

plication of the angular momentum equation (equation A.36) to the vaneless diffuser section.

$$\tau = \dot{m}(r_3 C_{\theta 3} - r_2 C_{\theta 2}) \tag{A.36}$$

In the absence of wall friction force, the torque τ is null, reducing equation A.36 to the free vortex relationship reported below.

$$r_3 C_{\theta 3} = r_2 C_{\theta 2} \tag{A.37}$$

By combining equation A.37 with the continuity equation, equation A.38 can be obtained. This relation can be used to calculate the discharge flow angle α_3.

$$\tan \alpha_3 = \frac{\rho_3 b_3}{\rho_2 b_2} \tan \alpha_2 \tag{A.38}$$

The selection of the vaneless diffuser passage width (b_3) directly impacts the discharged flow angle. Hence, different vaneless arrangements have been created to have better control on the exit angle. This becomes particularly important for the correct coupling with a vaned section. Figures A.5 and A.6 illustrate different diffuser channel design options for purely vaneless and vaneless/vaned solutions. Reference [162] suggests that the most commonly used vaneless configuration is the pinched one because it provides a better stabilization of the high speed flow coming from the impeller. Examples of unpinched solution have also been reported in literature.

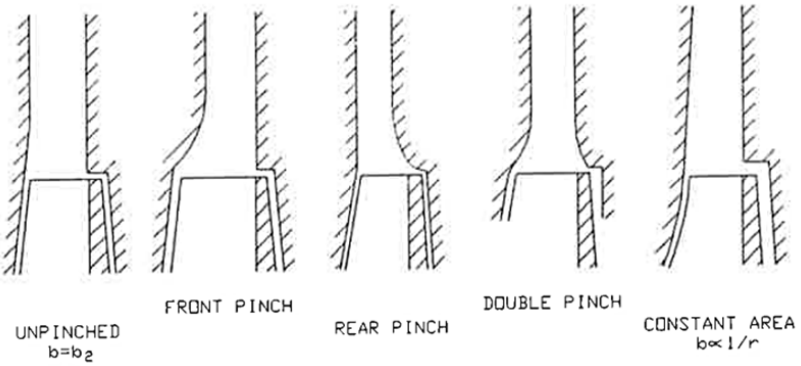

Figure A.5: Typical solely vaneless diffuser channel configurations [162]

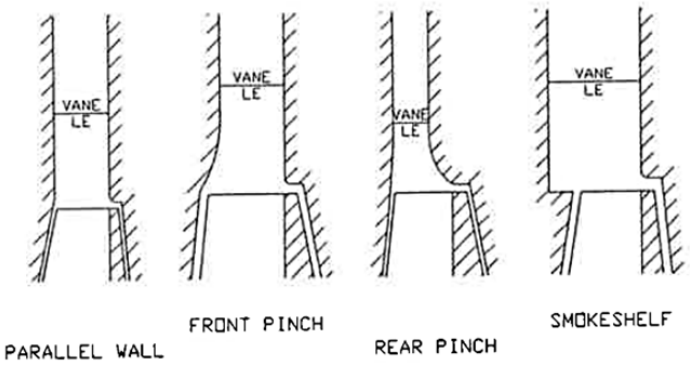

Figure A.6: Typical vaneless/vaned diffuser channel configurations [162]

Although sufficient for a preliminary design, the previously presented equations are not able to capture the pressure losses due to friction that typically occur in the vaneless space. Stanitz [43] developed a set of one dimensional differential equations for compressible flows relating Mach number, flow angle and total temperature to the vaneless diffuser radius ratio by means of

continuity, equilibrium, heat transfer and fluid state relations. Galvas [36, 37], simplifies those equations for adiabatic flow and geometrically constant depth passages. Equations A.39 and A.40 result using these assumptions. By discretizing these relations and using the inlet flow conditions known, the flow Mach number and flow angle can be locally calculated.

$$\frac{1}{M^2}\frac{\mathrm{d}M^2}{\mathrm{d}\overline{R}} = \frac{-2\left(1+\frac{\gamma-1}{2}M^2\right)}{M^2-\sec^2\alpha}\left[(\gamma M^2-\tan^2\alpha)\frac{\xi}{B\cos\alpha}+\frac{1}{B}\frac{\mathrm{d}B}{\mathrm{d}\overline{R}}-\frac{\sec^2\alpha}{\overline{R}}\right] \tag{A.39}$$

and

$$\frac{1}{\tan\alpha}\frac{\mathrm{d}\tan\alpha}{\mathrm{d}\overline{R}} = \frac{\sec^2\alpha}{M^2-\sec^2\alpha}\left\{\left[1+(\gamma-1)M^2\right]\frac{\xi}{B\cos\alpha}+\frac{1}{B}\frac{\mathrm{d}B}{\mathrm{d}\overline{R}}-\frac{M^2}{\overline{R}}\right\} \tag{A.40}$$

with

$$\xi = \frac{C_f r_2}{b_2} \qquad \overline{R} = \frac{r}{r_2} \qquad B = \frac{b}{b_2}$$

The effective passage depth (B) is influenced by the boundary layer displacement thickness. With the assumption of equally spaced parallel walls, the effective passage depth can be properly approximated as shown in [36, 37], thus solving numerically equations A.32 and A.33. The calculated Mach number and the flow angle distribution allow to compute the diffuser pressure losses due to friction as a function of diffuser length. This last will be determined via the iterating procedure presented in section A.2.2.

To reiterate, the advantage of this procedure lies in the possibility of estimating the friction losses within this component. This information would be totally absent with the previously treated method, giving justification for the additional modeling complexity.

Vaned diffuser For solutions that require a vaneless/vaned diffuser combination, a careful design is needed to obtain satisfactory compressor performance. In fact, the vaned diffuser constitutes the major source of losses after the impeller. Moreover, this element strongly affects the stability limits of the compressor, in particular, for off-design flow conditions [41]. Compressor performance can be enhanced by improving the diffuser pressure recovery and via proper matching between impeller and diffuser.

Al-Busaidi and Pilidis [114] have observed that a correct impeller-diffuser matching can be guaranteed in the majority of the cases. On the other hand, surge performance is more of a concern, being mostly dictated by features belonging solely to the vaned diffuser. To improve off-design performance, low-solidity diffusers have been investigated leading to higher stability ranges in comparison with conventional diffusers. The main characteristic of low-solidity diffusers is the absence of a geometrical throat. Because of this fact, the aerodynamic behavior of low-solidity diffuser is similar to the one experienced in vaneless diffusers where choking can only occur in the impeller throat. Thus, increasing the operating flow range of the compressor [113].

Furthermore, the individual vaned diffuser performance is influenced by the channel design and blade number. Reference [162] presents two different diffuser arrangements: the cascade diffuser and the channel diffuser. The first type is characterized by one or more rows of airfoil sections. Common practice is to employ consolidated axial compressors airfoils data, having detailed information on stall and overall performance. The second diffuser type is constituted by straight channels disposed at a certain angle with respect to the incoming flow. Japikse [162] reports that traditionally, the cascade diffuser have been considered to have performance and operational ranges in between vaneless and channel diffusers.

Regarding the blade number selection, Aungier [39] reports that the choice is influenced by both aerodynamic and resonances considerations. The author relates the vaned diffuser blade

number (Z_{VD}) with the impeller one (Z_I) as: $Z_{VD} = Z_I \pm 1$. A condition has to be included for the applicability of the previous relation since a low number of blades will improve stall margin with the disadvantage of increasing the vane loading. If the resultant number of blades falls in $10 \leqslant Z_{VD} \leqslant 20$ the selection can be considered satisfactory, otherwise Aungier suggests to apply: $|Z_{VD} - Z_I| \geqslant 8$. The final blade number choice will be influenced by more sophisticated consideration involving structural limitations as well, these guidelines can be used for preliminary assumptions.

As visible from this preliminary introduction, the complexity of the vaned compressor section design is considerable and multiple aspects have to be addressed during the detailed design. The purpose of this section is to provide simple preliminary guidelines to produce sufficient geometrical data to preliminary assess overall dimensions and performance of the vaned diffuser system. For this scope the methodology presented in references [113, 114] have been found satisfactory and in agreement with the goals of the project. Careful design involving also off-design part power considerations have to be addressed in subsequent phases. More details are reported below.

Modeling methodology As preliminary thing, it is necessary to relate the geometry of the vaned diffuser to the pressure recovery coefficient (C_p). C_p is an important parameter that allows to evaluate the diffuser performance, in fact, it measures the conversion of kinetic energy to static pressure between diffuser inlet and discharge [113]. The pressure recovery coefficient is defined as:

$$C_p = \frac{P_4 - P_3}{P_{03} - P_3} \tag{A.41}$$

If the diffuser efficiency (η_D) is available, the ideal pressure recovery coefficient can be calculated from equation A.41 according to the efficiency definition: $\eta_D = C_p/C_{p_{id}}$ [25]. Once the ideal pressure recovery coefficient is calculated it can be related to the vaned diffuser area ratio (equation A.42).

$$C_{p_{id}} = 1 - \frac{1}{AR^2} \tag{A.42}$$

Finally, the area ratio can be directly associated to the diffuser inlet and exit effective passage width as: $AR = W_4/W_3$, with $W_{3,4}$ defined as function of the blade angle with respect to the tangent direction, according to equation A.43.

$$W_{3,4} = \frac{2\pi r_{3,4} \sin \beta_{3,4}}{Z_{VD}} \tag{A.43}$$

Ultimately, the vaned diffuser length can be assessed from an assumed value of the effective divergence angle ($2\theta_c$) as shown by equation A.44, giving to the designer the sufficient level of detail requested in this preliminary phase.

$$L_v = \pi \frac{r_4 \sin \beta_4 - r_3 \sin \beta_3}{Z_{VD} \tan \theta_c} \tag{A.44}$$

Considerations on blockage factor have to be made for a better estimation of the diffuser geometrical characteristics and performance. As pointed out in [41], a crucial parameter controlling the channel diffuser performance is the inlet boundary layer blockage factor. As it is visible from Figure A.7, the inlet blockage coefficient has quite considerable effects on the peak pressure recovery coefficient for both high and low aspect ratio. This aspect will have to be taken into account in later design stages.

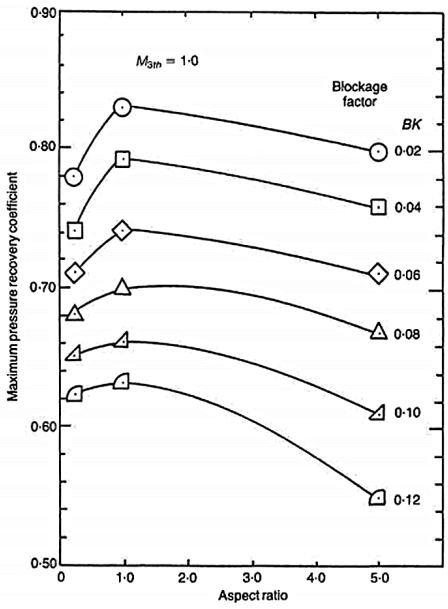

Figure A.7: Throat blockage and aspect ratio effects on pressure recovery coefficient [41]

This concludes the design of a conventional vaned diffuser. Information on inlet and exit flow area can be obtained from the continuity equation and the relations presented so far in this section. As support, a visual representation of the main vaned diffuser parameters discussed is reported in Figure A.8, showing the geometrical insight gained with the currently developed technique.

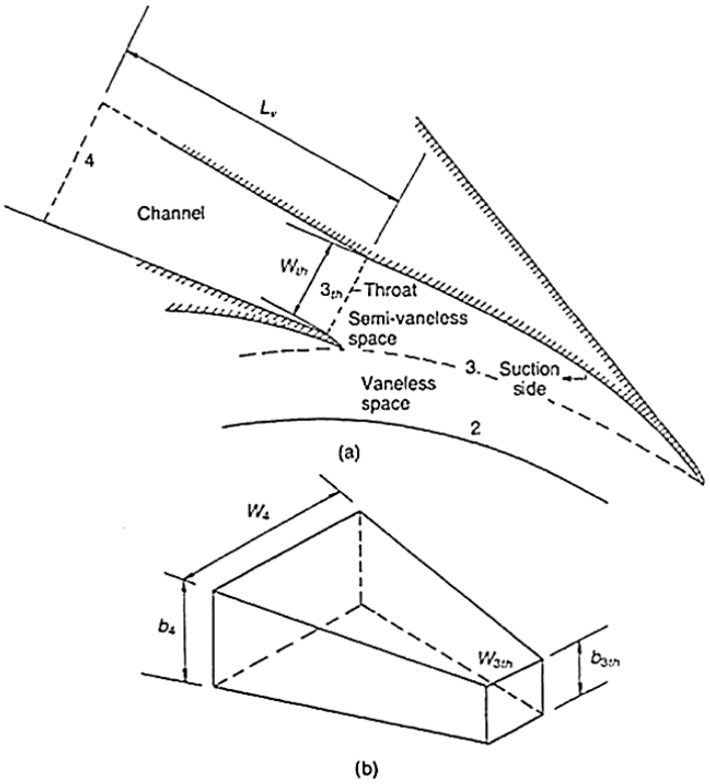

Figure A.8: Vaned diffuser channel [41]

The vane length expression for low-solidity diffusers differs from what presented for the conventional case. Kim et al. [113] have developed a preliminary sizing approach that is hereby

reported form completeness. Equation A.45 can be used to calculate L_v instead of equation A.44. In addition, the exit blade flow angle have to be calculated by means of equation A.46, which is explicitly function of the leading edge blade thickness (t_{LE}).

$$L_v = 2r_3 \sin\left(\frac{180}{Z_{VD}}\right) \cos\left(\beta_3 + \left(90 - \arccos\left[\sin\left(\frac{180}{Z_{VD}}\right)\right]\right)\right) \tag{A.45}$$

and

$$\beta_4 = \arctan\left[\tan\beta_3 + \frac{2\sin\left(180/Z_{VD}\right)}{\cos\beta_3} - \frac{t_{LE}}{2r_3\sin\beta_3}\right] \tag{A.46}$$

The optimal exit diffuser radius can be calculated from:

$$r_4 = r_3 \frac{\cos\beta_3}{\cos\beta_4} \tag{A.47}$$

The presented treatise can be concluded showing a typical vaned diffuser performance map that relates the main vaned diffuser geometrical parameters discussed with expected performance. In particular, Figure A.9 shows the pressure recovery coefficient as function of: diffusion angle, aspect ratio and non-dimensional length (L/W) defined as $L/W_{3_{th}}$ for a fixed inlet blockage factor ($2\delta^*/W$). This particular map has been extracted from reference [162] and it is related to a channel diffuser type. However, similar maps can be obtained for any diffuser type.

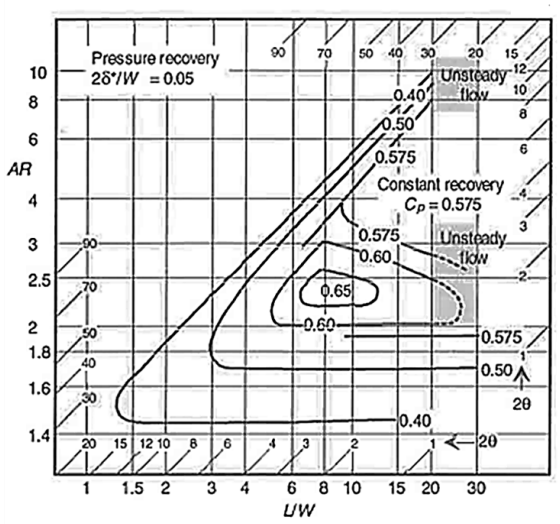

Figure A.9: Typical channel diffuser map [162]

A.2.2 Galvas Loss Model

As mentioned, the technique developed by Galvas has the advantage of being perfectly suitable for the 1D methodology presented in section A.2.1 and employed in this thesis work. The actual numerical implementation of the Galvas loss model used to characterized the compressor design point is discussed here. References [36, 37] provide additional information with respect to the off-design compressor modeling. Originally, the model proposed by Galvas accounts for the following loss factors: incidence, blade loading, skin friction, disk friction, clearance, recirculation, vaneless diffuser and vaned diffuser losses.

The treatise here is divided according to impeller and diffuser losses. The whole set of equations needed for modeling each loss contribution is provided. Moreover, the methodology implemented to account for the shock losses and for the estimation of the skin friction coefficient is also discussed. These aspects are not fully treated in the original documentation [36, 37].

Impeller loss model

For a swirl-free compressor inlet, the inlet velocity variation with radius can be calculated form the general velocity gradient equation, simplified for a swirl-free flow as reported in [36]. The final form is reported below.

$$C_m = C_{m1h} \exp\left(\int_0^n \Gamma dn\right) \tag{A.48}$$

Where Γ represents the streamline curvature, n the distance along the radius and C_m the absolute meridional velocity component. Galvas [36] suggests to approximate streamline curvature and slope by means of a linear interpolation of the values between hub and tip. In particular, the integration of equation A.48 is approximated using the trapezoidal rule from the hub to the root mean square location and the Simpson's rule between this last and the tip. Equations A.49 and A.50 have respectively reported.

$$C_{m1m} = C_{m1h} \exp\left(\left[\frac{h_0}{2}\left(\Gamma_{1h} + \Gamma_{1m}\right)\right]\right) \tag{A.49}$$

and

$$C_{m1t} = C_{m1h} \exp\left(\left\{\frac{h_0 + h_1}{6}\left[\left(2 - \frac{h_1}{h_0}\right)\Gamma_{1h} + \frac{(h_0 + h_1)^2}{h_0 h_1}\Gamma_{1m} + \left(2 - \frac{h_0}{h_1}\right)\Gamma_{1t}\right]\right\}\right) \tag{A.50}$$

Preliminary assumption of null hub and tip streamline curvature can be made to simplify the calculations as reported in reference [36]. With the established inlet axial velocity distribution, root mean square tangential velocity can be derived from equation A.51.

$$W_{1m} = \sqrt{C_{m1m}^2 + W_{\theta 1m}^2} \tag{A.51}$$

with

$$U_{1m} = U_{1s}\frac{D_{1m}}{D_{1t}} \tag{A.52}$$

Finally, the root mean square blade angle can be calculated from equation A.53. This initial root means square flow characterization is necessary in order to compute the incidence losses, as discussed in the following section.

$$\beta_{1m} = \tan^{-1}\left(\frac{W_{\theta 1m}}{C_{m1m}}\right) \tag{A.53}$$

Incidence loss Incidence losses depend on the extent that the actual inlet blade angle diverges from the optimal incidence angle (ϵ) for the given inlet flow conditions. ϵ is determined at the root mean square location from equation A.54. Compressibility effects are ignored, since much more significant compressibility impact is only visible at the impeller hub and negligible elsewhere [36].

$$\epsilon = \tan^{-1}\left(\frac{(1 - B_1)\tan\beta_{1m}}{1 + B_1 \tan^2\beta_{1m}}\right) \tag{A.54}$$

with

$$B_1 = 1 - \frac{Z_{FB} t_1}{2\pi r_1} \tag{A.55}$$

Therefore, the optimal relative flow angle can be obtained as: $\beta_{opt} = \beta_{1m} - \epsilon$. With this information available, equation A.56 can be solved and the component of relative velocity lost calculated.

$$W_L = W_{1m} \sin |\beta_{opt} - \beta_{1m}| \tag{A.56}$$

Finally, the enthalpy loss due to incidence effects can be assessed by means of the following equation:

$$\Delta h_{INC} = \frac{W_L^2}{2} \tag{A.57}$$

Blade loading The enthalpy loss due blade loading is calculated as function of the diffusion factor (D_f) from equation A.58.

$$\Delta h_{BL} = 0.05 D_f^2 U_2^2 \tag{A.58}$$

D_f is calculated in the Galvas's model with the following equation, taken from reference [164].

$$D_f = 1 - \frac{W_2}{W_{1s}} + \frac{K_{BL}\lambda}{\frac{W_{1s}}{U_2}\left[\frac{Z_{FB} + ZSB}{\pi}\left(1 - \frac{D_{1s}}{D_2}\right) + 2\frac{D_{1s}}{D_2}\right]} \tag{A.59}$$

Skin friction Skin friction losses are assessed by means of equation A.60

$$\Delta h_{SF} = K_{SF} C_f \frac{L/D_2}{D_{hyd}/D_2}\left(\frac{W}{U_2}\right)_{av}^2 U_2^2 \tag{A.60}$$

K_{SF} assumes values of 5.6 for conventional impellers and 7.0 impellers with splitter blades, C_f is the skin friction coefficient, which depends on surface roughness and Reynolds number as further illustrated in a dedicated section later on. L/D_2 is the mean flowpath blade length to diameter ratio defined according to [164] as:

$$\frac{L}{D_2} = \frac{r_2 - r_1}{D_2 \cos\beta_2} \tag{A.61}$$

The mean hydraulic to exit diameter ratio is calculated according to:

$$\frac{D_{hyd}}{D_2} = \frac{1}{\frac{Z_{FB} + Z_{SB}}{\pi \cos\beta_2} + \frac{D_2}{b_2}} + \frac{D_{1s}/D_2}{\frac{2}{1-\nu} + \frac{2(Z_{FB} + Z_{SB})}{\pi(1+\nu)}\sqrt{1 + \tan^2\beta_{1s}\left(\frac{1+\nu^2}{2}\right)}} \tag{A.62}$$

Finally, the mean relative velocity to impeller exit velocity ratio is computed from:

$$\left(\frac{W}{U_2}\right)_{av}^2 = \frac{1}{2}\left\{\left(\frac{C_{m1m}}{U_2}\right)^2 + \left(\frac{D_1}{D_2}\right)^2 + \left(\frac{W_2}{W_{1s}}\right)^2\left[\left(\frac{C_{m1m}}{U_2}\right)^2 + \left(\frac{D_{1s}}{D_2}\right)^2\right]\right\} \tag{A.63}$$

According to [36], studies have shown that the mean channel relative velocity is augmented in the splitter blades region, due to the employment of these lasts. The mean blade flow path length and the hydraulic diameter to exit diameter ratios remains almost unaltered. These aspects have been accounted in the different definition of the skin friction constant K_{SF}.

Disk friction The following relation is employed for calculating the enthalpy losses.

$$\Delta h_{DF} = 0.01356 \frac{\rho_2}{\dot{m} Re^{0.2}} U_2^3 D_2^2 \tag{A.64}$$

The Reynolds number in the previous equation is defined as function of the impeller exit dimensions and inlet total conditions. Equation A.65 reports the form to be used.

$$Re = \frac{\rho_{01} U_2 D_2}{\mu_{01}} \tag{A.65}$$

The total air viscosity can be calculated from inlet known conditions and using Sutherland's law.

Recirculation Losses associated to recirculation can be estimated from the equation reported below. The additional parameters are determined as previously presented.

$$\Delta h_{RC} = 0.02 \sqrt{\tan \alpha_2} D_f^2 U_2^2 \tag{A.66}$$

Shock Shock losses are not included in the Galvas's formulation; the equations presented have been taken from references [39, 40]. These losses occur when the inlet relative Mach number exceeds the inlet critical Mach number (M_{cr_r}). Equation A.67 is employed to calculate the enthalpy loss for this case.

$$\Delta h_{SH} = 0.2 \left[(M_{1m_r} - M_{cr_r}) \frac{W_{max}}{U_2} \right]^2 U_2^2 \tag{A.67}$$

where

$$W_{max} = \frac{W_1 + W_2 + \Delta W}{2} \tag{A.68}$$

And ΔW is the average blade velocity difference computed from standard irrotational flow relations, assuming the ideal blade loading style reported in Figure A.10.

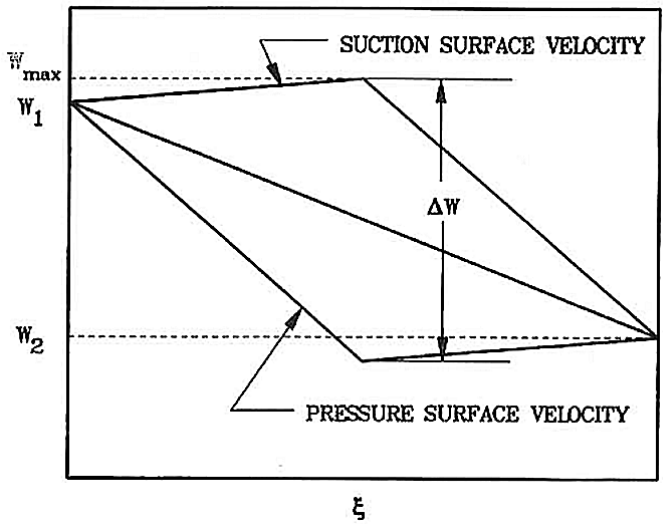

Figure A.10: Ideal or optimal blade loading model [39]

In the previous picture, ξ indicates the distance along the mean camberline. Equation A.69 allows to calculate ΔW with the previously mentioned assumptions.

$$\Delta W = \frac{2\pi D_2 U_2 \lambda_B}{Z_B L} \tag{A.69}$$

Where L is the length of the mean camberline, obtained from equation A.61 and λ_B represents the blade work input defined according to equation A.70, [39, 40]. Simplification can be made for a zero prewhirl angle.

$$\lambda_B = \sigma \left(1 - \frac{1}{1 - B_2}\phi_2 \cot \beta_2\right) - \frac{C_{\theta 1} U_1}{U_2^2} \tag{A.70}$$

Finally, the critical Mach number has to be defined to calculate the shock losses. Aungier [39, 40] calculates it according to equation A.71. Where, W^* represents the local sonic velocity calculated from relative total thermodynamic conditions at the midpassage.

$$M_{cr_r} = \frac{M_{1m_r} W^*}{W_{max}} \tag{A.71}$$

Diffuser loss model

Vaneless diffuser The vaneless diffuser losses can be calculated by means of equation A.72, once the component exit total pressure is known.

$$\Delta h_{VLD} = c_p T_{02} \left[\left(\frac{P_3}{P_{03}}\right)^{\frac{\gamma-1}{\gamma}} - \left(\frac{P_3}{P_{02}}\right)^{\frac{\gamma-1}{\gamma}} \right] \tag{A.72}$$

The exit total pressure can be determined from the discretization of equations A.39 and A.40. Since the effective passage width depends on the boundary layer growth within the vaneless diffuser, a model has been reported in [36, 37] to account for this aspect in the calculations. B can be discretized according to equation A.73, where $\Delta\delta^*$ is the incremental boundary layer displacement thickness.

$$B_{i+1} = B_i - \frac{2\Delta\delta^*}{b_2} \tag{A.73}$$

$\Delta\delta^*$ is calculated from:

$$\Delta\delta^* = 0.037 S^{-0.2} \left(\frac{C_2}{\nu_i}\right)^{-0.2} \Delta S \tag{A.74}$$

with

$$\Delta S = \frac{r_2 \Delta \overline{R}}{\cos \alpha_i} \qquad \text{and} \qquad S = \sum_{i=1}^{n} \Delta S_i$$

The total pressure loss in the vaneless space can be obtained from numerical integration of equation A.75 reported in [36, 37]. Alternatively, the assumption of conservation of total temperature within the channel can be made to further simplify the problem.

$$\frac{P_{02}}{P_{03}} = 1 + \frac{\gamma C_f}{\cos \alpha_2} \frac{r_2}{b_2} \frac{\int_1^{\overline{R}} M^3 \frac{a}{a_0} \frac{\rho}{\rho_0} \overline{R} d\overline{R}}{M_2 \left(\frac{a}{a_0}\right)_2 \left(\frac{\rho}{\rho_0}\right)_2} \tag{A.75}$$

Once the exit total pressure is know, the enthalpy loss in the vaneless diffuser can be finally determined with equation A.72.

Vaned diffuser Detailed diffuser loss models are available in [39, 165]. In these models, individual loss sources are defined similarly to this impeller case, and a more accurate diffuser description can be developed. Galvas [36, 37], calculates the vaned diffuser losses according to equation A.76. For the purpose of this work, this formulation has been found sufficient to characterize the component behavior.

$$\Delta h_{VD} = c_p T_{02} \left[\left(\frac{P_4}{P_{04}} \right)^{\frac{\gamma-1}{\gamma}} - \left(\frac{P_4}{P_{03}} \right)^{\frac{\gamma-1}{\gamma}} \right] \tag{A.76}$$

Efficiency definition Once all the individual loss contributions have been calculated, the impeller isentropic total-to-total efficiency (η_I) and stage isentropic total-to-total efficiency (η_S) can be calculated with equation A.77 and A.78 respectively.

$$\eta_I = \frac{\Delta h_{aero} - (\Delta h_{INC} + \Delta h_{BL} + \Delta h_{SF} + \Delta h_{SH})}{\Delta h_{aero} + \Delta h_{DF} + \Delta h_{RC}} \tag{A.77}$$

and

$$\eta_S = \frac{\Delta h_{aero} - (\Delta h_{INC} + \Delta h_{BL} + \Delta h_{SF} + \Delta h_{SH} + \Delta h_{VLD} + \Delta h_{VD})}{\Delta h_{aero} + \Delta h_{DF} + \Delta h_{RC}} \tag{A.78}$$

Skin friction coefficient

An accurate prediction of the skin friction coefficient is important, since skin friction losses constitute one of the major enthalpy loss source in both impeller and diffuser. A common skin friction model has been reported in [39], where, the value of C_f is estimated from generalized pipe friction data. In this treatise, the skin friction coefficient is determined as function of the Reynolds number based on pipe diameter ($Re_d = \rho V d/\mu$) and the peak-to-valley surface roughness coefficient (e).

Equations have been derived to compute the skin friction coefficient depending on the flow regime in the pipe. Distinction between laminar and turbulent regions is made from consideration on the Reynolds number. In particular, if $Re_d < 2000$ the flow is considered laminar and C_f is calculated from:

$$C_{f_l} = \frac{16}{Re_d} \tag{A.79}$$

For $Re_d > 4000$ the flow is fully turbulent, equation A.80 has to be employed for a smooth surface, while equation A.81 has to be used for a non negligible surface roughness.

$$\frac{1}{\sqrt{4C_{f_{t,s}}}} = -2 \log \left[\frac{2.51}{Re_d \sqrt{4C_{f_{t,s}}}} \right] \tag{A.80}$$

and

$$\frac{1}{\sqrt{4C_{f_{t,r}}}} = -2 \log \left[\frac{e}{3.71 d} \right] \tag{A.81}$$

For Reynolds number between 2000 and 4000 transition between laminar and turbulent flow regime is experienced. This phenomenon is model by means of a weighed average of the quantities previously introduced. The effects of the surface roughness starts to become significant after a certain region. This is accounted by defining an alternative Reynolds number (Re_e) that directly includes the roughness dependency. Equation A.82 has been derived for such cases.

$$Re_e = (Re_d - 2000) \frac{e}{d} \tag{A.82}$$

The turbulent skin friction is defined as:

$$\begin{aligned} C_{f_t} &= C_{f_{t,s}} \qquad \text{for} \qquad Re_e < 60 \\ C_{f_t} &= C_{f_{t,s}} + (C_{f_{t,r}} - C_{f_{t,s}}) \left(1 - \frac{60}{Re_e}\right) \qquad \text{for} \qquad Re_e \geqslant 60 \end{aligned} \tag{A.83}$$

Finally, the skin friction coefficient in this region can be calculated as:

$$C_{f_{tr}} = Cf_l + (Cf_t - Cf_l) \left(\frac{Re_d}{2000} - 1\right) \tag{A.84}$$

With these approximations, the so called Moody chart can be plotted as shown in Figure A.11.

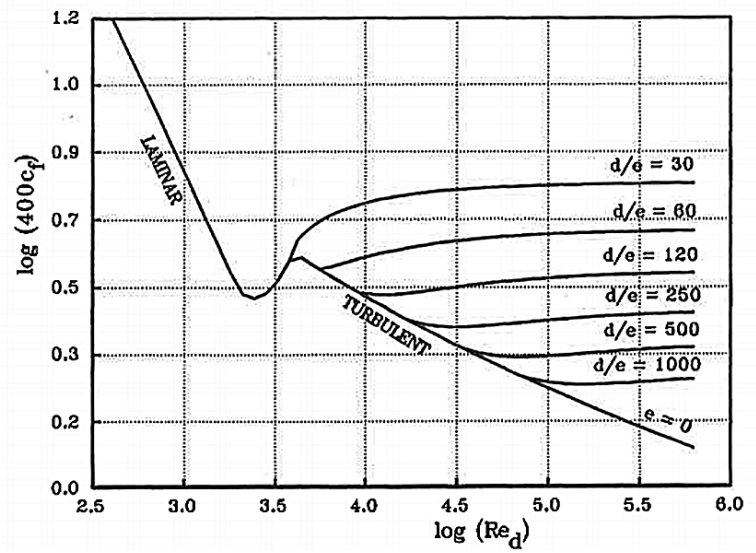

Figure A.11: Skin friction coefficient correlations plot [39]

According to [39], these equations can be adapted to describe the skin friction coefficient behavior within the compressor. In particular, the Re_d definition can be adapted to the impeller case if the pipe diameter d is replaced by the hydraulic diameter D_{hyd}, obtained from equation A.62, and to the vaneless diffuser using $d = 2b_2$ instead. Moreover, the author provides equation A.85 to convert root mean square surface roughness (e_{rms}), commonly employed to describe the compressor surface roughness, into the peak-to-valley equivalent. The assumption of a sine-wave roughness distribution has been made.

$$e = \frac{2e_{rms}}{0.707} = \frac{e_{rms}}{0.3535} \tag{A.85}$$

from what reported here the skin friction coefficient to be used in equations A.60, A.39, A.40 and A.75 can be properly determined. In the following part of this appendix, a detailed discussion on the actual implementation will be presented.

A.3 Model Implementation

The detailed compressor model built in Matlab is constituted by three main parts: (1) impeller design, (2) diffuser design, and (3) performance evaluation. Considering inlet flow condition known from NPSS, the compressor building blocks are preliminary sized for assumed impeller and stage total to total efficiencies, following the treatise presented in section A.2.1. In this way, the geometrical dimensions needed for the compressor loss and weight model are established.

Throughout further iteration between the detailed design model and the loss model, the efficiency and main geometry of the compressor are further refined. This section discusses the implementation of the whole compressor model, dividing the treatise according to the constitutive elements previously listed. More details on the selection of compressor key design parameters are given, providing a more complete explanation on the modeling choices made throughout the project development.

A.3.1 Impeller Design

As visible from equation A.20, three main parameters are strongly influencing the impeller design: the pressure ratio (Π_C), the rotational speed (N) and the impeller exit radius (r_2). These lasts two variables are embedded in the M_{u2} definition, considering that $U_2 = (2\pi N r_2)/60$. Typically, the compressor design is carried out by specifying a target overall pressure ratio. Therefore, ignoring for a moment the contribution of η_S and λ in equation A.20, the design can be generated by specifying one of the two remaining variables (r_2 or N).

Fixed rotational speed is the technique adopted in this project for the cycle optimization, since a much easier interaction with the NPSS compressor element is possible. Nonetheless, the impeller block allows for sufficient customization which has helped during the validation phase. This section discusses the implementation of the impeller model, showing how the code has been built in Matlab, using the theory discussed in section A.2. Details on the aerodynamic evaluation of the output design are given, together with reasons behind impeller design variables and bounds used for the cycle optimization.

Model Description

The following inputs are used to design the impeller: gas constant (γ), dimensionless mass flow (θ), design pressure ratio (Π_C) or dimensionless rotational speed (M_{u2}), inlet tip to hub radius ratio (ν), exit flow angle (α_2), backsweep angle (β_2) and slip factor (σ), defined from the equivalent blade number (equation A.34), according to one of the methods previously presented. In addition, a maximum value of M_{1s} and/or M_2 can be specified. For such cases, the code attempts to design the impeller according to the specified Mach number, otherwise, the standard design procedure discussed in references [26, 41] is adopted.

Figure A.12 summarizes the design steps necessary to characterize the impeller geometry. Reference to the mathematical equations needed for the model are reported in the picture as well. Starting from the input data listed previously, the code performs the standard design of the impeller, which has the objective of minimizing inlet relative Mach number and exit Mach number (solid lines), unless $M_{1s,max}$ and/or $M_{2,max}$ are specified. The code allows to design the impeller for a given dimensionless rotational speed or pressure ratio. This last mode has been applied in this project.

If a maximum inlet Mach number is given, the codes simply calculated the required β_{1s} for satisfying the condition, otherwise, an iterative procedure starts to determine the optimal inlet blade angle from an initial guess of M_{1s}, by means of equation A.18. On the other hand, if a maximum value of $M_{2,max}$ has been set, the code iteratively varies β_2, initially assumed null, to meet the exit Mach number condition. If unsuccessful, an error is returned.

Note that if the unconventional design mode is set, the overall compressor efficiency might not be optimal. Increased incidence and friction losses should be expected with respect to the standard design procedure [26, 41]. During the optimization, a maximum inlet Mach number has been defined for the HPC to ensure proper component matching with the previous element as explained in section 5.4 for each engine model.

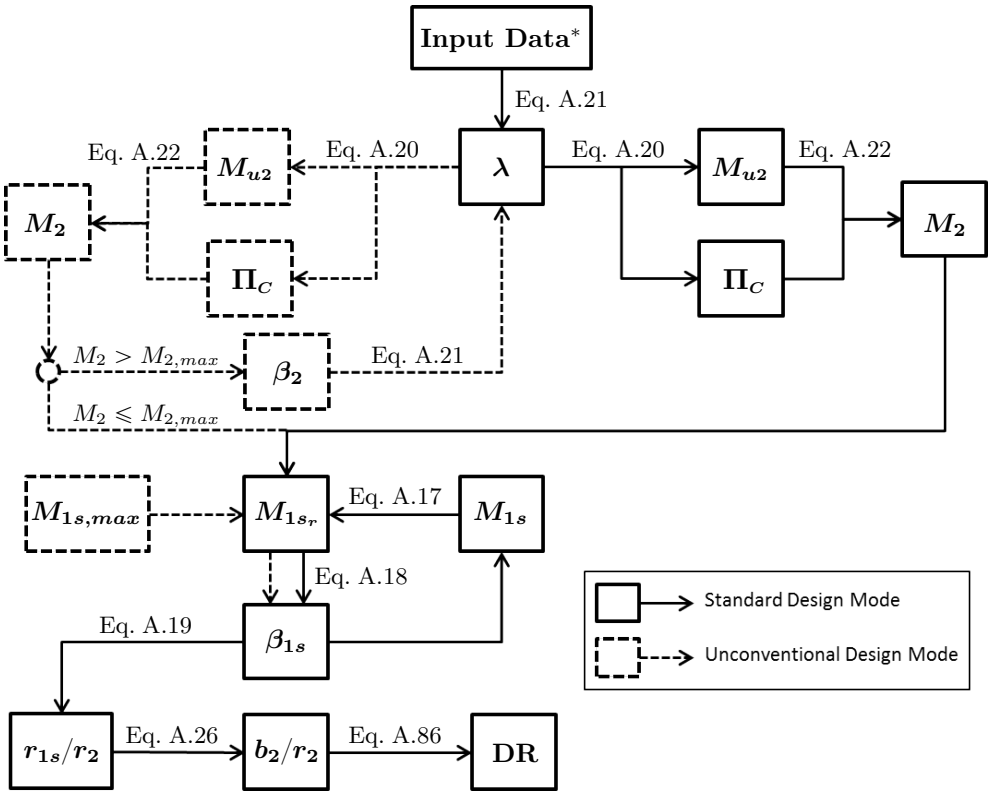

Figure A.12: Impeller design code schematic

From the known inlet flow conditions, the dimensionless groups, obtained from the presented impeller design methodology, can be easily transformed into a dimensional form. Thus, fully characterizing the impeller geometry and flow mechanism. Inlet-outlet flow continuity is ensured by this procedure through the definition of the θ-parameter. The resultant impeller design has to be assessed to ensure its aerodynamic feasibility. Further details are provided in the following paragraph.

Design Assessment

References [26, 41] report a discussion on the impeller internal diffusion limitations that the final design should satisfy. High diffusion rates have been associated by many author to the inception of the impeller stall. Harley [42] employs a diffusion ratio (DR) value of 2.4 in his analysis to identify impeller surge. A precautionary value of 2.0 has been set in this work as limitation for the impeller design acceptability, as indicated in [112]. The definition of DR is given in equation A.86. Any impeller design resulting in a DR grater than 2.0 will be discarded.

$$DR = \frac{W_{1s}}{W_2} = \frac{r_{1s}/r_2}{(1 - 2\lambda + \lambda^2/\sin^2\alpha_2)^{1/2}\sin\beta_{1s}} \tag{A.86}$$

Figure A.13 shows the influence of the impeller exit flow and blade angles on the diffusion ratio. In particular, increasing α_2 leads to relatively high DR values, while, a more negative backsweep angle contributes to the reduction of this parameter. Although high impeller diffusion rates are desirable to limit the diffuser size, boundary layer separation problems are likely to occur [26]. Therefore, the final selection of α_2 and β_2 depends on trade-off considerations between diffusion requirements and flow stability margin.

*As suggested in [26, 41], η_I and η_S have been initially assumed 0.9 and 0.8, and updated using empirical loss models. Typically, this initial assumption is pessimistic for low pressure ratio designs, while optimistic for high pressure ratio.

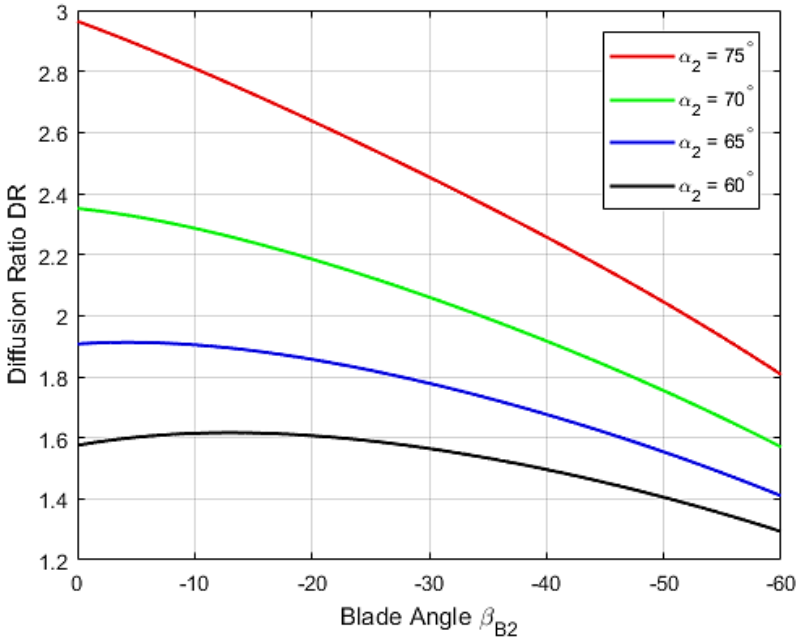

Figure A.13: Diffusion ratio as function of α_2 and β_2, assuming $\sigma = 0.85$, $r_{1s}/r_2 = 0.70$ and $\beta_{1s} = -60°$; adapted from [41]

Whitfield and Baines [41] indicate that optimal specific speed (equation A.87) range should be within 0.705 and 1.018, for typical centrifugal compressor designs. These values have been originally identified by Galvas [37] to be proper of the region of maximum efficiency for backsweep impellers. However, this range cannot be considered a strict design requirement, applicable to any design pressure ratio [26]. Hence, it has not been included within the compressor feasibility assessment.

$$n_s = \frac{\omega\sqrt{\dot{V}}}{\Delta h_{0s}^{3/4}} = \frac{(r_{1s}/r_2)^{3/2}(pi/\tan\beta_{1s})^{1/2}(1-\nu^2)^{1/2}}{(\lambda\eta_S)^{3/4}} \tag{A.87}$$

Considerations gathered from this paragraph have been used during the optimization to perform the aerodynamic design assessment of the resultant LP and HP compressors. Furthermore, guidance has been found here to constrain the selection of primary impeller inputs, such as: α_2, β_2, ν and Z_B, that have a strong impact on the overall compressor efficiency. Thus, supporting the definition of the impeller design bounds during the optimization (section 5.3.2). The following paragraph treats these aspects with further details.

Design Variables Considerations

Large flow angles are associated to the inception of stall and flow reversal phenomena, which might lead to a violent compressor surge [26]. References [26, 41] indicate that optimal α_2 values lay between 60° and 70°.

The positive effects of using negative backsweep angles can be appreciated from Figure A.3. Significant reduction of the impeller discharge Mach number is experienced for any given pressure ratio, even though impeller higher rotational speeds are needed. Typical backsweep angles are selected between 0° and -60° [26, 41]. Because high β_2 values are associated to significant blade stress levels, a maximum backsweep angle of -40° has been admitted for the optimization.

Since the definition of the inlet hub to tip radius ratio is mostly influenced by structural reasons as well as by aerodynamic blockage considerations [26, 41, 143], common practices can be only adopted at this stage. A small ν value is beneficial for the reduction of the impeller

inlet Mach number, however, sufficient space has to be guarantee to accommodate the selected blade number. Typical hub to tip ratios lay between 0.3 and 0.7, according to [37].

The selection of the blade number is much more critical. Rodgers [145] reports a study conducted on the effects of the blade number onto centrifugal compressor impellers. It has been shown that the optimum blade number is function of specific speed, blade backsweep and M_{u2}. Typically, the compressor efficiency decreases with low blade numbers due to the augmented impeller slip effects. On the other hand, an excessive blade number causes an increase of skin friction penalties, thus having a negative impact on the overall machine performance. Moreover, associated manufacturing and blockage problems have to be expected.

Splitter blades may be employed to limit the issues presented. A study reported in [166] shows a 2.7% efficiency improvement if splitter blades are located at 50% of the impeller hub curve. Finally, Rodgers [145] concluded that, due to manufacturing costs, it is uncommon to exceed a total blade count of 30, even when splitter blades are employed. Furthermore, the author shows that a value of approximately 20 blades leads to the minimum efficiency decrements for typical compressor specific speed ranges. Hence, this last number has been assumed for the compressors defined in this project. No splitter blades have been considered.

Once the blade number has been chosen the slip factor can be calculated using one of the available models. Since, extremely high accuracy at this stage is not required, a widely employed model is the Wiesner's model [159], given as equation A.33. With all these considerations, the impeller can be sized and the optimization bounds can be defined accordingly.

A.3.2 Diffuser Design

As previously discussed, the compressor diffuser has been modeled as a vaned diffuser preceded by a vaneless interspace. This section briefly presents the assumptions and the implementation of the whole diffuser model, dividing the treatise according to the two diffuser types considered: vaneless and vaned.

Vaneless Diffuser Design

The design of the vaneless diffuser has been defined according to the methodology proposed by Galvas in [37]. The inputs required by the code for the analysis are available after the impeller design block has been completed. In fact, impeller exit flow conditions and channel geometrical data are used by this function to characterize the vaneless diffuser exit flow and dimensions.

The whole design is based on equations A.39 and A.40, opportunely discretized and assuming a constant vaneless depth ($b_2 = b_3$). Ten nodes have been chosen for the discretization in order to speed up the calculations [36, 37]. The vaneless exit radius (r_3) has been set as suggested by in reference [37]. Initially, an exit to inlet radius ratio (r_3/r_2) value of 1.02 has been assumed and this value has been increase by 0.001 each iteration until the calculated exit Mach number (M_3) has been found less that 0.8 [37]. If the calculated impeller exit Mach number already satisfied this requirement, a vaneless diffuser radius ratio of 1.02 have been maintained for clearance between impeller and vaned diffuser.

Furthermore, a maximum impeller exit Mach number ($M_{3,max}$) can also be specified. The code will vary the vaneless exit to inlet radius ratio to meet the new condition, if feasible. Note, this mode has not been used in the optimization section and the indication of Galvas [37] have been respected. At this level, the losses associated to the vaneless space have been calculated following the procedure presented in section A.2.2 and assuming conservation of total temperature within the channels.

Vaned Diffuser Design

The vaned diffuser design can be directly generated from the equations provided in section A.2.1, assuming known inlet flow condition and channel dimensions from the vaneless section. In particular, the vaneless diffuser exit Mach number and flow area have been considered representative of the vaned diffuser throat as suggested in [37]. An assumption has to be made regarding the desired exit Mach number in order to perform the calculations.

Galvas [37] suggests to employ a value of 0.2 which leads to a desirable combustor entry velocity. In case multiple compressors have been used or flow links with different elements (intercooler or mixer) have to be made, a maximum exit Mach number variable ($M_{4,max}$) has been created and left to the user to set. This facilitates component flow matching, and it has been widely used during the cycle optimization, as discussed in section 5.3.2.

Assuming conservation of total temperature within the vaned diffuser, the exit flow condition can be fully determined from the total to total design pressure ratio and diffuser exit Mach number requirements. This allows for the definition of the theoretical pressure coefficient that meets this condition (equation A.41). The diffuser length can be calculate from equation A.44 and the diffuser ares using continuity and equation A.43. Where, the vane number has been defined according to [39].

Two constraints have to be applied on the vaned diffuser section. The former is associated to the equivalent divergence angle ($2\theta_c \leqslant 11^\circ$) and the latter to the vane loading ($V_L \leqslant 1/3$). These limits have been reported in [39, 113]. As it is visible from equation A.44, a great divergence angle would be beneficial to contain the vaned diffuser length. On the other hand, a θ_c value too large leads to diffuser stall problems [113]. Moreover, since the vane loading measures the average vane-to-vane pressure difference to the inlet discharge pressure difference, its value should not exceed what indicated [39]. Equation A.88 reports the definition of V_L. This value has been used as compressor constraint in addition to the diffusion ratio defined for the impeller.

$$V_L = \frac{2\pi(r_3 C_{\theta 3} - r_4 C_{\theta 4})}{Z_{VD} L_v (C_3 - C_4)} \tag{A.88}$$

Finally, Aungier [39] suggests the following limitations as optimal for a well designed vaned section. Since it will not always be possible to satisfy those indications, they have been reported here for completeness, while the the previously listed thresholds have been instead used.

$$\begin{aligned} 10^\circ \leqslant 2\theta_c \leqslant 11^\circ \\ 0.3 \leqslant V_L \leqslant 0.33 \end{aligned} \tag{A.89}$$

A.3.3 Performance Evaluation

Once all the individual elements have become ready, the full compressor can be assembled. The compressor code performs the design using the general input data discussed in section 4.2.1. In particular, flow data are gathered from the NPSS thermodynamic cycle calculations, while geometrical and design data are specified by the optimizer or according to common practice. The compressor is normally designed for a given pressure ratio and rotational speed, alternatively the impeller exit radius can be specified.

Depending on the running mode and the slip model chosen, different iterations will be required to define the necessary inputs to be sent to the impeller function. Once the impeller has been designed the remaining components can also be sized as explained. The matching between elements have been guaranteed by verifying that the continuity equation holds between elements.

After the full compressor has been designed, the performance loss model (section A.2.2) can be applied and the initially assumed impeller and stage efficiencies are updated. The iteration continues until a default tolerance has been satisfied or the maximum amount of iterations

has been reached. A final diagram summarizing the complete compressor sizing procedure is reported in Figure A.14.

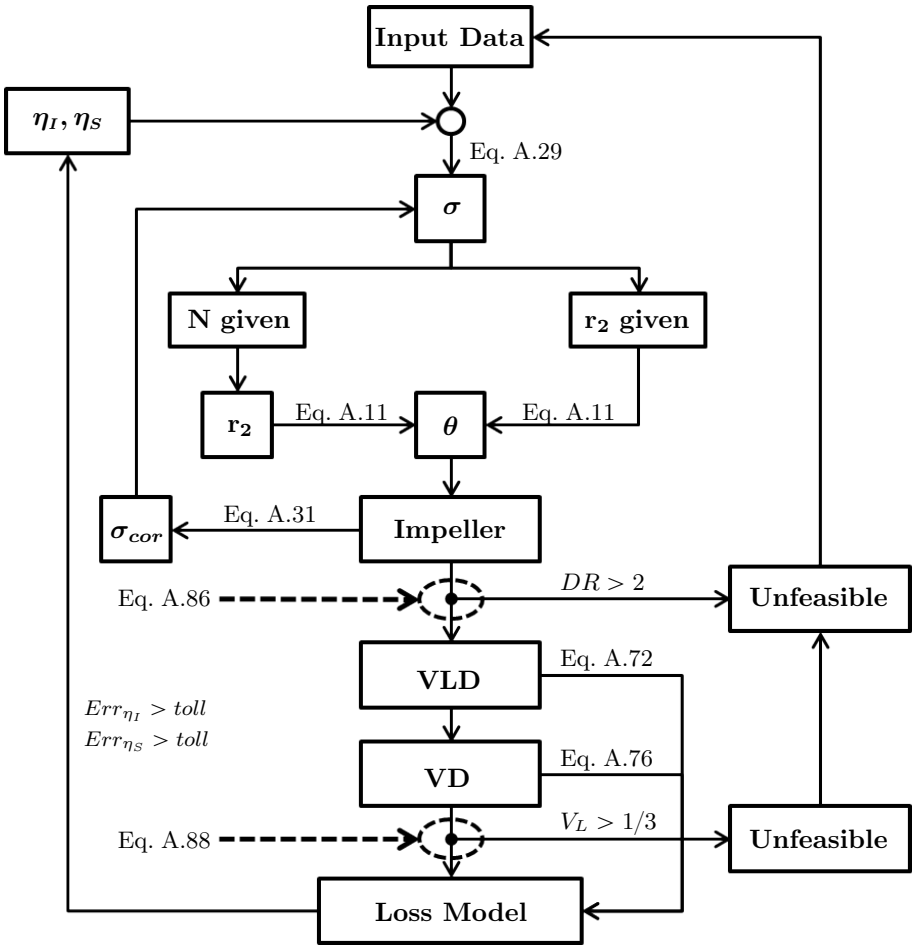

Figure A.14: Centrifugal compressor design code schematic

Since Wiesner's slip factor model [159] is employed in this analysis, an additional iteration is needed to properly define the value of σ for impellers having the radius ratio (r_1/r_2) beyond the limit given by equation A.30. Once completed the full aerodynamic compressor design, enough geometrical insight has been gained for the weight model.

APPENDIX B

Radial Turbine

This appendix provides information regrading the turbine modeling techniques employed in this thesis. Following what presented for the compressor model, a preliminary section focused on literature review aspects is firstly presented. Detailed information on radial turbine simple models is presented in section B.1, followed by a discussion on the more complete model used in this project (section B.2). A detailed description of the three loss models briefly introduced in the main body of this document is presented in section B.2.2. Furthermore, the actual implementation of the radial turbine model is treated in section B.3.

B.1 Simple Models

A similar approach to the one discussed for the compressor, is also conventionally employed in the performance modeling of radial turbines. Typically, simple relations have been proposed to adapt reference turbine data to a reduced scale machine, according to the similarity principle reported in [22, 23, 27]. Efficiency correction models have been introduced to account for scale effects and manufacturing limitations. According to Rodgers [16], radial turbines do not suffer significantly form pressure ratio and Mach effects, as for the compressor case. Therefore, only a brief discussion on the first two aspects listed will be presented in section B.1.1. Alternatively, simple equations have been derived to model the turbine design behavior as function of general thermodynamic cycle data. Similar limitations already pointed out for the compressor modeling can be identified in this simplified treaties. Thus, giving justification for the more advanced model presented in section B.2.

B.1.1 Turbine Scaling Technique

Compressor and turbine scaling techniques differ only slightly. Since pressure ratio and Mach effects are not extremely determinant in the overall turbine performance, in particular for a given pressure ratio below 5.0 [16], only models to account for size and manufacturing considerations are discussed below.

Size effects

According to [30], equations A.1 and A.4 are applicable to model scaling effects in radial turbines. The Reynolds ratio exponent (n) assumes a value of 0.16 in the first formulation and 0.2 for the second, while a is selected within the range defined for compressors. References [16, 31] propose a simplified version of the previously mentioned equations, where the scaling factor is defined as direct function of the diameter ratio instead of the Reynolds ratio. Similar considerations made in appendix A.1.1 hold here.

Lunnan [30] has shown that compressor models have been improved by correlating the scaled efficiency as function of the skin friction coefficient, instead of the Reynolds number. No documentation is available regarding the applicability of a similar approach to radial turbines. However, since theoretical aspects behind the Reynolds dependent losses are similar, the models used for compressors might result applicable to turbines as well.

Manufacturing considerations

Similarly to the compressor, manufacturing aspects represent a constraint that has to be accounted in the estimation of the maximum efficiency achievable. Rodgers [16] discusses the impact of clearance on the turbine efficiency, presenting a model which relates these losses to the effective clearance gap to blade height ratio parameter (C_t/h_t). Equation B.1 is used to model this loss contribution. Moreover, the author states that for radial turbines minimal absolute gaps achievable are of about 0.015in (∼0.0381cm).

$$\Delta\eta_t = 0.10\frac{C_t}{h_t} \tag{B.1}$$

Surface roughness constitutes another limiting aspect since it directly affects the skin fiction losses, as shown in the compressor section. No simple models have been found for radial turbines that relates the scaled efficiency directly to the skin friction coefficient, although the validity of equation A.5 might be extendable [30].

B.1.2 Empirical Relations

Simple relations have been proposed by Korakianitis and Wilson [32, 33] that can be employed for a preliminary analysis. Equation B.2, reported in the first document, predicts the total-to-total polytropic efficiency as function of the turbine pressure ratio defined as: $\Pi_T = P_{00}/P_{03}$.

$$\eta_{t,poly} = 0.90 - \frac{\Pi_T - 1}{250} \tag{B.2}$$

A slightly more advanced equation is reported in [33], valid only for radial machines. Equation B.2 allows for the determination of the turbine total-to-static polytropic efficiency as function of the total to static pressure ratio and the rotor exit tip diameter.

$$\eta_{poly,ts} = 0.6984 D_{3h}^{0.0449} - \frac{\Pi_{T,ts} - 1}{200} \tag{B.3}$$

Similar issues belonging to the compressor simple models can be identified here for the turbine case. More sophisticated techniques are needed to improve the performance modeling and to provide sufficient geometrical insight for a component based engine weight model. The following section deals with these aspects with more detail.

B.2 Advanced Models

The goal of this section is to present a more advanced model able to overcome the limitations observed for simplified techniques. The treatise proposed by Whitfield and Baines [41] have been found perfectly suitable for the commonly employed turbine loss models. In addition, sufficient geometrical insight can be derived to predict the influence of thermodynamic cycle parameters on the turbine weight and feasibility.

This section initially provides details on the meanline method employed within this project for the rotor and the nozzle turbine parts. Finally, the loss models presented by Rohlik [47, 48] and Glassman [49, 50] are accordingly discussed. Furthermore, the Glassman's loss model improvements proposed by Baines [51] are presented.

B.2.1 Turbine Meanline Method

Radial turbines are composed by a rotor, with the function of extracting power from the working fluid, preceded by a nozzle which imparts some swirl and accelerate the flow. For industrial and turbocharger applications, a volute might be present before the nozzle, introducing similar limitation discussed for the compressor case. Therefore, models have been investigated only for the nozzle-rotor combination.

Particular focus is dedicated to the rotor modeling because this component has a determinant impact on the overall turbine performance. The nozzle analysis has been kept as simple as possible, since this element has not to deal with an adverse pressure gradient such as the diffuser section of a centrifugal compressor.

Rotor considerations

The preliminary technique presented in [41, 46] has the objective of estimating the primary rotor geometrical features to meet the design performance requirements. The methodology mainly focuses on those aerodynamic aspects that strongly affect the overall turbine performance, leading to a geometrical output as close as possible to the optimum. However, because of the complexity of the flow pattern, an optimized solution can only be obtained in later design stages, involving structural considerations as well.

Nonetheless, this preliminary method has been found in agreement with the objective of this work and it represents a good starting point for further analysis. Sufficient data can be derived to characterize the component design performance behavior as well as to estimate its weight. This methodology is applicable under the following assumptions:

1. The working medium behaves as an ideal gas.
2. The flow leaving the rotor is fully axial ($\alpha_3 = 0$).
3. The rotor blades are radially disposed ($\beta_{B2} = 0$)

Similarly to the compressor impeller method, this approach employs turbine quantities in a dimensionless form to perform the design. An important parameter for the turbine is the design power output, expressed into a non-dimensional form by means of equation B.4.

$$S_w = \frac{\dot{W}}{\dot{m} h_{01}} = 1 - \frac{T_{03}}{T_{01}} \tag{B.4}$$

The power ratio (S_w) is related to the turbine total to static pressure ratio from:

$$\frac{P_{01}}{P_3} = \left(1 - \frac{S_w}{\eta_{S_{ts}}}\right)^{-\gamma/(\gamma-1)} \tag{B.5}$$

Where $\eta_{S_{ts}}$ is the total-to-static efficiency defined as:

$$\eta_{S_{ts}} = \frac{1 - T_{03}/T_{01}}{1 - (P_{01}/P_3)^{(\gamma-1)/\gamma}} \tag{B.6}$$

Moreover, a non dimensional mass flow rate coefficient (θ) and the dimensionless rotational speed (M_{u2}) are also used here. The former is defined according to equation B.7, as for the compressor case.

$$\theta = \frac{\dot{m}}{\pi r_2^2 \rho_{01} a_{01}} = \frac{r_{3s}^2}{r_2^2}(1 - \nu^2)\frac{\rho_3}{\rho_{01}}\frac{C_{3s}}{a_{01}} \tag{B.7}$$

The rotor design has been divided into two primary sections: the rotor inlet design and the rotor discharge design. A separate treatise is presented below for both rotor ares, underlining

key modeling aspects of their design. Moreover, the link between these sections is explained, providing a better understanding of the whole rotor flow dynamic model.

Inlet design Reference [41] reports that higher turbine efficiency has been experienced for inlet flow angles that do not match exactly with the radial blade direction. This phenomenon has been attributed to a flow mechanism analogous to the compressor slip factor. In fact, the pressure difference between the blade pressure and suction side pushes the flow towards this last against the direction of rotation. Therefore, the flow is designed to enter the impeller with a negative relative angle β_2. Results of studies have been summarized in [41] showing that an optimal inlet relative angle lays between -20° and -40° degrees. On the other hand, excessively negative relative inlet flow angles make the flow more likely to separate on the blade suction surface [45]. Figure B.1 illustrates the rotor inlet flow mechanism briefly discussed.

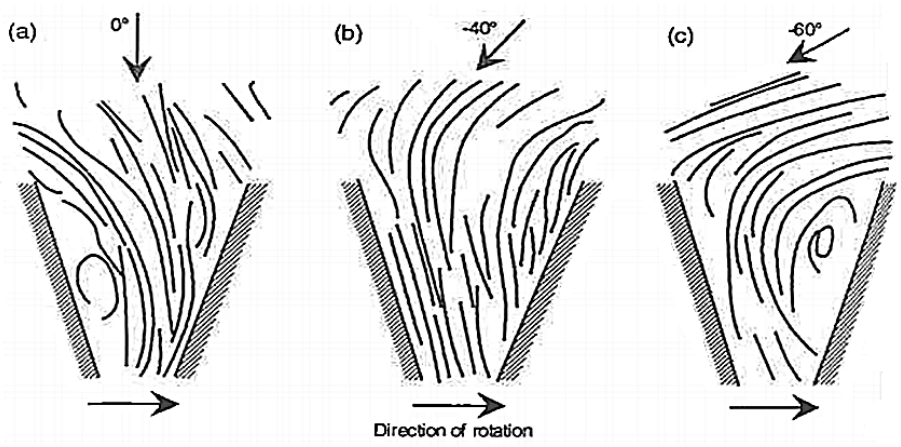

Figure B.1: Typical flow streaklines disposition as function of turbine relative inlet flow angle [45]

Using Euler's equation specialized to the radial turbine and simplified for an purely axial exit flow direction ($\dot{W}/\dot{m} = U_2 C_{\theta 2} - U_3 C_{\theta 3} = U_2 C_{\theta 2}$), equation B.8 can be derived.

$$\frac{U_2}{a_{01}} \frac{C_{\theta 2}}{a_{01}} = \frac{S_w}{\gamma - 1} \tag{B.8}$$

Considering the rotor inlet velocity triangle reported in Figure B.2, it is possible to derive an equation that correlates the inlet flow angles with the turbine power demand. In fact, noticing that: $C_{\theta 2} = U_2 + C_{m2} \tan \beta_2$ and $C_{\theta 2} = C_2 \sin \alpha_2$, the following equation can be derived:

$$\tan^2 \alpha_2 \left(1 - \frac{U_2 C_{\theta 2}}{a_{01}^2} \frac{a_{01}^2}{C_2^2} \right) - \tan \alpha_2 \tan \beta_2 - \frac{U_2 C_{\theta 2}}{a_{01}^2} \frac{a_{01}^2}{C_2^2} = 0 \tag{B.9}$$

Equation B.9 is quadratic in $\tan \alpha_2$ and has physical meaning only if the solution has a positive square root. This can be used to set a condition on the discriminant of the previous equation as shown from equation B.10.

$$\tan^2 \beta_2 + 4 \left(1 - \frac{U_2 C_{\theta 2}}{a_{01}^2} \frac{a_{01}^2}{C_2^2} \right) \frac{U_2 C_{\theta 2}}{a_{01}^2} \frac{a_{01}^2}{C_2^2} = 0 \tag{B.10}$$

Combining equation B.10 with B.8, and following the procedure discussed in [41], equation B.11 can be obtained. This equation gives the minimum possible inlet Mach number for a given power ratio and relative flow angle.

$$\left(\frac{C_2}{a_{01}} \right)^2 = \frac{S_w}{\gamma - 1} \frac{2 \cos \beta_2}{1 + \cos \beta_2} \tag{B.11}$$

and

$$\left(\frac{C_2}{a_{01}}\right)^2 = \left(\frac{C_2}{a_{02}}\right)^2 = \left\{\frac{M_2^2}{1+[(\gamma-1)/\gamma]M_2^2}\right\}^{1/2} \tag{B.12}$$

Moreover, the non-dimensional rotational speed correspondent to the minimum possible inlet Mach number is given by the following relation:

$$\left(\frac{U_2}{a_{01}}\right)^2 = \frac{1}{\gamma-1}\frac{S_w}{\cos\beta_2} \tag{B.13}$$

Simplifying equation B.9 for minimum inlet Mach number, the following relation can be derived to calculate the inlet absolute flow angle [41]:

$$\tan\alpha_2 = \frac{\sin\beta_2}{\cos\beta_2 - 1} \tag{B.14}$$

With this information, the whole characterization of the inlet velocity triangle is made in a dimensionless form for minimum M_2. According to [41, 46], it is possible to specify an inlet Mach number that exceeds the minimum admissible. However, an excessively high Mach number leads to augmented stator losses, increased rotor velocities and stronger incidence losses in off-design flow conditions. Therefore, the minimization of M_2 for a given S_w and β_2 is highly recommended.

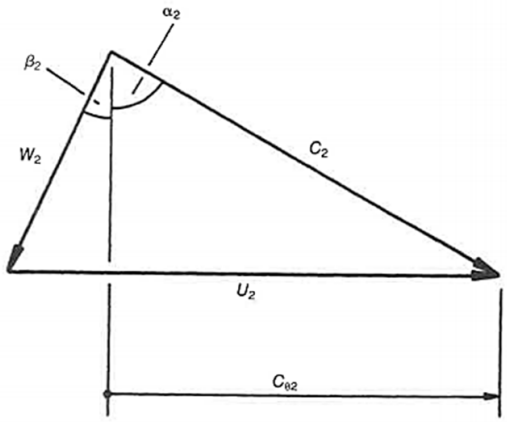

Figure B.2: Rotor inlet velocity triangles [41]

Optimal flow angles References [41, 46] presents a method to quantify the optimal rotor incidence flow angle and consequently β_2. Since the flow mechanism at the rotor inlet is governed by a phenomenon similar to the compressor slip effect, the incidence factor (λ) has been correlated using compressor slip factor equations. Equation B.15 is commonly used [41].

$$\lambda = \frac{C_{\theta 2}}{U_2} = U_2\left(1 - \frac{0.63\pi}{Z_B}\right) \tag{B.15}$$

For minimum inlet Mach number condition, equation B.16 can be obtained by combining the previously shown expressions as reported in [41]. This equation directly associates the relative inlet flow angle with the blade number. Since the minimum inlet Mach number solution represents the optimum for a radial turbine, equation B.16 also defines the optimal β_2 for a given blade number.

$$\cos\beta_2 = 1 - \frac{0.63\pi}{Z_B} \tag{B.16}$$

As visible from Figure B.3, radial turbines rotors with a blade number between 12 and 20 have optimal relative flow angles between -33 and -26 degrees.

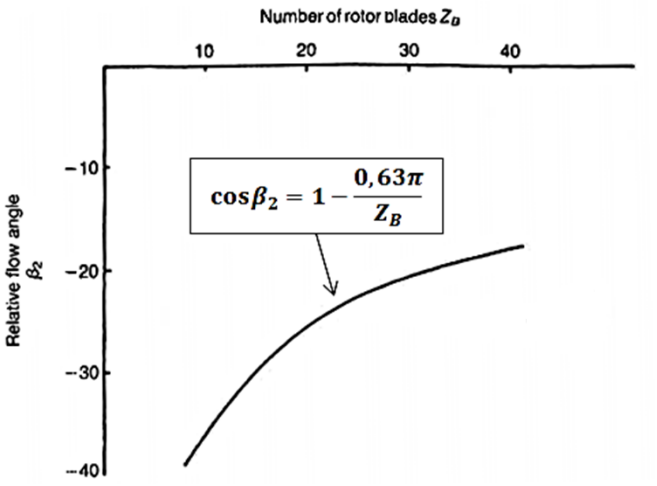

Figure B.3: Optimal relative inlet flow angle as function of blade numbers, adapted from [41]

Criteria for optimal blade number selection have been initially developed by Jamieson (equation B.17) and Glassman (equation B.18) [41], as function of the inlet flow angle.

$$Z_{B,min} = 2\pi \tan \alpha_2 \tag{B.17}$$

and

$$Z_{B,min} = \frac{\pi}{30}(110 - \alpha_2) \tan \alpha_2 \tag{B.18}$$

Equation B.17 is preferable since the Jamieson's formulation leads to an excessive blade number in particular at high inlet flow angles [41]. Visual representation of the two previously discussed equations is reported below.

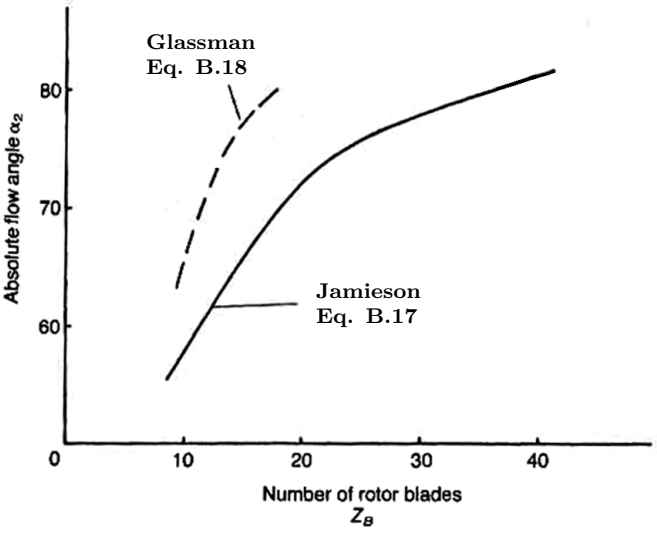

Figure B.4: Absolute inlet flow angle as function of blade numbers, adapted from [41]

Exit design Similarly to the compressor inducer modeling, the design procedure developed for the turbine rotor exit has the objective of minimizing the relative Mach number (M_{3s_r}). With the assumption of zero absolute exit flow angle, equation B.19 is derived [41].

$$M_{3s_r}^2 = M_{3s}^2 + \frac{\theta M_{u2}^2}{(1-\nu^2)} \frac{1}{M_{3s}} \left(1 + \frac{\gamma - 1}{2} M_{3s}^2\right)^{\frac{1}{2}} \left(\frac{T_{01}}{T_{03}}\right)^{\frac{1}{2}} \frac{P_{01}}{P_3} \tag{B.19}$$

where ν is the rotor exit hub to shroud/tip ratio ($\nu = r_{3h}/r_{3s}$), while, the compressor total to total temperature ratio (T_{01}/T_{03}) and total to static pressure ratio (P_{01}/P_3) can be expressed in terms of S_w according to equations B.4 and B.5. Figure B.5 reports a visual representation of equation B.19, showing that minimum exit relative Mach number occurs for a value of β_3 of about 55°. The selection of larger relative flow angles leads to the reduction of the exit losses, while values from 0 to -50 degrees have been ruled as unsatisfactory, according to [41].

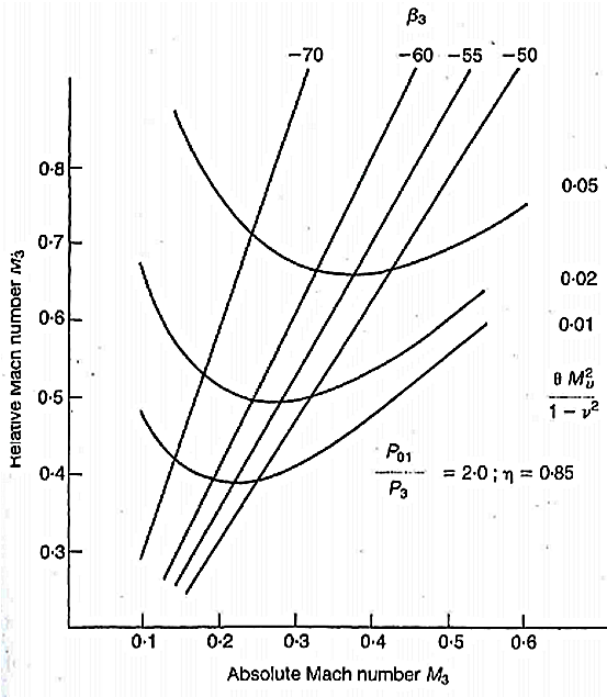

Figure B.5: Absolute and relative exit Mach number as function of relative flow angle [41, 46]

With these considerations, a preliminary estimation of β_3 can be made, thus, fully defining the rotor exit velocity triangle. The magnitude of the absolute exit velocity is derived according to one of the best practice design rules summarized in [41]:

- Since a value of the relative velocity ratio ($W_R = W_{3s}/W_2$) significantly greater than one ensures good expansion in the rotor, Rohlik [47] suggests to use a magnitude of W_R equal to 2.0.
- Rodgers and Geiser [167] have correlated the turbine total to static effciency against the discharge velocity ratio (C_{m3}/U_2), as reported in Figure B.6. A value of 0.25 for the discharge velocity ratio has been indicated as optimal [41].

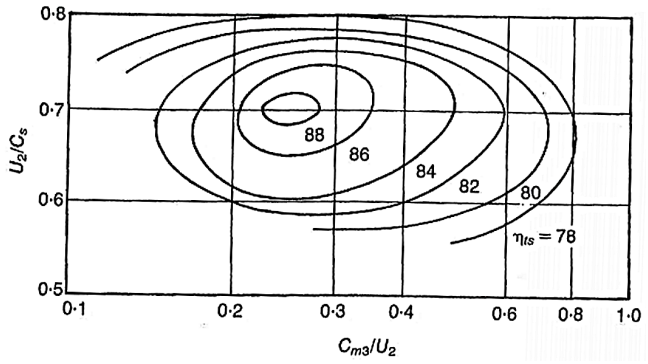

Figure B.6: Attainable radial turbine efficiency as function of velocity ratio, taken from [41]

References [41, 46] employ the approach proposed in the first item of the previous list to complete the exit design. However, since the discharge velocity ratio and relative velocity ratio parameters refer to the same velocity triangles, they can be easily correlated using basic trigonometric relations. Equation B.20 results from the previously discussed approach.

$$W_R = \frac{C_{m3}}{U_2} \frac{\sin\beta_2 + \cos\beta_2 \tan\alpha_2}{\cos\beta_{3s}} \tag{B.20}$$

With W_R specified, the exit relative Mach number can be calculated from equation B.21, [41, 46].

$$M^2_{3s_r} = W^2_R M^2_{2_r} \frac{T_2}{T_{02}} \frac{T_{02}}{T_{03}} \frac{T_{03}}{T_3} \tag{B.21}$$

where T_3/T_{03} and W_{3s}/a_{03} are defined according to equation B.22 and B.23, respectively.

$$\frac{T_3}{T_{03}} = 1 - \frac{\gamma - 1}{2} \frac{W^2_{3s} \cos^2\beta_{3s}}{a^2_{03}} \tag{B.22}$$

and

$$\frac{W_{3s}}{a_{03}} = W_R \frac{W_2}{a_{01}} \left(\frac{T_{01}}{T_{03}}\right)^{1/2} \tag{B.23}$$

Once established the rotor inlet and outlet velocity triangle, the rotor area ratio (A_3/A_2) is calculated by means of equation B.24, resulting from the application of the continuity equation between inlet and outlet [41].

$$\frac{A_3}{A_2} = \frac{\theta_2 \rho_{02} a_{02}}{\theta_3 \rho_{03} a_{03}} = \frac{\theta_2 \rho_{02}}{\theta_3 \rho_{03}} \left(\frac{T_{01}}{T_{03}}\right)^{1/2} \tag{B.24}$$

θ_2 and θ_3 represent respectively the inlet and exit dimensionless mass flow coefficients. Since the correspondent absolute Mach numbers are available at this stage, these two parameters can be expressed according to the following equations, [41]:

$$\theta_2 = \frac{\dot{m}}{\rho_{02} a_{02} A_2} = M_2 \cos\alpha_2 \left(1 + \frac{\gamma - 1}{2} M^2_2\right)^{-\frac{\gamma+1}{2(\gamma-1)}} \tag{B.25}$$

and

$$\theta_3 = \frac{\dot{m}}{\rho_{03} a_{03} A_3} = M_3 \left(1 + \frac{\gamma - 1}{2} M^2_3\right)^{-\frac{\gamma+1}{2(\gamma-1)}} \tag{B.26}$$

The calculation of the area ratio can be completed upon determination of the rotor density ratio (ρ_{02}/ρ_{03}). This can be done as shown in equation B.27, using the assumption of ideal gas.

$$\frac{\rho_{02}}{\rho_{03}} = \frac{P_{02}}{P_{03}}\frac{T_{03}}{T_{02}} = \frac{P_{02}}{P_{01}}\frac{P_{01}}{P_{03}}\frac{T_{03}}{T_{01}} \tag{B.27}$$

Each parameter in equation B.27 can be determined by combining previously discussed relations, with the exception of the stagnation pressure across the stator (P_{02}/P_{01}). This parameter can be obtained from the total to static stator efficiency definition (equation B.28) and the rotor inlet Mach number previously determined.

$$\eta_{N_{ts}} = \frac{1-(T_2/T_{01})}{1-(P_2/P_{01})^{(\gamma-1)/\gamma}} \tag{B.28}$$

Finally, the design methodology is completed by determining the exit radius to inlet radius ratio (r_{3s}/r_2), from equation B.7, and the inlet blade height to radius ratio (b_2/r_2) using equation B.29.

$$\frac{b_2}{r_2} = \frac{1}{2}\left(\frac{r_{3s}}{r_2}\right)^2(1-\nu^2)\frac{A_2}{A_3} \tag{B.29}$$

Stator considerations

The function of the nozzle stator section is to provide the rotor inlet with the optimal incidence flow angle. Furthermore, the flow is further accelerated before entering the rotor and any flow non-uniformity removed [41]. Since the losses occurring in the nozzle section account for a small percentage over the overall turbine [47], between 5% and 15% for a very restricted throat area [41], preliminary calculations are normally conducted with the assumption of isentropic flow.

According to [124], it is common practice to maintain the nozzle passage width constant and coincident with the rotor inlet dimension ($b_2 = b_0$). Conservation on angular momentum is typically assumed, which allows for the calculation of the exit radius.

$$C_{\theta 2} r_2 = C_{\theta 0} r_0 \tag{B.30}$$

Moreover, the inlet flow angle is assumed to be coincident with the nozzle blade angle and the continuity equation is used to determine the remaining inlet unknowns [124].

According to [41], it is common practice to include a vainless interspace between the vaned nozzle section and the rotor. This is typically done to ensure a circumstantially uniform flow at the rotor entry and to reduce the influence of the nozzle wake on the downstream component.

Watanabe et al. [168] have empirically determined that the maximum radial turbine efficiency occurs for an interspace geometrical parameter k defined according to equation B.31, also reported in [41, 124].

$$k = \frac{\Delta r}{b_2 \cos\alpha_2} \simeq 2 \tag{B.31}$$

where Δr is the radial distance between the nozzle exit and the rotor tip. Combining equation B.30, specialized to the interspace, with the continuity equation, the following relation can be derived to calculate the interspace exit flow angle [41].

$$\tan\alpha_2 = \tan\alpha_1 \left(\frac{\rho_2}{\rho_1}\right)\left(\frac{r_2}{r_1}\right)\left(\frac{A_2}{A_1}\right) \tag{B.32}$$

For constant height interspace, the area ratio can be further simplified since $A_1 = 2\pi r_1 b_1$ and $A_2 = 2\pi r_2 b_2$. Moreover, the assumption of constant density can be made at this stage assuming no losses in the interspace section [41].

B.2.2 Turbine Loss Models

Mainly two empirical loss models have been developed for radial turbines. In particular, the initial model proposed by Rohlik [47, 48] has been more recently updated by Glassman [49, 50]. Relations for stator losses and rotor incidence, passage, disk friction, clearance and kinetic energy losses have been similarly presented by both authors.

Furthermore, Baines [51] proposed an alternative set of equations for passage and clearance losses to improve the prediction of Glassman's loss model. Since, the geometrical data required for the employment of these sets of equations are available from the modeling approach discussed in section B.2.1, all three loss models have been implemented within this thesis work.

This section presents the full set of equations necessary to model each individual loss contribution. Modeling differences between each author will accordingly be discussed.

Stator losses

The stator loss is computed from equation B.33.

$$\Delta h_S = e_s (KE)_{S,id} \tag{B.33}$$

where e_s is the stator loss coefficient, defined according to equation B.34 [47, 50], and $(KE)_{S,id}$ represents the stator ideal kinetic energy, calculated using B.35.

$$e_s = \frac{0.0076}{\cos\alpha_2 - 0.025}\left(1 + \frac{\cos\alpha_{st}}{0.7}\right) \tag{B.34}$$

The stagger angle (α_{st}) is assumed as average between the stator inlet and outlet flow angle: $\alpha_{st} = (\alpha_0 + \alpha_2)/2$, as indicated in reference [47]. With e_s available, the ideal kinetic energy can be calculated according to:

$$(KE)_{S,id} = \frac{(KE)_S}{1 - e_s} \tag{B.35}$$

The actual kinetic energy $(KE)_S$ is calculated as:

$$(KE)_S = \frac{C_1^2}{2} \tag{B.36}$$

Rotor losses

Incidence loss Incidence losses are not directly computed in Rohlik's model [47]. Instead, reference [50] accounts for this loss contribution according to the following equation :

$$\Delta h_{INC} = \frac{1}{2} W_2^2 \sin^2 i \tag{B.37}$$

where i represents the difference between the actual and the best efficiency point relative flow angles ($i = \beta_2 - \beta_{2,opt}$). As shown in [50], this losses are negligible at design stage.

Passage loss The passage losses are calculated in a significantly different manner between the three main loss models illustrated. Rohlik [47] calculates the passage losses according to the following equation.

$$\Delta h_P = e_r (KE)_{R,id} \tag{B.38}$$

where $(KE)_{R,id}$ is the rotor ideal kinetic energy defined as function of the rotor loss coefficient (e_r) and the actual kinetic energy $(KE)_R = W_3^2/2$ as:

$$(KE)_{R,id} = \frac{(KE)_R}{1 - e_r} \tag{B.39}$$

with e_r defined as:

$$e_r = \left(\frac{0.017\sigma_R}{\cos\beta_{3s} - 0.003Z_B - 0.017\sigma_R} \right) \left(1 + \frac{1.9s}{b_2 + b_3} \right) \tag{B.40}$$

where σ_R is the rotor blade-row solidity and s is the average of the rotor inlet and exit blade spacing, defined as equation B.41 and B.42 respectively.

$$\sigma_R = \frac{0.8D_{3m}\left(\frac{D_{3m}}{D_2} - 1 \right)}{s} \tag{B.41}$$

and

$$s = \frac{\pi D_{3m}}{Z_B} \left(\frac{1}{2} \frac{D_2}{D_{3m}} + 1 \right) \tag{B.42}$$

- Glassman [50] uses a simpler relation (equation B.43) to estimate the passage losses. Where i is the incidence angle defined before and K_P is a constant which assumes a value of 0.3, as reported in [51].

$$\Delta h_P = \frac{1}{2} K_p (W_2^2 \cos^2 i + W_3^2) \tag{B.43}$$

- According to [51], equation B.43 oversimplifies the passage loss assessment. The author suggests that a better approximation can be achieved by means of equation B.44.

$$\Delta h_P = K_p \left\{ \left(\frac{L_{hyd}}{D_{hyd}} \right) + 0.68 \left[1 - \left(\frac{\overline{r}_3}{r_2} \right)^2 \right] \frac{\cos\beta_{3s}}{b_3/c} \right\} \frac{1}{2} (W_2^2 + W_3^2) \tag{B.44}$$

where D_{hyd} is the mean of the hydraulic exit diameters calculated by means of equation B.45, L_{hyd} is the hydraulic length from equation B.46 and c is the rotor blade chord computed as presented in equation B.47.

$$D_{hyd} = \frac{1}{2} \left\{ \left(\frac{4\pi r_2 b_2}{2\pi r_2 + Z_B b_2} \right) + \left[\frac{2\pi(r_{3s}^2 - r_{3h}^2)}{\pi(r_{3s} - r_{3h} + Z_B b_3)} \right] \right\} \tag{B.45}$$

L_{hyd} is approximated according to [51] as:

$$L_{hyd} = \frac{\pi}{4} \left[\left(z - \frac{b_2}{2} \right) + \left(r_2 - r_{3s} - \frac{b_3}{2} \right) \right] \tag{B.46}$$

Where z is the axial length to radius ratio, which can be assumed equal to 0.7 according to [41]. Finally, the rotor blade chord can be calculated by means of:

$$c = \frac{z}{\cos\overline{\beta}} \quad \text{and} \quad \tan\overline{\beta} = \frac{1}{2}(\tan\beta_2 + \tan\beta_3) \tag{B.47}$$

In this model, the value of the coefficient K_P is normally set to 0.2 if the following relation holds, otherwise to 0.1 [51].

$$\frac{r_2 - r_{3s}}{b_3} < 0.2$$

Disk friction loss Disk friction losses are commonly estimated equation from equation B.48, where the Reynolds number is defined as: $Re_2 = \rho_2 U_2 r_2/\mu_2$.

$$\Delta h_{DF} = 0.02125 \frac{\rho_2 U_2^3 r_2^2}{\dot{m} Re_2^{0.2}} \tag{B.48}$$

Clearance loss The conventional loss model reported in [47, 49], calculates the enthalpy losses due to clearance effect as direct function of the average clearance to blade-height ratio (c/b):

$$\Delta h_{CL} = \Delta h_y \left(\frac{c}{b}\right) \tag{B.49}$$

where Δh_y represents the Eulerian work and c/b is calculated according to equation B.50. c_2/b_2 and c_3/b_3 are the blade-shroud clearance to blade height ratio at the rotor inlet and outlet respectively.

$$\frac{c}{b} = \frac{1}{2}\left[\left(\frac{c}{b}\right)_2 + \left(\frac{c}{b}\right)_3\right] \tag{B.50}$$

Rohlik [47] suggests to estimate the absolute axial and radial clearances (c_2 and c_3 respectively) as a percentage of the reference diameters:

$$c_2 = 0.002 D_2$$

$$c_3 = 0.0025 D_{3s}$$

- Baines [51] proposed a more sophisticated model to account for clearance losses. Equation B.49 has been replaced with:

$$\Delta h_{CL} = \frac{U_2^3 Z_B}{8\pi}(K_2 c_2 C_2 + K_3 c_3 C_3 + K_{23}\sqrt{c_2 c_2 C_3 C_3}) \tag{B.51}$$

K_2 and K_3 are the axial and the radial portion of the tip gap discharge coefficients. A value of 0.4 and 0.75 has been respectively indicated [51]. K_{23} is a coefficient that accounts for the cross-coupled influence of axial and radial clearance effects on the overall turbine efficiency, experimentally determined in reference [51]. A value of -0.3 has been attributed to K_{23}. C_2 and C_3 are defined according to:

$$C_2 = \frac{1 - (r_{3s}/r_2)}{C_{2m} b_2} \quad \text{and} \quad C_3 = \frac{r_{3s}}{r_2}\frac{z - b_2}{C_{3m}\overline{r}_3 b_3} \tag{B.52}$$

Exit loss The kinetic energy loss is commonly accounted by means of equation B.53.

$$\Delta h_{EX} = \frac{C_3^2}{2} \tag{B.53}$$

Efficiency definition Once calculated the individual loss contributions, the total to static turbine stage efficiency ($\eta_{S_{ts}}$) can be calculated by means of equations B.54, reported in [47], and ($\eta_{N_{ts}}$) is consequently updated.

$$\eta_{S_{ts}} = \frac{\Delta h_y - (\Delta h_{DF} + \Delta h_{CL})}{\Delta h_y + \Delta h_s + \Delta h_{INC} + \Delta h_P + \Delta h_{EX}} \tag{B.54}$$

To conclude this section, Figure B.7 reports the individual loss contribution impact on the overall turbine total to static efficiency as function of the specific speed (n_s). The radial turbine maximum efficiency should be expected for a value of n_s around 0.6, as shown in [41].

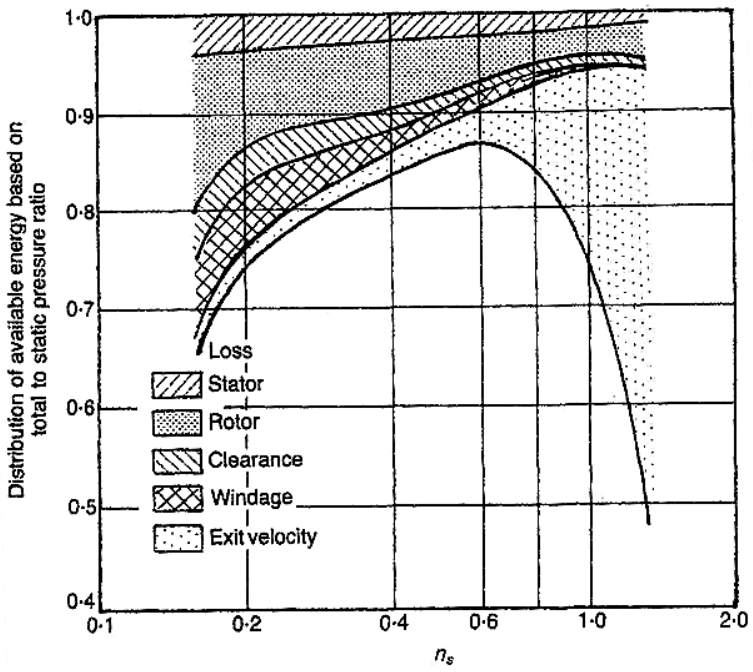

Figure B.7: Predicted individual efficiency loss contribution as function of specific speed [41]

B.3 Model Implementation

The radial turbine detailed performance model is composed by two primary sections: (1) rotor design, and (2) stator design. The inlet and outlet turbine flow and power characteristics are fully determined by NPSS, once the cycle thermodynamic design has been completed. With this information, the turbine rotor and stator can be geometrically characterized, assuming an initial value for the total to static nozzle and stage efficiencies. These efficiencies are iteratively refined with the loss model chosen (section B.2.2) and the final geometry is obtained.

This section discusses in detail the Matlab implementation of the radial turbine model, starting from the rotor design approach and concluding with the stator model. A final section is presented to show how these main turbine building blocks are coupled together and assessed by means of the loss model. Considerations on turbine design performance parameters and optimization bounds will be given throughout the development of this section.

B.3.1 Rotor Design

Although the stator component precedes the rotor, from a modeling perspective is the rotor design performance which dictates stator parameters, since the first is responsible of the whole turbine power output. The rotor is normally designed for a given power demand ($\dot{W}_T$) and inlet flow conditions. Moreover, the rotational speed (N) or the rotor inlet radius (r_2) have to be specified. Because the turbine is directly coupled with the compressor, the first running option ensures the correct mechanical matching between the components.

Initially, this section discusses the rotor model implementation, displaying how the theory discussed in section B.2.1 has been used. Subsequently, a brief description on design criteria for maximum efficiency and feasibility assessment is reported. These data have been employed as guidance for the selection of the turbine design vector bounds during the optimization.

Model Description

The following inputs are necessary to perform the rotor design characterization: gas constant (γ), dimensionless mass flow (θ), dimensionless power ratio (S_w), rotor exit hub to tip radius ratio (ν) and exit tip/shroud blade angle (β_{3s}). Additionally, the dimensionless rotational speed (U_2/a_{00}) can be specified, if the rotor has to be mechanically coupled with the compressor. The code attempts to design the rotor for minimum inlet Mach number (M_2) and exit relative Mach number (M_{3s_r}), to minimize the rotor losses, following the procedure discussed in [41, 46]. Figure B.8 summarizes the design methodology.

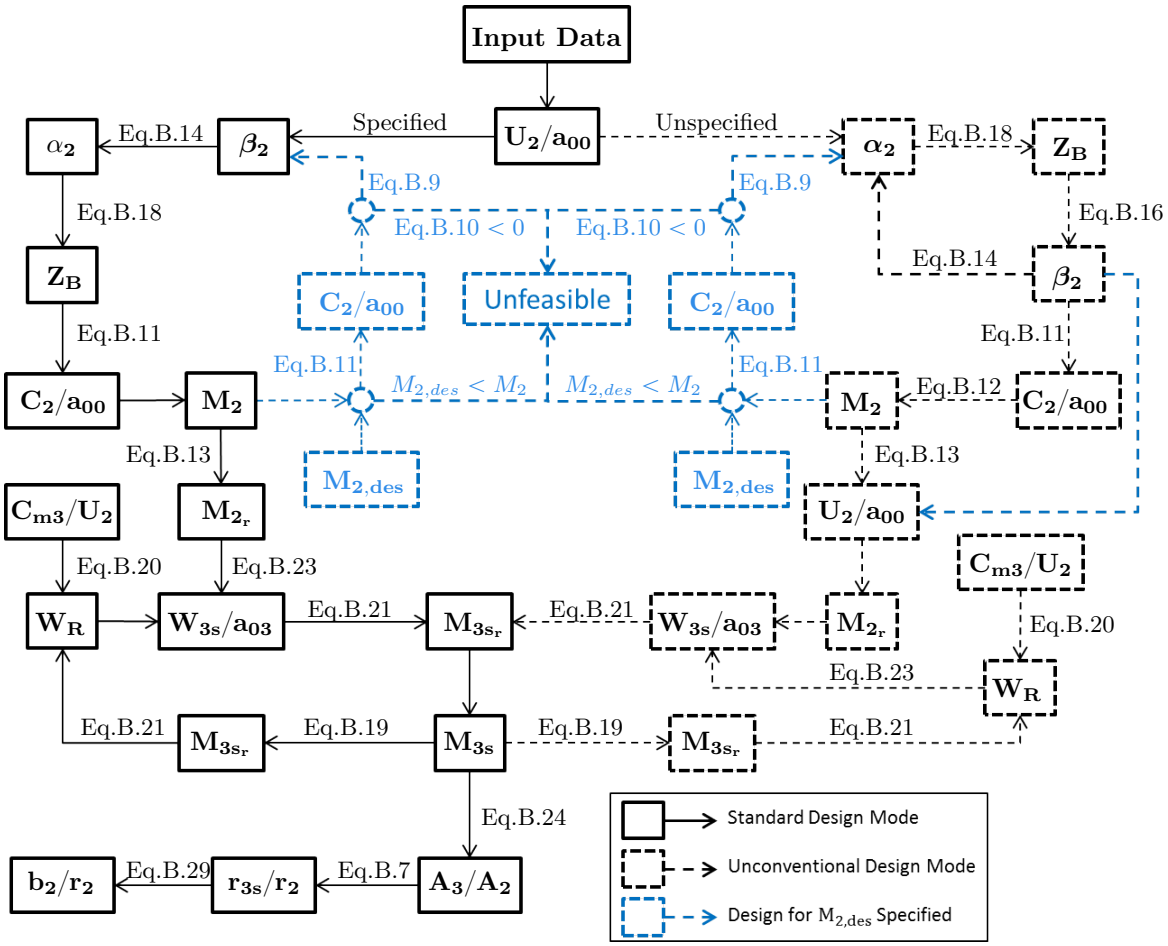

Figure B.8: Rotor design code schematic

An initial guess of the relative velocity ratio (W_R) or the discharge velocity ratio (C_{m3}/U_2) is needed to preform the calculations. A value of 2.0 for the W_R variable or of 0.25 for C_{m3}/U_2 have been recommended in [47] and [167] respectively, for highly efficient radial turbines. Since the design approach discussed in [41, 46] employs the first parameter to perform the calculation, this running option has been normally preferred, although, as shown by equation B.20, these two variables are interchangeable.

It is also possible to specify a design rotor inlet Mach number ($M_{2,des}$), which will lead to higher rotor losses. This option has been created to facilitate the turbine model validation phase of this project. No use of this feature has been done for optimization purposes, since it has been assumed that the stator is designed to ensure the optimal inlet Mach number condition. If the $M_{2,des}$ variable has been defined by the user, two feasibility checks are performed to ensure the correctness of the given input, see Figure B.8.

Performance Consideration

Different parameters can be used to evaluate the rotor performance of a radial turbine. Two parameters have been already mentioned during explanation of the rotor design procedure: the relative velocity ratio (W_R) and the discharge velocity ratio (C_{m3}/U_2). As mentioned in section B.2.1, optimal values are around 2.0 and 0.25 respectively. Reference [41] employs a more effective group of parameters to evaluate the resultant design performance, which is constituted by specific speed (equation B.55) and specific diameter (equation B.56).

$$n_s = \frac{\omega\sqrt{\dot{V}}}{\Delta h_{0s}^{3/4}} = \frac{D_{3,M}}{D_2}\left(\frac{\eta_s}{\lambda}\right)\left[2\pi k\left(\frac{1-\nu^2}{1+\nu^2}\right)\right]^{1/2} \tag{B.55}$$

and

$$d_s = \frac{D_2 \Delta h_{0s}^{1/4}}{\sqrt{\dot{V}}} = \frac{D_2}{D_{3,M}}\left(\frac{\lambda}{\eta_s}\right)\left[\frac{\pi}{2}k\left(\frac{1-\nu^2}{1+\nu^2}\right)\right]^{-1/2} \tag{B.56}$$

since k represents the discharge velocity ratio (C_{m3}/U_2), n_s and d_s can be directly associated to the rotor design methodology of Figure B.8. As visible from both Figures 4.4 and B.7, optimal specific speed values lay between 0.4 and 0.8 for radial turbines, while optimal specific diameters are around 3.4 [41]. Other authors have provided different guidelines to evaluate the rotor sizing procedure, which have been efficiently summarized by Aungier [124]. In particular, Baljé [27] suggested the following limitations:

$$0.2 \leqslant C_{m3}/U_2 \leqslant 0.4 \tag{B.57}$$

and

$$r_{3s}/r_2 \leqslant 0.78 \tag{B.58}$$

Rohlik [47] instead suggests a value of 0.7 as maximum threshold for equation B.58, while Aungier [124] recommends that this ratio should not exceed 0.9. Additional limitations have been provided on the meridional velocity ratio (C_{m3}/C_2) and the reaction parameter (R), defined according to equation B.59. Wood [169] suggests to limit C_{m3}/C_2 between 1.0 and 1.5 for a highly efficient rotor design. According to [124], fairly different recommendations have been given in literature for the selection of R. An indication has been provided by the author to define a preferred range for this parameter (B.60), although it might not be universally valid.

$$R = \frac{h_2 - h_3}{h_{02} - h_{03}} \tag{B.59}$$

and

$$0.45 \leqslant R \leqslant 0.65 \tag{B.60}$$

Since dissimilar and sometimes contrasted indications have been given by different authors, it becomes difficult to define strict performance requirements that must be satisfied by the rotor design. Although, these parameters have been evaluated during the turbine design procedure, the optimization has not been strongly constrained to respect these bounds. Because a detailed loss model has been coupled with the design, already sufficient performance insight is given. Far advanced turbomachinery detailed design phases, should address these aspects more carefully.

Design Variables Considerations

Indications have been provided in [41, 46] to defined typical geometrical design parameter that will be used during the rotor sizing. Thus, helping the turbine design vector bound definition during the optimization phase. As mentioned, a low relative exit Mach number (M_{3s_r}) is beneficial to reduce the passage losses, while a reduced absolute exit Mach number (M_{3s}) positively affects the exit kinetic energy losses. Therefore, it is of interest to minimize these variables through the optimal selection of the exit blade angle (β_{3s}).

As visible from Figure B.5, minimum M_{3s_r} occurs for an exit blade angle of approximately -55°, although more negative flow angles lead to a reduction of M_{3s}. Hence, the final selection of β_{3s} depends on trade-off considerations to maximize the overall turbine efficiency. As suggested in [41], flow angles up to -70° are admissible for their beneficial impact on the absolute exit Mach number, while lower value than -50° can be considered unsatisfactory.

The rotor exit hub to tip radius ratio (ν) selection is dictated by stress requirements and by the necessity of providing sufficient space to accommodate the blades [46]. Since further refinement is needed in later design stages, general indications from literature have been used to set the optimization bounds for this parameter. Rohlik [47] employs ν values limited between 0.4 and 0.7 for his analysis. The lower bound has been justified to avoid excessive blockage, while the upper bound to prevent an excessive shroud curvature.

It has to be noted that the radial turbine exhibits a similar behavior to the compressor, in the sense that at lower ν values correspond higher efficiency levels. Therefore, for this study, the minimum hub to tip radius ratio has been limited to 0.3, as indicated in [146], while an upper bound of 0.7 has been maintained according to [47].

Whitfield and Baines [41] provide additional indication on the typical order of magnitude that the inlet blade angle (β_2) should have. The authors indicate that optimal β_2 angle lies between -20 and -40 degrees. Although this parameter is defined throughout the rotor design procedure (Figure B.8), checks have been built in the code to verify whether this suggested range has been met by the resultant calculations.

B.3.2 Stator Design

The stator has been modeled following the procedure discussed in section B.2.1, assuming conservation of angular momentum [124]. Moreover, the nozzle has been designed to ensure that the required rotor inlet flow conditions are met. An interspace has been modeled to ensure sufficient nozzle wake mixing before entering the rotor [41], using equation B.31 reported in [168]. Although it is possible to specify a stator inlet Mach number (M_0), the design has been carried out for a given nozzle radius ratio (r_0/r_1), assuming that the resultant inlet Mach number condition can be met within the turbine inlet ducts.

Indications have been proposed by Aungier [124] to constraint the nozzle radius ratio between 1.1 and 1.7. This observation has been used to define the turbine nozzle related optimization bound presented in Table 5.5. As discussed in [169], typical straight blade nozzles exhibit efficiencies in the order of 97% to 99%. Therefore, such a simple design procedure is more than justified at this stage of the project.

B.3.3 Performance Evaluation

Once the rotor and stator designs have been completed, sufficient geometrical data are available to assemble the whole turbine model and assess its performance. Figure B.9 shows the overall turbine model implementation, which connects the stator and rotor blocks to the chosen loss model. Depending on the running mode chosen, given rotational speed (N) or specified rotor inlet radius (r_2), additional iterations with the design rotor code are needed to properly characterize the rotor geometry.

Finally, the design performance are evaluated by means of the loss model discussed in section B.2.2. Glassman's loss model [49, 50] have been preferred in this work due to the reasons given in section 4.3.1. Using the individual loss contribution equations, a better estimation of the rotor and stator total to static efficiency can be made. Through further iterations with the component design blocks, a more accurate geometrical refinement is obtained.

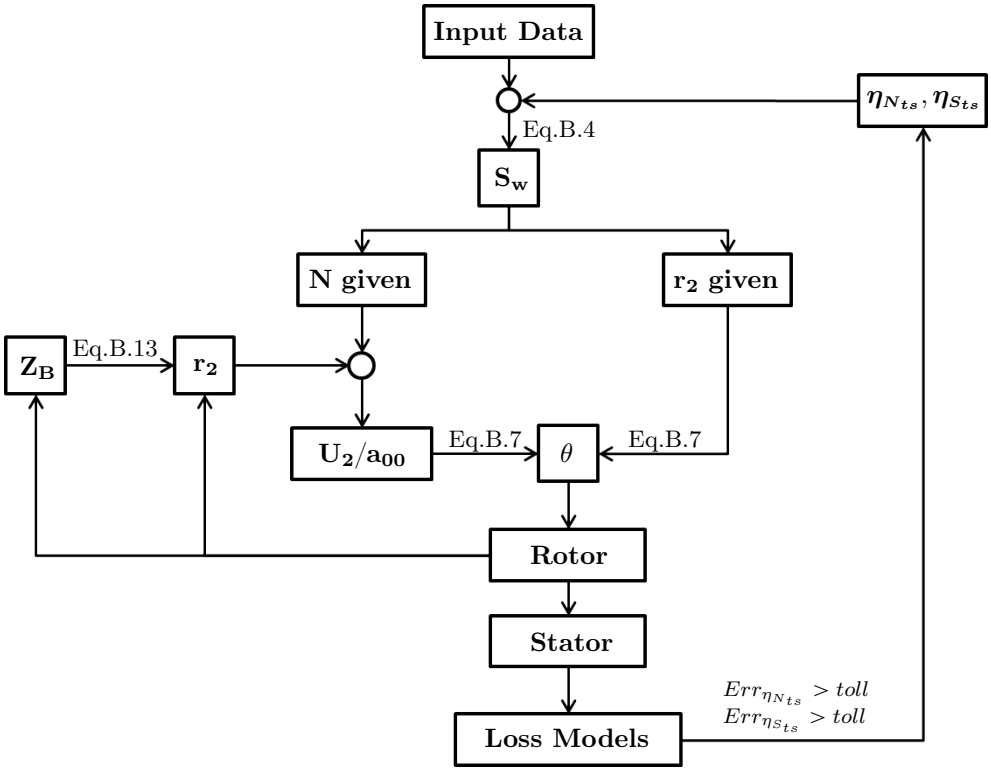

Figure B.9: Radial turbine design code schematic

During the optimization, the input flow and geometrical data needed are provided respectively by NPSS and the system optimizer. Consistency has been guarantee in the current turbine model by ensuring that continuity and component matching are respected between rotor and stator elements. After having completed the this turbine analysis, sufficient geometrical insight has been obtained for the turbine weight assessment.

APPENDIX C

Combustor

This appendix chapter describes the combustor model implemented in this project. The burner design sizing procedure has been discussed in section C.1, which leads to the definition of main geometrical features used by the weight model. Section C.2 describes a preliminary procedure to estimate the flame temperature in the different combustor areas: recirculation zone, primary zone, secondary zone and dilution zone.

These information are employed in section C.3 to characterized the uncooled wall temperature and establish liner cooling requirements. If the uncooled wall analysis (section C.3.1) establishes that cooling should be employed, a procedure to opportunely distribute the available coolant is discussed (section C.3.2).

In the event this procedure leads to an insufficient cooling design, a failure message is transmitted to the optimizer which deals with it as explained in section 4.4 of the main document. The hereby discussed combustor model has been built in Matlab as shown in Figure 4.6. Thus, this section provides the theoretical background used to build the model presented in section 4.4.1.

C.1 Design Methodology

As explained in [16], the difficulties encountered in obtaining satisfactory combustor design performance are inversely proportional to the size of the combustor. In fact, as the dimensions are reduced, the possibility of efficiently controlling the fluid flow diminishes, sealing and cooling problems becomes more severe. Hence, common scaling techniques cannot be easily defined for combustors [68], making necessary the investigation of more advanced techniques to gain the component geometrical and performance data needed for this project.

A general methodology has been developed by Melconian and Modak [70], based on empirical work and experience accumulated across the years, which allows to establish preliminary geometrical and aerodynamic features to support the initial combustor development. The procedure discussed is based on the following four steps:

(1) Selection of the combustor type

(2) Case and liner cross-sections characterization

(3) Sizing of combustor zones and associated features

(4) Specification of liner cooling requirements

A detailed description of the originally developed methodology is also available in references [71, 72, 74, 170]. The combustor type selected for the current project is annular, since this configuration exhibits less problems related to the close coupling with compressor and turbine,

and to the high rotational speed typical of small gas turbines [74]. Nonetheless, this methodology is applicable to can, annular and can-annular combustors arrangements, with only minor modifications that will be illustrated.

This section discusses the whole geometrical characterization of the combustor, defining those parameters that are used in the weight assessment. In particular, the case and liner sizing methodology, which allows to establish the width of the burner, is initially presented. Subsequently, the main combustor zones (diffuser, primary, secondary and dilution) are fully characterized, defining the whole length of the combustion chamber.

C.1.1 Case and Liner Characterization

The case and liner area sizing procedures are presented in this section, leading to the complete combustor width characterization. Slight differences in the sizing approach can be identified depending on the combustor type selected. Proper explanation is given accordingly.

Determination of Reference Area

The determination of the combustor reference area (A_{ref}), coincident with the casing area, is based on aerodynamic and chemical considerations. The first methodology produces an A_{ref} value which ensures satisfactory aerodynamic performance, with limited pressure losses, while, the second, focuses more on combustor chemical performance, ensuring that a good efficiency is obtained [72]. The two procedures might lead to a different reference area value. Typical preliminary design approach is to prefer the aerodynamic procedure to size the combustor, while, good overall performance are ensured through later and more advanced design refinements.

Figure C.1 shows the reference area meaning with respect to the different combustor architectures available: can, annular and can-annular. Depending on the combustor type, equation C.1 can be use to calculate the reference area for can/multi-can combustors, while equation C.2 for annular and can-annular.

$$A_{ref} = \pi \frac{D_{ref}^2}{4} \tag{C.1}$$

and

$$A_{ref} = \frac{\pi}{4}\left[(2D_{ref} + D_i)^2 - D_i^2\right] \tag{C.2}$$

where D_{ref} is the reference diameter and D_i is the internal diameter (Figure C.1), determined assuming a 5% clearance from the shaft. Once established the reference area with the methodology discussed below, equations C.1 and C.2 are used to calculate the actual diameter of the combustor case.

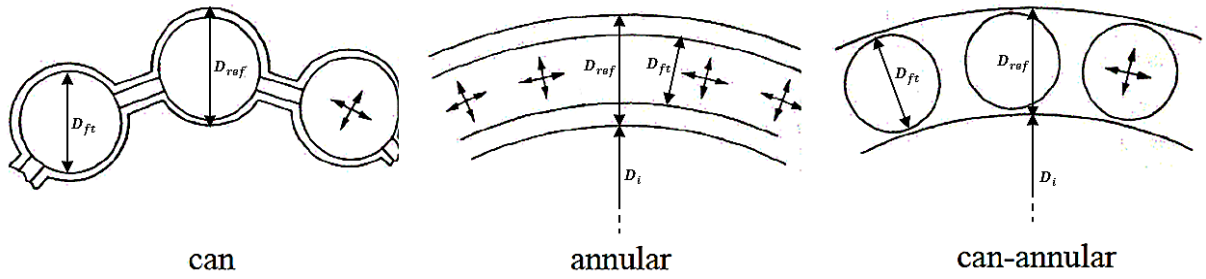

Figure C.1: Reference area definition for different combustor types, adapted from [71]

Aerodynamic Design As mentioned, the combustor aerodynamic design is a critical aspect to be firstly considered because of its direct impact on burner performance at every engine operating point. In particular, since strong mixing occurs between fresh air and burnt products, a proper aerodynamic design is needed to limit the total pressure losses in the chamber [74].

A set of reference quantities has to be defined before introducing the actual reference area calculation procedure. The reference velocity (U_{ref}) is defined as the mean velocity across the plane of maximum cross-sectional area of the case, in the absence of the liner (equation C.3).

$$U_{ref} = \frac{\dot{m}_3}{\rho_3 A_{ref}} \tag{C.3}$$

The reference dynamic pressure (q_{ref}) is defined according to equation C.4 as function of the reference velocity.

$$q_{ref} = \frac{1}{2}\rho_3 U_{ref}^2 \tag{C.4}$$

Once discussed these quantities, equation C.5 have been developed in [70] to calculate the combustor reference area as function of combustor design pressure losses and given inlet flow conditions.

$$A_{ref} = \left[\frac{R}{2}\left(\frac{\dot{m}_3\sqrt{T_{03}}}{P_{03}}\right)^2 \frac{\Delta P_{3-4}}{q_{ref}}\left(\frac{\Delta P_{3-4}}{P_3}\right)^{-1}\right] \tag{C.5}$$

where, $\Delta P_{3-4}/P_3$ is the combustor total pressure loss and $\Delta P_{3-4}/q_{ref}$ is the pressure loss factor, given as the sum of diffuser pressure drop ($\Delta P_{diff}/q_{ref}$) and the liner pressure drop ($\Delta P_L/q_{ref}$), as equation C.6.

$$\frac{\Delta P_{3-4}}{q_{ref}} = \frac{\Delta P_{diff}}{q_{ref}} + \frac{\Delta P_L}{q_{ref}} \tag{C.6}$$

This quantity is a characteristic propriety of the combustor, which depends only on the selected burner type and not on the operating conditions. Typical values are given in Table C.1, taken from reference [74].

Combustor Type	$\boldsymbol{\Delta P_{3-4}/P_3}$	$\boldsymbol{\Delta P_{3-4}/q_{ref}}$
Can	0.07	37
Can-Annular	0.06	28
Annular	0.06	20

Table C.1: Typical combustor pressure losses, adapted from [74]

The values indicated under the $\Delta P_{3-4}/P_3$ column in Table C.1 represent the commonly used cold total pressure loss values for a given combustor type. As indicated in [74], the cold losses represent the major contribution to the overall pressure drop within the combustion chamber, since they depends entirely on turbulence and friction phenomena.

Further combustor pressure losses are associated to the heat addiction. Exact quantification of these loss source is quite complex at this stage, since it is normally experimentally determined. Nonetheless, this loss contribution is significantly lower than cold losses. A typical range lies between 0.005 and 0.01, for moderate temperature combustors [74]. Hence, the whole combustor pressure losses have reasonably been modeled as cold losses in this preliminary work.

Chemical Design The reference area can also be defined from efficiency considerations, which are representative of the whole chemical process occurring in the combustor [70, 71, 74]. For any operating condition, the combustion efficiency can be expressed as function of the so called θ-parameter, defined according to equation C.7.

$$\theta = \frac{P_{03}^{1.75} A_{ref} D_{ref}^{0.75} \exp(T_3/b)}{\dot{m}_3} \tag{C.7}$$

where b is a constant typically assumed equal to 300 [74], or more precisely obtained as reported in [70], according to:

$$b = 245(1.39 + \ln(\phi_{PZ})) \qquad \text{for} \qquad 0.6<\phi_{PZ}<1.0$$
$$b = 170(2.00 - \ln(\phi_{PZ})) \qquad \text{for} \qquad 1.0<\phi_{PZ}<1.4$$

The primary zone equivalence ratio (ϕ_{PZ}) can be determined from the overall equivalence ratio (ϕ), representing the ratio between the actual fuel to air ratio to the stoichiometric fuel to air ratio, and the primary zone mass flow ($\dot{m}_{PZ}$), according to equation C.8, [71].

$$\phi_{PZ} = \phi \frac{\dot{m}_3}{\dot{m}_{PZ}} \tag{C.8}$$

The primary zone equivalence ratio has to be determined within the flame rich and weak stability limits to makes sure that the combustion takes place. According to [70], most of the hydrocarbons burnt in air have shown a flame limiting temperature of 1600K for weak mixtures, assuming no influence of pressure on this limit.

Hence, the limiting equivalence ratio correspondent to weak mixtures is given by any condition that produces a temperature rise of: $1600K - T_3 = \Delta T$. The correspondent weak equivalence ratio can be calculated interpolating data available in Figure C.2, which gives the adiabatic flame temperature rise as function of the equivalence ratio and the combustor inlet temperature, [70].

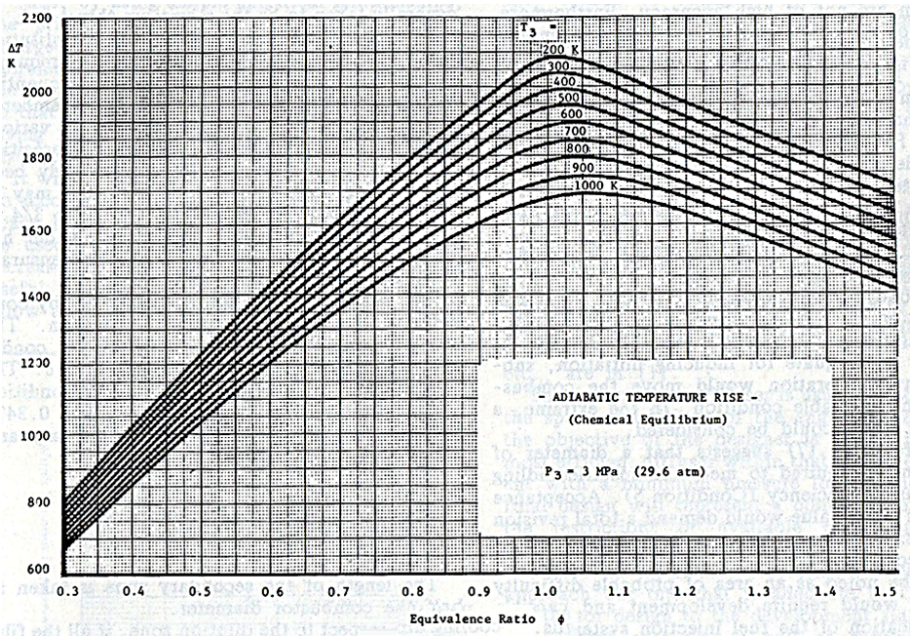

Figure C.2: Typical adiabatic temperature rise [70]

Moreover, reference [70] suggested to limit the rich equivalence ratio to a maximum value of 1.5 to ensure the minimization of smoke, CO and UHC, which corresponds to a primary zone inlet mass flow of about 23% of the total combustor inlet air.

Once the weak and rich limits have been defined, the actual primary zone equivalence ratio can be calculated from equation C.8, assuming a more conservative $\dot{m}_{PZ}$ value of 25%, as suggested in [70]. If the resultant ϕ_{PZ} satisfies the flame stability limits just defined, the constant b can be accurately determined and substituted in equation C.7.

Finally, equation C.7 can be used to determine the reference area assuming a value of $73 \cdot 10^6$ for the θ-parameter, since, as pointed out in [70], this number leads to a burner efficiency close to 100% for the majority of the combustor types (Figure 2.8).

Determination of Liner Areas

The selection of the liner area (A_{ft}) has a strong impact on the overall liner performance. In particular, a great liner cross-sectional area is beneficial since it contributes to reduce the flow velocity within the liner, improving: ignition, stability and combustion efficiency [74].

However, the more A_{ft} is increased, the less becomes the annulus area, with the consequent rising of the annulus velocity and dropping of static pressure. Sufficient annulus static pressure has to be maintained because it is necessary to ensure a good mixing between air and combustion products [74]. Therefore, the liner area has to be selected considering both aspects just mentioned.

A simple relation is commonly used to determine the liner sectional area (A_{ft}), where its value is assumed as a certain percentage of the reference area (equation C.9). According to [70], assuming the constant k equal to 0.7 gives satisfactory results for can and annular combustors, while, for can-annular arrangements, k should be selected between 0.65 and 0.67.

$$A_{ft} = k \cdot A_{ref} \tag{C.9}$$

A more accurate approach to define this constant has been developed by Lefebvre and Norster [73] from consideration on liner static pressure drop (ΔP_L) to primary zone dynamic pressure (q_{PZ}) ratio, given by equation C.10. In particular, this ratio should be maximized to ensure good annulus and liner performance. Derivation of equation C.10 with respect to k, leads to equation C.11 which defines the optimal constant value (k_{opt}) to be used in equation C.9 to maximize the static pressure drop across the liner and minimize the liner dynamic pressure.

$$\frac{\Delta P_L}{q_{PZ}} = 1 + \frac{T_3}{T_{PZ}} \left(\frac{k}{m_{PZ}} \right)^2 \left\{ \frac{\Delta P_{3-4}}{q_{ref}} - \frac{(1 - m_{sn})^2 + \lambda[r^2(1-k)^2 - 1]}{(1-k)^2} \right\} \tag{C.10}$$

where T_{PZ} is temperature in the primary zone, m_{PZ} and m_{sn} represent the ratio of the air mass flow in the primary zone to the total chamber air and the ratio of the air entering the snout to total chamber air respectively. r is the ratio between reference area and compressor outlet area and λ is the diffuser pressure loss coefficient, which depends on the diffuser type employed [74].

$$k_{opt} = 1 - \left[\frac{(1 - m_{sn})^2 - \lambda}{(\Delta P_{3-4}/q_{ref}) - \lambda r^2} \right]^{1/3} \tag{C.11}$$

Graphical representation of equations C.10 and C.11 is given in Figure C.3 as function of a given set of combustor parameters. Since these more detailed calculations assume the availability of certain combustor variables, the simplified approach discussed in reference [70] has been employed in this preliminary work. As visible from Figure C.3, this approach does not lead to a significant difference with respect to the employment of equation C.11.

C.1.2 Combustor Zone Characterization

This section discusses in detail the geometrical characterization of the major combustor zone, defining length and primary features of: diffuser and swirler, recirculation zone, primary zone, secondary zone and dilution zone. This information is used by the combustor weight model to estimate the whole weight of the component.

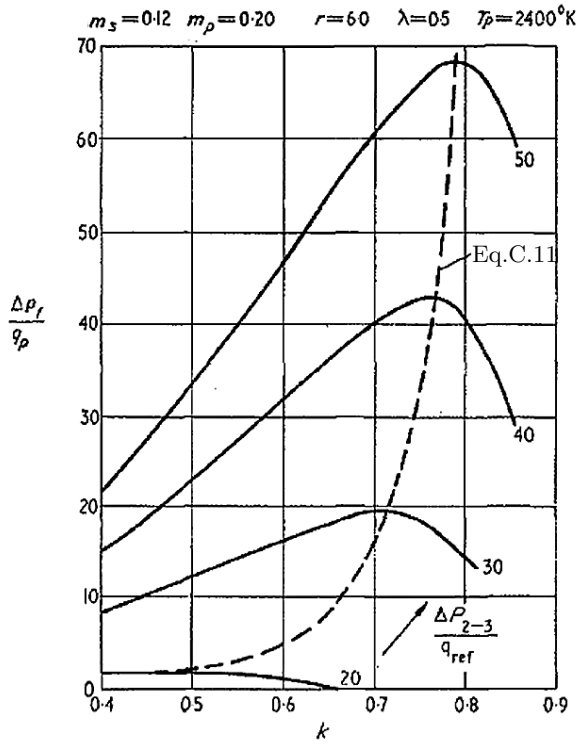

Figure C.3: Liner pressure loss influence on optimum liner to case area ratio, adapted from [73]

Determination of Liner Zones Length

The liner primary zones length characterization is made in this section. Practical suggestions to determine the longitudinal dimensions of primary zone, secondary zone and dilution zone has been provided in references [70–72]. In particular, the primary zone length is assumed equal to: $L_{PZ} = 0.75D_{ft}$ and the secondary zone to: $L_{SZ} = 0.5D_{ft}$, as indicated in [70, 71]. The dilution zone length is determined as function of the pressure loss factor and the pattern factor (PF), according to Table C.2, provided in [71].

$\mathbf{\Delta P_{3-4}/q_{ref}}$	$\mathbf{L_{DZ}/D_{ft}}$
15	3.78-6PF
20	3.83-11.83PF+13.4PF^2
30	2.96-9.86PF+13.3PF^2
50	2.718-12.64PF+28.51PF^2

Table C.2: Dilution zone length estimation [71]

The pattern factor is an important parameter for life and durability of the hot components which follow the combustor, since it measures the temperature difference between the average burner exit temperature (T_{04}) and the maximum recorded temperature ($T_{04,max}$), as given form equation C.12 [74]. Due to burner wall and turbine stator cooling flows, the burner exit temperature distribution is rarely flat. A pattern factor value of 0.20 could be initially assumed, as suggested in [70].

$$PF = \frac{T_{04,max} - T_{04}}{T_{04} - T_{03}} \tag{C.12}$$

The pattern factor can be more precisely calculated from equation C.13, valid for can and can-annular combustors, and equation C.14, only applicable to annular chambers [74]. Where

$\Delta P_L/q_{ref}$ is calculated from equation C.6, once the diffuser losses have been specified, and L_{ft} is the overall liner length, determined as the sum of primary, secondary and dilution zones length. An iterative procedure has been developed to refine the initially assumed PF value.

$$PF = 1 - \exp\left(-0.070 \frac{L_{ft}}{D_{ft}} \frac{\Delta P_L}{q_{ref}}\right)^{-1} \tag{C.13}$$

and

$$PF = 1 - \exp\left(-0.050 \frac{L_{ft}}{D_{ft}} \frac{\Delta P_L}{q_{ref}}\right)^{-1} \tag{C.14}$$

Diffuser Detailed Sizing

The basic design of the diffuser can be carried on by following the steps presented in [70, 71], assuming that the exit diffuser velocity is equal to the annulus inner. Hence, the exit diffuser area (A_o) is calculated from equation C.15.

$$\frac{A_o}{A_{an}} = \frac{\dot{m}_3}{\dot{m}_{an}} \tag{C.15}$$

The annulus area (A_{an}) is determined as difference between the reference area and the liner area and the annulus mass flow ($\dot{m}_{an}$) assuming a conventional combustor design, where half of the primary zone mass flow is admitted through the swirler as dome-cooling [70].

The diffusion angle (ψ) can be calculated by means of the equation C.16, reported in [70, 71, 77]. Where, $\Delta P_{diff}/P_3$ represents the total pressure losses in the diffuser, which should be assumed equal to 0.01, as indicated in [70].

$$\frac{\Delta P_{diff}}{P_3} = 1.75R \left[\frac{\dot{m}_3\sqrt{T_{03}}}{P_{03}}\right]^2 \frac{(\tan\psi)^{1.22}}{A_3} \left[1 - \frac{A_3}{A_o}\right]^2 \tag{C.16}$$

Once the diffuser angle is available, the diffuser length can be estimated as follows:

$$L_{diff} = \frac{D_o - D_3}{2\tan\psi} \tag{C.17}$$

Finally, the inlet snout area (A_s) can be calculated by means of equation C.18, where $\dot{m}_s$ indicates the mass flow through the snout and $C_{d,s}$ is the snout discharge coefficient, which, as first approximation, should be assumed equal to the unity [70].

$$\frac{A_s}{A_o} = \frac{1}{C_{d,s}} \tag{C.18}$$

Figure C.4 visually summarizes the combustor diffuser features described during the development of this procedure. Once the diffuser angle has been calculated, the case inner length ($L_{C,in}$) can be calculated using equation C.17 and substituting D_o with D_{ref}.

Swirler Design

The swirler design is entirely based on the work done by Knight and Walker [79], cited in references [70, 71]. According to these documents, three main geometrical parameters can be used to fully define the swirler configuration: the turning angle β_{SW}, which lies between 45° and 70°, the swirler area (A_{SW}) and the concordance factor (K_{SW}), which assumes a value of 1.3 for thin straight blades and 1.15 for thin curved blades.

Another important parameter is the swirler mass flow ($\dot{m}_{SW}$). Experiments have shown that for a well designed combustor this value should lie between 3% and 12% of the total mass flow [70]. Finally, equation C.19 can be used to calculate the swirler area. In this project, the average

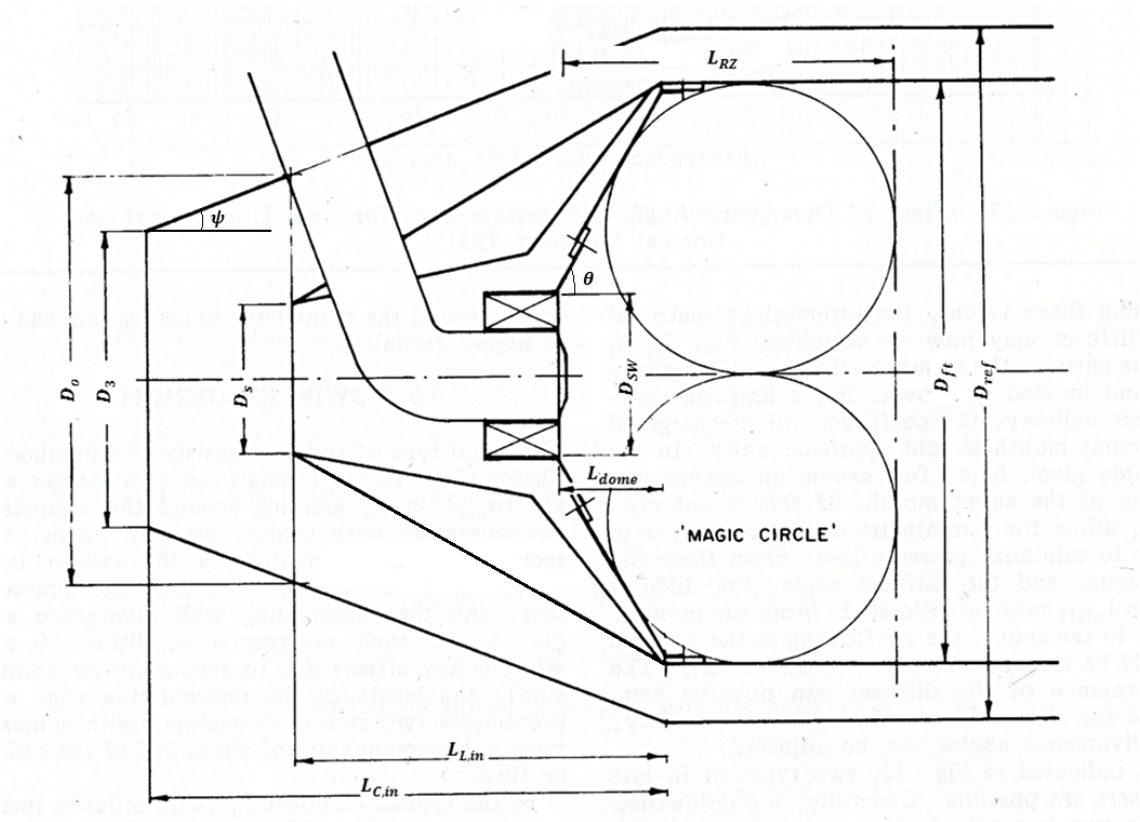

Figure C.4: Combustor front end geometrical diagram, adapted from [70]

of the range provided has been assumed for β_{SW} and $\dot{m}_{SW}$. Furthermore, a straight configuration has been selected for the swirler blades.

$$\frac{\Delta P_{SW}}{q_{ref}} = K_{SW}\left[\left(\frac{A_{ref}}{A_{SW}}\right)^2 \sec^2\beta_{SW} - \left(\frac{A_{ref}}{A_{ft}}\right)^2\right]\left(\frac{\dot{m}_{SW}}{\dot{m}_3}\right)^2 \tag{C.19}$$

Considering that the swirler total pressure loss is given subtracting from the combustor total pressure losses the pressure drop across snout and diffuser, equation C.20 can be derived [70]. Thus, substituting equation C.20 into C.19, the swirler area can finally be calculated.

$$\frac{\Delta P_{SW}}{q_{ref}} = \frac{\Delta P_{3-4}}{q_{ref}} - \frac{\Delta P_s}{q_{ref}} - \frac{\Delta P_{diff}}{q_{ref}} \tag{C.20}$$

where ΔP_s is the total loss across the snout, which is typically set to 25% of the dynamic pressure at the snout mouth (equation C.21), according to [70].

$$\frac{\Delta P_s}{q_{ref}} = 0.25\frac{q_s}{q_{ref}} = 0.25\left(\frac{A_{ref}}{A_s}\right)^2 \tag{C.21}$$

Finally, the swirler outer diameter (D_{SW}) is assumed 30% of the combustor liner diameter, as indicated in [70].

Recirculation Zone Characterization

References [70, 71] provide a general rule of thumb to define the recirculation zone length (L_{RZ}), which is coincident with the downstream portion of the so called "magic circle" in Figure C.4. In particular, L_{RZ} is approximately given by two swirler diameters, verification has to be made to ensure that the resultant value is smaller than the primary zone length [71].

References [71, 77] provide useful relations to calculate the dome angle (equation C.22) and, subsequently, the dome length (equation C.23), thus, fully characterizing the recirculation zone geometry and concluding the whole combustor geometrical characterization.

$$\theta = \arccos\left[\frac{-D_{ft}(D_{ft}-2D_{SW})-(D_{ft}-4L_{RZ})\sqrt{D_{ft}^2-4D_{ft}D_{SW}+4D_{SW}^2-8D_{ft}L_{RZ}+16L_{RZ}^2}}{2D_{ft}^2-4D_{ft}D_{SW}+4D_{SW}^2-8D_{ft}L_{RZ}+16L_{RZ}^2}\right] \tag{C.22}$$

and

$$L_{dome} = \frac{D_{ft}-D_{SW}}{2\tan\theta} \tag{C.23}$$

C.2 Flame Temperature

The preliminary estimation of the flame temperature is important for the characterization of the liner wall temperature and the establishment of cooling requirements. Calculations are performed to determine the exit temperature of: recirculation, primary, secondary and dilution zones, assuming a liner variation between inlet and outlet total temperatures (T_{in} and T_{out}) of each zone. Therefore, the temperature distribution assumes the form of equation C.24, according to [70, 71].

$$T_{out} = T_{in} + \eta\Delta T_{\phi} \tag{C.24}$$

where η is the combustion efficiency of each zone, determined as shown in the following sections, and ΔT_{ϕ} is the ideal temperature rise from the inlet value T_{in} to the adiabatic flame temperature for the given equivalence ratio (ϕ) of each combustor zone.

Recirculation Zone

The recirculation zone entry temperature is considered equal to the combustor inlet temperature (T_{03}), and the ideal temperature rise can be estimated from Figure C.2 assuming an equivalence ratio of 1.0, as indicated in [70]. Substituting these considerations into equation C.24, equation C.25 is determined.

$$T_{RC} = T_{03} + \eta_{RC}\Delta T_{\phi=1} \tag{C.25}$$

The recirculation zone efficiency is given by equation C.26 [70], where P_3 is the static pressure at the combustor inlet.

$$\eta_{RC} = 0.56 + 0.44\tanh\left[1.5475\cdot 10^3(T_{03}+108\ln P_3 - 1863)\right] \tag{C.26}$$

Since the recirculation zone is partly stirred, the temperature calculated through equation C.26 is only locally existing, hence, reference [70] suggests to define the zone exit temperature according to the following mean:

$$T_{out,RC} = \frac{T_{03}+2T_{RC}}{3} \tag{C.27}$$

Primary Zone

The temperature at the exit of the primary zone is calculated using equation C.28 [70], where the primary zone equivalence ratio has been previously determined from equation C.8, and the primary zone combustion efficiency is given by equation C.29.

$$T_{out,PZ} = T_{03} + \eta_{PZ}\Delta T_{\phi=\phi_{PZ}} \tag{C.28}$$

and

$$\eta_{PZ} = 0.71 + 0.29\tanh\left[1.5475\cdot 10^3(T_{03} + 108\ln P_3 - 1863)\right] \tag{C.29}$$

Secondary Zone

The secondary zone inlet temperature is coincident with the primary zone exit temperature, given by equation C.28. The zone exit temperature is normally determined from equation C.24, once appropriate substitutions have been made. The zone combustion efficiency calculation procedure differs for secondary zone rich or weak mixtures.

Weak Mixtures Equation C.30 can be used to estimate the secondary zone combustion efficiency (η_{SZ}) in case of weak mixtures.

$$\log\left[\log\left(1/\eta_{SZ}\right)\right] = 0.911\log\psi_{300} + 8.02\phi_{SZ} - 1.097 + D^* \tag{C.30}$$

where D^* is a constant that is typically experimentally determined. Nonetheless, reference [70] provides a relation that can be used in the absence of experimental data (equation C.31) for a preliminary estimation of this variable.

$$D^* = 0.736 - 0.0173\frac{P_3}{\Delta P_{3-4}} \tag{C.31}$$

ψ_{300} is the kinetic fuel loading which is defined for $T_{03} = 300$K according to equation C.32 [70]. In the following relation, V_{PZ} is the primary zone volume given according to equation C.33 [71], and n represents a constant which is function of the secondary flow equivalence ratio as follows: $n = 1.0$ for $\phi_{SZ} \leqslant 0.5$, $n = 2\phi_{SZ}$ for $0.5 < \phi_{SZ} \leqslant 1.0$, $n = 2/\phi_{SZ}$ for $1.0 < \phi_{SZ} \leqslant 2.0$ and $n = 1.0$ for $\phi_{SZ} > 2.0$.

$$\psi_{300} = \frac{\dot{m}_f}{V_{PZ}P_{03}^n} \tag{C.32}$$

and

$$V_{PZ} = \pi D_{ft}^2\left[\frac{L_{PZ} - L_{RZ}}{4} + \frac{L_{RZ}}{12}\right] \tag{C.33}$$

Since most likely the combustor inlet temperature differs from 300K, the kinetic fuel loading has to be corrected to adapt it to the given inlet flow conditions. References [70, 71] provide equation C.34 to accomplish this task. Once $\psi_{T_{03}}$ has been calculated, it can be substituted in equation C.30 instead of ψ_{300}.

$$\frac{\psi_{T_{03}}}{\psi_{300}} = \left(10^{-3.054y^{-1.205}}\right)\left(T_{03}^{1.2327y^{-1.205}}\right) \tag{C.34}$$

where y is a constant which depends on the secondary zone equivalence ratio, similarly to n. In particular, y assumes the following values: $y = \phi_{SZ}$ for $\phi_{SZ} \leqslant 1$ and $y = 1$ for $\phi_{SZ} > 1$.

Rich Mixtures Equation C.35 replaces equation C.30 in the event of rich mixtures in the secondary zone.

$$\eta_{SZ} = \frac{1}{\phi_{SZ}} \tag{C.35}$$

According to [70], the determination of the amount of fresh air entering the secondary zone should be made considering the combustor richest operating condition. In particular, the secondary zone equivalence ratio in these conditions should never exceed 0.8. The amount of air needed to satisfy this condition can be determined using equation C.36, with $\phi_{SZ} = 0.8$, as reported in [71].

$$\frac{\dot{m}_{PZ} + \dot{m}_{SZ}}{\dot{m}_3} = \frac{\phi_{rich}}{\phi_{SZ}} \tag{C.36}$$

where ϕ_{rich} is the overall combustor equivalence ratio in the richest operating condition. Normally, the richest operating point occurs at take-off. However, because take-off considerations have not be made for the baseline engines defined in this work, the only combustor operating condition available at this stage is represented by the cruise design point.

Therefore, the engine design NPSS data have been used to determine the secondary zone mass flow requirements, assuming a more conservative value of 0.6 for the secondary zone equivalence ratio (ϕ_{SZ}), as suggested in [77].

Dilution Zone

Melconian and Modak [70] suggested to calculate the dilution zone combustion efficiency (η_{DZ}) of the zone according to equation C.30, however, no clear indication has been given in the reference regarding the validity and variation of the previously given constants as function of the dilution zone equivalence ratio. On the other hand, Gosselin et al. [171] suggest to approximate η_{DZ} as equal to the secondary zone previously calculated. This last assumption has been kept in this work as well.

Finally, considering that the dilution zone inlet temperature is equal to the secondary zone exit temperature, equation C.24 is opportunely adapted to calculate the zone exit flame temperature. With this, the whole flame temperature distribution across the combustor primary zones is fully made. This information is employed in the wall temperature assessment, discussed next.

C.3 Wall Temperature

The determination of the wall temperature is essential to establish whether the combustor liner requires cooling flow and, in case this is needed, to evaluate the feasibility of the implemented cooling system. Reference [74] provides a complete methodology to preliminary estimate the uncooled and cooled wall temperatures under steady state conditions. This approach is more than sufficient for the current combustor model.

The combustor liner can be modeled as a container of hot gasses surrounded by the casing, with fresh air flowing in between. Hence, the heat is transferred from the hot mixture to the liner internal face through radiation and convection, and, in a similar manner from the external face towards the case. Conduction occurs between the two liner wall faces and along the liner length as well. Figure C.5 summarizes the liner heat transfer process just described.

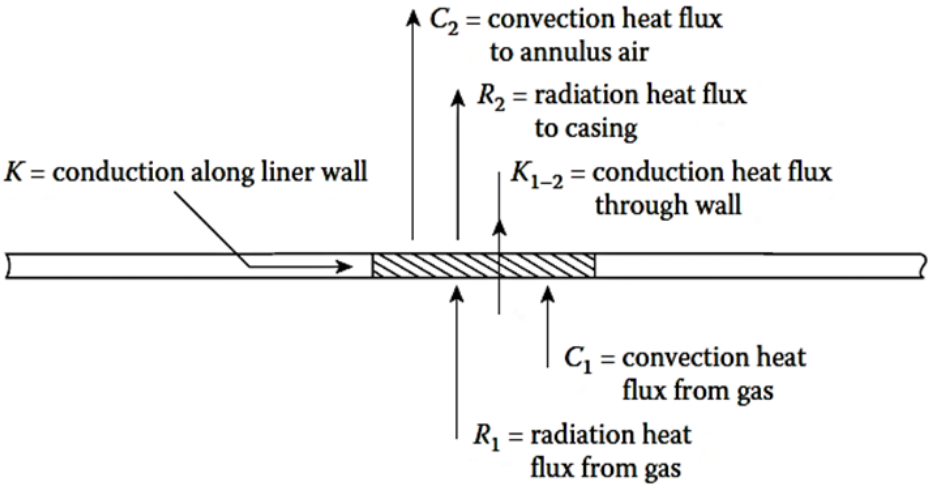

Figure C.5: Liner heat transfer process [74]

Under the reasonable simplification of considering the liner thin and neglecting the conduction along the liner ($K = 0$), equation C.37 can be written, which represent the heat balance under steady state condition. This relation can be used to determine the internal and external liner wall temperatures.

$$R_1 + C_1 = R_2 + C_2 = K_{1-2} \tag{C.37}$$

This equation holds only with the assumption of negligibly small liner longitudinal conduction and considering the liner wall as thin, meaning that the difference between internal and external liner surface area is negligible as well [74]. The conduction heat flux (K_{1-2}) through the liner wall is defined according to equation C.38.

$$K_{1-2} = \frac{k_w}{t_w} (T_{w1} - T_{w2}) \tag{C.38}$$

where k_w is the liner conduction coefficient, which depends on the combustor material, t_w is the liner wall temperature, T_{w1} and T_{w2} are the internal and external liner wall temperature respectively, which have to be determined from the system of equations resulting from C.37. Typical material employed for combustors are nickel-based alloys such as: Hastelloy X, Nimonic 75, 80 and 90, which have gradually replaced the originally used austenitic stainless steels [111, 132]. A general value of 26 W/mK, typical of Nimonic alloys, has been assumed for k_w, as suggested in [74], while the thickness t_w has been determined as presented in section 2.4.4.

The remaining terms of equation C.37 are differently determined for uncooled and cooled walls. The following sections discuss the calculation procedure of T_{w1} and T_{w2} for both cases. For this project, cooling has been assumed to take place when the calculated uncooled liner wall temperature exceeds 1300K, as suggested in [70]. No wall coating has been modeled here.

C.3.1 Uncooled Wall Temperature

The uncooled wall temperature is always a priori calculated to establish whether the liner has to be cooled. The procedure to establish the individual terms of equation C.37 has been taken from reference [74]. This chapter summarizes the cited approach dividing the treatise in: internal radiation (R_1), external radiation (R_2), internal convection (C_1) and external convection (C_2).

Internal Radiation

The total internal radiation is function of two contributions: (1) the non-luminous radiation emanated by gasses like carbon dioxide and water vapor and (2) the luminous radiation which

is dependent on the number of solid particles (soot) inside the burnt gasses. By taking into account these two contributions a final expression for R_1 assumes the form of equation C.39.

$$R_1 = 0.5\sigma(1+\varepsilon_w)\varepsilon_g T_g^{1.5}(T_g^{2.5} - T_{w1}^{2.5}) \tag{C.39}$$

where ε_w and ε_g are the wall emissivity, typically varying between 0.7 and 0.8 for Nimonic and stainless steel [74] and of the gas emissivity (equation C.40), respectively. σ is the Stefan-Boltzmann factor ($5.67 \cdot 10^{-8}$ W/m^{2}K^4) and T_g is the bulk gas temperature of each liner zone, determined as shown in section C.2. The gas emissivity can be calculated as follows by considering luminous and non-luminous contributions [74]:

$$\varepsilon_g = 1 - \exp\left[-290PL(ql_b)^{0.5}T_g^{-1.5}\right] \tag{C.40}$$

where P is the gas pressure in kPa, assumed equal to P_{03}, q is the fuel to air ratio by mass given by NPSS, L is the luminosity factor, determined as shown below and l_b is the beam length, which depends on the size and shape of the gas volume and varies between $0.6D_{ft}$ and $0.9D_{ft}$ for can combustors, and, is equal to $1.0D_{ft}$ for the inner liner and to $1.2D_{ft}$ for the outer liner in annular combustors [74].

Several relations have been developed to determine the luminous factor, which are mainly dependent on fuel carbon to hydrogen ratio by mass (C/H). Equation C.41 has been originally presented in [172].

$$L = 7.53(C/H - 5.5)^{0.84} \tag{C.41}$$

According to [74], this equation has been subsequently modified to:

$$L = 3(C/H - 5.2)^{0.75} \tag{C.42}$$

Kretschmer and Odgers [173] have proposed an alternative expression (equation C.43) to the previously developed to calculate the luminosity factor.

$$L = 0.0691(C/H - 1.82)^{2.71} \tag{C.43}$$

Finally, Lefebvre [174] has more recently developed equation C.44, which is dependent on H, defined as the fuel hydrogen content by mass in percentage. According to [74], any of these equations can be used, since they lead to similar results. In this project, equation C.44 has been employed.

$$L = 336/H^2 \tag{C.44}$$

External Radiation

The external radiation (R_2) can be calculated using equation C.45. Where ε_c is the case emissivity constant, set equal to 0.8, assuming the case made of steel [74], in agreement with the combustor weight model. A_w/A_c is the liner surface area to casing surface area ratio, differently determined depending on the combustor type.

$$R_2 = \sigma \frac{\varepsilon_w \varepsilon_c}{\varepsilon_c + \varepsilon_w(1-\varepsilon_c)(A_w/A_c)}(T_{w2}^4 - T_{03}^4) \tag{C.45}$$

Internal Convection

The internal convection (C_1) is determined from equation C.46 [74], where k_g and μ_g are the gas conductivity and viscosity coefficients respectively, which have been determined interpolating data tabulated in reference [175], and $\dot{m}_g$ is the hot gas mass flow in the correspondent combustor

zone. The coefficient 0.020 of equation C.46 has been substituted by 0.017 for primary zone calculations, as indicated in [74], to account for the fact that lower than average T_g are present near the wall.

$$C_1 = 0.020 \frac{k_g}{D_{ft}^{0.2}} \left(\frac{\dot{m}_g}{A_{ft}\mu_g} \right)^{0.8} (T_g - T_{w1}) \tag{C.46}$$

External Convection

The eternal convection (C_2) is calculated using equation C.47 given in [74]. Where, k_a and μ_a are the air conductivity and viscosity coefficients respectively, again determined form the tabulated data of reference [175].

$$C_2 = 0.020 \frac{k_a}{D_{ft}^{0.2}} \left(\frac{\dot{m}_{an}}{A_{an}\mu_a} \right)^{0.8} (T_{w2} - T_{03}) \tag{C.47}$$

Substituting equations C.39, C.45, C.46 and C.47 into equation C.37, the system can be solved for T_{w1} and T_{w2}, determining the internal and external uncooled liner wall temperatures.

C.3.2 Cooled Wall Temperature

As mentioned, if the calculated uncooled wall temperatures in any of the combustor primary zones exceed 1300K, cooling is required. The amount of cooling air necessary can be estimated using equation C.48, given in reference [70]. This relation provides the percentage of the total mass flow entering the combustion chamber that has to be used as coolant ($\dot{m}_{cool,\%}$) as function of the inlet flow temperature.

$$\dot{m}_{cool,\%} = 0.1 T_{03} - 30 \tag{C.48}$$

Although multiple techniques are available to cool the liner, film cooling has been traditionally employed on combustors of different dimensions due to its manufacturing simplicity [176]. This technique is based on the idea of isolating the combustor liner from the hot gasses by creating a cold film of coolant in between. Because of turbulence, the film becomes less effective after a certain distance form the cooling slot.

Hence, slots are repeated with an interval of 40 to 80 millimeters to ensure a sufficient cooling effectiveness (ξ_c), [176]. Other important geometrical parameters that have to be establish for an effective film cooling are: the slot height (s), which typically assumes values between 1.5mm and 3mm, the slot wall thickness (t) and the liner wall thickness (t_w) Some of the above mentioned parameters are summarized in the Figure C.6.

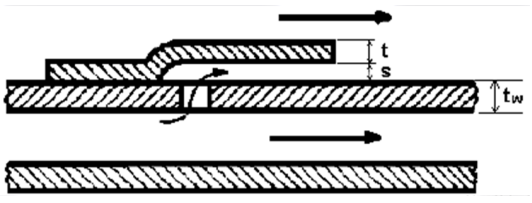

Figure C.6: Cooling slots main geometrical parameters [71]

The slot height and the distance between cooling holes have been assumed equivalent to the minimum of the intervals given to ensure sufficient cooling performance. The slot wall thickness has been calculated assuming a t/s ratio of 0.4, as given in reference [74]. These values might not be accurate for extremely small combustors, however, since no further guidance has been found in literature, further combustor development has been recommended in these cases.

Once these geometrical parameters have been determined, the slot area (A_{slot}) can be calculated using equation C.49 for can and can-annular chambers and equation C.50 for annular combustor [71]. The determination of the slot area is essential to estimate the amount of mass flow flowing through the slot ($\dot{m}_{slot}$).

$$A_{slot} = \pi D_{ft} s \tag{C.49}$$

and

$$A_{slot} = (D_i + D_{an})s + \pi(D_i + 2D_{ref} - D_{an})s \tag{C.50}$$

The slot mass flow can be calculated from equation C.51 [71], after having opportunely defined the slot flow area.

$$\dot{m}_{slot} = \dot{m}_{an} \frac{A_{slot}}{A_{an}} \tag{C.51}$$

The cooling performance are assessed through the evaluation of the wall temperature at a point located just before the next cooling slot. This can be done once the film cooling effectiveness at that particular location has been established. Reference [74] provides a set of empirical relations to determine ξ_c at a certain distance (x) from the slot. In particular, equation C.52 is valid for $0.5 < m < 1.3$ and equation C.53 for $1.3 < m < 4.0$, where m is the mass velocity ratio given as equation C.54 [71].

$$\xi_c = 1.10 m^{0.65} \left(\frac{\mu_a}{\mu_g}\right)^{0.15} \left(\frac{x}{s}\right)^{-0.2} \left(\frac{t}{s}\right)^{-0.2} \tag{C.52}$$

and

$$\xi_c = 1.28 \left(\frac{\mu_a}{\mu_g}\right)^{0.15} \left(\frac{x}{s}\right)^{-0.2} \left(\frac{t}{s}\right)^{-0.2} \tag{C.53}$$

with

$$m = \frac{\rho_a U_a}{\rho_g U_g} = \frac{\dot{m}_{slot}}{\dot{m}_g} \frac{A_{ft}}{A_{slot}} \tag{C.54}$$

From the definition of cooling effectiveness (equation C.55) the adiabatic wall temperature ($T_{w,ad}$) is calculated, which measures the gas temperature close to the liner internal wall.

$$\xi_c = \frac{T_g - T_{w,ad}}{T_g - T_{03}} \tag{C.55}$$

Finally, the wall temperatures T_{w1} and T_{w2} can be established from equation C.37. The only term that is modified by the application of cooling flow is the internal radiation (C_1). Therefore, equations C.56 and C.57 replace equation C.46 for $0.5 < m < 1.3$ and $1.3 < m < 4.0$ respectively.

$$C_1 = 0.069 \frac{k_a}{x} Re_x^{0.7} (T_{w,ad} - T_{w1}) \tag{C.56}$$

and

$$C_1 = 0.1 \frac{k_a}{x} Re_x^{0.8} \left(\frac{x}{s}\right)^{-0.36} (T_{w,ad} - T_{w1}) \tag{C.57}$$

where Re_x is given as:

$$Re_x = \rho_a U_a \frac{x}{\mu_a} \tag{C.58}$$

APPENDIX D

Weight

A sufficient description has been provided in sections 2.4 and 4.5 to understand how the weight model has been built for heat exchangers, combustor, gearbox and accessories. More details are here given for compressor, turbine and shaft weight estimation to provide the reader with a more complete overview of the implemented model.

D.1 Compressor Weight Model

The compressor weight model has been based on what reported in references [83, 84]. The overall compressor stage weight can be approximated with the sum of: blades, disk, shroud, diffuser and case weight. The last three contributions can be easily determined with the information given in section 2.4.2. However, no sufficient level of detail is available in [84] for a complete component weight evaluation, since the calculation procedure for the disk and blades has been just briefly mentioned. Therefore, a model have been developed, using the available geometrical data and considerations reported in literature, to assess their weight contribution. Furthermore, criteria for defining the compressor material and assess its feasibility with respect to the design operating conditions have been discussed here as well.

D.1.1 Material Considerations

Since the component weight can only be assessed once the material density (ρ) has been established, it is necessary to spend few words on material selection criteria, before diving into disk and blades weight modeling. The material is defined from considerations on component operating conditions and minimum weight requirements. In particular, the material has to be able to cope with centrifugal stresses along every operating point within the compressor map.

This imposes a limitation on the maximum rotational speed that the compressor can withstand. Therefore, important material proprieties, which allow to assess the compressor structural feasibility, are: the ultimate yield stress (UYS) and the ultimate tensile stress (UTS). Moreover, these material specifications are dramatically affected by the compressor operating temperatures. In fact, UTS and UYS can drop more that 50% of their value at ambient temperature when the material is exposed to a high temperature environment [132].

Therefore, a library of commonly employed materials has been created using data from [45, 111, 132, 177], including major proprieties used for later feasibility calculations (Table **??**). Depending on the compressor operating temperatures, the following materials have been considered: ferritic stainless steel (AISI416 - Greek Ascoloy), precipitation hardening stainless steel (17-4PH) and titanium based alloys (Ti-6Al-4V and Ti-6Al-2Sn-4Zr-6Mo) for low operating gas temperatures, and, nickel-based alloys (INCO718) for higher temperature ranges.

Table D.1: Compressor materials main parameters

Material	$\boldsymbol{\rho}$ (kg/m^3)	$\boldsymbol{E}$ (GPa)	$\boldsymbol{T_{max}}$ $(^\circ C)$
AISI416	7800	200	750
17-4PH	8030	196	370
Ti-6Al-4V	4500	120	350
Ti-6Al-2Sn-4Zr-6Mo	4540	120	400
IN718	8220	208	580

where, ρ is the material density, E is the Young's modulus and T_{max} is the maximum operating temperature. Important parameters such as UTS and UYS, are strongly function of the operating temperatures and their values drops sharply at high temperatures [132]. Hence, curves similar to Figure D.1 have been digitized and linearly interpolated to model the strength reduction at the impeller exit due to contact with the hot gasses.

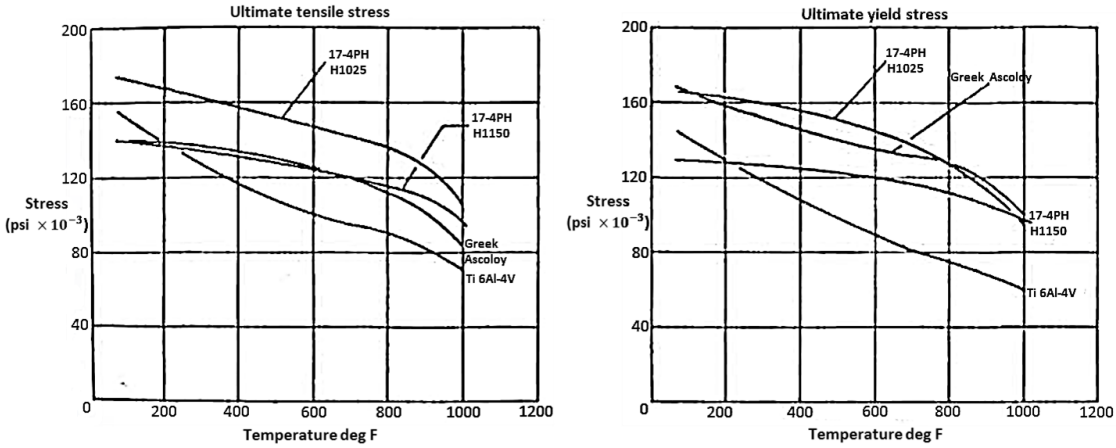

Figure D.1: Temperature effects on UTS and UYS for typical compressor materials [132]

Uniform proprieties and identical materials have been assumed for disk and blades. The library has been linked to the weight model as displayed in Figure 4.7 in the main document.

D.1.2 Disk and Blades

A considerable portion of the compressor overall weight has to be attributed to the contribution of the rotating parts, since most of the stress concentration is there located. In particular, the impeller element is subjected to multiple stress sources such as: centrifugal loads, vibration, distortion at the blade attachment point, due to thermal and centrifugal loads, and, thermal stresses within the blades [178]. In addition, blade tip bending stresses might become significant for heavily backswept impellers [131, 132].

Because these considerations strongly affect the maximum attainable performance of the compressor, it is common practice to integrate the aerodynamic design with the structural design to ensure that feasibility in both domains is maintained. Hence, the final compressor weight is resultant of an optimization tailored towards the maximization of compressor performance for minimal mass [178].

At this stage, it is not possible to completely assess the stress level within disk and blades when defining their volumes. However, simplified structural considerations can be made to verify whether the geometry obtained from the aerodynamic module can be structurally sustainable. Starting from these introductory considerations a disk and blade weight model has been built.

This model has been integrated with the relations presented in section 2.4.2 to compute the full compressor weight.

Stress Calculations

The compressor disk and blades weight assessment starts with an initial material definition. Considering the typical compressor operating conditions given by NPSS in this project, the titanium alloy Ti-6Al-4V has been preliminary selected as candidate material. According to [178], this material offers good strength to weight ratios and it is an optimal solution for typical centrifugal compressor applications.

Two structural checks are subsequently performed on the selected material to assess the resultant impeller disk and blades design feasibility. Centrifugal stresses are calculated by means of equation D.1, given in [131], which allows to estimate the impeller hub peak stress (σ_{disk}) as function of the angular velocity (ω) and the given material density (ρ).

$$\sigma_{disk} = \frac{K_{disk}}{3}\rho\omega^2 r_2^2 \tag{D.1}$$

According to [131], the minimum value achievable of the constant K_{disk} is 0.9. This value can be reached after a careful design with finite elements analysis, which results in an impeller smooth stress distribution. More typical values are between 1.5 and 2.0 for impellers with straight backfaces. Theoretically, the maximum value of K_{disk} possible is 3.0 for cases where the hub bore radius is large with respect to the hub rim radius (thin hoop) [131].

Since centrifugal forces are the only source of stresses considered for the disk at this stage, a value of 3.0 has been conservatively employed. The second source of stresses analyzed is the blade bending stress that have been computed using equation D.2, reported in [132].

$$\sigma_{blade} = \frac{\rho\omega^2 r_2 b_2^2}{t_{hub}^2}(t_{hub} + 2t_{tip})\sin\beta_2 \tag{D.2}$$

Although normally blade bending forces are less meaningful than disk centrifugal stresses, this contribution might become significant in the event of strongly backswept impellers. t_{hub} and t_{tip} are the blade hub and tip thickness that have to be assumed before performing the calculations. Hale [84] suggests to employ a thickness of 0.076cm at the blade tip and to calculate the hub thickness with equation D.3.

$$t_{hub} = \frac{0.15(2\pi r_{1h})}{Z_B} \tag{D.3}$$

However, the WATE-S model discussed in [84] has been developed for compressors having core corrected mass flows between 0.23 and 4.54 kg/s. Considering the operating corrected flow values of this analysis, it has been observed that a better approach to estimate the blade thickness is needed. Reference [179] reports typical blade hub thickness trends as function of the impeller exit radius. These data have been imported and interpolated for a more realistic blade thickness estimation. The blade tip thickness has been calculated assuming a taper ratio (t_{hub}/t_{tip}) of 2.0 [178].

The calculated stresses have been compared with the UTS of the selected material, corrected for the compressor exit temperature as discussed previously. If the calculated values exceeds the material maximum stress, attempt will be made to find, among the available materials of the library, one that can cope with the calculated σ_{disk} and σ_{blade}. In the event that no material can be found, the aerodynamic compressor design has to be refined and failure message will be sent to the optimizer (Figure 4.7). On the other hand, for a successful design, the disk and blades weight is calculated as shown below.

Blades Weight Calculation

The weight of the blades can be calculated by means of equation D.6 once the material has been established and the blade volume has been computed. Several simplifying assumptions are necessary for a preliminary weight estimation. In particular, the flow path has been assumed to be included between two ellipses [84] and a linear taper has been assumed between the blade tip and hub with constant thickness along the blade length [178]. The blade hub and tip thickness has been determined as previously discussed.

Hale [84] suggested to set the axial length to radial height ratio (D_A/D_R) to 2.0 (Figure 2.12). However, current compressor blade design practice involves the application of a circular-arc technique to define the gas path [39]. For this design methodology, references [180, 181] present a relation to calculate the radius of the meridional line (r_m) that allows to better assess the compressor axial length (L_{ax}). This approach has been preferred here.

$$L_{ax} = r_m + \frac{1}{2}b_2 \tag{D.4}$$

with

$$r_m = \frac{2r_2 - (r_{1s} + r_{1h})}{2\cos 4^\circ} \tag{D.5}$$

With this assumption, the ratio D_A/D_R can be properly estimated, improving the original assumption made in reference [84]. Subsequently, the blade volume (V_{BL}) can be finally computed and the blade weight estimated using equation D.6. Where, the coefficient K_{BL} has been introduced to account for the blade curvature not modeled with the presented technique. The value has been set to 1.75 after calibration with the detailed compressor weight breakdown available in [178].

$$W_{BL} = K_{BL}(\rho V_{BL})Z_B \tag{D.6}$$

Disk Weight Calculation

The calculation of the disk weight is much more complex and it is determined by a set of simplifying assumptions made. The volume of the disk (V_{DK}) can be roughly considered as the the volume of the cylinder having as radius r_2 and as height the impeller axial length (L_{ax}), minus the blade channel volume and the shaft volume. The first has been modeled as a quarter of the torus having the ellipse generated by the blade channel, while, the second, with the cylinder created by the shaft.

The disk weight has been calculated as: $W_{DK} = K_{DK}(\rho V_{DK})$. As for the blades, the coefficient K_{BL} has been introduced to calibrate the disk weight model with the general trend defined in reference [83]. A value of 1.45 has been set after this calibration was made.

D.2 Turbine Weight Model

The radial turbine weight estimation strongly resembles the compressor one, since the structure of the rotor is almost identical to the impeller [83, 84]. The overall weight is given as the sum of: blades, disk, shroud and rear frame weights. These lasts two terms have been computed with the equations given in section 2.4.2, while, for the previous terms, a similar approach used for the compressor has been developed.

As shown form the simple turbine weight relation given in [83] and reported as equation 2.48, the primarily weight difference between compressors and turbines is attributed to the higher density materials used in this last components. Section D.2.1 initially discusses turbine

material and structural considerations. Finally, differences with the compressor disk and blades weight calculation procedure are explained in section D.2.2.

D.2.1 Material Considerations

The selection of turbine materials is far more complicated than the compressor case, due to the more complex stress distribution associated to the far greater operating temperatures involved [131, 132]. Typically, cobalt-based or nickel-based alloys are commonly selected for turbine disks and blades, since they offer superior strength capabilities at high temperatures. However, as indicated in [111, 132], different materials may be employed for disk, blades and nozzle, depending on the stress and temperature involved.

Moreover, the simple theory used to preliminary assess compressors disk and blades stresses cannot be comfortably applied to turbines [131, 132], which makes difficult to identify suitable turbine materials at this early stage of the project. Hence, a general value of 7920kg/m^3 has been assumed for the turbine density (ρ), which is in agreement with the typical nickel-based materials employed in turbine disks and wheels, as suggested in [84].

D.2.2 Disk and Blades

The procedure discussed for the calculation of the impeller blades and disk weight contributions has been applied here for the rotor. The same value for the constants K_{BL} and K_{DK} has been reasonably assumed here, considering that the weight difference with the compressor is almost entirely given by the different material densities used [83, 84]. The only remaining difference in the WATE-S model with the compressor weight calculations lies in the definition of the blade flow channels.

Hale [84] suggests to employ an axial length to radial height ratio of 2.1, which slightly differs from the compressor WATE-S model assumption. On the other hand, reference [41] calculates the rotor axial length as function of the rotor inlet tip radius according to: $L_{ax} = 0.7r_2$. Since this approach has been employed in the turbine performance loss models, consistency has been maintained in the weight model by calculating D_A/D_R, having L_{ax} defined as recommended in reference [41].

D.3 Shaft Weight Model

The shaft weight contribution is calculated following the procedure discussed in section 2.4.5. The subsequent assumptions have been made to define the internal and external shaft diameters, and the shaft length used in equations 2.59 and 2.60 to calculate the component weight:

(1) Since the shaft has to fit within the compressor and turbine disks, the maximum possible external diameter (D_o) is given by the smallest available impeller/rotor hub diameter, determined from the component performance model. A 5% clearance has been assumed between the disk hub and the shaft to ensure proper fitting of this last.

(2) Either the inner or outer shaft diameter has to be assumed, and the remaining quantity is calculated from equation 2.59, ensuring structural integrity. The shaft inner diameter (D_i) has been initially assumed null, as suggested in [80], and iteratively modified to meet the previous fitting condition.

(3) The shaft length (L_{sh}) has been determined from the sum of: compressors, combustor and turbines axial length, augmented by an assumed 10% factor to account for combustor, bearings and gearbox spacing [85].

According to [111], the typically employed shaft material is the IN718, which has a density of about 8220kg/m^3, as reported in Table **??**. This material has been assumed for the shaft weight calculation. Since the shaft operating temperature is not available at this stage to determine the maximum admissible shear stress (τ) needed for the component sizing, an average temperature of 300°C has been assumed for the estimation of τ, using data available in [132]. A safety factor of 1.4 has been applied on the resultant τ, as indicated in [182].